Universiteit Leiden
The Netherlands

Microstructural and metabolic alterations in the zebrafish brain induced by toll-like receptor 2 deficiency: insights from ultra-high field magnetic resonance imaging and spectroscopy

Singer, R.

Citation

Singer, R. (2025, March 25). *Microstructural and metabolic alterations in the zebrafish brain induced by toll-like receptor 2 deficiency: insights from ultra-high field magnetic resonance imaging and spectroscopy*. Retrieved from https://hdl.handle.net/1887/4208928

Version:	Publisher's Version
License:	Licence agreement concerning inclusion of doctoral thesis in the Institutional Repository of the University of Leiden
Downloaded from:	https://hdl.handle.net/1887/4208928

Note: To cite this publication please use the final published version (if applicable).

Microstructural and Metabolic Alterations in the Zebrafish Brain Induced by Toll-Like Receptor 2 Deficiency

Insights from Ultra-High Field Magnetic Resonance Imaging and Spectroscopy

Rico Singer

Cover illustration: Ward van Zeijl
Layout: Susanne Ottenheym
Printing: Ridderprint, The Netherlands

© Rico Singer, 2025
All rights reserved. No part of this thesis may be reproduced in any matter or by any means without prior permission from the author.

Microstructural and Metabolic Alterations in the Zebrafish Brain Induced by Toll-Like Receptor 2 Deficiency

Insights from Ultra-High Field Magnetic
Resonance Imaging and Spectroscopy

Proefschrift

ter verkrijging van
de graad van doctor aan de universiteit Leiden,
op gezag van rector magnificus prof.dr.ir. H. Bijl,
volgens besluit van het college voor promoties
ter verdediging op dinsdag 25 maart 2025
klokke 13:00 uur

door

Rico Singer
geboren te 's-Gravenhage, Nederland
in 1993

Promotor

Prof. dr. H.J.M. de Groot

Co-promotor

Dr. A. Alia

Promotiecommissie

Prof. dr. M. Ubbink

Prof. dr. H.P. Spaink

Prof. dr. J.J. Prompers (Maastricht University)

Prof. dr. M. Baldus (Universiteit Utrecht)

Dr. A. Pandit

TABLE OF CONTENTS

List of Abbreviations 06

CHAPTER 1 10
General introduction and theoretical background

CHAPTER 2 64
Unveiling the Exquisite Microstructural Details and White Matter Tracts in Adult Zebrafish Brain Using 28.2 T MRI

CHAPTER 3 88
Ultra-high field diffusion MRI uncovers intriguing microstructural changes in the adult zebrafish brain caused by TLR2 genomic deletion

CHAPTER 4 122
Unbeatable super-resolution of voxel-based MR spectroscopy of zebrafish brain achieved at 28.2 T

CHAPTER 5 152
Localized MRS at 28.2 T reveals alteration of cerebral metabolites in toll-like receptor 2 deficient zebrafish

CHAPTER 6 180
Conclusions and Future Outlook

Summary 192
List of Publications 202
Curriculum Vitae 204
Acknowledgements 205

LIST OF ABBREVIATIONS

ABBREVIATIONS	DEFINITION
ADC	Apparent diffusion coefficient
ADHD	Attention deficit hyperactivity disorder
Ala	Alanine
Asp	Aspartate
Cans	Ansulate commissure
CB	Cerebellum
CCeg	Granular layer of the cerebellar corpus
CCem	Molecular layer of the cerebellar corpus
Cgus	Commissure of the secondary gustatory nuclei
Cho	Choline
Chol	Cholesterol
CNR	Contrast-to-noise ratio
CNS	Central nervous system
CPMG	Carr-Purcell Meiboom-Gill
Cpost	Posterior commissure
CSD	Constraint spherical deconvolution
CSF	Cerebrospinal fluid
CT	Computed tomography
Cven	Ventral rhombencephalic commissure
CW	Continuous wave
$D_{\parallel}$	Axial diffusivity
$D_{\perp}$	Radial diffusivity
DALY	Disability-adjusted life year
DAMP	Danger-associated molecular pattern
DC	Diencephalon
DEC	Directional encoded colour
DIL	Diffuse nucleus of the inferior lobe
DKI	Diffusion kurtosis imaging

DM	Medial zone of dorsal telencephalon
dMRI	Diffusion-based magnetic resonance imaging
DTI	Diffusion tensor imaging
DW	Diffusion weighted
DWI	Diffusion-weighted imaging
EPI	Echo-planar imaging
ETL	Echo train length
FA	Fractional anisotropy
FID	Free-induction decay
fODF	Fibre orientation distribution functions
FOV	Field of view
GABA	γ-aminobutyric acid
G_{diff}	Diffusion gradient
G_f	Frequency encoding gradient
Gln	Glutamine
Glu	Glutamate
GM	Grey matter
G_p	Phase encoding gradient
G_s	Slice encoding gradient
HR-MAS	High-resolution magic angle spinning
ISIS	Image selected *in vivo* spectroscopy
$K_{\parallel}$	Axial kurtosis
$K_{\perp}$	Radial kurtosis
KFA	Kurtosis Fractional anisotropy
KO	Knock-out
Lac	Lactate
LASER	Localization by adiabatic selective refocusing
LLF	Lateral longitudinal fascicle
MC	Mesencephalon
MD	Mean diffusivity
m-Ins	*Myo*-inositol
MK	Mean kurtosis
MLF	Medial longitudinal fascicle

MRI	Magnetic resonance imaging
MRS	Magnetic resonance spectroscopy
MSME	Multi-slice multi-echo
msmt	Multi-shell multi-tissue
NAA	N-acetylaspartate
NAAG	N-acetylaspartyl-glutamate
NMR	Nuclear magnetic resonance
OB	Olfactory bulb
OT	Optic tract
OVS	Outer volume suppression
PA	Pallium
PAMP	Pathogen-associated molecular pattern
pCho	Phosphocholine
PRESS	Point resolved spectroscopy
PRR	Pattern recognition receptors
RARE	Rapid acquisition with relaxation enhancement
RC	Rhombencephalon
RF	Radio frequency
ROI	Region of interest
SNR	Signal-to-noise ratio
STEAM	Stimulated echo acquisition mode
stTDI	Short-track track-density imaging
T	Tesla
T_1	Longitudinal relaxation time
T_2	Transverse relaxation time
Tau	Taurine
tBW	Transmission bandwidth
tCr	Total creatine
TE	Echo time
TeO	Optic tectum
TL	Longitudinal torus
TLR	Toll-like receptor
TR	Repetition time

UHF	Ultra-high field
WM	White matter
WS	Water suppression
YLD	Years lived with disability

1

GENERAL INTRODUCTION AND THEORETICAL BACKGROUND

Neurological disorders are the leading cause of diminished health and disabilities worldwide[1]. Approximately 43.1% of the world population, or 3.40 billion individuals, are estimated to have a neurological disorder affecting their central nervous system (CNS); an increase of 58.8% compared with 1990. In addition to the growing number of individual cases, the total disability-adjusted life years (DALYs) of neurological disorders, a method to measure the burden of a disease or condition, increased by 18.2% since 1990[1] (see Figure 1.1). Strokes, neonatal encephalopathy, migraine, dementia, diabetic neuropathy, meningitis, epilepsy, pre-term birth, autism spectrum disorder, and nervous system cancer constitute the top ten major contributors of neurological conditions with the highest DALYs, many of which reported an increase in occurrence since 1990 (see Figure 1.1). Besides significant personal

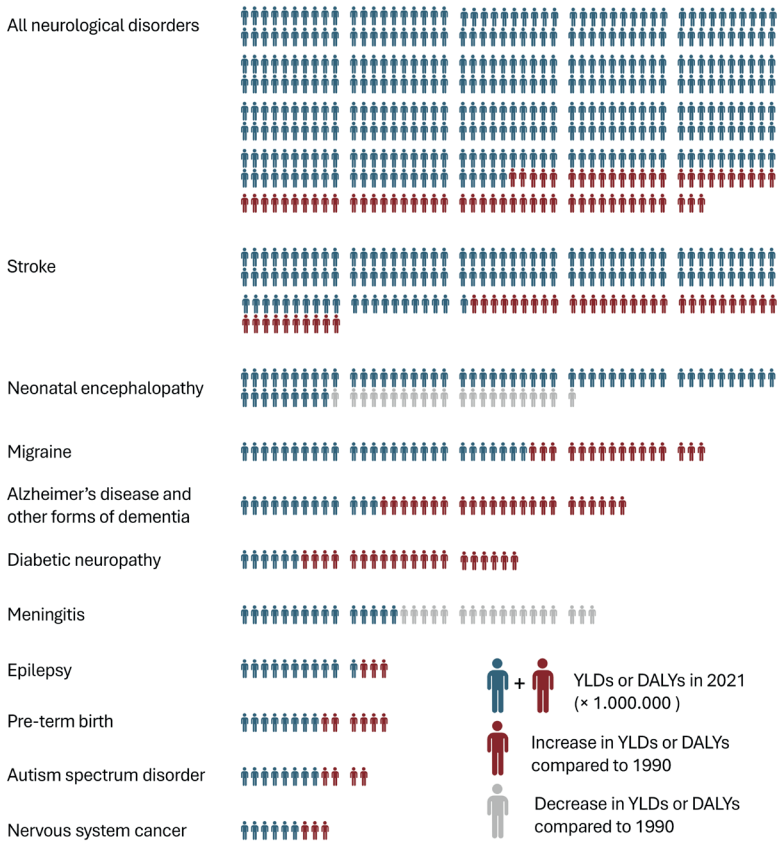

Figure 1.1 *Total number of years lived with disability (YLDs) or disability-adjusted life-years (DALYs) for the top ten neurological disorders from 204 countries and territories in 2021, compared to 1990. Each Figure represents one million (1 000 000) counts. For visualization purposes, numbers have been rounded to the nearest million count. Data obtained from the G. B. D. Nervous System Disorders Collaborators[1].*

impact, neurological disorders impose a substantial economic impact; the annual costs were estimated at approximately 800 billion US dollars in both the United States of America and Europe[2,3]. These numbers are expected to escalate in the coming decades. For instance, the number of people suffering from Alzheimer's disease, the most common form of dementia, is projected to rise from 48 million in 2015 to 131.5 million in 2050, an astonishing increase of 274% in 35 years[4]. The projected growth in the number of patients, combined with rising costs and a current lack of effective treatments for many neurological disorders, underscores the urgent need for scientific research focused on understanding the underlying pathological mechanisms and developing potential therapies.

Animal models of human neurological disorders play a crucial role in many scientific studies[5,6]. These models allow researchers to study the complexities of neurological diseases, facilitating a comprehensive understanding of their development and progression. To a much higher level than possible with human subjects, animal models enable longitudinal studies that track the pathological progression from very early stages, or even before the onset of the disease, providing invaluable insights into the earliest detectable changes. Additionally, animal models offer the unique advantage of controlled experimental conditions, which are often not feasible in human studies. This control allows for precise manipulation of variables and detailed observation of the effects of potential therapies over extended periods. Researchers can systematically explore the efficacy and safety of new treatments, identify potential side effects, and refine therapies with a level of detail and accuracy that is unattainable in human clinical trials. Moreover, animal models allow studying the genetic, molecular, and cellular mechanisms underlying neurological disorders. By replicating specific aspects of human diseases in animals, scientists can investigate the role of genes, proteins, and cellular processes in disease onset and progression. This knowledge is essential for identifying novel therapeutic targets and developing treatments that can more effectively address the root causes of these conditions.

1. NEUROLOGICAL CONDITIONS, THE IMMUNE SYSTEM, AND TOLL-LIKE RECEPTORS

1.1 The immune system

Many neurological disorders are intricately linked to the immune system. Conditions including multiple sclerosis[7], Alzheimer's disease[8], and Parkinson's disease[9] show significant associations with immune system dysregulation. The immune system operates on two primary defence mechanisms: innate immunity and adaptive immunity. The adaptive immunity is a specialised defence mechanism that recognises and targets specific pathogens. Its receptors

are formed through the somatic recombination of gene segments, allowing the immune system to recognise a wide variety of pathogens and mount specific responses against them. This process enables the immune system to adapt to the extensive diversity of antigenic structures and the adaptive capabilities of pathogens to mutate[10]. Despite the versatility of the adaptive immune system, it is slow, potentially requiring weeks to mount a specific response against new pathogens[10]. This timeframe includes the activation and proliferation of antigen-specific T and B lymphocytes, leading to the production of antibodies and memory cells that provide long-term immunity. Conversely, the innate immune system is the body's first line of defence against many pathogens. It encompasses physical barriers such as the skin and immune cells that engulf and eliminate invaders. These immune responses are facilitated by recognition receptors encoded in the germline genome, enabling rapid reactions against a broad spectrum of pathogens. Part of innate immunity relies on specific molecular determinants that initiate immune responses, recognised by pattern recognition receptors (PRRs). PRRs recognise a broad range of pathogen-associated molecular patterns (PAMPs), originating from potential invasive pathogens, including fungi, bacteria, parasites, and viruses[11]. Due to their indispensable roles, many PAMPs exhibit high degrees of conservation and are resistant to mutations that could potentially compromise their functionality[12]. Beyond PAMPs, PRRs recognise danger-associated molecular patterns (DAMPs), endogenous molecular determinants released during processes including infection, inflammation, and cellular stress[13,14]. DAMPs signal danger to the immune system, triggering inflammatory responses and facilitating tissue repair. The PRRs of the innate immunity are categorised in eight groups: toll-like receptors (TLR), C type lectin receptors (CLR), nucleotide-binding oligomerisation domain-like receptors (NLR), retinoic acid-inducible gene-I-like receptors (RLR), opsonic receptors, AIM2-like receptors (ALR), scavenger receptors, and stimulator of interferon genes (STING)[15].

1.2 Toll-like receptors

Of the eight PRR groups, TLRs are the most studied for they are seen as the primary triggers of innate immune responses[15]. Specific TLRs are essential for distinguishing unique PAMPs and DAMPs, playing a crucial role in the immune response. TLRs are type I integral transmembrane proteins consisting of three main regions: the N-terminal domain, the transmembrane domain, and the C-terminal domain. The ligand binding domain at the N-terminus is responsible for the recognition and binding of PAMPs and DAMPs and located in the ectodomain, extending into the extracellular space. This TLR region is crucial for ligand binding and consists of 16 – 28 Leucine-rich repeats (LRRs) with a horseshoe shape, resembling structures formed by parallel β strands[16]. Conventionally, TLRs are categorised based on their cellular location, either on the cell surface or within the intracellular endosomal membrane. The key differences between TLRs located on the cell surface and those within the endosomal membrane are the types of molecular determinants they recognise and their roles in immune signalling. For

humans, TLR1, TLR2, TLR4, TLR5, TLR6, and TLR10 are located on the cell surface recognizing microbial ligands expressed in the cell wall of pathogens. TLR2 forms heterodimers with TLR1, TLR6, and TLR10 and recognises a wide range of microbial ligands, including triacylated lipoproteins, diacylated lipoproteins, and peptidoglycan (PGN)[17]. Furthermore, TLR4 recognises lipopolysaccharide (LPS) and TLR5 recognises the flagella of motile bacteria[12]. Conversely, TLR located on endosomal membranes bind and recognise pathogen-derived nucleic acid motifs present inside the intracellular space[12]. In humans, these concern TLR3, TLR7, TLR8, and TLR9. TLR3 recognises viral double-stranded RNA (dsRNA), TLR7 and TLR8 single-stranded RNA (ssRNA), and TLR9 the nonmethylated 5'-C-phosphate-G-3' motifs in the DNA (CpG DNA) of viruses and bacteria[12]. The transmembrane domains of TLRs are characteristic of

Table 1.1 *Toll-like receptors identified in humans, mice, and zebrafish*[17,22,23]

Human (*Homo sapiens*)	**Mouse (*Mus musculus*)**	**Zebrafish (*Danio rerio*)**
TLR1	TLR1	TLR1
TLR2	TLR2	TLR2
TLR3	TLR3	TLR3
TLR4	TLR4	TLR4al TLR4ba TLR4bb
TLR5	TLR5	TLR5a TLR5b
TLR6	TLR6	
TLR7	TLR7	TLR7
TLR8	TLR8	TLR8 TLR8a TLR8b
TLR9	TLR9	TLR9
TLR10		
	TLR11	
	TLR12	
	TLR13	
		TLR14
		TLR18
		TLR19
		TLR20a TLR20b
		TLR21
		TLR22

single-pass membrane proteins, consisting of a single transmembrane α-helix that connects the N-terminal extracellular domain to the C-terminal intracellular domain. This region is responsible for anchoring the receptor to the membrane[18]. Finally, the toll-interleukin-1 receptor homology (TIR) at the C-terminus extends into the intracellular space. The TIR is composed of approximately 150 amino acids and initiates signalling. Downstream signalling of TLR after activation is, roughly, defined through two pathways. The majority of TLRs in humans, except TLR3, initiate downstream signalling by recruiting myeloid differentiation primary response 88 (MyD88)[12,19]. Subsequently, MyD88 interacts with Interleukin-1 receptor-associated kinase-4 (IRAK-4), interacting with IRAK-1 and IRAK-2[20]. The IRAKs dissociate from MyD88 and interact with tumor necrosis factor (TNF) receptor-associated factor adaptor protein (TRAF6). TRAF6 subsequently generates the formation of an unconjugated free polyubiquitin chain onto itself[21], which leads to the release of nuclear factor-kappa B (NF-κB), regulating a wide range of immune response genes[12,19]. The second pathway, utilized by TLR3 after dsRNA stimulation, involves the TIR domain-containing adaptor-inducing interferon-β (TRIF). This pathway activates interferon regulatory factor 3 (IRF3), leading to the induction of type I interferons[12,19]. Additionally, TLR4 can initiate the TRIF pathway through the TRIF-related adaptor molecule (TRAM), alongside the MyD88 pathway[12,19].

The number of TLRs varies across species; humans (*Homo sapiens*) possess 10 TLRs, mice (*Mus musculus*) have at least 12 TLRs, and zebrafish (*Danio rerio*) have 20 functional TLRs encoded in their genomes[17,22,23] (see Table 1.1). Additionally, the expression patterns of TLRs differ among species. For instance, in zebrafish, TLRs are highly expressed in the skin, indicating that the skin plays a crucial role in the immune system of zebrafish[24].

1.3 Toll like receptors in neurological disorders

Aside from their presence in cells of the innate immune system, TLRs are expressed in different cells in the CNS. For example, human microglia express TLR 1-9, astrocytes express TLR2, TLR3, and TLR9, oligodendrocytes express TLR2 and TLR3, and neurons express TLR3 and TLR7-9[12]. While TLRs play a positive role in the brain by contributing to neurogenesis, cognitive functioning, behaviour, and neuronal growth and morphology (reviewed by Acioglu, Heary, and Elkabes[25]), their involvement is not without complications. TLR-mediated neuroinflammation, for instance, has been linked to the development of various neurological disorders, encompassing both infectious and non-infectious conditions.

Bacterial meningitis is a prime example of an infectious condition where TLR-initiated pathways cause severe neurological damage. During bacterial meningitis, pathogens breach the blood-brain barrier (BBB) and enter the subarachnoid space. In this space, pathogens rapidly replicate because the immune system is not activated until a high density of pathogens is reached[26].

This delay in immune response allows the infection to escalate unchecked. Bacterial meningitis results in severe, life-threatening inflammation within the subarachnoid space. However, the tissue damage associated with this condition is primarily due to an overreaction of the immune system rather than the direct effect of the pathogens themselves[27,28]. In this context, TLRs, specifically TLR2 and TLR4, play a critical role in initiating the biological processes and pathways that lead to immune dysregulation and subsequent neurological damage. These TLR-mediated pathways highlight the dual role of TLRs in both protecting the CNS and contributing to its vulnerability during infections.

TLRs were revealed to potentially play a role in the pathology of non-infectious neurological disorders, including in Alzheimer's disease[29]. Alzheimer's disease is the most prevalent form of dementia, characterised by progressive cognitive decline that interferes with daily functioning. Amyloid beta (Aβ) plaques, composed of misfolded and aggregated Aβ peptides, play a pivotal role in Alzheimer's pathology. These plaques accumulate outside neurons and are implicated as the driving force behind subsequent abnormalities in the brain, triggering events leading to neurodegeneration. Aβ plaques stimulate neuroinflammatory responses, involving microglia and astrocytes, which further exacerbate neuronal damage. It also has been proposed that neuroinflammatory processes are the main event in Alzheimer's disease pathology[29-31]. The exact role TLRs play in Alzheimer's disease pathology is still under debate. Increased expression of TLR1, TLR2, TLR4, and TLR6 was found in human Alzheimer's disease patients and in Alzheimer's disease animal models or animal models with increased Aβ[32-39]. In the case of TLR9, research reports are inconsistent, showing both increased[34,36] and decreased[32] expression levels in Alzheimer's disease. In addition, there is evidence of disrupted TLR signalling pathways in Alzheimer's disease[40]. However, the activation of several TLRs, specifically TLR2 and TLR4, show conflicting effects on the pathology of Alzheimer's disease. In the case of TLR4, activation on the one hand leads to enhanced removal of cellular waste[41], increased Aβ clearance[42], lower memory disfunction, Aβ deposition, and the increased production of neuroprotective factors and anti-inflammatory cytokines[43,44]. Conversely, other reports show that Aβ induced activation of TLR4 promotes the production of pro-inflammatory cytokines, which triggers astrocyte activation and contributes to amyloid-dependent neuronal death[45]. Similarly, activating TLR2 can enhance Aβ clearance[46]. Animal models of Alzheimer's disease deficient in TLR2 exhibit a more rapid decline in memory and cognitive functions compared to a control group[47]. These models also show elevated levels of Aβ and TGF-β[48], greater neuronal death, brain atrophy, learning impairments, and diminished glial activity[49] compared to control groups. However, other studies suggest TLR2 activation may significantly contribute to Alzheimer's disease pathology through TLR2 induced NF-κB signalling leading to excessive Aβ production[50].

Besides Alzheimer's disease, TLRs potentially play an important role in the pathology of other non-infectious neurological disorders, including in Parkinson's disease[51], amyotrophic lateral sclerosis (ALS)[52], and ischemic strokes[53]. Despite evidence suggesting their involvement, the precise mechanisms by which TLRs influence disease progression are not fully understood. This highlights the need for further research to elucidate their functions and therapeutic potential in neurological disorders.

To study the role specific TLRs play in normal functioning and in pathology, many studies utilize TLR-deficient models. These models help in understanding the intricate mechanisms and pathways associated with TLRs. Among these, zebrafish models have become increasingly popular due to their genetic similarities to humans and the ease of genetic manipulation. TLR-deficient zebrafish models offer valuable insights into the physiological and pathological roles of TLRs, providing a robust platform for further research. In this thesis, a TLR2-deficient zebrafish model is utilized to study the role of TLR2 on normal brain function. The TLR2-deficient zebrafish model is the tlr2^{sa19423} mutant, referred to as *tlr2*$^{-/-}$. It has a thymine to adenine point mutation that creates a premature stop codon. This mutation occurs in the sequence coding for the C-terminus of the leucine-rich repeat (LRR) domain. As a result, the protein is truncated and lacks the Toll/IL-1 receptor (TIR) domain[54]. Previously, Hu *et al*. utilized this TLR2-deficient zebrafish model to study the effect of TLR2 on the metabolic profile in zebrafish larvae[15]. Their research demonstrated that the absence of TLR2 significantly altered the metabolic pathways, providing crucial insights into how TLR2 influences metabolic processes[15].

2. ZEBRAFISH IN NEUROLOGICAL BIOMEDICAL RESEARCH

Mammalian models, particularly rodents, are intensively used for studying neurological conditions for their anatomical and physiological similarities to humans. Many mammalian species have genetic sequences highly homologous to human, allowing gene function studies and disease mechanisms relevant to human conditions. For example, mice share approximately 85% of their protein-encoding genomes with humans[55-58]. Despite these advantages, mammalian models often provide limited high-throughput screening capabilities due to their labour-intensive care requirements[59]. This necessitates a large, specialised staff and infrastructure, significantly increasing both research costs and time. Given these challenges, the zebrafish, a tropical fish native to the southern regions of Asia, developed as a popular alternative model organism in biomedical research. Following its first use as a model organism for studying vertebrate neuronal development by George Streisinger in the 1960s, a groundbreaking paper in 1981 introduced genetic techniques for generating homozygous diploid zebrafish clones[60]. However, it wasn't until the late 1990s that the zebrafish gained

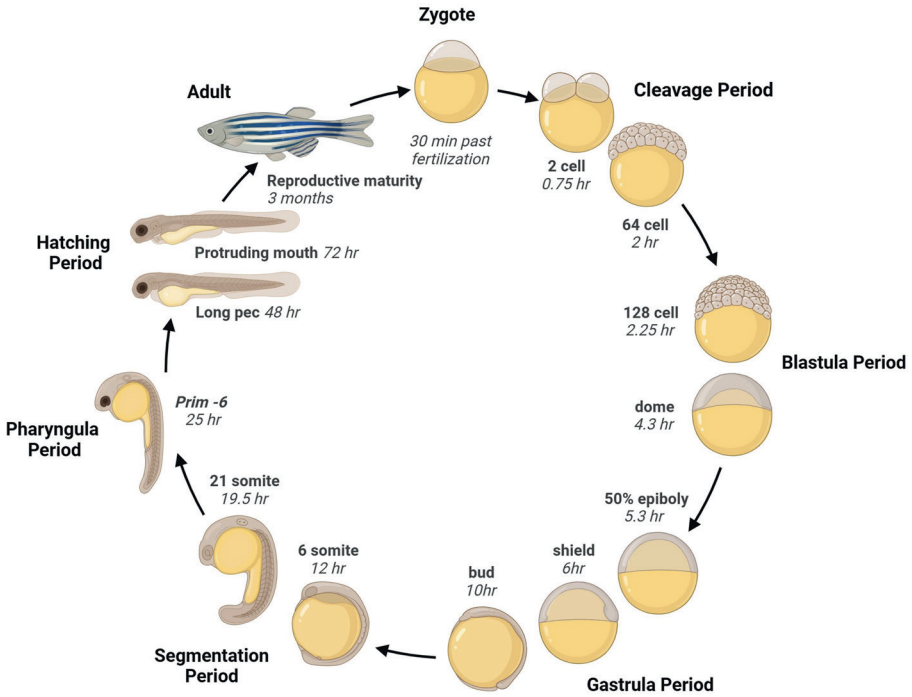

Figure 1.2 *Developmental stages of the zebrafish. After fertilization, the zebrafish embryo develops rapidly, hatching as free-swimming larvae after approximately two days. Next, they reach reproductive maturity after approximately three months. Created with zebrafish developmental timeline template of Biorender.com and printed with permission.*

significant popularity as a model organism in biomedical research, largely due to the pioneering work of Christiane Nüsslein-Volhard (Tübingen, Germany), and Wolfgang Driever and Mark Fishman (Boston, USA)[61].

Compared to other model organisms used in biomedical research, zebrafish offer various advantages to explain their widespread popularity. Female zebrafish reach reproductive maturity within three months and produce approximately 200 to 300 eggs per week. This enables rapid reproduction of transgenic models, facilitating high-throughput experimental screening. In addition, the development of zebrafish embryos and larvae progresses swiftly after *ex vivo* fertilization (see Figure 1.2). Additionally, the transparent nature of zebrafish embryos and larvae allows for internal structures visualization under microscopes. This transparency makes zebrafish exceptionally suitable for monitoring developmental processes. Furthermore, the complete sequencing of the zebrafish genome revealed 84% of genes

associated with human diseases possess corresponding homologous genes in the zebrafish genome. This, coupled with the relative ease of manipulating zebrafish genes, facilitated the creation of numerous mutations in the zebrafish genome, paving the way for the development of many zebrafish models for studying a broad spectrum of pathological conditions.

For biomedical research specifically focussed on neurological disorders, zebrafish gained significant popularity in the last few decades as illustrated in Figure 1.3. Given the obvious anatomical and physiological differences between humans and zebrafish, the organisation of their central nervous systems exhibits remarkable similarities[62]. Various structures in the zebrafish brain exhibit homology with those found in the human brain. For example, the zebrafish telencephalon, situated in the forebrain, consists of the olfactory bulb, pallium, and subpallium. The olfactory bulb is involved in processing of smell related sensory information in both humans and zebrafish, whereas the zebrafish dorsal pallium, medial pallium, lateral pallium, and ventral pallium, are homologues of the human isocortex, amygdala, hippocampus, and piriform cortex, respectively[62]. Furthermore, the zebrafish and human brain alike contain a similar blood brain barrier, protecting the brain from potentially harmful substances while maintaining the brain's internal environment[63]. At the cellular level, the composition of the zebrafish brain closely resembles that of the human brain. Alongside neurons, the zebrafish brain contains similar cells including oligodendrocyte and microglia cells. However, notable differences exist, as zebrafish lack classic stellate astrocytes[64]. Instead, zebrafish fulfil the

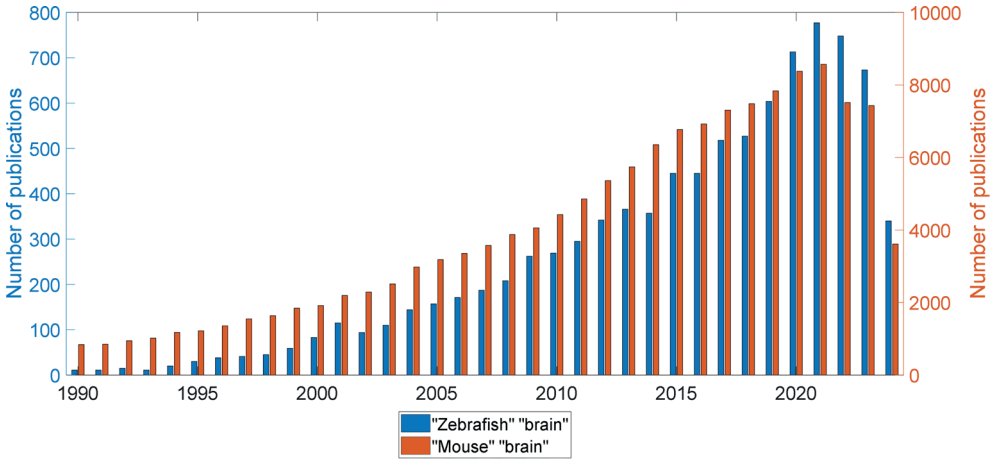

Figure 1.3 *Publication count concerning the zebrafish brain and mouse brain in the pubmed database (National Library of Medicine, National Center for Biotechnology Information, Bethesda, MD, USA). Data acquired by searching for "zebrafish" "brain", and "mouse" "brain", respectively.*

functions typically carried out by mammal astrocytes through radial glial cells[64]. Despite these distinctions, the zebrafish radial glial cells are commonly referred to as astrocytes in literature due to their striking similarities. At the molecular level, the cerebral metabolic profile of zebrafish is remarkably similar to humans and other mammals[65-67], containing identical neurotransmitters, including the main excitatory and inhibitory neurotransmitters glutamate and γ-aminobutyric acid (GABA), respectively. Furthermore, both the zebrafish and human brain contain the same various cell-specific metabolites, including *myo*-inositol (m-Ins) and N-acetylaspartate (NAA), for glial cells and neurons, respectively.

Today, a wide range of transgenic zebrafish models are available for use in biomedical research, covering various neurological disorders. Transgenic models have been developed for neurodevelopmental disorders, including attention deficit hyperactivity disorder (ADHD)[68] and autism spectrum disorders (ASDs)[69]. In the field of neurodegenerative disorders, zebrafish models exist for Alzheimer's disease[70], amyotrophic lateral sclerosis (ALS)[71], Huntington's disease[72], and Parkinson's disease[73]. Additionally, there are models for stroke[74] and cerebrovascular disorders[75], epilepsy and other seizure disorders[76], autoimmune conditions including multiple sclerosis (MS)[77], Schizophrenia[78], traumatic brain injury[79], and brain cancers including glioblastoma[80]. Most biomedical research utilizing zebrafish as a model for neurological conditions focus on several key areas. These include the pathological impact on developmental progression to monitor how neurological disorders manifest and progress over time. Behavioural studies are utilized to monitor behavioural changes associated with neurological disorders, providing insights into the effects of these conditions on motor function, cognition, and social behaviours. Furthermore, transcriptomic studies help identify key genes and molecular pathways involved in the onset and progression of these disorders, while metabolomic studies can identify metabolic changes related to neurological disorders. These studies provide insights into the biochemical pathways and metabolites involved in disease mechanisms, potentially revealing new targets for therapeutic intervention[81]. Finally, for their advantages in comparison to rodents, zebrafish are employed in high-throughput drug screening to identify potential therapeutic compounds and test for toxicity.

3. MAGNETIC RESONANCE IMAGING AND MAGNETIC RESONANCE SPECTROSCOPY

Among the various techniques utilized and discussed in this thesis, magnetic resonance imaging (MRI), diffusion-based MRI (dMRI), and localized magnetic resonance spectroscopy (MRS) stand out as the most important contributors. This section serves as an introduction to the theoretical and technical background of these techniques.

MRI is a well-established non-invasive technique for neurological diagnostics and in biomedical research. Up to date, MRI is the most precise technique for producing highly detailed images of the brain, outperforming other techniques including computed tomography (CT) or Röntgen radiation (X-ray). MRI is a versatile imaging technique capable of creating various types of contrast by exploiting different tissue properties such as proton density, T_1, T_2, diffusion characteristics, or magnetization transfer. This allows for a wide range of contrast options tailored to specific needs. MRI not only differentiates between various cerebral tissue types, including white matter, grey matter, and cerebrospinal fluids, MRI is applied in the diagnostics of a wide range of neurological conditions including brain tumours[82], brain infections[83], brain damage[84], strokes[85], hydrocephalus[86], and intracranial haemorrhage[87]. For many of these conditions, non-invasive diagnostics would not be possible without MRI.

Closely related to NMR, localized MRS is a non-invasive technique to locally provide quantitative biochemical information. However, unlike traditional NMR, localized MRS allows for the selection of a specific region of interest (ROI) through the MRI gradient systems. Hence, the biochemical composition of specific tissue can be monitored in their native biological environment, eliminating the need for laborious extraction procedures. Although MRS is employed for various tissue types[88-91], clinical applications mainly focus on brain tissue and neurological disorders[92-98]. Significant changes in cerebral metabolites have been detected in various neurodegenerative diseases[49,99-111], providing invaluable quantitative biochemical information regarding pathological progression.

In Section 1.3.1, the basics of nuclear magnetic resonance (NMR) are discussed, the foundation upon which MRI, dMRI, and localized MRS are built. Section 1.3.2 treats MRI, covering MRI image construction, generating contrast in MRI, and various MRI pulse sequences utilized in the main work of this thesis. In Section 1.3.3, dMRI is discussed, covering the basic concept of dMRI, diffusion-weighted imaging (DWI), diffusion tensor imaging (DTI), diffusion kurtosis imaging (DKI), and dMRI tractography. Next, in Section 1.3.4, the theoretical background of localized MRS is discussed. Finally, as the main work discussed in this thesis was performed using ultra-high field (UHF) MRI systems, the opportunities and challenges of utilizing these systems is treated in Section 1.3.5.

3.1 Physical basis of nuclear magnetic resonance techniques

MRI and localized MRS are based on the principles of NMR. The NMR phenomenon was first observed in 1946 by two independent research groups; the group of Bloch, Hansen, and Packard[112], and the research group of Purcell, Torrey, and Pound[113], for which Bloch and Purcell received the Nobel Prize for physics in 1952[114]. In this section, the basics of the NMR phenomena are discussed, essential for understanding the foundations upon which this thesis

is constructed. The information provided in this section is mainly provided by "Basic one- and two-dimensional NMR spectroscopy, by Horst Friebolin"[115], unless stated otherwise.

NMR spectroscopy is based upon the interaction between nuclei with a non-zero nuclear spin I and an external magnetic field $\mathbf{B}_0$. Biologically significant chemical elements with NMR detectable isotopes are ^{1}H, ^{13}C, ^{31}P, and ^{15}N, with spin I = ½. Nuclei with I = 0 include ^{12}C and ^{16}O, implying two of the abundant isotopes found in organic compounds cannot be detected through NMR. Isotopes with I > ½ also exist, *e.g.* ^{14}N (I = 1), ^{23}Na (I = 3/2), or ^{43}Ca (I = 7/2). The focus of this thesis is on the abundant I = ½ ^{1}H nuclei.

In a simplified view, nuclear spins may be seen as tiny magnets. In the absence of an external magnetic field, the individual nuclear moments ($\boldsymbol{\mu}_i$) are randomly oriented, and their sum results in no net magnetization $\mathbf{M}$ (see Figure 1.4). However, in an external static magnetic field $\mathbf{B}_0$, the z-component of the nuclear spin angular momentum $\mathbf{I}_z$ is quantified over $2I + 1$ possible spin states. The spin states are indicated by the magnetic quantum number m, with $m = I, I\text{-}1, \ldots -I$. For nuclear spins with I = ½, the spin states are commonly referred to as α (m = ½, parallel to $\mathbf{B}_0$) and β (m = -½, anti-parallel to $\mathbf{B}_0$). The energy difference ΔE between the spin states α and β is

$$\Delta E = \gamma \cdot \hbar \cdot B_0 \tag{1.1}$$

where γ is the gyromagnetic ratio ($26.7522 \cdot 10^7$ rad T^{-1} s^{-1} for ^{1}H), $\hbar$ is $h/2\pi$, with h being

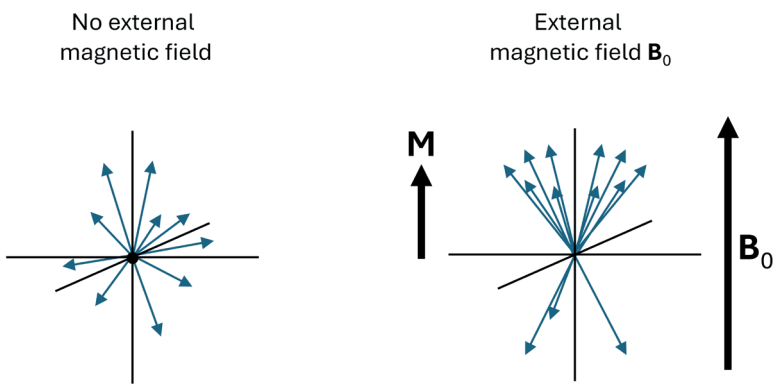

Figure 1.4 *Without an applied magnetic field, spins are randomly oriented, and there is no net nuclear magnetization* ***M****. When an external magnetic field* $\mathbf{B}_0$ *is applied, the z-component of the nuclear spin angular momentum aligns either parallel or antiparallel to* $\mathbf{B}_0$*. Due to a slight preference for parallel alignment over antiparallel alignment, a net magnetization* ***M*** *is generated.*

Table 1.2 *Magnetic field strengths used in NMR and MRI, denoted in Tesla (T) and the Larmor frequency of hydrogen (MHz). *Larmor frequencies were rounded to their conventionally used value.*

Magnetic field strength (T)	Larmor frequency ^{1}H (MHz)*
1.5	64
3	128
7	300
14.1	600
17.6	750
22.3	950
28.2	1200

Planck's constant (6.6256 · 10^{-34} J s), and B_0 is the magnetic field strength in Tesla, with $1\mathrm{T} = 1\left(\frac{\mathrm{N}}{\mathrm{A \cdot m}}\right)$. The energy difference between the α and β spin states leads to a difference in population due to the Boltzmann distribution, where nuclei occupy the lower-energy α-state more frequently at thermal equilibrium. The nuclear spin state population ratio

$$\frac{N_\beta}{N_\alpha} = e^{\left(\frac{-\Delta E}{k_\mathrm{B} T}\right)} \tag{1.2}$$

is estimated using the Boltzmann distribution. Here, k_B is the Boltzmann constant (1.3805·10^{-23} J K^{-1}) and T is the absolute temperature in K.

The energy difference between the spin states α and β creates a minimal population disparity between β and α states, resulting in a relatively small **M**. Consequently, NMR based techniques have a low sensitivity compared to other analytical techniques. A way of improving the sensitivity of NMR is to increase $\mathbf{B}_0$. Table 1.2 provides an overview of magnetic field strengths (in T and Hz) typically utilized in NMR and MRI systems, as well as in the present study. It is common practice to denote the field strength by referencing the precession frequency of ^{1}H at the corresponding magnetic field strength. The precession frequency, or Larmor frequency ν_L, is given by

$$\nu_\mathrm{L} = \left|\frac{\gamma}{2\pi}\right| B_0 = \frac{\Delta E}{h} \tag{1.3}$$

Hence, a 14.4 T NMR system is also commonly referred to as a 600 MHz system.

3.2 Magnetic resonance imaging

Magnetic resonance imaging (MRI) is a well-established, powerful, non-invasive technique primarily used in the clinical field for imaging soft tissues. Its popularity in clinical settings can be attributed to its relative safety. It does not involve ionizing radiation as used in computed tomography (CT) scans, while offering superior image quality with exceptional detail. MRI can provide remarkable structural details in various soft tissues, including the lungs[116], stomach[117], brain[118], muscles[119], liver[120], breasts[121], kidneys[122], and the heart[123], making it invaluable for monitoring a wide range of pathologies and disorders. Outside the clinical field, MRI is extensively used in research, not only for humans but also for other organisms including rodent models[124], zebrafish models[125], and plants[126]. MRI offers a diverse range of experimental sequences designed for specific imaging needs; from fundamental T_1, and T_2 weighted images, to multi-slice and fast acquisition sequences. Beyond anatomical imaging, MRI extents its utility to advanced applications, including quantification of tissue properties such as T_1 and T_2 relaxation times, assessing diffusion characteristics, specific imaging of lipid signals for estimation of the fat composition, and unravelling neural connectivity patterns through tractography. Central to the diversity of MRI sequences lies the interplay between radio frequency (RF) pulses and the gradient systems utilized for spatial encoding. This chapter serves to introduce fundamental components of MRI sequences and to elucidate the pivotal sequences employed in this thesis.

3.2.1 Spin echo and gradient echo sequences

MRI experiments are generally characterised as spin echo- or gradient echo-based sequences. Basic pulse programs of these sequences are shown in Figure 1.5. While both are widely used in MRI, most experiments in this thesis rely on spin echo sequences. This sub-section will focus on exploring and understanding spin echo-based MRI techniques.

Spin echoes, or Hahn echoes, named after E.L. Hahn who first discovered them in 1950[127], are generated by a sequence of RF pulses. In their most basic form, shown in Figure 1.6, spin echo sequences start with a 90° (1/2 π) RF excitation pulse that rotates the magnetization away from the *z*-axis into the *xy*-plane (Figure 1.6A&B). After the excitation pulse, the spins start to fan out due to loss of coherence from T_2^* and T_2 relaxation processes (Figure 1.6C). Next, a 180° (π) RF refocusing pulse is applied (Figure 1.6D), compensating the local heterogeneities in the magnetic field causing T_2^* relaxation. Consequently, the spins realign, the magnetization is refocused, and an echo of the initial NMR signal is observed at the echo time *TE*, which is in the millisecond range. The 180° refocusing pulse compensates T_2^* relaxation, while the loss of spin coherence caused by pure T_2 relaxation processes develops further during the refocusing period. This feature is utilized in the estimation of T_2 relaxation times of tissue (see Section 1.3.2.4). After the echo signal is recorded, a waiting period is initiated allowing

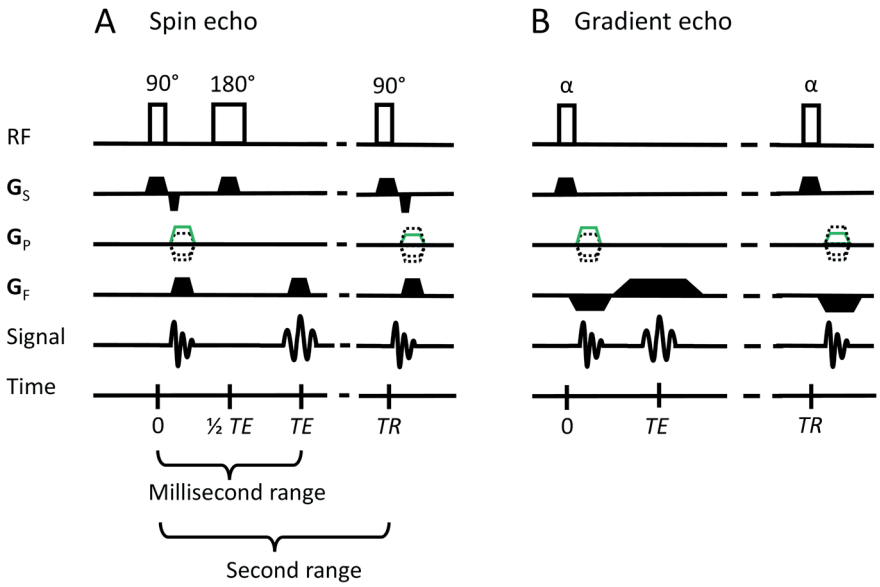

Figure 1.5 Basic [A] spin echo and [B] gradient echo MRI sequences. *Typically, the echo time TE is in the millisecond range, while the repetition time TR is in the second range. However, the precise values depend on the sample, desired contrast, and applied magnetic field strength. Three magnetic gradient systems are utilized for the spatial encoding, namely the slice selection gradient (**G_S**), the phase encoding gradient (**G_P**), and the frequency encoding gradient (**G_F**).*

T_1 and T_2 relaxation processes to complete. A next scan starts with a 90° excitation pulse at repetition time *TR*, which is in the order of seconds. Thus, *TE* << *TR*. The *TE* and *TR* utilized depend on the sample, desired contrast, and $\mathbf{B}_0$.

3.2.2 The rapid acquisition with relaxation enhancement (RARE) sequence

As previously stated, basic spin echo MRI experiments record one phase encoding gradient line per excitation cycle, making the number of phase encoding lines a significant factor in the total measurement time. However, since *TE* << *TR*, with *TE* being in the millisecond range and *TR* in the second range, there is a time interval between *TE* and *TR*. During this interval, T_1 and T_2 relaxation processes are progressing. The rapid acquisition with relaxation enhancement (RARE) sequence utilizes this time interval by implementation of additional 180° refocussing pulses to acquire multiple phase encoding gradient lines per excitation cycle[128]. The total number of 180° refocussing pulses utilized is referred to as the echo train length (ETL), or RARE factor. The MRI sequence of RARE is shown in Figure 1.7.

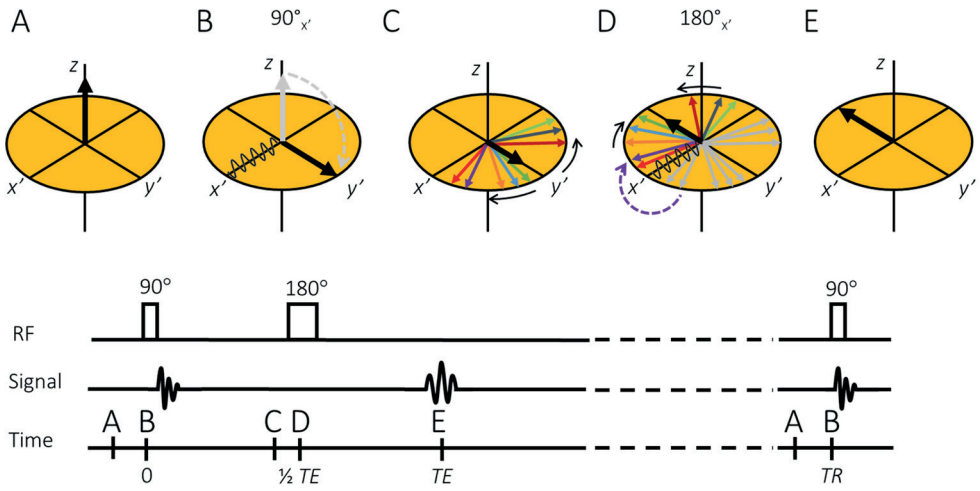

Figure 1.6 Spin echo sequence, illustrating the origin of the echo signal at TE. [A] Initial state. *The system starts in the initial equilibrium state, with the magnetization M along the z-axis, so M_z = M and M_{xy} = 0. [B] Excitation state. A 90° RF pulse is applied, rotating M into the xy-plane, so M_z = 0 and M_{xy} = M. [C] Relaxation period. Over time, relaxation processes reduce the magnitude of M_{xy}. In panel C, T_2 and T_2^* dephasing are shown. [D] Refocusing pulse. A 180° x' RF pulse rotates the spins around the x'-axis. [E] Echo formation. As individual spins continue to precess at their respective ω, they rephase at TE, restoring M_{xy}. An MR signal is recorded as the magnetization is rephased. [A] Recovery. Over time, the system will relax to the equilibrium state, so M_z = M and M_{xy} = 0 and [B] a new experiment can be initiated.*

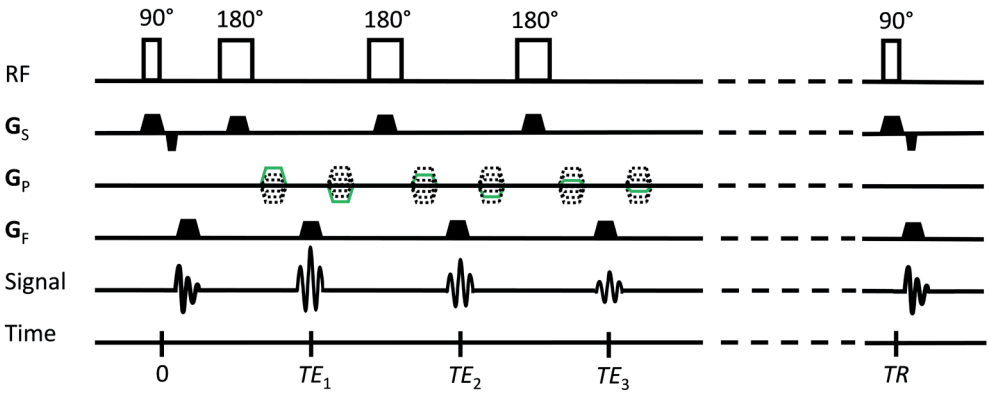

Figure 1.7 Rapid acquisition with relaxation enhancement (RARE) MRI sequence. *After the initial 90° RF excitation pulse, multiple 180° RF refocusing pulses are applied, each with a different phase encoding gradient. Consequently, MRI acquisition is significantly faster through the RARE MRI sequence, compared to the basic spin echo sequence shown in Figure 1.6, which employs a single phase encoding step per excitation cycle.*

Compared to the basic spin echo sequence utilizing one phase encoding step per excitation cycle, the RARE sequence is significantly faster. However, as the ETL increases, relaxation effects accumulate, leading to a progressive decline of the MR signal for each subsequent echo. This effect becomes more prominent at higher magnetic field strengths, where T_2 relaxation times tend to decrease[129,130]. Consequently, the effectiveness of very long ETL diminishes, rather leading to increased noise in the acquired data. Nonetheless, RARE provides a distinct advantage over fast gradient echo MRI sequences due to its inherent refocussing of transverse magnetization. 180° refocusing pulses correct for T_2^*-induced spin dephasing, responsible for susceptibility artifacts[131].This makes the RARE sequence less susceptible to artifacts from magnetic susceptibility compared to sequences based on gradient echo, a benefit that becomes even more pronounced at ultra-high magnetic field strengths where susceptibility artifacts tend to worsen[132]. This phenomenon is further elaborated in Section 1.3.5.2.

Additionally, a dominant observation in anatomical imaging with the RARE sequence is an atypical bright fat signal. This phenomenon is believed to stem from the utilization of echo spacings that disrupt the *J*-modulation dephasing pattern of lipid protons[133]. These unusual bright lipid signals can significantly affect MRI images through chemical shift displacement effects (see Section 1.3.5.2). Such artifacts misalign the fat signal, resulting in the merging of the fat signal with surrounding tissues. Therefore, implementing fat suppression methods in RARE is essential to mitigate these effects.

3.2.3 Ultra-fast data acquisition with echo planar imaging (EPI)

Echo planar imaging (EPI) is an ultra-fast method for MRI data acquisition[134]. An example of a basic spin echo EPI MRI sequence is shown in Figure 1.8. After the standard 90° RF excitation pulse and the 180° RF refocusing pulse, multiple gradient echoes are generated by the frequency encoding gradient and a train of short phase encoding gradient pulses, called blips, are utilized to fill the *k*-space. EPI MRI measurements filling the total *k*-space in a single excitation curve is commonly referred to as single shot EPI. In multi-shot EPI, the number of excitation cycles utilized to fill the *k*-space is referred to as the EPI factor, the echo train length, or shot factor.

Although the total MRI acquisition time is significantly reduced by EPI, EPI is highly sensitive to susceptibility artifacts, particularly as the magnetic field strength and the EPI factor increase[134]. This sensitivity can substantially limit the applicable EPI factor in UHF MRI, as discussed in Section 1.3.5.2. In this thesis, EPI is utilized to significantly reduce the total acquisition time of multi-shell diffusion tensor imaging measurements. These measurements inherently require

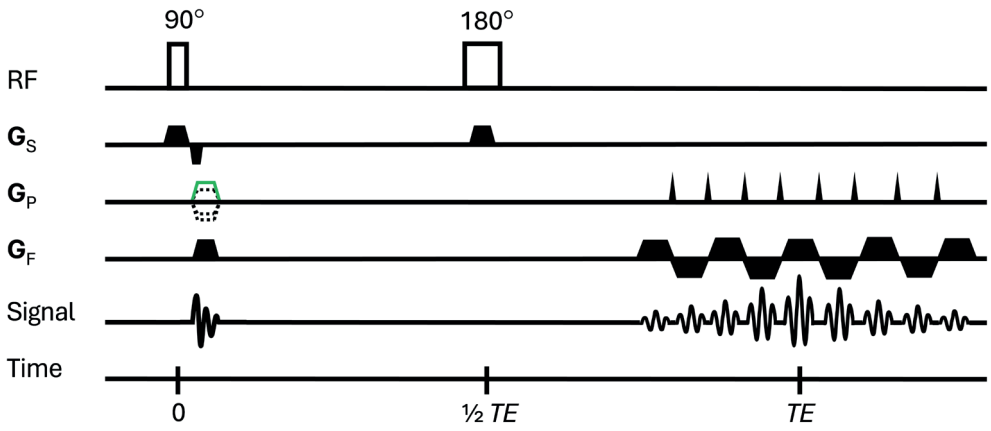

Figure 1.8 *Spin echo – echo planar imaging (EPI) MRI sequence for ultra-fast MRI data acquisition.*

extended durations due to their utilization of multiple diffusion-sensitizing factors (*b*-values) and diffusion-encoding directions (see Section 1.3.3.2).

3.2.4 T_1 and T_2 relaxation time estimation

The longitudinal and transverse relaxation times T_1 and T_2 in tissue depend on the chemical and physical environment in which molecules are present[135]. Relaxation times directly influence MRI sequence parameters, determining the optimal *TE* and *TR* needed to achieve sufficient signal-to-noise ratio (SNR) and desired MRI contrast. Furthermore, pathology can induce local changes in the microstructural environment and consequently modulate relaxation times. This is utilized in clinical applications to create contrast between healthy brain tissue and affected tissue, including tumours[136]. Additionally, quantitative analysis of relaxation times provides detailed information of the progression in microstructural changes in pathologies[135].

For the estimation of T_2 relaxation times, the work presented in this thesis relies on the multi-slice multi-echo (MSME) sequence[137], which is based on the Carr-Purcell-Meiboom-Gill (CPMG) sequence[138]. Although both the RARE MRI sequence (Figure 1.7) and the MSME MRI sequence (Figure 1.9) employ a train of 180° refocussing pulses, they obtain different results. These differences arise from the difference in their use of the MRI gradient systems. In RARE, the phase encoding gradient is employed to acquire multiple echoes each with different phases. This allows for anatomical imaging with short total scan time, as discussed in the previous chapter. In MSME, however, all echoes within a single excitation cycle are acquired with one phase encoding step. Instead, MSME utilizes the 180° refocussing echo train to

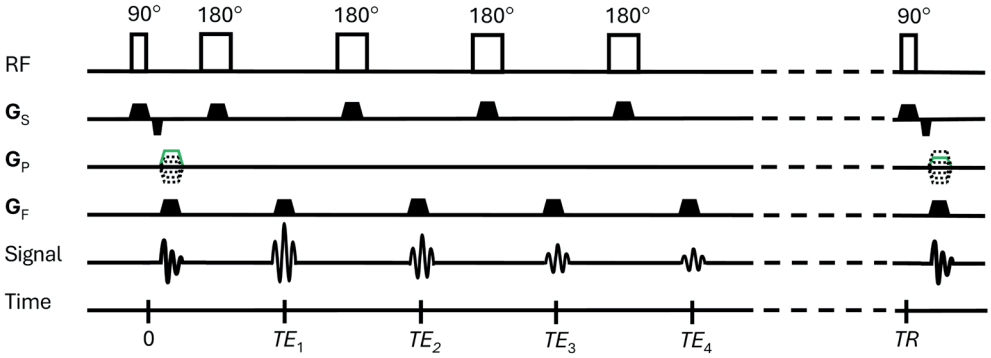

Figure 1.9 *Multi-slice multi-echo (MSME) MRI sequence. The MSME sequence is in the current thesis utilized for the estimation of T_2 relaxation times. The 180° refocusing echo train utilizes a single encoding gradient line per excitation cycle, allowing to acquire the exponential decay of the MR signal at increasing TE.*

monitor the progression of the signal intensity per voxel at increasing echo times. As stated previously, the 180° refocussing pulse compensates for the loss of coherence caused by T_2^* processes from local heterogeneities of the magnetic field, but not for the T_2 processes from molecular and atomistic interactions. Therefore, T_2 relaxation continues to evolve, and the signal intensities decrease with each new echo depending on the local T_2.

Figure 1.10A shows the signal loss progression in the brain area of an adult wild-type male zebrafish with increasing *TE*. The MR signal intensity decays exponentially and the transverse relaxation time T_2 is estimated through mono-exponential line fitting of the MR signal to

$$I_{\mathrm{TE}} = A + I_0 \cdot \exp^{\frac{-TE}{T_2}} \quad . \tag{1.4}$$

Here, I_{TE} is the MR signal intensity at *TE*, *A* is the absolute bias, and I_0 is the signal intensity at *TE* = 0. During data analysis of the MSME MR signal intensities, uneven echoes should be excluded as an extension of the workflow proposed by Milford *et al.*[139]. Inhomogeneities in the RF magnetic field $\mathbf{B}_1$ can locally lead to imperfect refocussing pulses (Φ < 180°)[140-142]. Consequently, the coherence losses caused by T_2^* processes are not fully compensated, negatively impacting the observed signal intensity of the echo. However, as the $\mathbf{B}_1$ inhomogeneities remain stable during the measurements, all even echoes fully compensate for T_2^* processes and thus represent T_2 relaxation. This effect can be significant, often resulting in a lower intensity for the first MSME echo compared to the second. Figure 1.10B shows the results of uncorrected data fitting, which includes all MSME echoes, and corrected data fitting, which excludes uneven MSME echoes. As shown, different T_2 are estimated by corrected and

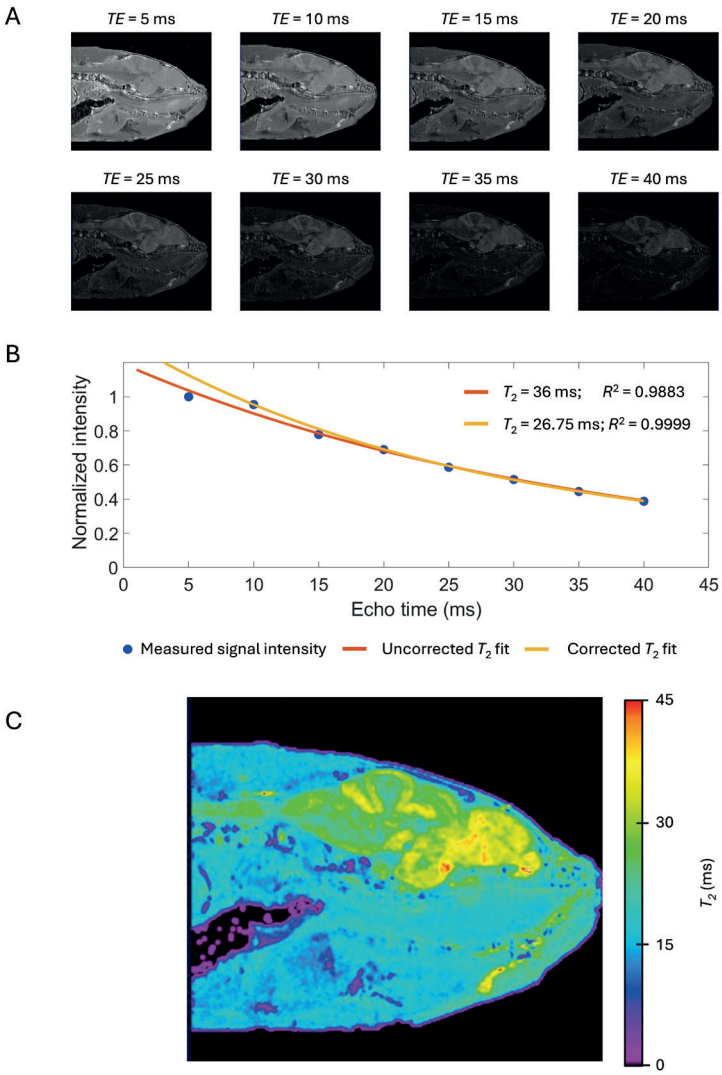

Figure 1.10 Utilization of the MSME MRI sequence for T_2 relaxation time estimation. [A] *MRI images of the zebrafish brain area, acquired with the multi-slice multi-echo (MSME) sequence at increasing TE. Image intensities were scaled to the first echo (TE 5 ms) for comparison of signal intensities.* ***[B]*** *Utilization of MSME data to estimate T_2 relaxation times. With increased TE, T_2 relaxation causes exponential decay in the signal intensity, described by [$I_{TE} = A + I_0 \cdot \exp(-TE/T_2)$]. Mono-exponential data fitting is utilized to estimate local T_2 relaxation times. As stated by Milford et al. (2015)[139], uneven echoes should be excluded in data fitting. Both uncorrected data fitting, which includes all MSME echoes, and corrected data fitting, which excludes uneven MSME echoes, are shown here. In the current example, an area in the zebrafish pallium was selected for data analysis.* ***[C]*** *T_2 map of the zebrafish brain area. Acquisition details – Sample information: wild-type young adult male zebrafish, 3 months old, fixated in paraformaldehyde for 4 days – MRI hardware: Bruker vertical bore system (Bruker Biospin GmbH, Germany), $\mathbf{B}_0$ 17.6 T, Micro5 gradient system (Bruker Biospin GmbH, Germany), G_{max} 3 T/m – MSME parameters: TR 2500 ms, τ 5 ms, ns = 4, resolution 23 × 23 µm, and a slice thickness 200 µm.*

uncorrected data fitting, with improved fitting obtained by the corrected fitting method, as evident from the coefficient of determination (R^2). Additionally, Figure 1.10C shows a T_2 map constructed from MSME estimation on a voxel-to-voxel basis, providing a full overview of the T_2 times distribution in the zebrafish brain region.

T_1 relaxation times are estimated by monitoring the longitudinal magnetization $\mathbf{M}_z$ recovery, accomplished by measuring the MR signal at various repetition times. To reduce the total measurement time, the work in this thesis utilizes a sequence combining the RARE MRI sequence presented in Section 1.3.2.2 with variable repetition times (RAREVTR). The RAREVTR MRI sequence is shown in Figure 1.11.

Figure 1.12A shows the increasing signal intensity progression observed by measuring at increasing repetition times in the brain area of an adult wild-type male zebrafish. The exponential recovery of the longitudinal magnetization is shown in Figure 1.12B, utilizing the MR signal of an ROI selected in the pallium of the zebrafish brain. The longitudinal repetition time T_1 is estimated through mono-exponential line fitting of the MR signal to

$$I_{\mathrm{TR}} = A + I_0 \cdot \left(1 - \exp^{\frac{-TR}{T_1}}\right) . \tag{1.5}$$

Here, I_{TR} is the signal intensity at TR and I_0 is the signal intensity at TR = 0. Additionally, T_1 can be estimated on a voxel-by-voxel basis, for the construction of T_1 maps (see Figure 1.12C).

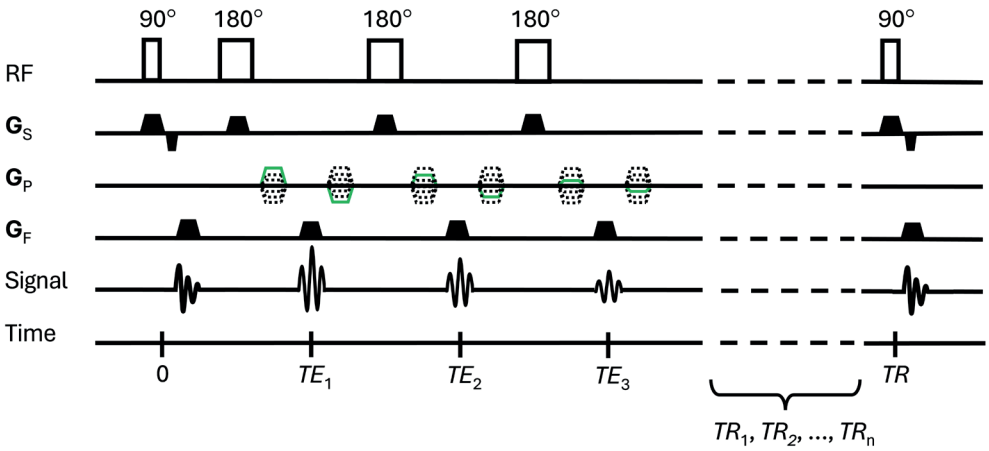

Figure 1.11 *RARE with variable repetition times (RAREVTR) MRI sequence for the estimation of T_1 relaxation times.*

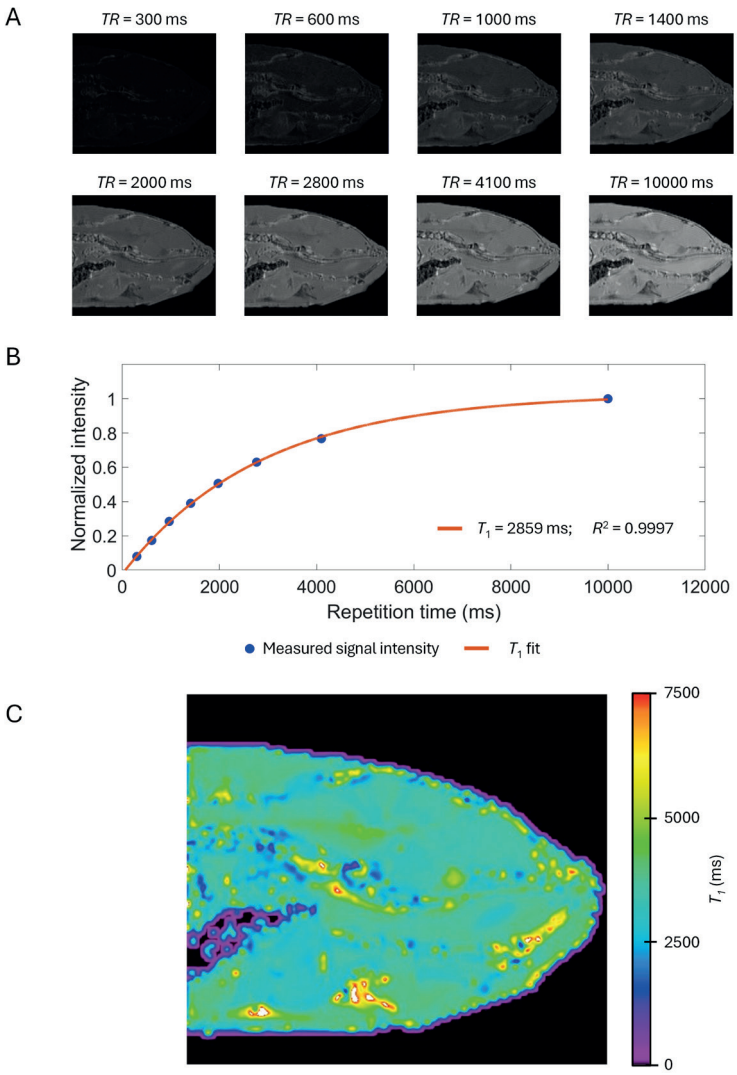

Figure 1.12 Utilization of the RAREVTR MRI sequence for T_1 relaxation time estimation. [A] *MRI images of the zebrafish brain area, acquired with the rapid acquisition with relaxation enhancement with variable repetition time (RAREVTR) MRI sequence at increasing TR. Image intensities were scaled to the longest repetition time echo (TR 10000 ms) for visualization of the longitudinal magnetization* $\mathbf{M}_z$ *recovery.* ***[B]*** *Utilization of RAREVTR data to estimate T_1 relaxation times. With increased TR, T_1 relaxation gives rise to exponential recovery with increasing TR, described by $[I_{TR} = A + I_0 \cdot (1- \exp(-TR/T_1))]$. Mono-exponential data fitting is utilized to estimate local T_1 relaxation times. Here, an area in the zebrafish pallium was selected for data analysis as example.* ***[C]*** *T_1 map of the zebrafish brain area. Acquisition details – Sample information: wild-type young adult male zebrafish, 3 months old, fixated in paraformaldehyde for 4 days – MRI hardware: Bruker vertical bore system (Bruker Biospin GmbH, Germany),* $\mathbf{B}_0$ *17.6 T, Micro5 gradient system (Bruker Biospin GmbH, Germany) G_{max} = 3 T/m – RAREVTR parameters: TR = 300, 600, 1000, 1400, 2000, 2800, 4100, or 10000 ms, TE = 3 ms, ns = 2, resolution 47 × 47 µm, and a slice thickness 200 µm.*

3.3 Diffusion-based MRI

Molecular diffusion describes the spontaneous and random movement of molecules, known as Brownian motion, driven by the thermal energy of molecules. This phenomenon was for the first time thoroughly elucidated by Albert Einstein in 1905[143]. Diffusion-based MRI stands out as a unique tool with the extraordinary ability to non-invasively monitor the random movements of water within biological tissue[144]. Particularly in the realm of brain imaging, dMRI has demonstrated its invaluable utility in investigating neurological disorders. However, the versatility of dMRI extends beyond neuroimaging to applications in other fields including oncology[145], musculoskeletal imaging[146], and cardiovascular research[147], making it a powerful tool in modern medical diagnostics and research. dMRI offers a diverse array of non-invasive analytical tools that surpass the capabilities of conventional MRI and other clinical techniques, enabling unprecedented insights into the complexities of brain structure and connectivity. In its most fundamental form, dMRI provides additional contrast beyond those provided by T_1, T_2, and proton density differences, exhibiting exceptional sensitivity in both detecting and precisely localizing acute ischemic brain lesions[148]. Furthermore, fundamental dMRI is utilized for estimating the apparent diffusion coefficient (*ADC*), quantifying the diffusion rate of water molecules within tissues, thereby providing information about tissue microstructure and integrity[149-151]. Advanced dMRI techniques offer rich data by capturing higher-dimensional information, including estimation of the diffusivity anisotropy[152], deviation from Gaussian distribution[153], axonal diameter[154], and white matter connectivity[155]. In this thesis, various dMRI techniques were utilized for the analysis of the zebrafish brain including its pathology; diffusion-weighted imaging (DWI), diffusion tensor imaging (DTI), diffusion kurtosis imaging (DKI), and diffusion tractography. The basic principles of these techniques are discussed in this section.

3.3.1 Diffusion-weighted imaging

DWI is the most fundamental diffusion-based MRI technique, first described by Le Bihan *et al.* in 1986[156], nowadays vastly utilized in clinical MRI to generate diffusion-based MRI contrast or to estimate local *ADC*[157]. Figure 1.13A shows the spin echo DWI sequence. Diffusion sensitivity is introduced in MRI through its gradient system $\mathbf{G}_{diff}$, utilized on both sides of the 180° RF refocussing pulse. The "dephasing" $\mathbf{G}_{diff}$ applied prior to the 180° RF refocussing pulse, induces phase variations across spins in three dimensions, linking spin phase to their spatial distribution within the sample. For stationary nuclei, the rephasing $\mathbf{G}_{diff}$ applied after the 180° RF refocussing pulse would reinstate the spin phase, yielding an MR signal intensity similar to a conventional spin echo sequence. However, thermally induced random motions cause the nuclei to move between the dephasing and rephasing $\mathbf{G}_{diff}$. As a result, the rephasing $\mathbf{G}_{diff}$ will not fully rephase those spins that moved away from their starting position, resulting in MR signal loss. Consequently, the observed MR signal intensity reflects local diffusivity: samples

with high diffusivity exhibit weak signal intensity, whereas those with low diffusivity display strong signal intensity. This is visualized in Figure 1.13B.

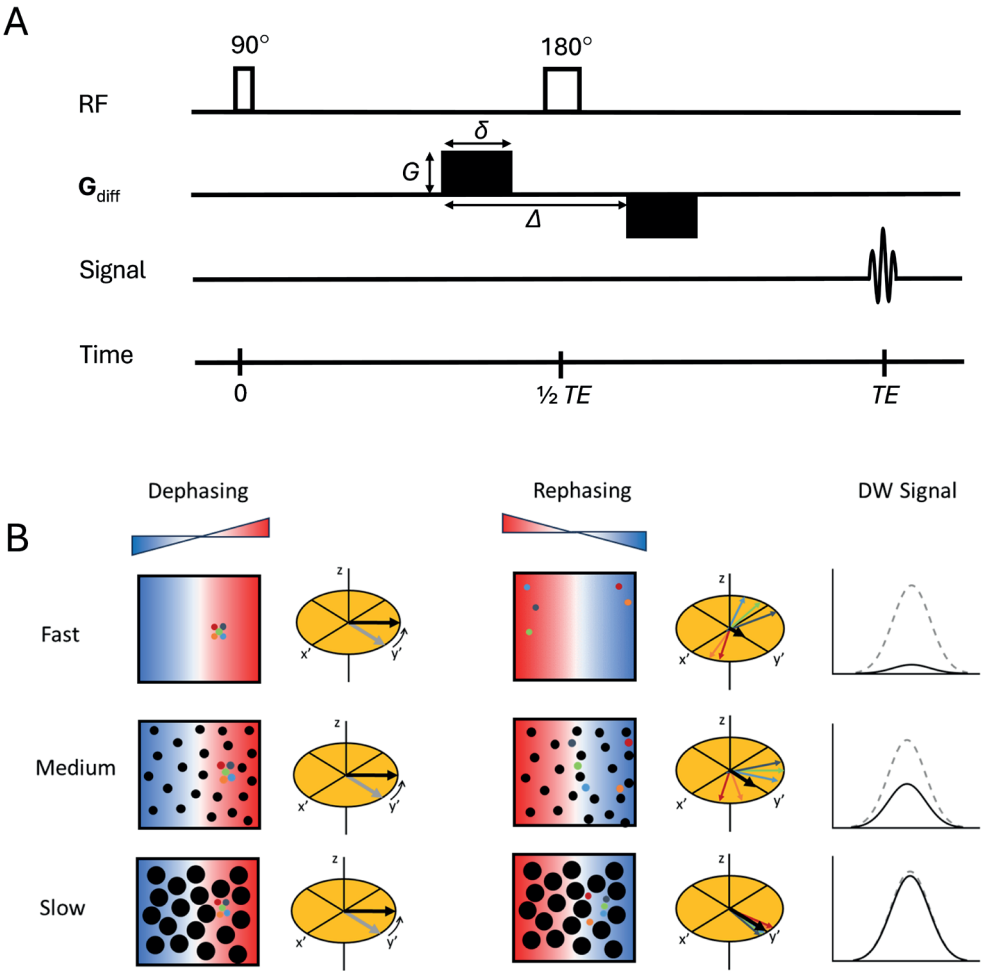

Figure 1.13 [A] *Pulse sequence of a basic diffusion-based MRI sequence. [B] Effect of diffusivity on observed signal as a consequence of the dephasing and rephasing gradient pulses. A sample with a high diffusivity will lead to a low diffusion-weighted (DW) signal, while a sample with a low diffusivity will lead to a high DW signal. In this example, only the effect of dephasing and rephasing for one of the three gradient directions is visualized.*

The total diffusion weighting of a dMRI experiment is determined by the gradient amplitude (*G*), gradient duration (*δ*), and gradient time interval (*Δ*). Conventionally, these are summarised in the *b*-value, according to

$$b = \gamma^2 \cdot G^2 \cdot \delta^2 \cdot \left(\Delta - \frac{\delta}{3} \right) . \tag{1.6}$$

In DWI, the diffusion-weighted MR signal is measured at a specific, or at various *b*-values. In this work, the DWI methods utilize fixed values for *δ* and *Δ*, and the *b*-values are set by changing the gradient strengths *G*. A lower *b*-value signifies minimal diffusion weighting, whereas a higher *b*-value signifies heightened diffusion weighting.

Figure 1.14A shows the loss of MR signal intensity at increasing *b*-values, indicating strong diffusion weighting is applied. Notably, diffusion-weighted MRI enhances the contrast between the zebrafish brain and its surroundings compared to conventional MRI techniques discussed earlier. This heightened contrast arises from the diminished water diffusivity within brain tissue relative to other tissues, accentuating tissue boundaries. Figure 1.14B demonstrates how the local diffusion rate of water molecules can be estimated by fitting the MR signal to a mono-exponential decay function at increasing *b* according to

$$I_{\mathrm{b}} = A + I_0 \cdot \exp^{-b \cdot ADC} . \tag{1.7}$$

Here, I_b is the signal intensity at *b* and I_0 is the signal intensity at b_0. *ADC* analysis performed on a voxel-to-voxel basis generates *ADC* maps as demonstrated in Figure 1.14C.

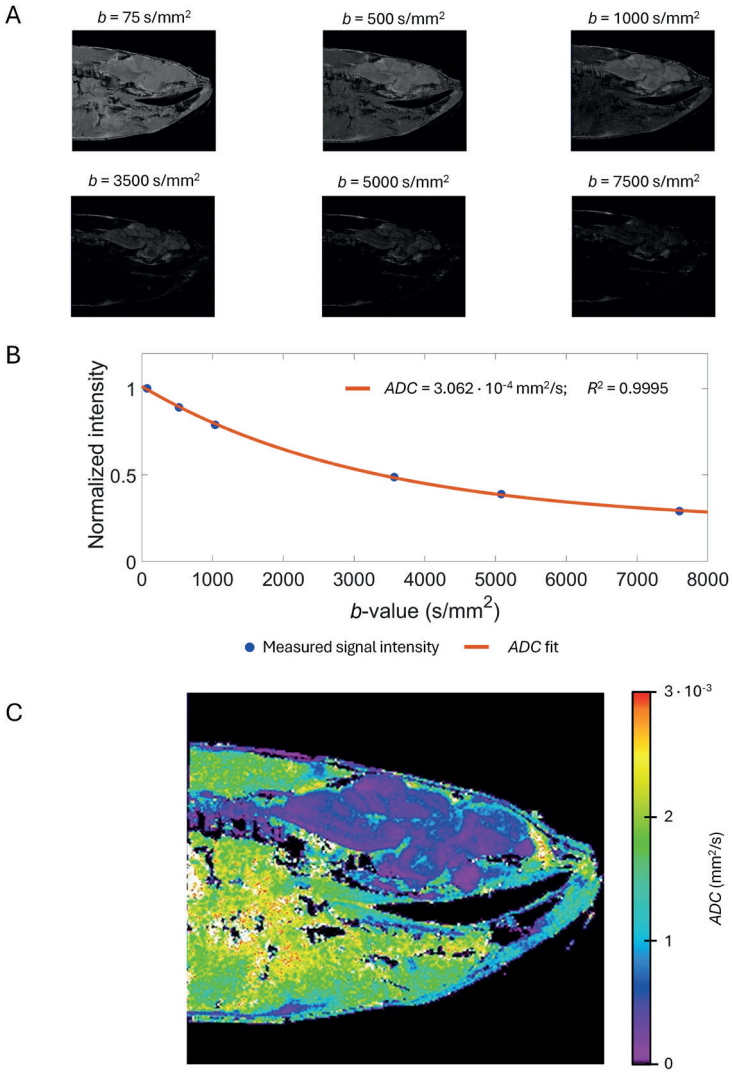

Figure 1.14 Utilization of the DWI MRI sequence for apparent diffusion coefficient estimation. [A] *MRI images of the zebrafish brain area, acquired with the spin echo diffusion-weighted imaging (DWI) MRI sequence at increasing b-values. Image intensities were scaled to the lowest diffusion-weighting image (b = 75 s/mm²) for visualization MR signal loss by diffusion.* ***[B]*** *Utilization of DWI data to estimate ADC through mono-exponential line fitting. With increased b, diffusion processes cause an exponential decay of the MR signal, described by [$I_b = A + I_0 \cdot \exp(-b \cdot ADC)$]. Here, an area in the zebrafish pallium was selected for data analysis as example.* ***[C]*** *ADC map of the zebrafish brain area. Acquisition details – Sample information: wild-type young adult male zebrafish, 3 months old, fixated in paraformaldehyde for 4 days – MRI hardware: Bruker vertical bore system (Bruker Biospin GmbH, Germany),* $\boldsymbol{B}_0$ *17.6 T, Micro5 gradient system (Bruker Biospin GmbH, Germany)* G_{max} *3 T/m – DWI parameters: TR = 1000 ms, TE = 20.2 ms, ns = 4, resolution 23 × 23 µm, slice thickness 200 µm, δ = 4 ms, Δ = 10 ms, b-values 75, 500, 1000, 3500, 5000, or 7500 s/mm².*

3.3.2 Diffusion tensor imaging

In a free medium, such as free flowing water, the Brownian motion induced displacement of molecules is described by a Gaussian distribution towards all three spatial dimensions. The distance travelled by these molecules is described by the diffusion coefficient *D*, depending on the molecular mass, the temperature, and the viscosity of the medium. A diffusion ellipsoid of such a medium is isotropic and the eigenvalues (λ_1, λ_2, λ_3) of its eigenvectors ($\boldsymbol{\varepsilon}_1$, $\boldsymbol{\varepsilon}_2$, $\boldsymbol{\varepsilon}_3$) identical; $\lambda_1 = \lambda_2 = \lambda_3 = D$ (Figure 1.15A). Biological tissue contains cell membranes, fibres, macromolecules, and other obstacles hindering the motion of its water content. Anisotropic diffusion, characterised by directional preferences, is observed in many types of tissue, including muscle[158], kidney[159], liver[160], and heart[147] tissue. However, the most profound instances of anisotropic diffusion occur in white matter structures of the spinal cord[161] and brain[162]. The long axonal fibre bundles of white matter create directional preferences, amplified by their myelin insulation. The myelin sheet acts as a barrier, confining water movement to parallel trajectories along the axons while hindering perpendicular diffusion. Consequently, the diffusion ellipsoid and tensor in biological tissues exhibit anisotropic characteristics, where the eigenvalues of the diffusion tensor vary accordingly, with $\lambda_1 > \lambda_2 > \lambda_3$ (Figure 1.15B).

DTI is an advanced dMRI technique, providing orientational information of diffusion characteristics in tissue. Whereas DWI assumes isotropic diffusion, DTI measures the MR signal in various diffusion-encoding directions to construct the diffusion ellipsoid and tensor matrix **D**. **D** has six degrees of freedom, necessitating the MR signal to be determined across a minimum of six orthogonal orientations[163]. Yet, employing additional diffusion-encoding

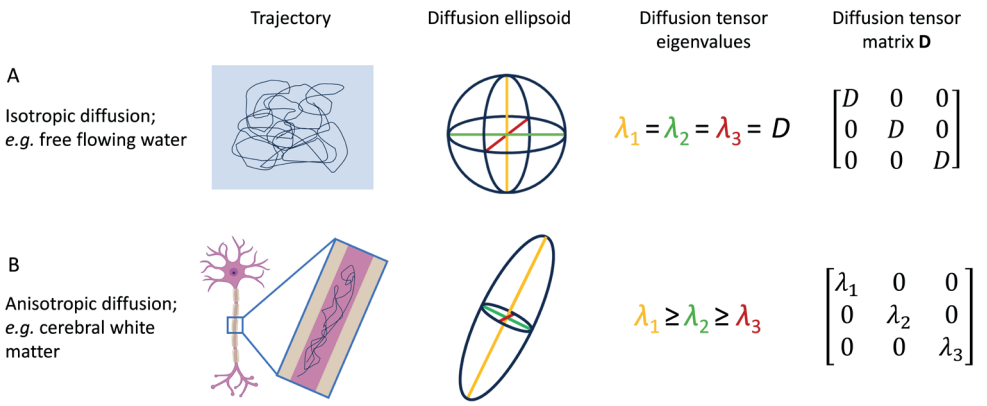

Figure 1.15 *The diffusion trajectories and corresponding diffusion ellipsoid, diffusion tensor eigenvalues, and diffusion tensor matrix* ***D*** *in* ***[A]*** *isotropic diffusion, e.g. free flowing water and* ***[B]*** *anisotropic diffusion, e.g. white matter structures.*

directions significantly enhances the data quality[164]. The diffusion tensor eigenvalues are utilized to estimate the diffusion tensor metrices; the axial diffusivity ($D_{\parallel}$), the radial diffusivity ($D_{\perp}$), the mean diffusivity (*MD*), and the fractional anisotropy (*FA*).

$D_{\parallel}$ represents the diffusivity along the principal eigenvector $\boldsymbol{\varepsilon}_1$ and is represented by the principal eigenvalue λ_1, $D_{\perp}$ is the average diffusivity along the two non-principal eigenvectors $\boldsymbol{\varepsilon}_2$ and $\boldsymbol{\varepsilon}_3$, *MD* is the average diffusivity along $\boldsymbol{\varepsilon}_1$, $\boldsymbol{\varepsilon}_2$, and $\boldsymbol{\varepsilon}_3$, and *FA* represents the degree of anisotropy of the water diffusion between the eigenvectors, ranging from 0 – 1. Hence,

$$D_{\parallel} = \lambda_1 \ , \tag{1.8}$$

$$D_{\perp} = \frac{\lambda_2+\lambda_3}{2} \ , \tag{1.9}$$

$$MD = \frac{\lambda_1+\lambda_2+\lambda_3}{3} \ , \qquad \text{and} \tag{1.10}$$

$$FA = \frac{\|D-MD\cdot I^{(2)}\|}{\|D\|} = \sqrt{\frac{\frac{3}{2}\left((\lambda_1-MD)^2+(\lambda_2-MD)^2+(\lambda_3-MD)^2\right)}{{\lambda_1}^2+{\lambda_2}^2+{\lambda_3}^2}} \ . \tag{1.11}$$

Here, $I^{(2)}$ represents the fully symmetric rank 2 isotropic tensor, while $||..||$ denotes the application of the Frobenius norm[165].

Nowadays, DTI is extensively utilized in clinical studies to monitor pathologically induced microstructural changes in the brain. Various neurological disorders including Alzheimer's disease[166], Huntington's disease[167], and Parkinson's disease[168] show significant changes in the diffusion tensor metrices correlating to the pathological progression. However, non-neurodegenerative brain disorders, including strokes[169], brain tumours[170], and attention deficit hyperactivity disorder (ADHD)[171] also show clear changes in the diffusion tensor metrices. Broadly, it is understood that $D_{\parallel}$ is a potential marker for axonal degeneration, $D_{\perp}$ is particularly sensitive to shifts in white matter myelin integrity, *MD* serves as a potential indicator for edema and cellular proliferation in neoplastic growth, and *FA* stands out as a widely utilized marker for assessing the integrity of white matter structures[163,172,173]. However, it's important to approach the direct correlation of specific changes in diffusion tensor metrics with potential microstructural alterations cautiously. Such associations should be carefully validated with additional techniques, as various factors can induce similar changes and might cause misinterpretation of DTI data[174].

3.3.3 Diffusion kurtosis imaging

DWI and DTI operate under the assumption that diffusivity within the brain conforms to a Gaussian distribution, assuming a mono-exponential decay of the MR signal with increasing *b*-value as described by equation 1.7, thereby oversimplifying the actual complexity of diffusivity in brain tissue[175]. For both grey matter and white matter this assumption was proven to be invalid at high *b*-values, when dMRI becomes more sensitive towards shorter diffusion distances[153]. Consequently, beyond highlighting DWI's and DTI's inability to fully utilize all available information provided by MR diffusion measurements for understanding tissue microstructure, this also restricts the use of high *b*-values in DWI and DTI. High *b*-values introduce deviations from the mono-exponential fit used by DTI, thereby introducing deviation in the estimated DTI metrics through line-fitting[153]. Furthermore, DTI fails to consider the complexity of biological tissue, especially in the brain, such as crossing fibres, which have a direct influence on estimated diffusion tensor metrics potentially leading to incorrect conclusions[174].

In the realm of dMRI, the deviation of water diffusion displacement from a normal distribution is referred to as kurtosis. A kurtosis of 0 indicates the diffusion profile perfectly follows a normal Gaussian distribution, expected for free-flowing water. In biological tissue, a positive kurtosis (kurtosis > 0) is anticipated, indicating diffusion initially occurs at a rapid pace, gradually slowing down as water molecules increasingly interact with cellular structures. Elevated kurtosis values indicate greater obstacles to regular diffusion and heightened complexity[175].

DKI is a dMRI method building upon DTI to account for non-Gaussian diffusivity towards various diffusion-encoding directions. Diffusion kurtosis is characterised by a fully symmetrical 3 × 3 × 3 × 3 diffusion tensor matrix **W** with 15 degrees of freedom, necessitating a minimum 22 MR images, taken across at least 15 diffusion-encoding directions recorded at a minimum of 3 unique *b*-values[176]. Moreover, unlike DWI and DTI, DKI mandates the use of high *b*-values (> 2000 s/mm^2), as diffusion at low *b*-values are predominantly influenced by Gaussian diffusion[177]. A full explanation of the methodology describing the construction of **W** is provided by Veraart *et al.*[178].

From **W**, the diffusion kurtosis metrics can be estimated; the axial kurtosis ($K_\parallel$), the radial kurtosis ($K_\perp$), the mean kurtosis (*MK*), and the kurtosis fractional anisotropy (*KFA*). $K_\parallel$ represents the kurtosis along the principal eigenvector $\boldsymbol{\varepsilon}_1$ thus in the same orientation as $D_\parallel$, $K_\perp$ is the average kurtosis along the two non-principal eigenvectors $\boldsymbol{\varepsilon}_2$ and $\boldsymbol{\varepsilon}_3$ thus in the same orientations as $D_\perp$, *MK* is the average kurtosis along $\boldsymbol{\varepsilon}_1$, $\boldsymbol{\varepsilon}_2$, and $\boldsymbol{\varepsilon}_3$, and *KFA* represents the degree of anisotropy of the kurtosis.

3.3.4 Diffusion MRI tractography

Diffusion tractography, also known as diffusion fibre tracking, is uniquely distinguished as the sole non-invasive method capable of mapping intricate white matter connections in the brain by leveraging the directional preferences of water diffusion within axons, offering invaluable insights into neural connectivity and function. Strictly ordered white matter fibre bundles in combination with their myelin sheets give rise to a high order of directional diffusion preference of the water molecules inside their axons. The applications of diffusion MRI tractography include white matter structure visualization and identification[179] assessment of white matter deformation as a consequence of tumours[180], preoperative assessment and strategizing[181], and detection of the early stages of neurodegenerative diseases[182].

In diffusion MRI tractography the dMRI signal is collected towards multiple diffusion-encoding directions for each voxel, revealing local fibre orientations. Diffusion MRI tractography utilizes tracking algorithms to translate local fibre orientations to pathways, of which the first were introduced in 1998[183,184]. Today, there exists a multitude of diffusion MRI tractography algorithms and data processing tools, too numerous to cover comprehensively in this work. Broadly, diffusion MRI tractography algorithms are categorised into deterministic or probabilistic approaches[185]. In their most basic form, tractography algorithms are deterministic. For each voxel, a single fibre orientation is estimated, and pathways are generated based on the principal eigenvectors of the diffusion tensors[186]. However, deterministic algorithms are highly susceptible to signal noise and artifacts. Furthermore, they cannot consider the crossing or closely passing of white matter fibres in a single voxel, which can lead to erroneous or false fibre tracts[187,188]. Probabilistic diffusion tractography algorithms utilize seed points, which define ROIs in the brain through which a large distribution of trajectories is generated. The regions in the brain exhibiting a high density of trajectories are considered to possess an elevated likelihood to be connected to the seed point[185]. Diffusion MRI tractography described in the current work is based on the probabilistic approach proposed by Dhollander *et al.*[189]. It utilizes constrained spherical deconvolution (CSD) to generate fibre orientation distribution functions (fODF) based on the response function of the white matter fibre populations. In short, a white matter response function is generated based on the diffusion-weighted MR signal from voxels assumed to contain a single fibre orientation. The response function is used to generate fODF's through CSD by relating the fODF coefficient vectors, the vectors of the diffusion-weighted MR signal intensities, and the CSD operation. This process transforms the CSD operation into a linear least-squares problem[190]. Following this, a probabilistic algorithm is employed wherein, at each step of the streamline, random samples are drawn from the local fODF via trilinear interpolation. This workflow offers the advantage of integrating biophysical data, which helps mitigating the occurrence of false-positive tracks from grey matter tissue[190,191]. The exploration of diffusion MRI tractography in the zebrafish brain is an

emerging field, with Ullmann *et al.*'s publication[192] being the only other known reference so far. The compact size of the zebrafish brain, coupled with the inherent low SNR of MRI techniques presents considerable challenges. In this work, diffusion MRI tractography primarily aims to visually map the exact localization of white matter structures within the zebrafish brain, allowing to examine their integrity through DTI and DKI metrics.

3.4 Localized magnetic resonance spectroscopy

^{1}H MRS is a unique technique offering a window into the local biochemical composition of tissue. Where traditional NMR provides ^{1}H NMR spectra of the whole sample inside the scanner, localized ^{1}H MRS allows for *in vivo* selection of regions by utilization of the MRI gradient systems. For the brain, MRS enables the non-invasive detection and quantification of various cerebral metabolites crucial for understanding brain function and pathology. Predominant cerebral metabolites detectable with localized ^{1}H MRS in the human brain include glutamate and GABA, two important neurotransmitters in the brain providing valuable insights into the brain function and health[193,194]. Specific metabolites may serve as markers for cell types, and NAA, primarily found in neuronal cell bodies and axons, stands as a promising indicator for tracking neuronal integrity[195]. Conversely, m-Ins, mainly located in glial cells, serves as a potential marker for osmotic stress or neuroinflammation[196].

Although various sequences are available for performing localized one-dimensional ^{1}H MRS, including stimulated echo acquisition mode (STEAM)[197], image selected *in vivo* spectroscopy (ISIS)[198], and localization by adiabatic selective refocusing (LASER)[199], the point resolved spectroscopy (PRESS) sequence is the most conventional method applied in MRS[200]. The PRESS sequence, visualized in Figure 1.16A, utilizes two spin echoes with three orthogonal slice selective RF pulses (90° - 180 ° - 180°). At the intersection of the three slices (fig 1.16B) the free induction decay (FID) is captured and converted to the frequency domain using Fourier transformation, providing the localized ^{1}H MRS spectra (fig 1.16C). Prior to the initial 90° RF excitation pulse, outer volume suppression (OVS) and water suppression (WS) pulses are typically applied (see fig 1.16A). OVS selectively removes signals originating from outside the selected ROI. This technique is commonly employed to suppress lipid signals, which significantly overlap with important cerebral metabolites such as lactate and NAA. OVS utilizes three repetitions of six narrow suppression slices positioned parallel to the voxel surface. OVS reduces the need for high gradient spoilers in the PRESS sequence, thereby lowering the minimum *TE*. Additionally, MRS often necessitates the usage of water suppression pulses. The water signal in ^{1}H MRS spectra is typically several orders of magnitude stronger than signals from metabolites of interest. This dominant water signal can obscure the detection and accurate quantification of these metabolites. By suppressing the water signal, MRS can achieve a clear and precise measurement of low concentration metabolites, enhancing the

overall quality and reliability of the spectral data. In the current work, water suppression is achieved through the variable pulse power and optimized relaxation delays (VAPOR) pulse sequence, consisting of 7 RF pulses with variable pulse powers and optimized relaxation delays for excellent water suppression with little sensitivity for T_1 and $\mathbf{B}_1$ inhomogeneities.

3.5 MRI and MRS at ultra-high magnetic fields

Terms like "ultra-high field" or "ultra-strong gradient" are inherently relative to the user's perspective. In clinical MRI, a 7 T field for human imaging is considered ultra-high, as are gradients of 300 mT/m. By comparison, systems operating at 17.6 T and 28.2 T with gradient strengths (G_{max}) of 3 T/m would need to be described with even more emphatic terms, such as "super-ultra-high". To provide clarification on the term usage in this thesis, distinction needs to be created between different MRI research fields. Commonly, these are made between three

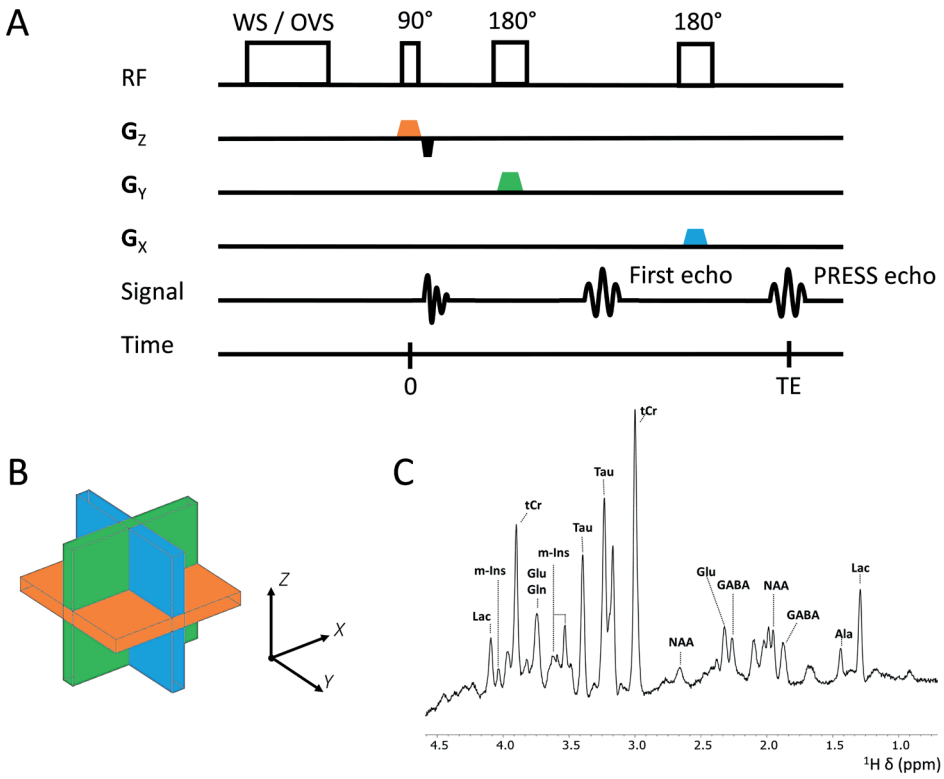

Figure 1.16 [A] *Point resolved spectroscopy (PRESS) MRI sequence.* ***[B]*** *Each of the three RF pulses (90°-180°-180°) is accompanied by a slice selective gradient pulses perpendicular to each other. The region where the three slices overlap, the ROI is selectively excited and* ***[C]*** *an MRS spectrum is recorded.*

main groups: clinical MRI, pre-clinical MRI, and micro-MRI, also known as MR microscopy. In this thesis, micro-MRI systems are employed and magnetic field strengths above 14.1 T (600 MHz) are regarded as ultra-strong, for they fall outside the range of more commonly used field strengths (7 T – 14.1 T). However, we acknowledge that recent hardware developments, such as the availability of 28.2 T (1.2 GHz) for imaging, may alter this perspective to some extent.

3.5.1 SNR and relaxation times

The push to employ higher magnetic field strengths in MRI and MRS primarily stems from the enhanced SNR[201] and improved spectral resolution achieved at elevated $\mathbf{B}_0$. Particularly in MRS, higher magnetic fields have greatly enhanced spectral resolutions, facilitating better identification and quantification of metabolites[202]. Metabolites that exhibit significant spectral overlap at lower fields may become completely separable at higher fields. Moreover, the increased SNR enables the use of smaller ROIs, facilitating metabolic exploration in finer tissue areas. Often, the relation $SNR \sim B_0^{7/4}$ is cited[203], although, in practice, experimentally comparing SNR across different magnetic fields is challenging[201].

Despite the clear benefits of increased SNR and enhanced spectral resolution, using ultra-high magnetic fields comes with specific challenges that require method adaptation. One major challenge is the influence of $\mathbf{B}_0$ on the relaxation times T_1 and T_2. T_1 relaxation time increases with $\mathbf{B}_0$, while the differences in T_1 between different tissues decrease. This leads to a theoretical reduction in T_1-based contrast at higher field strengths, but the practical increase in SNR at higher $\mathbf{B}_0$ also enhances the contrast-to-noise ratio (CNR). Moreover, longer T_1 relaxation times at elevated $\mathbf{B}_0$ require a longer *TR* to ensure proper recovery of longitudinal magnetization between RF pulses. However, the improved SNR and CNR at higher field strengths result in a significantly shorter total acquisition time[201].

Regarding T_2 relaxation times, they are theoretically expected to be unaffected by the magnetic field strength[204]. However, in practice, the T_2 relaxation times of biological tissues decrease significantly with increasing $\mathbf{B}_0$[129,130]. Longer T_2 relaxation times are preferred, as the MR signal decays exponentially with T_2. This necessitates the use of shorter echo times at higher $\mathbf{B}_0$ to avoid losing the SNR improvement provided by the increased magnetic field strength.

3.5.2 MRI artifacts at UHF

A common challenge during MRI data acquisition is the presence of MRI artifacts[205]. MRI artifacts are distortions or anomalies in MRI images that can potentially result in misdiagnosis or misinterpretation of the MRI data. There are various types of MRI artifacts, each with its own unique origin and specific methods to reduce their impact on the data. Some commonly observed examples of MRI artifacts include motion artifacts[206], chemical shift displacement

artifacts[207,208], aliasing artifacts[209], Gibbs/truncation artifacts[210], and susceptibility artifacts[211]. In this discussion, we will specifically focus on chemical shift displacement artifacts and susceptibility artifacts due to their dependence on the strength of the applied magnetic field.

Chemical shift displacement effects

Chemical shift displacement effects, also known as chemical shift misregistration or chemical shift artifacts, were first described in 1984 through the observation of the fat signal shift[207]. The chemical shift displacement (s_δ) depends on $\mathbf{B}_0$ and the field gradient strengths[208]. Chemical shift displacement artifacts arise along the frequency encoding gradient direction, where the gradient causes variations in Larmor frequencies within columns of the selected slice (see Figure 1.17A). Consequently, the Larmor frequency of water molecules, which predominantly contribute to the signals observed in MRI, varies depending on their position, $\mathbf{B}_0$, and the applied gradient strength. For instance, with an excitation bandwidth of 50 kHz and a field of view of 6 × 6 mm, the gradient strength is approximately 8333 Hz per mm. This implies that for every millimetre distance in the sample, the ^{1}H Larmor frequency varies by 8333 Hz (see Figure 1.17A). However, due to the broad excitation bandwidths utilized, not only the ^{1}H signal of water is excited but also signals from various other metabolites. These compounds do not precess with the same Larmor frequency as water but at a frequency depending on $\mathbf{B}_0$. For example, at 28.2 T (1.2 GHz), the Larmor frequency difference between water protons and lipid protons is approximately 4080 Hz. Consequently, during data processing, the lipid signals are assumed to originate from a position that corresponds to a shift of 4080 Hz from their true position (see Figure 1.17B), or approximately 0.5 mm with the specified parameters. This results in the mismapping of the fat signal commonly observed in anatomical MRI (see Figure 1.17C). Although the absolute magnitude of chemical shift displacement artifacts is reduced by the increased gradient strengths applied in UHF MRI, the significantly improved spatial resolution of these systems results in these artifacts still posing a significant challenge during MRI data processing. Increasing the gradient bandwidth can help mitigate these issues, although fat-suppression is often the easiest solution.

Beyond anatomical imaging, single voxel ^{1}H localized MRS also experiences significant effects from chemical shift displacement. This displacement occurs in three directions due to the way the ROI is selectively excited (see Figure 1.16A). As a result, the MRS signal of any metabolite not exactly positioned at the excitation frequency—often chosen at 4.7 ppm—originates not from the ROI but from a shifted position depending on its Larmor frequency, $\mathbf{B}_0$, and the applied gradient strengths. This effect can become pronounced if the measurement parameters are not sufficiently optimized. For instance, at 28.2 T (1.2 GHz), using excitation pulses of 4200 Hz and an ROI of 1 × 1 × 1 mm, s_δ = 0.97 mm in the *x*, *y*, and *z* axes (see Figure 1.17D). Consequently, hardly any of the observed lipid signals originate from the selected ROI. Although OVS helps

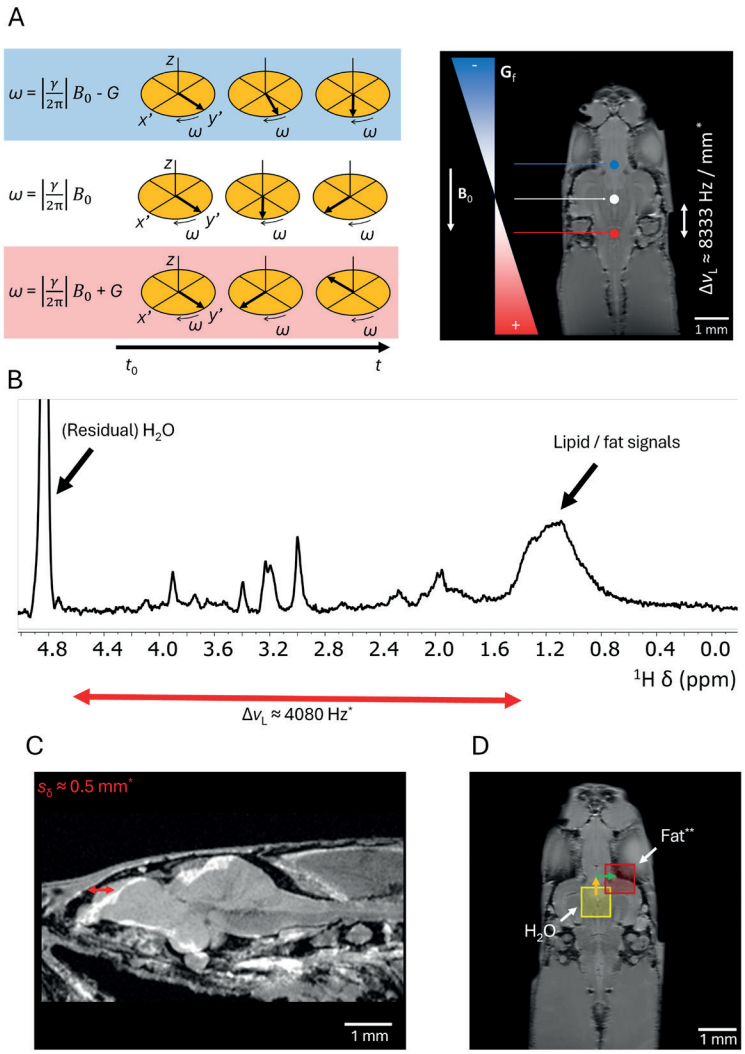

Figure 1.17 Chemical shift displacement artifacts [A] *In the frequency encoding direction, the Larmor frequency of the spins are modified relative to* $(\gamma/2\pi)B_0 \pm G_{local}$. *These variations in Larmor frequency are utilized for image reconstruction. Chemical shift displacement artifacts occur when the Larmor frequencies of metabolites differ from the excitation frequency. During image reconstruction, this frequency difference is erroneously attributed to the gradient rather than the actual frequency difference, leading to incorrect visualization of the metabolite signals.* ***[B]*** *For example, at 28.2 T the difference in the Larmor frequency of water protons and lipid protons is approximately 4080 Hz*.* ***[C]*** *In RARE, this results in significant MR lipid chemical shift displacement artifacts of approximately 0.5 mm*.* ***[D]*** *In single voxel localized MRS, chemical shift displacement effects cause the signals of metabolites that do not match the excitation frequency to originate from a spurious location. * s_δ for fat in RARE estimated assuming* B_0 *= 28.2 T / 1200 MHz, a gradient bandwidth of 50 kHz, excitation frequency of 4.7 ppm, and an ROI of 6 × 6 mm resulting in* G_F *= 8333 Hz/mm. ** s_δ for fat in PRESS estimated assuming* $\boldsymbol{B}_0$ *= 28.2 T / 1200 MHz, excitation bandwidths of 4200 Hz, excitation frequency of 4.7 ppm, and an ROI of 0.8 × 0.8 × 0.8 mm.*

to suppress signals from outside the ROI, the signal intensities observed for metabolites with different chemical shifts compared to the excitation frequency are significantly reduced. To mitigate this effect, it is essential to increase the gradient strength and optimize the excitation frequency for the metabolites of interest. Properly optimized measurement parameters can significantly reduce the impact of chemical shift displacement, improving the accuracy and reliability of the MRS data.

Magnetic susceptibility artifacts

Magnetic susceptibility refers to the tendency of a material to become magnetized when exposed to an external magnetic field[211]. A distortion in the primary magnetic field arises at the interface of two materials with different magnetic susceptibility. This distortion in the primary magnetic field causes a change in the local Larmor frequency, resulting in T_2^* dephasing signal loss and a misplacement of the MR signal in the phase encoding direction. Consequently, the characteristic pattern of a susceptibility artifact is observed, which is an area without signal next to a bright region as a consequence of misplaced signal accumulation (see Figure 1.18). Common places showing susceptibility artifacts in human MRI include the paranasal sinuses and the interface between bones and soft tissue[211]. In the paranasal sinuses, these artifacts stem from susceptibility differences between paramagnetic molecular oxygen in air and soft tissue, while in the bone-soft tissue interface, they are primarily due to the presence of diamagnetic calcium salts in bones. Additionally, just as paranasal sinuses can cause susceptibility artifacts, air bubbles can also induce significant artifacts, particularly in UHF micro-MRI, and should therefore be minimized whenever possible. Several imaging parameters contribute to the severity of susceptibility artifacts. First, the magnetization M (A/m) of a material increases linearly with the external magnetic field[132] according to $M = \chi_m \cdot B_0$, with χ_m the magnetic susceptibility of a material and B_0 the applied magnetic field strength (A/m). Since the severity of susceptibility artifacts increases with the magnetization of tissue, they also increase linearly with $\mathbf{B}_0$. Second, due to the T_2^* refocussing properties of the spin echo sequence, these are less affected by susceptibility artifacts compared to gradient echo sequences, which do not refocus T_2^* relaxation processes. This becomes especially clear in sequences incorporating EPI, which utilizes a train of gradient echoes for ultra-fast image acquisition (see Figure 1.18). Furthermore, utilization of longer *TE* will further escalate susceptibility artifacts for it provides more time for dephasing. Additionally, lower gradient strengths contribute to more pronounced susceptibility artifacts due to the mechanism by which spatial information is encoded by the frequency encoding gradient, as explained above for chemical shift displacement artifacts. Since magnetic susceptibility variations lead to localized changes in the Larmor frequency, MRI data reconstruction produces larger susceptibility artifacts at lower gradient strengths.

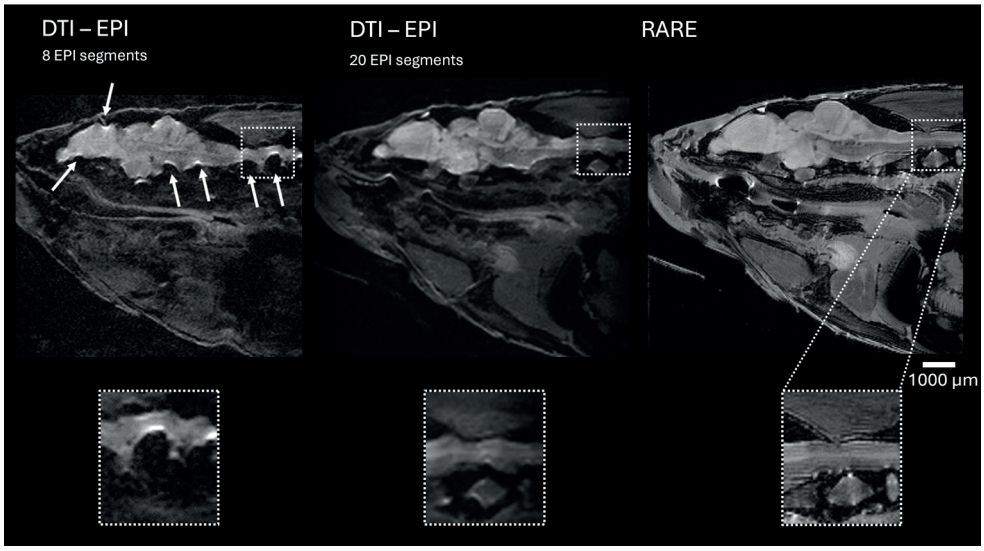

Figure 1.18 Susceptibility artifacts at UHF MRI (17.6 T / 750 MHz) *The first two images* ***[left & middle]*** *show DTI images each obtained with EPI, but at 8 and 20 segments, respectively. As the DTI image obtained with 8 EPI segments utilizes a longer gradient-echo train length, the susceptibility artifacts are more severe compared to the DTI image obtained with 20 EPI segment, although the susceptibility artifacts are still present. Contrary, the image obtained with a RARE MRI sequence shows very little susceptibility artifacts around the brain. From all three images, a zoomed image of the spinal cord is shown to highlight the severity of the susceptibility artifacts. All images were obtained with leptin deficient adult male zebrafish, at* $\boldsymbol{B}_0$ *17.6 T, Micro2.5 gradient system (Bruker Biospin GmbH, Germany)* G_{max} *= 1.5 T/m.*

4. MRI AND MRS OF THE ZEBRAFISH BRAIN

Although zebrafish are increasingly being used as an animal model for neurological disorders, the use of MRI or MRS to analyse the zebrafish brain is very limited compared to other model organisms (https://pubmed.ncbi.nlm.nih.gov/). The first report utilizing MRI to study anatomical structures in adult zebrafish, which included the zebrafish brain, was reported in 2006[125]. In 2010 the first high-resolution MRI images at 10 µm isotropic resolution of the zebrafish brain were reported[212]. This study utilized isolated zebrafish brains and employed contrast agents to enhance image quality for generating a three-dimensional digital atlas of the zebrafish brain[213]. In 2015, the same research group achieved another milestone by publishing the first whole-brain fibre tracking maps of the zebrafish brain through super-resolution track density imaging at 5 µm isotropic resolution, revealing intricate white matter structures in an isolated brain treated with contrast agents[192]. In 2023, Hamilton, Allen, and Reynolds conducted the first *in vivo* longitudinal examination of the zebrafish brain[214]. In addition, in 2009, the first and only known publication on performing localized MRS specifically on the zebrafish brain

was reported[65]. These advancements highlight the potential of MRI and MRS in zebrafish brain research, although technical challenges continue to limit their widespread application. These mainly arise from the tiny size of the zebrafish brain. As illustration in Table 1.3, the total volume of the zebrafish brain is approximately 4 mm^3, significantly smaller than the brain volume of other animal models or the human brain[213,215-225].

Obtaining high-resolution images of the zebrafish brain with good SNR within a reasonable measurement time, essential for visualizing and studying small structures, remains a challenge. It is well known that the SNR in MRI acquisition increases with the applied magnetic field strength[226], which can be leveraged to significantly reduce the required acquisition time needed to achieve the SNR[201]. To obtain near cellular resolution of 15 – 50 µm requires ultra-strong gradient systems. Strong gradients allow for superior encoding of spatial information, leading to the ability to distinguish smaller structures within the tissue. Since 1960, magnetic field strengths for MRI and MRS have increased almost linearly over the years (see Figure 1.19). Cellular level resolution (7 × 7 × 7 µm) in imaging of small biological structures has been demonstrated for visualizing individual bacteroids in root nodules[126]. In these experiments ultra-high magnetic field strength $\mathbf{B}_0$ = 22.3 T was used in combination with ultra-strong gradients (G_{max} = 3 T/m). By applying these advanced technologies to zebrafish brain imaging, we can potentially overcome many of the limitations posed by lower field strengths and gradient systems.

Table 1.3 *Comparison of average reported weight, volume, and number of neurons in the brain of humans, macaques, rats, mice, and zebrafish [213,215-225]. Created with biorender.com.*

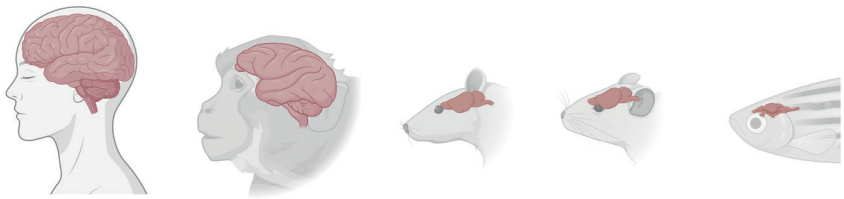

Species	Human (*Homo sapiens*)	Rhesus macaque (*Macaca mulatta*)	Rat (*Rattus*)	Mouse (*Mus musculus*)	Zebrafish (*Danio rerio*)
Brain weight (g)	1198 ♀ 1336 ♂	86.1 ♀ 96.1 ♂	1.8	0.4	0.001
Brain volume (mm^3)	$1130 \cdot 10^3$ ♀ $1260 \cdot 10^3$ ♂	$91.3 \cdot 10^3$ ♀ $98.7 \cdot 10^3$ ♂	1765	415	4
No. neurons	$86 \cdot 10^9$	$6.4 \cdot 10^9$	$200 \cdot 10^6$	$71 \cdot 10^6$	$10 \cdot 10^6$

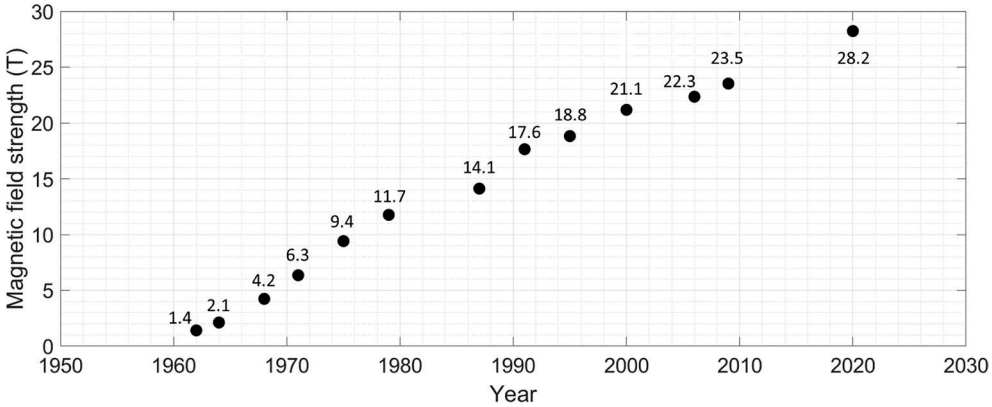

Figure 1.19 *Historical milestones of narrow bore (0.5 cm) magnetic field strength systems developed by Bruker Biospin GmbH, Germany. Data obtained from Bruker.*

5. THESIS SCOPE

In 2020, the introduction of technology operating at the highest commercially available magnetic field strength of 28.2 T marked the next historical milestone in the field of micro imaging. This UHF strength MRI system promises unparalleled spatial resolution and sensitivity, offering new opportunities for detailed anatomical and functional studies. This thesis aims to investigate the potential and challenges associated with using this advanced technology specifically for the examination of the zebrafish brain, an increasingly popular model organism in neurological research. The research presented in this work will focus on several key areas: conventional MRI for high-resolution anatomical imaging, dMRI for mapping the microstructural properties of neural tissues, and MRS for assessing the biochemical composition of the zebrafish brain. Each of these modalities will be evaluated for their efficacy in capturing the intricate details of zebrafish neuroanatomy and neurophysiology, which are critical for understanding fundamental biological processes and disease mechanisms. The ultra-high magnetic field strength of 28.2 T presents both opportunities and challenges. On the one hand, it enhances signal-to-noise ratio and spatial resolution, potentially allowing for unprecedented visualization of fine neural structures and subtle biochemical changes. On the other hand, it introduces technical challenges such as increased susceptibility and chemical shift artifacts. This thesis will systematically address these challenges, optimizing imaging protocols and developing strategies to mitigate artifacts and other issues.

In **Chapter 2**, various MRI and dMRI sequences are optimized for microstructural analysis of the zebrafish brain at exceptionally high spatial resolutions ranging from 23 to 50 μm. These optimizations are performed using the highest commercially available magnetic field strength of 28.2 T for imaging. Additionally, this chapter documents the first known instance of dMRI tractography of an intact zebrafish brain, employing advanced tractography algorithms to isolate white matter signals, thereby reducing noise. This enables the visualization and identification of tiny white matter structures at an extraordinary isotropic resolution of 5 μm.

Chapter 3 details the application of optimized MRI and dMRI techniques at 17.6 T to investigate microstructural changes resulting from toll-like receptor 2 (TLR2) deficiency in the zebrafish brain. In addition to analysing variations in the T_2 and *ADC* across different brain regions, advanced dMRI methods were employed. These included diffusion tensor imaging (DTI) and diffusion kurtosis imaging (DKI), which, alongside dMRI tractography, were used to specifically examine alterations in the integrity of small white matter structures in the zebrafish brain, revealing intriguing microstructural changes associated with compromised white matter integrity and axonal degeneration.

Chapter 4 describes the optimization of single voxel localized ^{1}H MRS at UHF MRI specifically for cerebral metabolic analysis in zebrafish. This chapter explores the potentials and challenges associated with UHF localized ^{1}H MRS on the zebrafish brain, with a focus on acquiring highly resolved spectra for targeted investigation of distinct brain regions. Highly resolved cerebral metabolite spectra were obtained from specific zebrafish brain regions, even from volumes as small as 125 nL. This enabled the identification and quantification of brain metabolites with exceptional resolution. Localized ^{1}H MRS at 28.2 T significantly enhanced the signal-to-noise ratio and improved the baseline separation of metabolite signals from these localized regions in the tiny zebrafish brain. This advancement extends the available techniques for utilizing zebrafish in neurological disorder research.

In **Chapter 5**, we delve into the cerebral metabolic changes occurring in the zebrafish brain as a direct consequence of TLR2 deficiency. This study employs a sophisticated combination of high-resolution magic angle spinning (HR-MAS) at 14.1 T to conduct whole-brain analysis and localized ^{1}H MRS at 28.2 T to focus on specific brain regions. Through these advanced techniques, we observed significant alterations in the levels of various neurotransmitters and metabolites that play critical roles in cerebral energy homeostasis. Notably, there was a substantial increase in lactate levels, which may be indicative of an elevated energy demand within the brain. Furthermore, we link the observed metabolic changes to previous findings to propose a model describing the effect of toll-like receptor 2 deficiency on the brain's microstructure.

Finally, **Chapter 6** presents a comprehensive discussion of the work presented in this thesis, offers a future outlook, and includes initial results of MRI and dMRI for other pathological zebrafish models. In this chapter I also provide suggestions of how the presented methods may be applied or modified for *in vivo* applications.

REFERENCES

1 G. B. D. Nervous System Disorders Collaborators, Global, regional, and national burden of disorders affecting the nervous system, 1990-2021: a systematic analysis for the Global Burden of Disease Study 2021. *Lancet Neurol* **23**, 344-381 (2024). https://doi.org/10.1016/S1474-4422(24)00038-3

2 Gooch, C. L., Pracht, E. & Borenstein, A. R. The burden of neurological disease in the United States: A summary report and call to action. *Ann Neurol* **81**, 479-484 (2017). https://doi.org/10.1002/ana.24897

3 Olesen, J. The cost of neurological disorders in Europe. *Public policy and health economics* **357** (2015). https://doi.org/https://doi.org/10.1016/j.jns.2015.09.303

4 Prince, M. *et al. World Alzheimer Report 2015. The Global Impact of Dementia. An Analysis of Prevalence, Incidence, Cost and Trends*. (2015).

5 Bovenkerk, B. & Kaldewaij, F. The use of animal models in behavioural neuroscience research. *Curr Top Behav Neurosci* **19**, 17-46 (2015). https://doi.org/10.1007/7854_2014_329

6 Montanari, M., Bonsi, P., Martella, G. & Wirz, A. Animal Models in Neuroscience: What Is the "Culture of Care"? *Encyclopedia* **4**, 215-233 (2024).

7 Attfield, K. E., Jensen, L. T., Kaufmann, M., Friese, M. A. & Fugger, L. The immunology of multiple sclerosis. *Nature Reviews Immunology* **22**, 734-750 (2022). https://doi.org/10.1038/s41577-022-00718-z

8 Jevtic, S., Sengar, A. S., Salter, M. W. & McLaurin, J. The role of the immune system in Alzheimer disease: Etiology and treatment. *Ageing Research Reviews* **40**, 84-94 (2017). https://doi.org/https://doi.org/10.1016/j.arr.2017.08.005

9 Tansey, M. G. & Romero-Ramos, M. Immune system responses in Parkinson's disease: Early and dynamic. *Eur J Neurosci* **49**, 364-383 (2019). https://doi.org/10.1111/ejn.14290

10 Bonilla, F. A. & Oettgen, H. C. Adaptive immunity. *Journal of Allergy and Clinical Immunology* **125**, S33-S40 (2010). https://doi.org/https://doi.org/10.1016/j.jaci.2009.09.017

11 Akira, S., Uematsu, S. & Takeuchi, O. Pathogen recognition and innate immunity. *Cell* **124**, 783-801 (2006). https://doi.org/10.1016/j.cell.2006.02.015

12 Hanke, M. L. & Kielian, T. Toll-like receptors in health and disease in the brain: mechanisms and therapeutic potential. *Clin Sci (Lond)* **121**, 367-387 (2011). https://doi.org/10.1042/cs20110164

13 Beg, A. A. Endogenous ligands of Toll-like receptors: implications for regulating inflammatory and immune responses. *Trends Immunol* **23**, 509-512 (2002). https://doi.org/10.1016/s1471-4906(02)02317-7

14 Matzinger, P. The danger model: a renewed sense of self. *Science* **296**, 301-305 (2002). https://doi.org/10.1126/science.1071059

15 Hu, W. & Spaink, H. P. The Role of TLR2 in Infectious Diseases Caused by Mycobacteria: From Cell Biology to Therapeutic Target. *Biology (Basel)* **11** (2022). https://doi.org/10.3390/biology11020246

16 Jin, M. S. & Lee, J.-O. Structures of the toll-like receptor family and its ligand complexes. *Immunity* **29**, 182-191 (2008).

17 Behzadi, P., Garcia-Perdomo, H. A. & Karpinski, T. M. Toll-Like Receptors: General Molecular and Structural Biology. *J Immunol Res* **2021**, 9914854 (2021). https://doi.org/10.1155/2021/9914854

18 Kornilov, F. D. *et al.* The architecture of transmembrane and cytoplasmic juxtamembrane regions of Toll-like receptors. *Nature Communications* **14**, 1503 (2023). https://doi.org/10.1038/s41467-023-37042-6

19 Takeuchi, O. & Akira, S. Pattern recognition receptors and inflammation. *Cell* **140**, 805-820 (2010). https://doi.org/10.1016/j.cell.2010.01.022

20 Kawagoe, T. *et al.* Sequential control of Toll-like receptor-dependent responses by IRAK1 and IRAK2. *Nat Immunol* **9**, 684-691 (2008). https://doi.org/10.1038/ni.1606

21 Xia, Z. P. *et al.* Direct activation of protein kinases by unanchored polyubiquitin chains. *Nature* **461**, 114-119 (2009). https://doi.org/10.1038/nature08247

22 Meijer, A. H. *et al.* Expression analysis of the Toll-like receptor and TIR domain adaptor families of zebrafish. *Mol Immunol* **40**, 773-783 (2004). https://doi.org/10.1016/j.molimm.2003.10.003

23 Chen, H., Liang, Y., Han, Y., Liu, T. & Chen, S. Genome-wide analysis of Toll-like receptors in zebrafish and the effect of rearing temperature on the receptors in response to stimulated pathogen infection. *Journal of Fish Diseases* **44**, 337-349 (2021). https://doi.org/https://doi.org/10.1111/jfd.13287

24 Li, Y., Li, Y., Cao, X., Jin, X. & Jin, T. Pattern recognition receptors in zebrafish provide functional and evolutionary insight into innate immune signaling pathways. *Cell Mol Immunol* **14**, 80-89 (2017). https://doi.org/10.1038/cmi.2016.50

25 Acioglu, C., Heary, R. F. & Elkabes, S. Roles of neuronal toll-like receptors in neuropathic pain and central nervous system injuries and diseases. *Brain, Behavior, and Immunity* **102**, 163-178 (2022). https://doi.org/https://doi.org/10.1016/j.bbi.2022.02.016

26 Tuomanen, E., Liu, H., Hengstler, B., Zak, O. & Tomasz, A. The Induction of Meningeal Inflammation by Components of the Pneumococcal Cell Wall. *The Journal of Infectious Diseases* **151**, 859-868 (1985). https://doi.org/10.1093/infdis/151.5.859

27 Koedel, U., Scheld, W. M. & Pfister, H.-W. Pathogenesis and pathophysiology of pneumococcal meningitis. *The Lancet infectious diseases* **2**, 721-736 (2002).

28 Weber, J. R. & Tuomanen, E. I. Cellular damage in bacterial meningitis: an interplay of bacterial and host driven toxicity. *Journal of neuroimmunology* **184**, 45-52 (2007).

29 Momtazmanesh, S., Perry, G. & Rezaei, N. Toll-like receptors in Alzheimer's disease. *Journal of Neuroimmunology* **348**, 577362 (2020). https://doi.org/https://doi.org/10.1016/j.jneuroim.2020.577362

30 Kinney, J. W. *et al.* Inflammation as a central mechanism in Alzheimer's disease. *Alzheimer's & Dementia: Translational Research & Clinical Interventions* **4**, 575-590 (2018).

31 Gomez, W., Morales, R., Maracaja-Coutinho, V., Parra, V. & Nassif, M. Down syndrome and Alzheimer's disease: common molecular traits beyond the amyloid precursor protein. *Aging (Albany NY)* **12**, 1011 (2020).

32 Chakrabarty, P. *et al.* TLR5 decoy receptor as a novel anti-amyloid therapeutic for Alzheimer's disease. *Journal of Experimental Medicine* **215**, 2247-2264 (2018).

33 Walter, S. *et al.* Role of the toll-like receptor 4 in neuroinflammation in Alzheimer's disease. *Cellular Physiology and Biochemistry* **20**, 947-956 (2007).

34 Walker, D. G., Tang, T. M. & Lue, L.-F. Increased expression of toll-like receptor 3, an anti-viral signaling molecule, and related genes in Alzheimer's disease brains. *Experimental neurology* **309**, 91-106 (2018).

35 Gold, M. & El Khoury, J. in *Seminars in immunopathology*. 607-611 (Springer).

36 Frank, S., Copanaki, E., Burbach, G. J., Müller, U. C. & Deller, T. Differential regulation of toll-like receptor mRNAs in amyloid plaque-associated brain tissue of aged APP23 transgenic mice. *Neuroscience letters* **453**, 41-44 (2009).

37 Kiasalari, Z. *et al.* Ellagic acid ameliorates learning and memory deficits in a rat model of Alzheimer's disease: an exploration of underlying mechanisms. *Psychopharmacology* **234**, 1841-1852 (2017).

38 Rangasamy, S. B. *et al.* Selective disruption of TLR2-MyD88 interaction inhibits inflammation and attenuates Alzheimer's pathology. *The Journal of Clinical Investigation* **128**, 4297-4312 (2018).

39 Bsibsi, M., Ravid, R., Gveric, D. & van Noort, J. M. Broad expression of Toll-like receptors in the human central nervous system. *Journal of Neuropathology & Experimental Neurology* **61**, 1013-1021 (2002).

40 Go, M., Kou, J., Lim, J.-E., Yang, J. & Fukuchi, K.-i. Microglial response to LPS increases in wild-type mice during aging but diminishes in an Alzheimer's mouse model: implication of TLR4 signaling in disease progression. *Biochemical and biophysical research communications* **479**, 331-337 (2016).

41 Trotta, T., Porro, C., Calvello, R. & Panaro, M. A. Biological role of Toll-like receptor-4 in the brain. *Journal of neuroimmunology* **268**, 1-12 (2014).

42 Tahara, K. *et al.* Role of toll-like receptor signalling in Aβ uptake and clearance. *Brain* **129**, 3006-3019 (2006).

43 Pourbadie, H. G. *et al.* Early minor stimulation of microglial TLR2 and TLR4 receptors attenuates Alzheimer's disease–related cognitive deficit in rats: behavioral, molecular, and electrophysiological evidence. *Neurobiology of aging* **70**, 203-216 (2018).

44 Yousefi, N. *et al.* Prestimulation of microglia through TLR4 pathway promotes interferon beta expression in a rat model of Alzheimer's disease. *Journal of Molecular Neuroscience* **67**, 495-503 (2019).

45 Wu, L. *et al.* Toll-Like Receptor 4: A Promising Therapeutic Target for Alzheimer's Disease. *Mediators Inflamm* **2022**, 7924199 (2022). https://doi.org/10.1155/2022/7924199

46 Xiang, W., Chao, Z.-Y. & Feng, D.-Y. Role of Toll-like receptor/MYD88 signaling in neurodegenerative diseases. *Reviews in the neurosciences* **26**, 407-414 (2015).

47 Richard, K. L., Filali, M., Prefontaine, P. & Rivest, S. Toll-like receptor 2 acts as a natural innate immune receptor to clear amyloid beta 1-42 and delay the cognitive decline in a mouse model of Alzheimer's disease. *J Neurosci* **28**, 5784-5793 (2008). https://doi.org/10.1523/JNEUROSCI.1146-08.2008

48 Jana, M., Palencia, C. A. & Pahan, K. Fibrillar amyloid-β peptides activate microglia via TLR2: implications for Alzheimer's disease. *The Journal of Immunology* **181**, 7254-7262 (2008).

49 Zhou, C. *et al.* Genomic deletion of TLR2 induces aggravated white matter damage and deteriorated neurobehavioral functionsin mouse models of Alzheimer's disease. *Aging* **11** (2019). https://doi.org/10.18632/aging.102260

50 Allen, H. B. Alzheimer's disease: assessing the role of spirochetes, biofilms, the immune system, and amyloid-β with regard to potential treatment and prevention. *Journal of Alzheimer's Disease* **53**, 1271-1276 (2016).

51 Heidari, A., Yazdanpanah, N. & Rezaei, N. The role of Toll-like receptors and neuroinflammation in Parkinson's disease. *Journal of Neuroinflammation* **19**, 135 (2022). https://doi.org/10.1186/s12974-022-02496-w

52 Casula, M. *et al.* Toll-like receptor signaling in amyotrophic lateral sclerosis spinal cord tissue. *Neuroscience* **179**, 233-243 (2011). https://doi.org/10.1016/j.neuroscience.2011.02.001

53 Tajalli-Nezhad, S., Karimian, M., Beyer, C., Atlasi, M. A. & Azami Tameh, A. The regulatory role of Toll-like receptors after ischemic stroke: neurosteroids as TLR modulators with the focus on TLR2/4. *Cellular and Molecular Life Sciences* **76**, 523-537 (2019). https://doi.org/10.1007/s00018-018-2953-2

54 Hu W, Yang S, Shimada Y, Münch M, Marín-Juez R, Meijer AH, Spaink HP. Infection and RNA-seq analysis of a zebrafish tlr2 mutant shows a broad function of this toll-like receptor in transcriptional and metabolic control and defense to Mycobacterium marinum infection. BMC Genomics. 2019 Nov 20;20(1):878. doi: 10.1186/s12864-019-6265-1. PMID: 31747871; PMCID: PMC6869251.

55 Makałowski, W., Boguski, M., Hughes, A. & Yeager, M. Synonymous and nonsynonymous substitution distances are correlated in mouse and rat genes. *Journal of molecular evolution* **47**, 119-121 (1998).

56 Makałowski, W. & Boguski, M. S. Evolutionary parameters of the transcribed mammalian genome: an analysis of 2,820 orthologous rodent and human sequences. *Proceedings of the National Academy of Sciences* **95**, 9407-9412 (1998).

57 Lamerdin, J. E. *et al.* Genomic sequence comparison of the human and mouse XRCC1 DNA repair gene regions. *Genomics* **25**, 547-554 (1995).

58 Koop, B. F. & Hood, L. Striking sequence similarity over almost 100 kilobases of human and mouse T–cell receptor DNA. *Nature genetics* **7**, 48-53 (1994).

59 Giacomotto, J. & Ségalat, L. High-throughput screening and small animal models, where are we? *British Journal of Pharmacology* **160**, 204-216 (2010). https://doi.org/https://doi.org/10.1111/j.1476-5381.2010.00725.x

60 Streisinger, G., Walker, C., Dower, N., Knauber, D. & Singer, F. Production of clones of homozygous diploid zebra fish (Brachydanio rerio). *Nature* **291**, 293-296 (1981). https://doi.org/10.1038/291293a0

61 Mullins, M. C., Acedo, J. N., Priya, R., Solnica-Krezel, L. & Wilson, S. W. The zebrafish issue: 25 years on. *Development* **148** (2021). https://doi.org/10.1242/dev.200343

62 Sarasamma, S., Karim, A. & Orengo, J. P. Zebrafish Models of Rare Neurological Diseases like Spinocerebellar Ataxias (SCAs): Advantages and Limitations. *Biology* **12**, 1322 (2023).

63 Quiñonez-Silvero, C., Hübner, K. & Herzog, W. Development of the brain vasculature and the blood-brain barrier in zebrafish. *Dev Biol* **457**, 181-190 (2020). https://doi.org/10.1016/j.ydbio.2019.03.005

64 Lyons, D. A. & Talbot, W. S. Glial cell development and function in zebrafish. *Cold Spring Harb Perspect Biol* **7**, a020586 (2014). https://doi.org/10.1101/cshperspect.a020586

65 Kabli, S., Spaink, H. P., De Groot, H. J. & Alia, A. In vivo metabolite profile of adult zebrafish brain obtained by high-resolution localized magnetic resonance spectroscopy. *J Magn Reson Imaging* **29**, 275-281 (2009). https://doi.org/10.1002/jmri.21609

66 Braakman, N., Oerther, T., de Groot, H. J. & Alia, A. High resolution localized two-dimensional MR spectroscopy in mouse brain in vivo. *Magn Reson Med* **60**, 449-456 (2008). https://doi.org/10.1002/mrm.21662

67 Veeraiah, P. & Jansen, J. F. A. Multinuclear Magnetic Resonance Spectroscopy at Ultra-High-Field: Assessing Human Cerebral Metabolism in Healthy and Diseased States. *Metabolites* **13** (2023). https://doi.org/10.3390/metabo13040577

68 Fontana, B. D. *et al.* Zebrafish models for attention deficit hyperactivity disorder (ADHD). *Neurosci Biobehav Rev* **100**, 9-18 (2019). https://doi.org/10.1016/j.neubiorev.2019.02.009

69 Rea, V. & Van Raay, T. J. Using Zebrafish to Model Autism Spectrum Disorder: A Comparison of ASD Risk Genes Between Zebrafish and Their Mammalian Counterparts. *Frontiers in Molecular Neuroscience* **13** (2020). https://doi.org/10.3389/fnmol.2020.575575

70 Saleem, S. & Kannan, R. R. Zebrafish: an emerging real-time model system to study Alzheimer's disease and neurospecific drug discovery. *Cell Death Discov* **4**, 45 (2018). https://doi.org/10.1038/s41420-018-0109-7

71 Oliveira, N. A. S., Pinho, B. R. & Oliveira, J. M. A. Swimming against ALS: How to model disease in zebrafish for pathophysiological and behavioral studies. *Neurosci Biobehav Rev* **148**, 105138 (2023). https://doi.org/10.1016/j.neubiorev.2023.105138

72 Kumar, V., Singh, C. & Singh, A. Zebrafish an experimental model of Huntington's disease: molecular aspects, therapeutic targets and current challenges. *Mol Biol Rep* **48**, 8181-8194 (2021). https://doi.org/10.1007/s11033-021-06787-y

73 Doyle, J. M. & Croll, R. P. A Critical Review of Zebrafish Models of Parkinson's Disease. *Front Pharmacol* **13**, 835827 (2022). https://doi.org/10.3389/fphar.2022.835827

74 Chen, W. *et al.* Zebrafish as a Model for In-Depth Mechanistic Study for Stroke. *Transl Stroke Res* **12**, 695-710 (2021). https://doi.org/10.1007/s12975-021-00907-3

75 Walcott, B. P. & Peterson, R. T. Zebrafish models of cerebrovascular disease. *J Cereb Blood Flow Metab* **34**, 571-577 (2014). https://doi.org/10.1038/jcbfm.2014.27

76 D'Amora, M. *et al.* Zebrafish as an Innovative Tool for Epilepsy Modeling: State of the Art and Potential Future Directions. *Int J Mol Sci* **24** (2023). https://doi.org/10.3390/ijms24097702

77 Kulkarni, P. *et al.* Novel Zebrafish EAE model: A quick in vivo screen for multiple sclerosis. *Multiple Sclerosis and Related Disorders* **11**, 32-39 (2017). https://doi.org/https://doi.org/10.1016/j.msard.2016.11.010

78 Richert, E. *Zebrafish Model of Schizophrenia*, (2021).

79 Tikhonova, M. A. *et al.* A Novel Laser-Based Zebrafish Model for Studying Traumatic Brain Injury and Its Molecular Targets. *Pharmaceutics* **14** (2022). https://doi.org/10.3390/pharmaceutics14081751

80 Reimunde, P. *et al.* Cellular and Molecular Mechanisms Underlying Glioblastoma and Zebrafish Models for the Discovery of New Treatments. *Cancers (Basel)* **13** (2021). https://doi.org/10.3390/cancers13051087

81 Hu, W. *et al.* Transcriptomic and Metabolomic Studies Reveal That Toll-like Receptor 2 Has a Role in Glucose-Related Metabolism in Unchallenged Zebrafish Larvae (Danio rerio). *Biology (Basel)* **12** (2023). https://doi.org/10.3390/biology12020323

82 Martucci, M. *et al.* Magnetic Resonance Imaging of Primary Adult Brain Tumors: State of the Art and Future Perspectives. *Biomedicines* **11** (2023). https://doi.org/10.3390/biomedicines11020364

83 Rangarajan, K., Das, C. J., Kumar, A. & Gupta, A. K. MRI in central nervous system infections: A simplified patterned approach. *World J Radiol* **6**, 716-725 (2014). https://doi.org/10.4329/wjr.v6.i9.716

84 Lee, H., Yang, Y., Xu, J., Ware, J. B. & Liu, B. Use of Magnetic Resonance Imaging in Acute Traumatic Brain Injury Patients is Associated with Lower Inpatient Mortality. *J Clin Imaging Sci* **11**, 53 (2021). https://doi.org/10.25259/jcis_148_2021

85 Tedyanto, E. H., Tini, K. & Pramana, N. A. K. Magnetic Resonance Imaging in Acute Ischemic Stroke. *Cureus* **14**, e27224 (2022). https://doi.org/10.7759/cureus.27224

86 Kartal, M. G. & Algin, O. Evaluation of hydrocephalus and other cerebrospinal fluid disorders with MRI: An update. *Insights Imaging* **5**, 531-541 (2014). https://doi.org/10.1007/s13244-014-0333-5

87 Heit, J. J., Iv, M. & Wintermark, M. Imaging of Intracranial Hemorrhage. *J Stroke* **19**, 11-27 (2017). https://doi.org/10.5853/jos.2016.00563

88 Sharma, U. & Jagannathan, N. R. Metabolism of prostate cancer by magnetic resonance spectroscopy (MRS). *Biophys Rev* **12**, 1163-1173 (2020). https://doi.org/10.1007/s12551-020-00758-6

89 Cowin, G. J. *et al.* Magnetic resonance imaging and spectroscopy for monitoring liver steatosis. *J Magn Reson Imaging* **28**, 937-945 (2008). https://doi.org/10.1002/jmri.21542

90 Ali, H. A. *et al.* Predictive Value of In Vivo MR Spectroscopy With Semilocalization by Adiabatic Selective Refocusing in Differentiating Clear Cell Renal Cell Carcinoma From Other Subtypes. *AJR Am J Roentgenol* **214**, 817-824 (2020). https://doi.org/10.2214/AJR.19.22023

91 Brown, J. J., Mirowitz, S. A., Sandstrom, J. C. & Perman, W. H. MR Spectroscopy of the heart. *American Journal of Roentgenology* **155** (1990).

92 Graff-Radford, J. & Kantarci, K. Magnetic resonance spectroscopy in Alzheimer's disease. *Neuropsychiatr Dis Treat* **9**, 687-696 (2013). https://doi.org/10.2147/NDT.S35440

93 Weinberg, B. D., Kuruva, M., Shim, H. & Mullins, M. E. Clinical Applications of Magnetic Resonance Spectroscopy in Brain Tumors: From Diagnosis to Treatment. *Radiol Clin North Am* **59**, 349-362 (2021). https://doi.org/10.1016/j.rcl.2021.01.004

94 Nakahara, T. *et al.* Glutamatergic and GABAergic metabolite levels in schizophrenia-spectrum disorders: a meta-analysis of (1)H-magnetic resonance spectroscopy studies. *Mol Psychiatry* **27**, 744-757 (2022). https://doi.org/10.1038/s41380-021-01297-6

95 Kalra, S. Magnetic Resonance Spectroscopy in ALS. *Front Neurol* **10**, 482 (2019). https://doi.org/10.3389/fneur.2019.00482

96 Pan, J. W. & Kuzniecky, R. I. Utility of magnetic resonance spectroscopic imaging for human epilepsy. *Quant Imaging Med Surg* **5**, 313-322 (2015). https://doi.org/10.3978/j.issn.2223-4292.2015.01.03

97 Sajja, B. R., Wolinsky, J. S. & Narayana, P. A. Proton magnetic resonance spectroscopy in multiple sclerosis. *Neuroimaging Clin N Am* **19**, 45-58 (2009). https://doi.org/10.1016/j.nic.2008.08.002

98 Shoeibi, A. *et al.* Brain proton magnetic resonance spectroscopy in patients with Parkinson's disease. *Curr J Neurol* **21**, 156-161 (2022). https://doi.org/10.18502/cjn.v21i3.11108

99 Eeza, M. N. H. *et al.* Metabolic Profiling of Suprachiasmatic Nucleus Reveals Multifaceted Effects in an Alzheimer's Disease Mouse Model. *J Alzheimers Dis* (2021). https://doi.org/10.3233/JAD-201575

100 Miller, B. L. *et al.* Alzheimer disease: depiction of increased cerebral myo-inositol with proton MR spectroscopy. *Radiology* **187**, 4 (1993). https://doi.org/10.1148/radiology.187.2.8475286.

101 Bitsch, A. *et al.* Inflammatory CNS demyelination: histopathologic correlation with in vivo quantitative proton MR spectroscopy. *Am J Neuroradiol* **9**, 1619-1627 (1999).

102 Mader, I., Rauer, S., Gall, P. & Klose, U. (1)H MR spectroscopy of inflammation, infection and ischemia of the brain. *Eur J Radiol* **67**, 250-257 (2008). https://doi.org/10.1016/j.ejrad.2008.02.033

103 Young, S. P. *et al.* The impact of inflammation on metabolomic profiles in patients with arthritis. *Arthritis Rheum* **65**, 2015-2023 (2013). https://doi.org/10.1002/art.38021

104 Cocco, E. *et al.* (1)H-NMR analysis provides a metabolomic profile of patients with multiple sclerosis. *Neurol Neuroimmunol Neuroinflamm* **3**, 1-9 (2016). https://doi.org/10.1212/NXI.0000000000000185

105 Kim, H. H. *et al.* Metabolomic profiling of CSF in multiple sclerosis and neuromyelitis optica spectrum disorder by nuclear magnetic resonance. *PLoS One* **12**, 21 (2017). https://doi.org/10.1371/journal.pone.0181758

106 Battini, S. *et al.* Metabolomics approaches in experimental allergic encephalomyelitis. *J Neuroimmunol* **314**, 94-100 (2018). https://doi.org/10.1016/j.jneuroim.2017.11.018

107 French, C. D. *et al.* NMR metabolomics of cerebrospinal fluid differentiates inflammatory diseases of the central nervous system. *PLOS Negl Trop Dis* **12**, 1-17 (2018). https://doi.org/10.1371/journal.pntd.0007045

108 Fernando, K. T. *et al.* Elevated white matter myo-inositol in clinically isolated syndromes suggestive of multiple sclerosis. *Brain* **127**, 1361-1369 (2004). https://doi.org/10.1093/brain/awh153

109 Kazama, M. *et al.* Astrocytes release glutamate via cystine/glutamate antiporter upregulated in response to increased oxidative stress related to sporadic amyotrophic lateral sclerosis. *Neuropathology* **40**, 587-598 (2020). https://doi.org/10.1111/neup.12716

110 Iovino, L., Tremblay, M. E. & Civiero, L. Glutamate-induced excitotoxicity in Parkinson's disease: The role of glial cells. *J Pharmacol Sci* **144**, 151-164 (2020). https://doi.org/10.1016/j.jphs.2020.07.011

111 Maszka, P. *et al.* Metabolomic Footprint of Disrupted Energetics and Amino Acid Metabolism in Neurodegenerative Diseases: Perspectives for Early Diagnosis and Monitoring of Therapy. *Metabolites* **13** (2023). https://doi.org/10.3390/metabo13030369

112 Bloch, F., Hansen, W. W. & Packard, M. The Nuclear Induction Experiment. *Physical Review* **70**, 474-485 (1946). https://doi.org/10.1103/PhysRev.70.474

113 Purcell, E. M., Torrey, H. C. & Pound, R. V. Resonance Absorption by Nuclear Magnetic Moments in a Solid. *Physical Review* **69**, 37-38 (1946). https://doi.org/10.1103/PhysRev.69.37

114 *The Nobel Prize in Physics 1952*, <https://www.nobelprize.org/prizes/physics/1952/summary> (

115 Friebolin, H. *Basic One- and Two-Dimensional NMR Spectroscopy, 5th, Completely Revised and Updated Edition*. 442 (Wiley-VCH, 2010).

116 Wielpütz, M. & Kauczor, H.-U. MRI of the lung: state of the art. Diagnostic and interventional radiology 18, 344 (2012).

117 Bertoli, D. et al. A novel MRI-based three-dimensional model of stomach volume, surface area, and geometry in response to gastric filling and emptying. Neurogastroenterology & Motility 35, e14497 (2023). https://doi.org/https://doi.org/10.1111/nmo.14497

118 Feinberg, D. A. *et al.* Next-generation MRI scanner designed for ultra-high-resolution human brain imaging at 7 Tesla. *Nat Methods* **20**, 2048-2057 (2023). https://doi.org/10.1038/s41592-023-02068-7

119 Menon, R. G., Chang, G. & Regatte, R. R. Musculoskeletal MR Imaging Applications at Ultra-High (7T) Field Strength. *Magn Reson Imaging Clin N Am* **29**, 117-127 (2021). https://doi.org/10.1016/j.mric.2020.09.008

120 Umutlu, L. *et al.* Contrast-enhanced ultra-high-field liver MRI: a feasibility trial. *Eur J Radiol* **82**, 760-767 (2013). https://doi.org/10.1016/j.ejrad.2011.07.004

121 Kataoka, M. *et al.* Ultrafast Dynamic Contrast-enhanced MRI of the Breast: How Is It Used? *Magn Reson Med Sci* **21**, 83-94 (2022). https://doi.org/10.2463/mrms.rev.2021-0157

122 Nikken, J. J. & Krestin, G. P. MRI of the kidney-state of the art. *Eur Radiol* **17**, 2780-2793 (2007). https://doi.org/10.1007/s00330-007-0701-3

123 Schreiber, L. M. *et al.* Ultra-high field cardiac MRI in large animals and humans for translational cardiovascular research. *Front Cardiovasc Med* **10**, 1068390 (2023). https://doi.org/10.3389/fcvm.2023.1068390

124 Braakman, N. *et al.* Longitudinal assessment of Alzheimer's beta-amyloid plaque development in transgenic mice monitored by in vivo magnetic resonance microimaging. *J Magn Reson Imaging* **24**, 530-536 (2006). https://doi.org/10.1002/jmri.20675

125 Kabli, S., Alia, A., Spaink, H. P., Verbeek, F. J. & De Groot, H. J. Magnetic resonance microscopy of the adult zebrafish. *Zebrafish* **3**, 431-439 (2006). https://doi.org/10.1089/zeb.2006.3.431

126 van Schadewijk, R. *et al.* Magnetic Resonance Microscopy at Cellular Resolution and Localised Spectroscopy of Medicago truncatula at 22.3 Tesla. *Sci Rep* **10**, 971 (2020). https://doi.org/10.1038/s41598-020-57861-7

127 Hahn, E. L. Spin Echoes. *Physical Review* **80**, 580-594 (1950). https://doi.org/10.1103/PhysRev.80.580

128 Hennig, J., Nauerth, A. & Friedburg, H. RARE Imaging: A Fast Imaging Method for Clinical MR *Magnetic Resonance in Medicine* **3**, 11 (1986). https://doi.org/https://doi.org/10.1002/mrm.1910030602

129 Kara, F. *et al.* In vivo measurement of transverse relaxation time in the mouse brain at 17.6 T. *Magn Reson Med* **70**, 985-993 (2013). https://doi.org/10.1002/mrm.24533

130 de Graaf, R. A. *et al.* High magnetic field water and metabolite proton T1 and T2 relaxation in rat brain in vivo. *Magn Reson Med* **56**, 386-394 (2006). https://doi.org/10.1002/mrm.20946

131 Lee, M. J. *et al.* Overcoming Artifacts from Metallic Orthopedic Implants at High-Field-Strength MR Imaging and Multi-detector CT1. *Radiographics* **27**, 13 (2007). https://doi.org/10.1148/rg.273065087

132 Lüdeke, K., Röschmann, P. & Tischler, R. Susceptibility artefacts in NMR imaging. *Magnetic Resonance Imaging* **3**, 15 (1985).

133 Hardy, P. A., Henkelman, R. M., Bishop, J. E., Poon, E. C. S. & Plewes, D. B. Why fat is bright in rare and fast spin-echo imaging. *Journal of magnetic Resonance Imaging* **2**, 8 (1992).

134 Poustchi-Amin, M., Mirowitz, S. A., Brown, J. J., McKinstry, R. C. & Li, T. Principles and Applications of Echo-planar Imaging: A Review for the General Radiologist. *RadioGraphics* **21**, 767-779 (2001). https://doi.org/10.1148/radiographics.21.3.g01ma23767

135 Bottomley, P. A., Foster, T. H., Argersinger, R. E. & Pfeifer, L. M. A review of normal tissue hydrogen NMR relaxation times and relaxation mechanisms from 1-100 MHz: dependence on tissue type, NMR frequency, temperature, species, excision, and age. *Med Phys* **11**, 425-448 (1984). https://doi.org/10.1118/1.595535

136 Abd-Ellah, M. K., Awad, A. I., Khalaf, A. A. M. & Hamed, H. F. A. A review on brain tumor diagnosis from MRI images: Practical implications, key achievements, and lessons learned. *Magn Reson Imaging* **61**, 300-318 (2019). https://doi.org/10.1016/j.mri.2019.05.028

137 Harms, S. E., Siemers, P. T., Hildenbrand, P. & Plum, G. Multiple spin echo magnetic resonance imaging of the brain. *RadioGraphics* **6**, 117-134 (1986). https://doi.org/10.1148/radiographics.6.1.3685481

138 Carr, H. Y. & Purcell, E. M. Effects of Diffusion on Free Precession in Nuclear Magnetic Resonance Experiments. *Physical Review* **94**, 630-638 (1954). https://doi.org/10.1103/PhysRev.94.630

139 Milford, D., Rosbach, N., Bendszus, M. & Heiland, S. Mono-Exponential Fitting in T2-Relaxometry: Relevance of Offset and First Echo. *PLoS One* **10**, e0145255 (2015). https://doi.org/10.1371/journal.pone.0145255

140 Majumdar, S., Orphanoudakis, S. C., Gmitro, A., O'Donnell, M. & Gore, J. C. Errors in the measurements of T2 using multiple-echo MRI techniques. I. Effects of radiofrequency pulse imperfections. *Magn Reson Med* **3**, 397-417 (1986). https://doi.org/10.1002/mrm.1910030305

141 Zelaya, F. O. *et al.* Direct visualisation of B1 inhomogeneity by flip angle dependency. *Magn Reson Imaging* **15**, 497-504 (1997). https://doi.org/10.1016/s0730-725x(96)00396-7

142 Dietrich, O., Reiser, M. F. & Schoenberg, S. O. Artifacts in 3-T MRI: physical background and reduction strategies. *Eur J Radiol* **65**, 29-35 (2008). https://doi.org/10.1016/j.ejrad.2007.11.005

143 Einstein, A. Über die von der molekularkinetischen Theorie der Wärme geforderte Bewegung von in ruhenden Flüssigkeiten suspendierten Teilchen. *Annalen der Physik* **322**, 549-560 (1905). https://doi.org/https://doi.org/10.1002/andp.19053220806

144 Campbell, J. S. W. & Bruce Pike, G. in *Encyclopedia of Biomedical Engineering* (ed Roger Narayan) 505-518 (Elsevier, 2019).

145 Messina, C. *et al.* Diffusion-Weighted Imaging in Oncology: An Update. *Cancers* **12**, 1493 (2020).

146 Guirguis, M., Sharan, G., Wang, J. & Chhabra, A. Diffusion-weighted MR imaging of musculoskeletal tissues: incremental role over conventional MR imaging in bone, soft tissue, and nerve lesions. *BJR|Open* **4** (2022). https://doi.org/10.1259/bjro.20210077

147 Mekkaoui, C., Reese, T. G., Jackowski, M. P., Bhat, H. & Sosnovik, D. E. Diffusion MRI in the heart. *NMR in Biomedicine* **30**, e3426 (2017). https://doi.org/https://doi.org/10.1002/nbm.3426

148 Srinivasan, A., Goyal, M., Azri, F. A. & Lum, C. State-of-the-Art Imaging of Acute Stroke. *RadioGraphics* **26**, S75-S95 (2006). https://doi.org/10.1148/rg.26si065501

149 Bollineni, V. R., Kramer, G., Liu, Y., Melidis, C. & deSouza, N. M. A literature review of the association between diffusion-weighted MRI derived apparent diffusion coefficient and tumour aggressiveness in pelvic cancer. *Cancer Treatment Reviews* **41**, 496-502 (2015). https://doi.org/10.1016/j.ctrv.2015.03.010

150 Nalaini, F., Shahbazi, F., Mousavinezhad, S. M., Ansari, A. & Salehi, M. Diagnostic accuracy of apparent diffusion coefficient (ADC) value in differentiating malignant from benign solid liver lesions: a systematic review and meta-analysis. *British Journal of Radiology* **94** (2021). https://doi.org/10.1259/bjr.20210059

151 Vollenbrock, S. E., Voncken, F. E. M., Bartels, L. W., Beets-Tan, R. G. H. & Bartels-Rutten, A. Diffusion-weighted MRI with ADC mapping for response prediction and assessment of oesophageal cancer: A systematic review. *Radiotherapy and Oncology* **142**, 17-26 (2020). https://doi.org/10.1016/j.radonc.2019.07.006

152 Trivedi, R., Rathore, R. K. S. & Gupta, R. K. Review: Clinical application of diffusion tensor imaging. *Indian J Radiol Imaging* **18**, 7 (2008). https://doi.org/10.4103/0971-3026.38505

153 Steven, A. J., Zhuo, J. & Melhem, E. R. Diffusion Kurtosis Imaging: An Emerging Technique for Evaluating the Microstructural Environment of the Brain. *American Journal of Roentgenology* **202**, W26-W33 (2014). https://doi.org/10.2214/ajr.13.11365

154 Harkins, K. D., Beaulieu, C., Xu, J., Gore, J. C. & Does, M. D. A simple estimate of axon size with diffusion MRI. *NeuroImage* **227**, 117619 (2021). https://doi.org/https://doi.org/10.1016/j.neuroimage.2020.117619

155 Zhang, F. *et al.* Quantitative mapping of the brain's structural connectivity using diffusion MRI tractography: A review. *NeuroImage* **249**, 118870 (2022). https://doi.org/https://doi.org/10.1016/j.neuroimage.2021.118870

156 Bihan, D. L. *et al.* MR imaging of intravoxel incoherent motions: application to diffusion and perfusion in neurologic disorders. *Radiology* **161**, 401-407 (1986). https://doi.org/10.1148/radiology.161.2.3763909

157 Baliyan, V., Das, C. J., Sharma, R. & Gupta, A. K. Diffusion weighted imaging: Technique and applications. *World J Radiol* **8**, 785-798 (2016). https://doi.org/10.4329/wjr.v8.i9.785

158 Heemskerk, A. M. & Damon, B. M. Diffusion Tensor MRI Assessment of Skeletal Muscle Architecture. *Curr Med Imaging Rev* **3**, 152-160 (2007). https://doi.org/10.2174/157340507781386988

159 Serai, S. D. *et al.* Diffusion tensor imaging of the kidney in healthy controls and in children and young adults with autosomal recessive polycystic kidney disease. *Abdominal Radiology* **44**, 1867-1872 (2019). https://doi.org/10.1007/s00261-019-01933-4

160 Lee, Y. & Kim, H. Assessment of diffusion tensor MR imaging (DTI) in liver fibrosis with minimal confounding effect of hepatic steatosis. *Magnetic Resonance in Medicine* **73**, 1602-1608 (2015). https://doi.org/https://doi.org/10.1002/mrm.25253

161 Vedantam, A. *et al.* Diffusion Tensor Imaging of the Spinal Cord: Insights From Animal and Human Studies. *Neurosurgery* **74** (2014).

162 O'Donnell, L. J. & Westin, C.-F. An Introduction to Diffusion Tensor Image Analysis. *Neurosurgery Clinics of North America* **22**, 185-196 (2011). https://doi.org/https://doi.org/10.1016/j.nec.2010.12.004

163 Alexander, A. L., Lee, J. E., Lazar, M. & Field, A. S. Diffusion tensor imaging of the brain. *Neurotherapeutics* **4**, 316-329 (2007). https://doi.org/10.1016/j.nurt.2007.05.011

164 Skare, S., Hedehus, M., Moseley, M. E. & Li, T.-Q. Condition Number as a Measure of Noise Performance of Diffusion Tensor Data Acquisition Schemes with MRI. *Journal of Magnetic Resonance* **147**, 340-352 (2000). https://doi.org/https://doi.org/10.1006/jmre.2000.2209

165 in *Studies in Mathematics and Its Applications* Vol. 28 (ed G. Meurant) 1-68 (Elsevier, 1999).

166 Lo Buono, V. *et al.* Diffusion tensor imaging of white matter degeneration in early stage of Alzheimer's disease: a review. *International Journal of Neuroscience* **130**, 243-250 (2020). https://doi.org/10.1080/00207454.2019.1667798

167 Estevez-Fraga, C., Scahill, R., Rees, G., Tabrizi, S. J. & Gregory, S. Diffusion imaging in Huntington's disease: comprehensive review. *Journal of Neurology, Neurosurgery & Psychiatry* **92**, 62-69 (2021). https://doi.org/10.1136/jnnp-2020-324377

168 Zhang, Y. & Burock, M. A. Diffusion Tensor Imaging in Parkinson's Disease and Parkinsonian Syndrome: A Systematic Review. *Front Neurol* **11**, 531993 (2020). https://doi.org/10.3389/fneur.2020.531993

169 Christidi, F. *et al.* Diffusion Tensor Imaging as a Prognostic Tool for Recovery in Acute and Hyperacute Stroke. *Neurology International* **14**, 841-874 (2022).

170 Davanian, F., Faeghi, F., Shahzadi, S. & Farshidfar, Z. Evaluation of Diffusion Anisotropy and Diffusion Shape in Grading of Glial Tumors. *J Biomed Phys Eng* **9**, 459-464 (2019). https://doi.org/10.31661/jbpe.v0i0.513

171 Parlatini, V. *et al.* White matter alterations in Attention-Deficit/Hyperactivity Disorder (ADHD): a systematic review of 129 diffusion imaging studies with meta-analysis. *Molecular Psychiatry* **28**, 4098-4123 (2023). https://doi.org/10.1038/s41380-023-02173-1

172 Song, S.-K. *et al.* Dysmyelination Revealed through MRI as Increased Radial (but Unchanged Axial) Diffusion of Water. *NeuroImage* **17**, 1429-1436 (2002). https://doi.org/https://doi.org/10.1006/nimg.2002.1267

173 Winklewski, P. J. *et al.* Understanding the Physiopathology Behind Axial and Radial Diffusivity Changes-What Do We Know? *Front Neurol* **9**, 92 (2018). https://doi.org/10.3389/fneur.2018.00092

174 Figley, C. R. *et al.* Potential Pitfalls of Using Fractional Anisotropy, Axial Diffusivity, and Radial Diffusivity as Biomarkers of Cerebral White Matter Microstructure. *Front Neurosci* **15**, 799576 (2021). https://doi.org/10.3389/fnins.2021.799576

175 Steven, A. J., Zhuo, J. & Melhem, E. R. Diffusion kurtosis imaging: an emerging technique for evaluating the microstructural environment of the brain. *AJR Am J Roentgenol* **202**, W26-33 (2014). https://doi.org/10.2214/AJR.13.11365

176 Collier, Q. *Robust estimation of diffusion tensor and diffusion kurtosis imagingparameters* PhD thesis, Universiteit Antwerpen, (2018).

177 Jensen, J. H., Helpern, J. A., Ramani, A., Lu, H. & Kaczynski, K. Diffusional kurtosis imaging: the quantification of non-gaussian water diffusion by means of magnetic resonance imaging. *Magn Reson Med* **53**, 1432-1440 (2005). https://doi.org/10.1002/mrm.20508

178 Veraart, J., Sijbers, J., Sunaert, S., Leemans, A. & Jeurissen, B. Weighted linear least squares estimation of diffusion MRI parameters: strengths, limitations, and pitfalls. *Neuroimage* **81**, 335-346 (2013). https://doi.org/10.1016/j.neuroimage.2013.05.028

179 Boucher, S. *et al.* Diffusion Tensor Imaging Tractography of White Matter Tracts in the Equine Brain. *Frontiers in Veterinary Science* **7** (2020). https://doi.org/10.3389/fvets.2020.00382

180 Yeh, F.-C., Irimia, A., Bastos, D. C. d. A. & Golby, A. J. Tractography methods and findings in brain tumors and traumatic brain injury. *NeuroImage* **245**, 118651 (2021). https://doi.org/https://doi.org/10.1016/j.neuroimage.2021.118651

181 Soni, N., Mehrotra, A., Behari, S., Kumar, S. & Gupta, N. Diffusion-tensor Imaging and Tractography Application in Pre-operative Planning of Intra-axial Brain Lesions. *Cureus* **9**, e1739 (2017). https://doi.org/10.7759/cureus.1739

182 Abhinav, K. *et al.* Advanced diffusion MRI fiber tracking in neurosurgical and neurodegenerative disorders and neuroanatomical studies: A review. *Biochimica et Biophysica Acta (BBA) - Molecular Basis of Disease* **1842**, 2286-2297 (2014). https://doi.org/https://doi.org/10.1016/j.bbadis.2014.08.002

183 Basser, P. Fiber-tractography via diffusion tensor MRI (DT-MRI). (1998).

184 Mori, S., Crain, B. J. & van Zijl, P. C. M. 3D Brain Fiber Reconstruction from Diffusion MRI. *NeuroImage* **7**, S710 (1998). https://doi.org/https://doi.org/10.1016/S1053-8119(18)31543-X

185 Jeurissen, B., Descoteaux, M., Mori, S. & Leemans, A. Diffusion MRI fiber tractography of the brain. *NMR Biomed* **32**, e3785 (2019). https://doi.org/10.1002/nbm.3785

186 Basser, P. J., Pajevic, S., Pierpaoli, C., Duda, J. & Aldroubi, A. In vivo fiber tractography using DT-MRI data. *Magnetic Resonance in Medicine* **44**, 625-632 (2000). https://doi.org/10.1002/1522-2594(200010)44:4<625::Aid-mrm17>3.0.Co;2-o

187 Jeurissen, B., Leemans, A., Jones, D. K., Tournier, J. D. & Sijbers, J. Probabilistic fiber tracking using the residual bootstrap with constrained spherical deconvolution. *Hum Brain Mapp* **32**, 461-479 (2011). https://doi.org/10.1002/hbm.21032

188 Jeurissen, B., Leemans, A., Tournier, J. D., Jones, D. K. & Sijbers, J. Investigating the prevalence of complex fiber configurations in white matter tissue with diffusion magnetic resonance imaging. *Hum Brain Mapp* **34**, 2747-2766 (2013). https://doi.org/10.1002/hbm.22099

189 Dhollander, T., Raffelt, D., Mito, R. & Connelly, A. Improved white matter response function estimation for 3-tissue constrained spherical deconvolution. *Conference Paper* (2019).

190 Jeurissen, B., Tournier, J. D., Dhollander, T., Connelly, A. & Sijbers, J. Multi-tissue constrained spherical deconvolution for improved analysis of multi-shell diffusion MRI data. *Neuroimage* **103**, 411-426 (2014). https://doi.org/10.1016/j.neuroimage.2014.07.061

191 Dhollander, T., Raffelt, D. & Connelly, A. *Unsupervised 3-tissue response function estimation from single-shell or multi-shell diffusion MR data without a co-registered T1 image*. (2016).

192 Ullmann, J. F., Calamante, F., Collin, S. P., Reutens, D. C. & Kurniawan, N. D. Enhanced characterization of the zebrafish brain as revealed by super-resolution track-density imaging. *Brain Struct Funct* **220**, 457-468 (2015). https://doi.org/10.1007/s00429-013-0667-7

193 Pal, M. M. Glutamate: The Master Neurotransmitter and Its Implications in Chronic Stress and Mood Disorders. *Front Hum Neurosci* **15**, 722323 (2021). https://doi.org/10.3389/fnhum.2021.722323

194 Kim, Y. S. & Yoon, B. E. Altered GABAergic Signaling in Brain Disease at Various Stages of Life. *Exp Neurobiol* **26**, 122-131 (2017). https://doi.org/10.5607/en.2017.26.3.122

195 Kalra, S. & Arnold, D. L. Magnetic Resonance Spectroscopy for Monitoring Neuronal Integrity in Amyotrophic Lateral Sclerosis. *Advances in experimental medicine and biology* **576** (2006). https://doi.org/https://doi.org/10.1007/0-387-30172-0

196 Bertran-Cobo, C. *et al.* A Neurometabolic Pattern of Elevated Myo-Inositol in Children Who Are HIV-Exposed and Uninfected: A South African Birth Cohort Study. *Front Immunol* **13**, 800273 (2022). https://doi.org/10.3389/fimmu.2022.800273

197 Haase, A. *et al.* MR imaging using stimulated echoes (STEAM). *Radiology* **160**, 787-790 (1986). https://doi.org/10.1148/radiology.160.3.3737918

198 Ordidge, R. J., Connelly, A. & Lohman, J. A. B. Image-selected in Vivo spectroscopy (ISIS). A new technique for spatially selective nmr spectroscopy. *Journal of Magnetic Resonance (1969)* **66**, 283-294 (1986). https://doi.org/https://doi.org/10.1016/0022-2364(86)90031-4

199 Garwood, M. & DelaBarre, L. The Return of the Frequency Sweep: Designing Adiabatic Pulses for Contemporary NMR. *Journal of Magnetic Resonance* **153**, 155-177 (2001). https://doi.org/https://doi.org/10.1006/jmre.2001.2340

200 Bottomley, P. A. 4480228 Selective volume method for performing localized NMR spectroscopy. (1985).

201 Krug, J. R. *et al.* Assessing spatial resolution, acquisition time and signal-to-noise ratio for commercial microimaging systems at 14.1, 17.6 and 22.3 T. *J Magn Reson* **316**, 106770 (2020). https://doi.org/10.1016/j.jmr.2020.106770

202 Gruetter, R. *et al.* Resolution Improvements inin Vivo1H NMR Spectra with Increased Magnetic Field Strength. *Journal of Magnetic Resonance* **135**, 260-264 (1998). https://doi.org/https://doi.org/10.1006/jmre.1998.1542

203 Hoult, D. I. & Richards, R. E. The signal-to-noise ratio of the nuclear magnetic resonance experiment. *Journal of Magnetic Resonance* **213**, 329-343 (2011). https://doi.org/https://doi.org/10.1016/j.jmr.2011.09.018

204 Takahashi, M., Uematsu, H. & Hatabu, H. MR imaging at high magnetic fields. *European Journal of Radiology* **46**, 45-52 (2003). https://doi.org/https://doi.org/10.1016/S0720-048X(02)00331-5

205 Krupa, K. & Bekiesińska-Figatowska, M. Artifacts in magnetic resonance imaging. *Pol J Radiol* **80**, 93-106 (2015). https://doi.org/10.12659/pjr.892628

206 Zaitsev, M., Maclaren, J. & Herbst, M. Motion artifacts in MRI: A complex problem with many partial solutions. *Journal of Magnetic Resonance Imaging* **42**, 887-901 (2015). https://doi.org/https://doi.org/10.1002/jmri.24850

207 Soila, K. P., Viamonte, M. & Starewicz, P. M. Chemical shift misregistraton effect in magnetic resonance imaging. *Radiology* **153** (1984).

208 Lufkin, R., Anselmo, M., Crues, J. & Smoker, W. Magnetic field strength dependence of chemical shift artifacts. *Computerized Medical Imaging and Graphics* **12**, 8 (1988). https://doi.org/https://doi.org/10.1016/0895-6111(88)90002-X

209 Pusey, E., Yoon, C., Anselmo, M. L. & Lufkin, R. B. Aliasing artifacts in mr imaging. *Computerized Medical Imaging and Graphics* **12**, 219-224 (1988). https://doi.org/https://doi.org/10.1016/0895-6111(86)90003-0

210 Czervionke, L., Czervionke, J., Daniels, D. & Haughton, V. Characteristic features of MR truncation artifacts. *American Journal of Roentgenology* **151**, 1219-1228 (1988). https://doi.org/10.2214/ajr.151.6.1219

211 Farahani, K., Sinha, U., Sinha, S., Chiu, L. C. L. & Lufkin, R. B. Effect of field strength on susceptibility artifacts in magnetic resonance imaging. *Computerized Medical Imaging and Graphics* **14**, 409-413 (1990). https://doi.org/https://doi.org/10.1016/0895-6111(90)90040-I

212 Ullmann, J. F. P., Cowin, G., Kurniawan, N. D. & Collin, S. P. Magnetic resonance histology of the adult zebrafish brain: optimization of fixation and gadolinium contrast enhancement. *NMR in Biomedicine* **23**, 341-346 (2010). https://doi.org/https://doi.org/10.1002/nbm.1465

213 Ullmann, J. F. P., Cowin, G., Kurniawan, N. D. & Collin, S. P. A three-dimensional digital atlas of the zebrafish brain. *NeuroImage* **51**, 76-82 (2010). https://doi.org/https://doi.org/10.1016/j.neuroimage.2010.01.086

214 Hamilton, N., Allen, C. & Reynolds, S. Longitudinal MRI brain studies in live adult zebrafish. *NMR Biomed* **36**, e4891 (2023). https://doi.org/10.1002/nbm.4891

215 Cosgrove, K. P., Mazure, C. M. & Staley, J. K. Evolving Knowledge of Sex Differences in Brain Structure, Function, and Chemistry. *Biological Psychiatry* **62**, 847-855 (2007). https://doi.org/https://doi.org/10.1016/j.biopsych.2007.03.001

216 Hartmann, P., Ramseier, A., Gudat, F., Mihatsch, M. J. & Polasek, W. [Normal weight of the brain in adults in relation to age, sex, body height and weight]. *Pathologe* **15**, 165-170 (1994). https://doi.org/10.1007/s002920050040

217 Azevedo, F. A. *et al.* Equal numbers of neuronal and nonneuronal cells make the human brain an isometrically scaled-up primate brain. *J Comp Neurol* **513**, 532-541 (2009). https://doi.org/10.1002/cne.21974

218 Herndon, J. G., Tigges, J., Klumpp, S. A. & Anderson, D. C. Brain Weight Does Not Decrease with Age in Adult Rhesus Monkeys. *Neurobiology of Aging* **19**, 267-272 (1998). https://doi.org/https://doi.org/10.1016/S0197-4580(98)00054-2

219 Scott, J. A. *et al.* Longitudinal analysis of the developing rhesus monkey brain using magnetic resonance imaging: birth to adulthood. *Brain Struct Funct* **221**, 2847-2871 (2016). https://doi.org/10.1007/s00429-015-1076-x

220 Herculano-Houzel, S., Collins, C. E., Wong, P. & Kaas, J. H. Cellular scaling rules for primate brains. *Proceedings of the National Academy of Sciences* **104**, 3562-3567 (2007). https://doi.org/doi:10.1073/pnas.0611396104

221 Herculano-Houzel, S. & Lent, R. Isotropic fractionator: a simple, rapid method for the quantification of total cell and neuron numbers in the brain. *J Neurosci* **25**, 2518-2521 (2005). https://doi.org/10.1523/jneurosci.4526-04.2005

222 Kovačević, N. *et al.* A three-dimensional MRI atlas of the mouse brain with estimates of the average and variability. *Cerebral cortex* **15**, 639-645 (2005).

223 Welniak–Kaminska, M. *et al.* Volumes of brain structures in captive wild-type and laboratory rats: 7T magnetic resonance in vivo automatic atlas-based study. *PloS one* **14**, e0215348 (2019).

224 Herculano-Houzel, S., Mota, B. & Lent, R. Cellular scaling rules for rodent brains. *Proceedings of the National Academy of Sciences* **103**, 12138-12143 (2006). https://doi.org/doi:10.1073/pnas.0604911103

225 Friedrich, R. W., Genoud, C. & Wanner, A. A. Analyzing the structure and function of neuronal circuits in zebrafish. *Front Neural Circuits* **7**, 71 (2013). https://doi.org/10.3389/fncir.2013.00071

226 Hoult, D. I. & Richards, R. E. The signal-to-noise ratio of the nuclear magnetic resonance experiment. *Journal of Magnetic Resonance (1969)* **24**, 71-85 (1976). https://doi.org/https://doi.org/10.1016/0022-2364(76)90233-X

2

UNVEILING THE EXQUISITE MICROSTRUCTURAL DETAILS AND WHITE MATTER TRACTS IN ADULT ZEBRAFISH BRAIN USING 28.2 T MRI*

*This chapter was published in Molecules 2024; doi:10.3390/molecules29194637

ABSTRACT

Zebrafish is firmly established as an animal model for a wide range of human diseases including neurodegenerative disorders. However, obtaining the microstructural details and studying neuronal network in zebrafish brain non-invasively remains challenging. MRI offers the possibility to non-invasively study zebrafish brain, however due to small brain size, unveiling the exquisite microstructural details from zebrafish brain is difficult. Exploiting higher magnetic fields for imaging can potentially improve the neurological analysis of zebrafish brain as signal-to-noise ratios (SNR) increase with the applied magnetic field strength. Here, we present the first neuroimaging findings of the zebrafish brain at 28.2 T, the highest magnetic field strength currently available for imaging. The performance of MRI at 28.2 T was compared to 17.6 T and an improvement of 20% in SNR was observed at 28.2 T, facilitating the accurate identification of numerous brain substructures. The normative T_1 and T_2 relaxation values were established over different zebrafish brain structures at 28.2 T. To zoom into the white matter structures, we applied diffusion tensor imaging and obtained axial, radial, and mean diffusivity, as well as fractional anisotropy information at a very high spatial resolution. Tractography maps were produced by short-track track-density imaging using the constrained spherical deconvolution method (stTDI CSD). A novel algorithm for stTDI with multi-shell multi-tissue (msmt) CSD was tested on zebrafish brain data, resulting in a significant reduction in false-positive tracks from grey matter compared to stTDI with single-shell single-tissue CSD. This allowed the identification of white matter structures with remarkable resolution and contrast. Our study demonstrates that neuroimaging at 28.2 T provides excellent microstructural details and yields reproducible and quantitative maps of fibre organisation in the intricate zebrafish brain. This work paves the way for future non-invasive studies at ultra-high magnetic field aimed at investigating disease-related microstructural alterations in zebrafish models of various brain diseases.

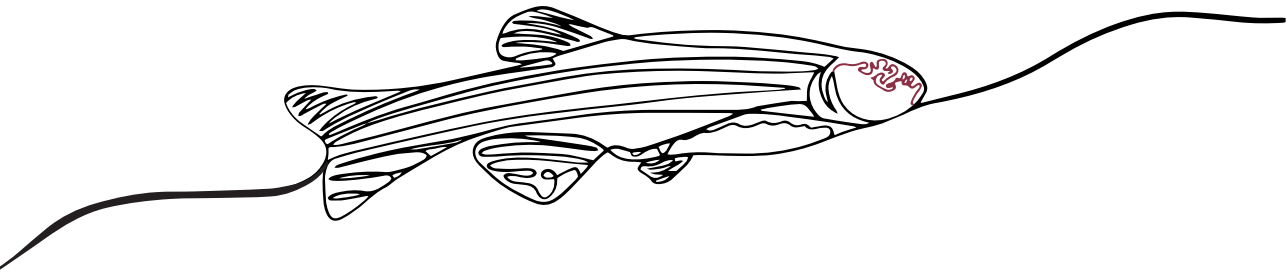

1. INTRODUCTION

Zebrafish (*Danio rerio*) is an excellent animal model in the studies of diseases, biological pathways, genetics, and toxicology[1-4]. In the field of neurodegenerative conditions, zebrafish offer various models including those for Alzheimer's, Parkinson's, and Huntington's disease[5-7]. Therefore, studying the zebrafish brain non-invasively might provide valuable information on the pathology and treatment of neurodegenerative disorders. Magnetic resonance imaging (MRI) is a well-established, non-invasive technique for neuroimaging in both human and animal models. In our previous reports, a successful examination of zebrafish was performed at high field (9.4 T)[8-10] and ultra-high field (17.6 T) MRI[11-13]. High-quality images gave access to anatomical details, allowing visualization of white matter (WM) lesions in zebrafish models of familial cystic leukoencephalopathy[9] and Lowe syndrome[10], as well as *in vivo* analysis of malignant melanoma tumors[13]. Additionally, *in vivo* high-resolution localized magnetic resonance spectroscopy (MRS) was successfully applied to obtain the neurochemical metabolite profile of adult zebrafish. However, obtaining the essential resolution for studying small structures with a high signal-to-noise ratio (SNR) remains challenging.

Insight into the microstructural organisation of the zebrafish brain could be obtained by diffusion-based MRI (dMRI), a powerful, non-invasive technique with high sensitivity for water movement[14]. Cellular structures hinder the microscopic random motion of water, making dMRI unique to study the microstructural organisation of tissue. Diffusion tensor imaging (DTI) is an extended dMRI method providing increased structural information by exploiting anisotropic diffusion effects. Diffusion tensors are calculated from directional differences in the MR signals and used to determine the axial diffusivity ($D_{\parallel}$) from the principal eigenvalue, the radial diffusivity ($D_{\perp}$) from the average of two non-principal eigenvalues, the mean diffusivity (*MD*), and the fractional anisotropy (*FA*), the extent of directional preference. In the brain, anisotropic diffusion effects are most prominent in WM due to the ordered structures of its myelinated axon tracts[14]. Changes in the diffusion anisotropy of WM structures have been reported for many neurodegenerative diseases including Alzheimer's disease, Parkinson's disease, amyotrophic lateral sclerosis (ALS), and Huntington's disease[15-25]. The directionality of WM structures is visualized by directional encoded colour (DEC) *FA* maps, combining *FA* with the directionality of the principal eigenvector. However, *FA* colour maps do not visualize the connectivity of WM tracks, nor does the technique account for crossing or closely passing fibres below the applied MRI resolution. In this regard, DTI tractography offers a solution for visualizing WM tracks. DTI tractography is a distinct processing technique of DTI tensors and the only known non-invasive imaging technique for visualizing WM connectivity in the brain. DTI has been successfully used to probe the changes in brain connectivity during neurogenerative diseases in human subjects[26-32]. Combined with the high spatial resolution required for the neurological analysis of zebrafish, dMRI is very challenging for the zebrafish brain. Consequently, knowledge

of diffusivity and connectivity in the zebrafish brain is limited. Freidlin *et al.*[33] obtained good contrast of the spinal cord in adult zebrafish by DTI, while Ullmann *et al.*[34], presented a DTI study in the zebrafish brain and obtained tractography maps using short-track track density imaging with single-shell single-tissue constrained spherical deconvolution (stTDI ssst-CSD). However, the analysis was performed on isolated brain tissue, rather than intact zebrafish. Additionally, Ullmann *et al.* performed DTI with a single non-zero *b*-value, eliminating the possibility of individually estimating WM, grey matter (GM), and cerebrospinal fluid (CSF) signals, therefore possibly resulting in errors and WM overestimation during tractography[35]. Recently, multi-shell multi-tissue (msmt) CSD algorithms were developed, deconvoluting WM, GM, and CSF responses[35]. By filtering GM- and CSF-like signals strongly present in ssst-CSD, false positive tracks are reduced[36,37]. However, msmt-CSD algorithms have so far not been tested for the zebrafish brain.

Exploiting higher magnetic fields for imaging can potentially improve the neurological analysis of zebrafish brain as SNR increases with the applied magnetic field strength (B_0)[38]. Consequently, increased spatial resolution can be obtained without the need for significant elongation of total acquisition time. In this study, the first MRI results at 28.2 T are presented that were obtained from the zebrafish brain. The performance of MRI at 28.2 T was compared to 17.6 T and a wide range of MR sequences were optimized, including anatomical imaging by rapid acquisition with relaxation enhancement (RARE). Moreover, diffusion-weighted imaging (DWI) was applied to quantify apparent diffusion coefficient (*ADC*) values in several zebrafish brain regions. Furthermore, WM tractography was conducted through DTI using stTDI CSD. Our findings not only include the initial results of stTDI through ssst-CSD on intact zebrafish, but also show the first outcomes of stTDI through msmt-CSD on the zebrafish brain.

2. METHODS

Zebrafish husbandry

The husbandry and use of adult zebrafish described in this study was approved by the local animal welfare committee of the University of Leiden (Licence numbers AVD1060020171767 and AVD10600202216175), following the international guidelines specified by the EU Animal Protection Directive 2010/63/EU, and was conducted according to standard protocols (www.zfin.org) and in compliance with the ARRIVE guidelines as described previously[12,39]. In this study, adult zebrafish (wild-type, male, n = 6) were used. Adult zebrafish aged around 4 months were euthanized through immobilization by submersion in ice water (0 – 4 ˚C) for at least 10 minutes following cessation of opercular movement and then fixed in 4% buffered paraformaldehyde (Zinc Formal-Fixx, ThermoShandon, UK) for 4 days prior to MRI measurements.

Magnetic resonance imaging

MRI was performed using 28.2 T (1.2 GHz) or 17.6 T (750 MHz) vertical bore systems (Bruker Biospin, Ettlingen, Germany). Both systems were equipped with a MICRO 5 gradient system (G_{max} = 3 T/m), a 5 mm birdcage RF coil, and a GREAT 60 gradient power supply. Data acquisition and processing were performed using Paravision 360 v3.3 (Bruker Biospin, Ettlingen, Germany). For all measurements, animals were transferred to 5 mm NMR tubes and embedded in perfluoropolyether (Fomblin Y, Solvay Solexis S.P.A.). To achieve maximal signal intensity, the position of the brain was aligned to the centre of the RF coil. Magnetic field homogeneity was achieved by second-order shimming. A variety of scan protocols was used and optimized for the magnetic field strength of 28.2 T. Identical scan protocols were then used for both MR systems (17.6 T and 28.2 T). For anatomical imaging, a two-dimensional (2D) RARE sequence was employed. Images were acquired with an echo time *TE* = 5.6 ms, a repetition time *TR* = 3000 ms, using 4 segmenting refocusing echoes (RARE factor), and a spatial resolution of 23 × 23 µm. RARE images were obtained with a slice thickness of either 100 µm or 200 µm, with the number of scan being *ns* = 64 or *ns* = 16, respectively, for averaging.

For the estimation of spin-spin relaxation times T_2 a 2D multi-slice multi-echo (MSME) protocol was used, based on the Carr-Purcell-Meiboom-Gill (CPMG) sequence[40]. MSME measurements were performed with 15 echo images per excitation at an echo spacing τ = 5 ms, *TR* = 2500 ms, *ns* = 4, at a spatial resolution of 23 × 23 µm, and with a slice thickness of 200 µm. For estimation of the spin-lattice relaxation times T_1, a 2D RARE protocol at variable repetition times (VTR) was used. Signal intensities were measured at *TR* = 300, 606, 967, 1408, 1974, 2767, 4100, or 10000 ms, *TE* = 3 ms, *ns* = 2, at a spatial resolution of 47 × 47 µm and a slice thickness of 200 µm.

DWI was performed with a 2D diffusion-weighted spin echo sequence with *TE* = 20.2 ms, *TR* = 1000 ms, *ns* = 4, at a spatial resolution of 23 × 23 µm and a slice thickness of 200 µm. MR signals were measured at *b*-values of 75, 500, 1000, 3500, 5000, or 7500 s/mm^2. 2D DTI with echo planar imaging (EPI) was performed at an anisotropic resolution of 25 × 25 µm, at a slice thickness of 200 µm, with *TE* = 12.4 ms, *TR* = 2000 ms, *ns* = 32, and an EPI factor of 8. Multi-shell experiments were performed with *b*-values of 4, 1000, 3500, or 6000 s/mm^2 with 8, 12, 24, or 36 diffusion-encoding directions respectively. Three-dimensional (3D) DTI was performed at an isotropic spatial resolution of 35 µm, with *TE* = 9.1 ms, *TR* = 2000 ms, *ns* = 4, and an EPI factor of 8. Multi-shell experiments were performed with *b*-values of 100, 1000, or 2500 s/mm^2 with 4, 12, or 24 diffusion-encoding directions respectively. Automatic drift compensation was applied to compensate for possible $\mathbf{B}_0$ drift.

Data processing

Identification of brain regions and WM structures was performed based on the adult zebrafish brain atlas[41] and the topological atlas[42].

For the estimation of *SNR*, RARE intensity images were processed in Matlab (mathworks.com). Brain tissue was selected using the volume segmenter tool and the average signal intensity was calculated. For noise, 10 × 10 voxels were selected outside the fish. From these data, *SNR* was calculated using,

$$SNR = \frac{\mu_{\mathrm{S}} - \mu_{\mathrm{N}}}{\sigma_{\mathrm{N}}} \tag{2.1}$$

Here μ_S is the mean intensity of the brain signal, μ_N is the mean intensity of the noise and σ_N is the standard deviation of the noise. SNR maps were created by estimating *SNR* for each voxel inside the RARE intensity image. Signals outside the fish were set to zero by a signal intensity threshold.

For the estimation of T_1, T_2, and *ADC*, nine regions of interest (ROIs) were manually selected in the zebrafish brain using Paravision 360 v3.3. T_1 was estimated by the image sequence analysis tool in Paravision using a non-linear least square algorithm for the mono-exponential fit function

$$I_{\mathrm{TR}} = A + I_0 \cdot \left(1 - \exp^{\frac{-TR}{T_1}}\right) \tag{2.2}$$

where I_t is the signal intensity at *TR*, *A* is the absolute bias, and I_0 is the signal intensity at TR_0. From MSME data, T_2 was estimated using the image sequence analysis tool in Paravision with a non-linear least square algorithm for the mono-exponential fit function

$$I_{\mathrm{TE}} = A + I_0 \cdot \exp^{\frac{-TE}{T_2}} \tag{2.3}$$

where I_t is the signal intensity at *TE* and I_0 is the signal intensity at TE_0. To reduce the effect of imperfect 180° pulses, uneven echoes were excluded from the data fitting[43]. *ADC* was estimated from DWI data by the image sequence analysis tool in Paravision with a non-linear least square algorithm for the mono-exponential fit function

$$I_b = A + I_0 \cdot \exp^{-b \cdot ADC} \tag{2.4}$$

Here, I_b is the signal intensity at *b* and I_0 is the signal intensity at b_0.

Processing of 2D and 3D DTI data was performed by MRtrix3[44]. Brain masks were manually created using the volume segmenter tool in Matlab. Using MRtrix3 functions, the denoising of DTI data was based on the random matrix theory[45]. Diffusion tensors (**D**) were calculated by fitting the diffusion tensor to the log of the denoised DTI data by minimizing the weighted least-squares and iterated weighted least-squares[46,47]. From the tensors, the $D_{\parallel}$, $D_{\perp}$, *MD*, and *FA* were calculated. *FA* colour maps were generated by adding the directionality of the principal eigenvalue of **D** to *FA* maps. MRtrix3 was used to generate super-resolution (5 µm) stTDI maps from 2D and 3D DTI data. Constrained spherical deconvolution (CSD) was used to resolve crossing fibres by estimating fibre orientation distribution functions (fODFs). Single-shell single-tissue (ssst) CSD response functions were estimated by the Tournier algorithm[48], using the highest *b*-value of the DTI dataset. fODFs were calculated with the ssst-CSD algorithm[49]. Multi-shell multi-tissue (msmt) CSD response functions were estimated by the Dhollander algorithm[36]. Crude segmentation of WM and GM/CSF voxels in 2D and 3D DTI data was performed at *FA* = 0.2. WM, GM, and CSF voxel selection of 3D DTI data for response function estimation was performed with the top 0.5% of refined WM voxels, 2.0% of refined GM voxels, and 10% of refined GM voxels. For the 2D DTI data, 10% of the refined WM voxels were used in the final selection due to the lower total number of available voxels compared to the 3D DTI data set. Finally, msmt-CSD fODFs were calculated with the msmt-CSD algorithm[37]. Whole brain fibre tracking was performed with the iFOD1 algorithm[50]. 1 million (2D DTI data) and 10 million (3D DTI data) tracks were generated with a minimal track length of twice the voxel size and a maximal track length of ten times the voxel size. Fibre generation was automatically terminated once leaving the pre-defined brain mask. Additional parameters were used in their default mode[44]. Tractography results were transformed into super-resolution track density imaging (TDI)[51], resulting in approximately 5µm isotropic resolution. The directionality of generated tracks is visualized by DEC.

3. RESULTS AND DISCUSSION

This study presents the first MRI findings of the zebrafish brain with a state-of-the-art magnetic field strength of 28.2 T. The zebrafish has become a popular species for studying neurological disorders due to the growing understanding of its nervous system and the availability of numerous transgenic zebrafish models[5,6,9,10,13]. Non-invasive MRI methods have significant potential for investigating brain pathology in these models. However, obtaining the essential resolution for studying microstructures and diffusion processes with a high SNR remains challenging for zebrafish brain. In this work, we have optimized and successfully applied MRI methods at 28.2 T magnetic field strength to resolve microstructural details and white matter tracts in the young adult zebrafish brain.

A

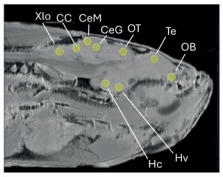

B

	OB	Te	CeG	Xlo	Cem	CC	OT	Hc	Hv
T_1 (ms)									
28.2 T	3000 ± 68	3182 ± 75	2928 ± 60	2942 ± 97	2923 ± 67	2940 ± 88	2812 ± 47	2842 ± 55	2961 ± 56
17.6 T	2746 ± 80	2972 ± 87	2554 ± 17	2638 ± 28	2565 ± 53	2780 ± 34	2539 ± 16	2648 ± 47	2812 ± 38
Factor	1.09	1.07	1.15	1.12	1.14	1.06	1.11	1.07	1.05
T_2 (ms)									
28.2 T	27.8 ± 0.7	26.9 ± 0.9	20.7 ± 0.4	27.2 ± 0.5	27.8 ± 0.5	31.7 ± 1.2	27.5 ± 0.6	28.0 ± 1.0	27.5 ± 2.0
17.6 T	31.3 ± 1.1	29.4 ± 0.4	23.6 ± 1.0	30.0 ± 0.8	30.2 ± 1.4	34.0 ± 0.7	27.7 ± 1.6	33.0 ± 0.6	32.7 ± 1.0
Factor	0.89	0.91	0.88	0.91	0.92	0.93	0.99	0.85	0.84

Figure 2.1. T_1 and T_2 relaxation time measurements in various brain regions of adult zebrafish. [A] *Anatomical RARE image of adult zebrafish indicating the location of ROIs selected for T_1 and T_2 quantification.* ***[B]*** *T_1 and T_2 relaxation time values in various zebrafish brain regions measured at 28.2 and 17.6 T. One-way analysis of variance (ANOVA) with the Bonferroni test for comparison of mean between T_1, T_2 values at two magnetic field was performed and statistically significant difference in both T_1 and T_2 values at two fields was observed ($p < 0.05$). The difference between T_1 and T_2 values measured at two different magnetic field strengths is presented as fold change (Factor). Selected ROIs; Xlo – Vagal lobe; CC – Cerebellar crest; CeM – Cerebellar corpus, molecular layer; CeG – Cerebellar corpus, granular layer; OT – Optic Tectum; Te - Telencephalon; OB – Olfactory bulb; Hc – Caudal zone of periventricular hypothalamus; Hv – Ventral zone of periventricular hypothalamus. Data represent the mean T_1 and T_2 in ms ± standard error (SE) (Error bars); n = 6.*

Relaxation times

The application of MRI at an ultra-high field of 28.2 T requires adjustment of image acquisition parameters, which are based on knowledge of the MR relaxation properties of the tissues being imaged. To establish regional T_1 and T_2 values of the zebrafish brain at 28.2 T, relaxation times were estimated in nine manually selected ROIs (Figure 2.1A); the vagal lobe (Xlo), granular layer of the cerebellar corpus (CeG), telencephalon (Te), olfactory bulb (OB), molecular layer of the cerebellar corpus (Cem), cerebellar crest (CC), optic tectum (OT), caudal zone of the periventricular hypothalamus (Hc), and the ventral zone of the periventricular hypothalamus (Hv). Figure 2.1B shows relaxation times T_1 and T_2 for selected ROIs at 28.2 T and compared them with values obtained at 17.6 T. A clear increase of T_1 and a decrease of T_2 were observed in all selected ROIs at 28.2 T compared to 17.6 T. On average, T_1 increased by a factor of 1.097 ± 0.015, while T_2 decreased by a factor of 0.905 ± 0.011 at 28.2 T compared to 17.6 T. The observed shift in relaxation times at increasing $\mathbf{B}_0$ is consistent with previous reports[52-54]. Generally, T_1 is proportional to $B_0^{1/3}$. Here, all brain regions report a T_1 increase below the theoretical expectations. This is consistent with T_1 reported in mouse brain tissue at 9.4 T and 17.6 T, where an average T_1 increase factor of 1.08 was reported, well below the theoretical increase factor of 1.23[55]. For T_2, the observed decrease at higher magnetic fields is consistent with previous reports as well. In mouse brain regions, increasing the magnetic field from 9.4 T to 17.6 T resulted in an average T_2 decrease by a factor 0.72[56], and changing field from 9.4 T to 11.7 T resulted in an average T_2 decrease by a factor 0.83[53]. Besides $\mathbf{B}_0$, the relaxation times of tissues depend on factors like age, gender, acquisition parameters, and pre-treatment (measuring *in vivo* or fixed)[57]. To minimize the effects of additional factors, measurements at 17.6 T and 28.2 T were performed for the same zebrafish and with identical acquisition

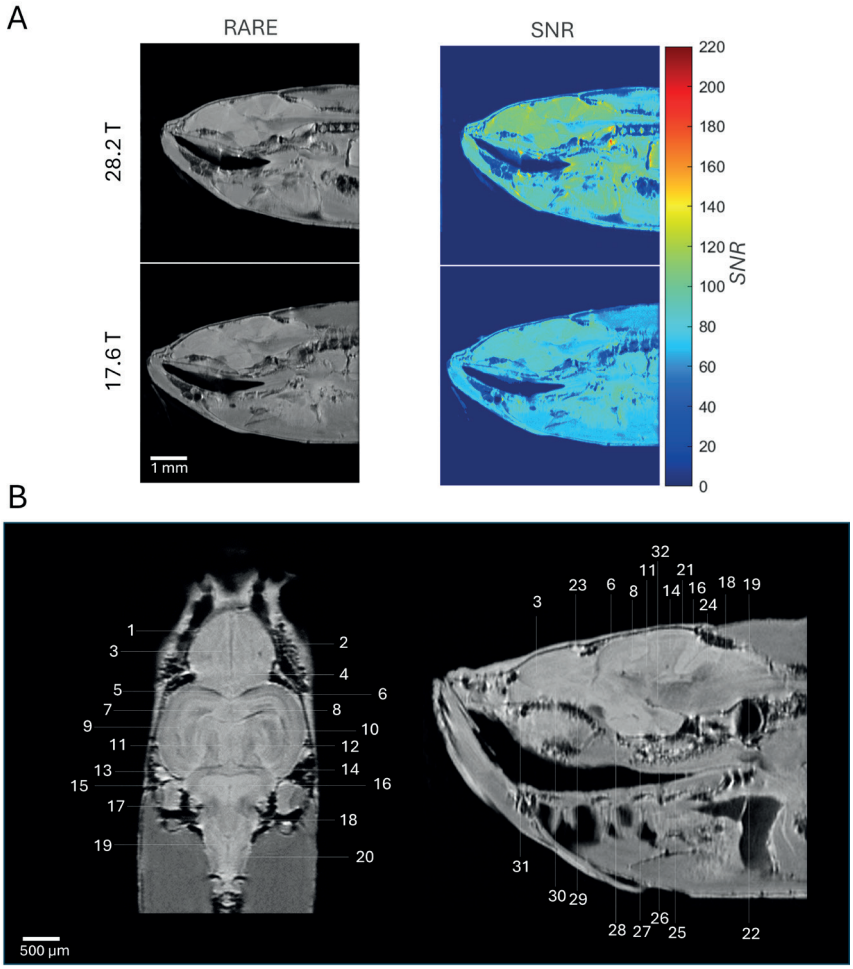

Figure 2.2. Comparison of the anatomical images of the zebrafish brain measured at 17.6 T and 28.2 T. [A] *Representative RARE images (left column) of the zebrafish brain acquired at 17.6 T and 28.2 T. Acquisition details: TR = 3000 ms, TE = 5.6 ms, ns = 16, resolution 23 µm × 23 µm × 200 µm, RARE factor 4. SNR maps generated from RARE images (right column);* ***[B]*** *RARE images of adult zebrafish brain region in coronal (left) and sagittal (right) view acquired at 28.2 T for structure identification. Acquisition details: TR = 3000 s, TE = 5.6 ms, ns = 64, resolution 23 µm × 23 µm × 100 µm, RARE factor 4. Identified structures are as follows: 1 – Central zone of dorsal telencephalon area; 2 – Lateral zone of the dorsal telencephalon; 3 – Medial zone of dorsal telencephalon; 4 – Posterior zone of dorsal telencephalon area; 5 – Dorsal habenular nucleus; 6 – Optic tectum; 7 – Tectal ventricle; 8 – Longitudinal torus; 9 – Periventricular grey zone of optic tectum; 10 – Ventrolateral nucleus of semicircular torus; 11 – Medial division of valvula cerebelli, molecular level; 12 - Medial division of valvula cerebelli, granular layer; 13 – Granular eminence; 14 – Cerebellar corpus, granular layer; 15 – Rhombencephalic ventricle; 16 – Caudal lobe of cerebellum; 17 – Medial octavolateralis nucleus; 18 – Facial lobe; 19 – Vagal lobe; 20 – Medial funicular nucleus; 21 – Cereberal corpus, molecular layer; 22 – Medial longitudinal fascicle; 23 – Dorsal sac, 24 – Cerebellar crest; 25 – Diffuse nucleus of the inferior lobe; 26 – Mammillary body; 27 – Caudal zone of periventricular hypothalamus; 28 – Ventral zone of periventricular hypothalamus; 29 – Parvocellular preoptic nucleus, anterior part; 30 – Ventral nucleus of ventral telencephalon area; 31 – Olfactory bulb; 32 – Interpeduncular nucleus.*

parameters including *TE*, *TR*, RARE factor, number of averages, and acquisition bandwidth. Furthermore, both MR systems contained similar RF coils, gradient power supplies, and software. To summarise, we have established the regional T_1 and T_2 values of the healthy zebrafish brain at 28.2 T. Our findings indicate that T_2 decreases while T_1 continues to rise with increasing magnetic field strength up to the ultra-high 28.2 T level. In future studies, accurate knowledge of T_1 and T_2 values of various brain regions at 28.2 T can serve as a reference point for detecting regional relaxation changes related to diseases in the zebrafish brain.

Anatomical imaging

Figure 2.2A shows representative slices of images of the zebrafish brain acquired using the RARE sequence at 17.6 T and 28.2 T. Images were acquired using the same zebrafish samples and identical acquisition parameters at both magnetic field strengths, obtaining a resolution of 23 μm × 23 μm and a slice thickness of 200 μm. A clear improvement in SNR is observed at 28.2 T as compared to 17.6 T. On average, an SNR improvement factor of 1.2 was found at 28.2 T as compared to 17.6 T in the zebrafish brain. Several brain structures could be clearly identified at 28.2 T (Figure 2.2B). Figure 2.2B shows anatomical images, obtained at 28.2 T, in the coronal and sagittal direction at a field of view (FOV) of 6 × 6 mm, an image size of 256 × 256 voxels, and a slice thickness of 100 μm, resulting in a spatial resolution of 23 × 23 × 100 μm. Excellent contrast, resolution, and SNR allowed for the identification of several brain structures that were verified by comparing them with detailed atlases of the zebrafish brain[41,42].

Diffusion-weighted imaging (DWI)

To get further contrast for the identification of WM structures such as commissures, fibre tracts, nerves, as well as the CSF system, we applied diffusion-based MRI techniques. dMRI provides contrast based on the Brownian motion of water molecules[58]. MRI is made sensitive to diffusion by strong gradient pulses before and after a 180° refocusing pulse, of which the magnitude (G), duration (δ), and time interval (Δ) are summarised in the b-value. In Figure 2.3A, the effect of the applied b-value in DWI experiments is shown for the zebrafish brain. At low b-values of 75 s/mm^2, high contrast and SNR are obtained for all regions in the zebrafish head. At moderate b-values of 500 or 1000 s/mm^2, the signal intensity of muscle and surrounding tissue is reduced, while a high contrast and SNR in the brain are maintained. In fact, DWI images obtained at 1000 s/mm^2 show improved contrast between various brain regions than those obtained at 75 or 500 s/mm^2. This is clearer in the forebrain where the olfactory bulb gained significant contrast compared to anatomical imaging (Figure 2.2B & 2.3A). This allowed better contrast for the identification of various structures in the brain compared to anatomical images obtained by the RARE sequence (Supplementary Figure S2.1). At a high b-values of

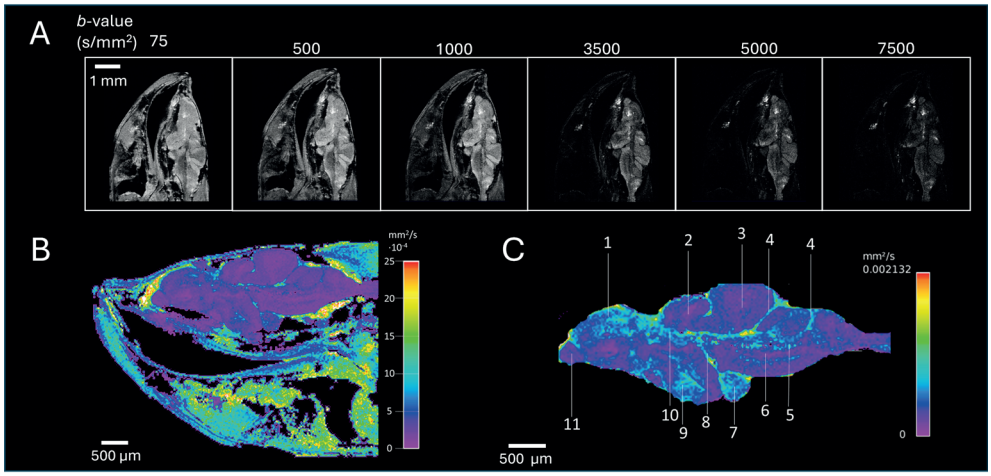

D

	OB	Te	CeG	Xlo	Cem	CC	OT	Hc	Hv
$ADC\left(\cdot 10^{-4}\frac{mm^2}{s}\right)$									
28.2 T	2.9 ± 0.1	4.5 ± 0.4	3.4 ± 0.6	3.9 ± 0.2	3.6 ± 0.3	3.7 ± 0,5	3.6 ± 0.5	3.0 ± 0.4	4.5 ± 0.4
17.6 T	2.4 ± 0.3	5.2 ± 0.4	4.6 ± 0.8	3.9 ± 0.4	4.2 ± 0.7	3.9 ± 0.4	4.5 ± 0.8	3.3 ± 0.2	5.1 ± 0.5
Factor	1.21	0.86	0.74	0.99	0.86	0.96	0.81	0.90	0.89

Figure 2.3. Diffusion-weighted imaging (DWI) of adult zebrafish brain acquired at 28.2 T. [A] *A representative sagittal slice of DWI measurement taken in the head of a zebrafish at increasing b-values. Acquisition details: TR = 1000 ms, TE = 20.2 ms, ns = 4, resolution 23 µm × 23 µm × 200 µm, and effective b-value range 75, 500, 1000, 3500, 5000, or 7500 s/mm²;* ***[B]*** *Apparent diffusion coefficient (ADC) map estimated in brain area of zebrafish, showing high contrast between brain and surrounding tissue;* ***[C]*** *ADC map calculated in brain of zebrafish, demonstrating identification of several structures based on diffusion characteristics; 1 – Medial zone of dorsal telencephalon; 2 – Longitudinal torus; 3 – Cerebellar corpus; 4 – Rhombencephalic ventricle; 5 – Ventral rhombencephalic commisure; 6 – Medial longitudinal fascicle; 7 – Diffusive nucleus of the inferior lobe; 8 – Vasular lacuna of area postrema; 9 – ventral zone of periventricular hypothalamus; 10 – Diencephalic ventricle; 11 – Olfactory bulb;* ***[D]*** *ADC values in various brain regions acquired at 28.2 T and 17.6 T. Data represent the mean ADC (10^{-4} mm² s^{-1}) ± standard error (SE) (Error bars); n = 6.*

3500 s/mm², the MR signal of all tissue drops, although the brain is still visible. Some signal from the brain was even visible at very high *b*-values of 5000 or 7500 s/mm². Figure 2.3B shows the *ADC* map. On average, the brain shows relatively low diffusivity (< 5 mm²/s) compared to most surrounding tissue (> 10 mm²/s), resulting in a clear high contrast between the brain and the surrounding tissue. Figure 2.3C shows an *ADC* map of the brain region from the central imaging slice. In addition to excellent contrast between various brain regions, the CSF system is clearly visible, allowing for the identification of several ventricles. Brain structures including

the diffusive nucleus of the inferior lobe, ventral zone of the periventricular hypothalamus, and medial zone of dorsal telencephalon, show relatively high diffusivity. On the other hand, structures, such as the olfactory bulb, cerebellar corpus, longitudinal torus, and medial longitudinal fascicle show relatively low diffusivity. Figure 2.3D shows estimated *ADC* values for selected ROIs obtained at 17.6 T and 28.2 T (see Figure 2.1A for ROI placement). At both magnetic fields, the highest diffusivity is found in the telencephalon and ventral zone of the periventricular hypothalamus, while the lowest diffusivity is found in the olfactory bulb. Some differences in *ADC* values were seen at 28.2 T as compared to 17.6 T. Although *ADC* values are independent of the applied magnetic field strength, they are affected by SNR. Thus, reported differences at 28.2 T and 17.6 T likely originate from differences in SNR[59].

Diffusion Tensor Imaging

Figure 2.4 shows representative 2D DTI results of adult zebrafish brain obtained at 28.2 T. All images show an identical sagittal slice, rostral (left) to caudal (right), acquired at a resolution of 25 µm x 25 µm, and a slice thickness of 200 µm. Figure 2.4A-C show $D_{\parallel}$, $D_{\perp}$, and *MD* maps of the zebrafish brain, respectively. Various structures could be identified by diffusivity-based contrast. The vascular system and specific brain regions, including the telencephalon, diffusive nucleus of the inferior lobe, and the ventral zone of the periventricular hypothalamus show a relatively high diffusivity. However, the olfactory bulb and the optic tectum show relatively low diffusivity compared to other brain structures. These results are consistent with observations made by DWI results shown in Figure 2.3. Furthermore, differences in the $D_{\parallel}$ and $D_{\perp}$ are observed, indicating anisotropic diffusivity effects. Figure 2.4D shows the *FA* map, visualizing the extent of anisotropic diffusivity in the zebrafish brain. High *FA* values (light colour) indicate anisotropic diffusion effects, while low *FA* values (dark colour) indicate more isotropic diffusion effects. It is well known that WM structures show the highest *FA* values in the brain due to the ordered structures of its myelinated axon tracts[14]. Due to high *FA* values, WM brain structures show very high image contrast, allowing the identification of various WM structures including the medial longitudinal fascicle, ansulate commissure, posterior commissure, and optic tract (indicated in Figure 2.4D). These structures could not be identified by anatomical imaging or DWI (Figure 2.2 & 3.3). Figure 2.4E shows the DEC *FA* colour map of the central sagittal slice of an adult zebrafish brain, obtained by combining directional information of the principal eigenvalues and *FA* maps. The *FA* colour map further confirms the identification of WM structures by *FA*, showing the rostral-caudal orientation of the medial longitudinal fascicle, and the medial-lateral orientation of the ansulate commissure, posterior commissure, and optic tract.

Figure 2.5A shows representative super-resolution short-track (st) track density imaging (TDI) tractography maps of 2D DTI data. Basic tractography algorithms are deterministic, which allow fitting the diffusion tensors to the diffusion data by tracking paths through the principal eigenvector of the tensor[60]. However, deterministic algorithms do not allow for crossing or closely passing fibres, potentially leading to non-existing connections[61,62]. dMRI tractography with CSD processes crossing and closely passing fibres, based on the first-order integration over fODFs[61]. These fODFs are estimated from response functions, in particular the estimated signal for single-fibre WM. In Figure 2.5A, CSD was performed by ssst algorithms to estimate the response function. The stTDI maps by ssst-CSD show high-resolution fibre-tracts, providing directional information beyond the DTI spatial resolution. Similar stTDI maps have been generated from the zebrafish brain in a previous DTI study performed at a lower magnetic field of 16 T[34]. However, the DTI measurement was accomplished on surgically isolated zebrafish brain treated with an MRI contrast agent. In our work, we performed all the measurements of intact zebrafish at 28.2 T without any contrast agent. One of the shortcomings of performing CSD with ssst-CSD algorithms is that it generates a track map without distinguishing individual

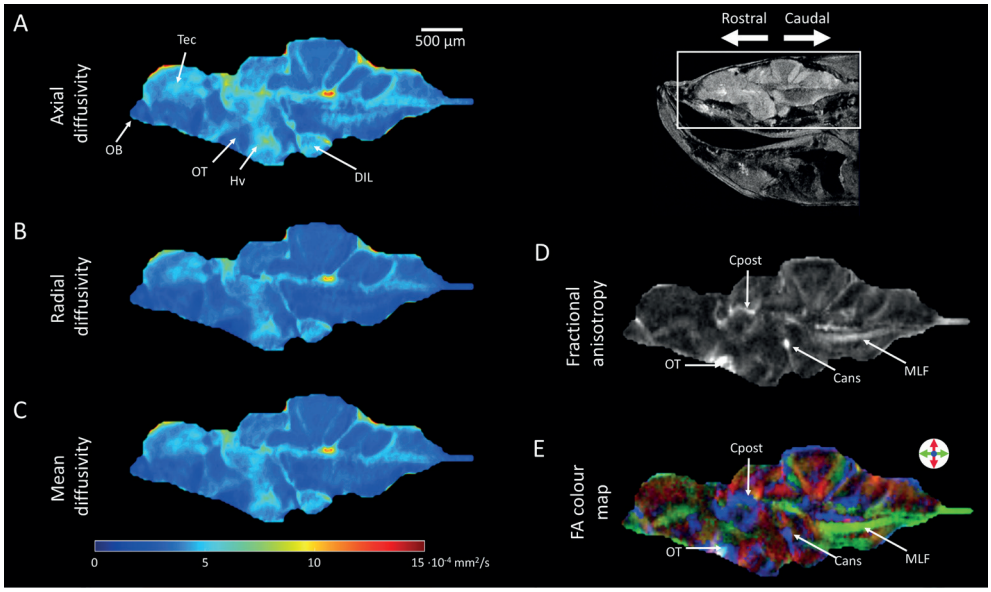

Figure 2.4. White matter structure characterisation based on 2D diffusion tensor imaging (DTI) results of adult zebrafish brain acquired at 28.2 T. *A representative central slice in sagittal view showing colour maps of* ***[A]*** *axial diffusivity ($D_{\parallel}$);* ***[B]*** *radial diffusivity ($D_{\perp}$), and* ***[C]*** *mean diffusivity (MD) calculated from diffusion tensor data.* ***[D]*** *Fractional isotropy (FA); and* ***[E]*** *diffusion-encoded-colour (DEC) map of FA. DEC is used to indicate orientation; green – rostral/caudal, red – dorsal/ventral, and blue – medial/lateral. Abbreviation: MLF – the medial longitudinal fascicle; Cans – ansulate commissure; Cpost – posterior commissure, and OT – optic tract.*

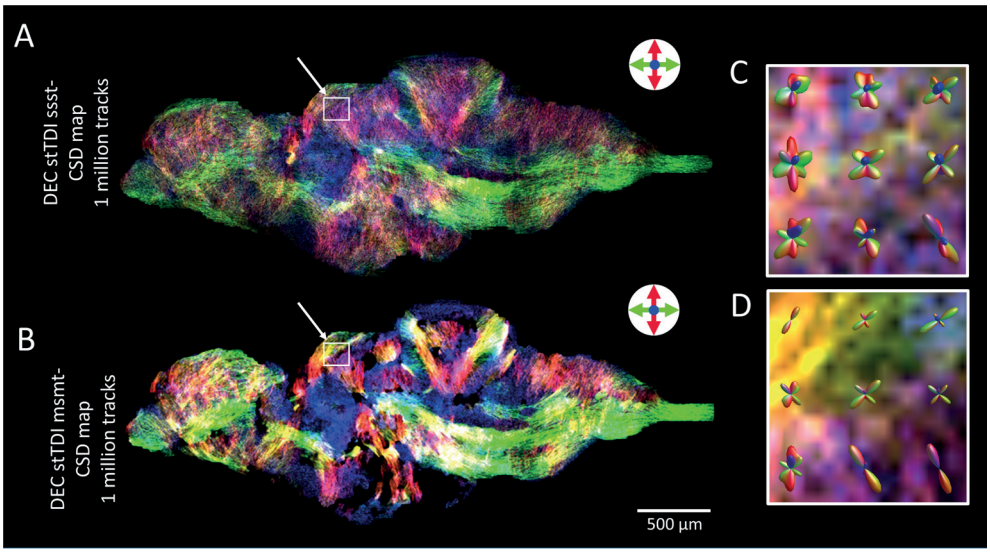

Figure 2.5. Whole brain tractography of zebrafish brain. [A] *Super-resolution DEC stTDI map calculated from single-shell single-tissue (ssst) CSD using the tournier algorithm[48] to estimate the response function.* ***[B]*** *Super-resolution DEC stTDI map calculated from white-matter response function estimated by multi-shell multi-tissue (msmt) CSD using the dHollander algorithm[35]. Tractography performed with one million streamlines, a minimal length of twice the voxel size (50 µm) and a maximum length of ten times the voxel size (250 µm);* ***[C&D]*** *fODFs located in the Optic Tectum isolated from the 2D stTDI ssst-CSD and msmt-CSD map, respectively. The location of these fODFs is highlighted in* ***[A&B]****, respectively. DEC is used to indicate orientation; green – rostral/caudal, red – dorsal/ventral, and blue – medial/lateral.*

anatomical structures, such as GM, CSF, and WM. This potentially produces WM tracking errors and overestimation[35]. To produce tracks exclusively in the WM area, we applied msmt algorithms to obtain stTDI maps (stTDI msmt-CSD). The msmt-CSD was originally developed and optimized for human brain data[37] and has also been applied to mouse brain DTI data[63]. However, it has not yet been applied to the zebrafish brain. In this study we implemented and successfully obtained the stTDI map by msmt-CSD in zebrafish brain (Figure 2.5B).

The response function estimation for WM, GM, and CSF obtained with msmt-CSD derived from our DTI data set is shown in Supplementary Figure S2.2. As can be seen from Figure 2.5B, stTDI by msmt-CSD produced tracks exclusively in WM areas. Furthermore, the stTDI map generated by msmt-CSD demonstrates a significant reduction in noise over those obtained by ssst-CSD (Figure 3.5), leading to improved identification of WM structures. Figure 2.5C&D show fODFs estimated by ssst and msmt CSD algorithms, respectively, from the optic tectum (see the highlighted area in Figure 2.5A&B). As shown in Figure 2.5D, the msmt-CSD fODFs have fewer lobes compared to the ssst-CSD shown in Figure 2.5C. This difference in lobe

number indicates a reduced number of possible tracks obtained by the msmt-CSD method. Our results are consistent with earlier reports in human and mouse brain[37,63]. An increased number of tracks with ssst-CSD indicates tracking errors due to overestimation resulting in false positive WM tracks. Unlike msmt-CSD algorithms, ssst-CSD does not individually characterise WM, GM, and CSF signals, resulting in WM tracking errors and overestimation[35]. The development of the msmt-CSD algorithm revealed that WM, GM, and CSF have distinct dependencies on *b*-values[35], enabling the deconvolution of their individual signals. By filtering GM- and CSF signals, strongly present in ssst-CSD, the number of false positive WM tracks is reduced with the msmt-CSD algorithm[36,37].

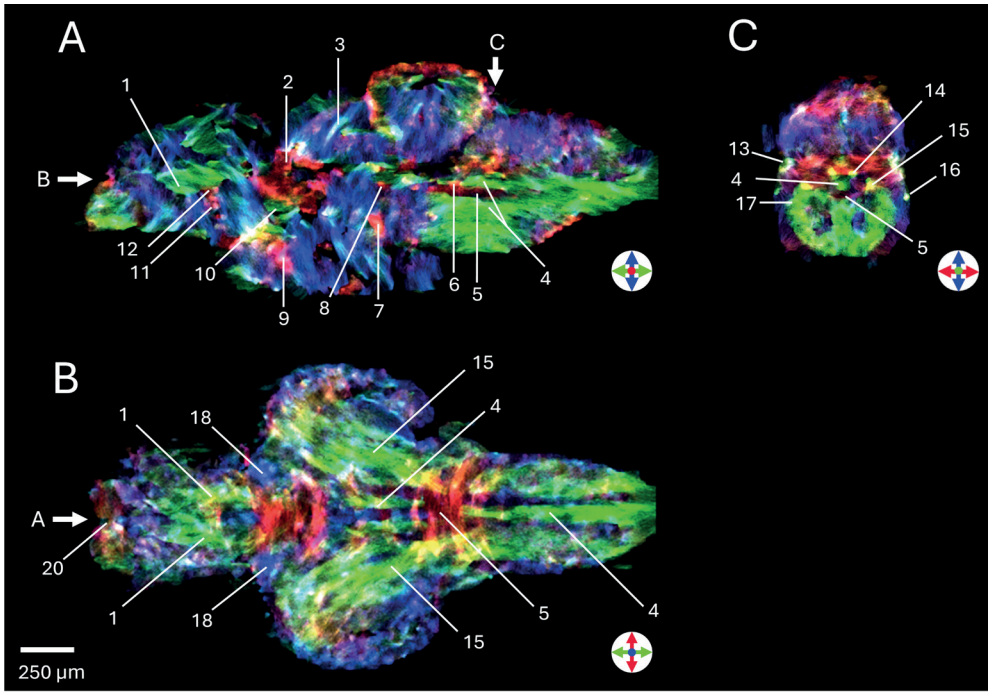

Figure 2.6. 3D super-resolution DEC stTDI msmt-CSD map of adult zebrafish brain. *The DEC stTDI msmt-CSD maps were generated from 3D DTI data measured at 28.2 T. Shown are representative map in* ***[A]*** *sagittal* ***[B]*** *coronal, and* ***[C]*** *axial view. 3D super-resolution DEC stTDI msmt-CSD map allowed identification of several WM structures in zebrafish brain: 1 (MOT) – Medial olfactory tract; 2 (Cpost) – Posterior commissure; 3 (Ctec) – Tectal commissure; 4 (MLF) – Medial longitudinal fascicle; 5 (Cven) – Ventral rhombencephalic commissure; 6 (IAF) – Inner arcuate fibres; 7 (Cans) – Ansulate commissure; 8 (DiV) – Diencephalic ventricle; 9 (Cpop) – Postoptic commissure; 10 (MFB) – Medial forebrain bundle; 11 (CantV) – Anterior commissure; 12 (CantD) – Anterior commissure; 13 (PLLN) - Posterior lateral line nerve; 14 (VIIs) – Sensory root of the facial nerve; 15 (LLF) – Lateral longitudinal fascicle; 16 (ALLN) – Anterior lateral line nerves; 17 (SGT) – Secondary gustatory tract; 18 (DOT) – Dorsomedial optic tract; 19 (Cgus) – Commissure of the secondary gustatory nuclei ; 20 (GL) – Glomerular layer of olfactory bulb. DEC is used to indicate orientation; green – rostral/caudal, blue – dorsal/ventral, and red – medial/lateral.*

Next, we acquire data using 3D DTI, as it allows for better visualization and quantification of white matter tracts, particularly in the areas with complex fibre orientation. The representative 3D DTI results of the adult zebrafish brain, acquired at an isotropic resolution of 35 μm, are shown in Supplementary Figure S2.3. From the 3D DTI data, *FA* maps and DEC *FA* colour maps were generated. Furthermore, 5 μm stTDI tractography maps were created from 3D DTI data (Supplementary Figure S2.3). Both ssst-CSD and msmt-CSD algorithms were used to estimate the response function. Enhanced resolution for crossing and closely passing fibres was clearly obtained with msmt-CSD as compared to ssst-CSD. Similar to 2D DTI data, visualization of WM structures by stTDI with msmt-CSD is significantly improved compared to ssst-CSD.

Figure 2.6 demonstrates the capability to identify WM structures in the zebrafish brain using 3D super-resolution stTDI msmt-CSD. In the sagittal (Figure 2.6A), coronal (Figure 2.6B), and axial (Figure 2.6C) view, WM structures were identified at high contrast and resolution, that were verified by comparing them with detailed atlases of the zebrafish brain[41,42]. A selection of the commissures, fibre tracts, and nerves that could be assigned are shown. This study shows that DTI at ultra-high field in conjunction with stTDI msmt-CSD provide great resolution for visualization of white matter tracts in intact zebrafish without the need to isolate the brain.

4. CONCLUSION

In conclusion, here we have shown the potential of MRI techniques at ultra-high magnetic fields (28.2 T) to study the zebrafish brain non-invasively. Excellent contrast and SNR were obtained allowing for the identification of brain structures, as well as fine white matter structures in intact zebrafish brain. Furthermore, ultra-high field DTI was capable of generating reliable and quantitative representations of the fibre organisation within the small brains of zebrafish. This opens up the possibility to study disease-related changes in white matter structure with super high resolution in a wide range of zebrafish models of human diseases.

ACKNOWLEDGEMENTS

Experiments at the 17.6 T and 28.2 T instruments were supported by the uNMR-NL Grid: A distributed, state-of-the-art Magnetic Resonance facility for the Netherlands (NWO grant 184.032.207). We thank Dr. Julia Krug & Dr. Jeanine Prompers for useful discussions and suggestions. We also acknowledge Dr. Andrei Gurinov for technical support at the uNMR-NL facility and Karthick Babu Sai Sankar Gupta and Fons Lefeber for help at 17.6 T. We would further like to thank Volker Lehmann and Thomas Oerther from Bruker for their help in troubleshooting.

REFERENCES

1 Bailone, R. L. *et al.* "Zebrafish as an animal model for food safety research: trends in the animal research". *Food Biotechnology* **33**, 283-302 (2019). https://doi.org/10.1080/08905436.2019.1673173

2 Cassar, S. *et al.* Use of Zebrafish in Drug Discovery Toxicology. *Chem Res Toxicol* **33**, 95-118 (2020). https://doi.org/10.1021/acs.chemrestox.9b00335

3 Choi, T. Y., Choi, T. I., Lee, Y. R., Choe, S. K. & Kim, C. H. Zebrafish as an animal model for biomedical research. *Exp Mol Med* **53**, 310-317 (2021). https://doi.org/10.1038/s12276-021-00571-5

4 Ding, Y. *et al.* Metabolomic and transcriptomic profiling of adult mice and larval zebrafish leptin mutants reveal a common pattern of changes in metabolites and signaling pathways. *Cell Biosci* **11**, 126 (2021). https://doi.org/10.1186/s13578-021-00642-0

5 Bashirzade, A. A. *et al.* Modeling neurodegenerative disorders in zebrafish. *Neurosci Biobehav Rev* **138**, 104679 (2022). https://doi.org/10.1016/j.neubiorev.2022.104679

6 Wang, X., Zhang, J. B., He, K. J., Wang, F. & Liu, C. F. Advances of Zebrafish in Neurodegenerative Disease: From Models to Drug Discovery. *Front Pharmacol* **12**, 713963 (2021). https://doi.org/10.3389/fphar.2021.713963

7 Wang, J. & Cao, H. Zebrafish and Medaka: Important Animal Models for Human Neurodegenerative Diseases. *Int J Mol Sci* **22** (2021). https://doi.org/10.3390/ijms221910766

8 Kabli, S., Alia, A., Spaink, H. P., Verbeek, F. J. & De Groot, H. J. Magnetic resonance microscopy of the adult zebrafish. *Zebrafish* **3**, 431-439 (2006). https://doi.org/10.1089/zeb.2006.3.431

9 Haud, N. *et al.* rnaset2 mutant zebrafish model familial cystic leukoencephalopathy and reveal a role for RNase T2 in degrading ribosomal RNA. *Proc Natl Acad Sci U S A* **108**, 1099-1103 (2011). https://doi.org/10.1073/pnas.1009811107

10 Ramirez, I. B. *et al.* Impaired neural development in a zebrafish model for Lowe syndrome. *Hum Mol Genet* **21**, 1744-1759 (2012). https://doi.org/10.1093/hmg/ddr608

11 Kabli, S., Spaink, H. P., De Groot, H. J. & Alia, A. In vivo metabolite profile of adult zebrafish brain obtained by high-resolution localized magnetic resonance spectroscopy. *J Magn Reson Imaging* **29**, 275-281 (2009). https://doi.org/10.1002/jmri.21609

12 Eeza, M. N. H. *et al.* Probing microstructural changes in muscles of leptin-deficient zebrafish by non-invasive ex-vivo magnetic resonance microimaging. *PLoS One* **18**, e0284215 (2023). https://doi.org/10.1371/journal.pone.0284215

13 Kabli, S. *et al.* In vivo magnetic resonance imaging to detect malignant melanoma in adult zebrafish. *Zebrafish* **7**, 143-148 (2010). https://doi.org/10.1089/zeb.2009.0649

14 Alexander, A. L., Lee, J. E., Lazar, M. & Field, A. S. Diffusion tensor imaging of the brain. *Neurotherapeutics* **4**, 316-329 (2007). https://doi.org/10.1016/j.nurt.2007.05.011

15 Auning, E. *et al.* White matter integrity and cognition in Parkinson's disease: a cross-sectional study. *BMJ Open* **4**, e003976 (2014). https://doi.org/10.1136/bmjopen-2013-003976

16 Bede, P. *et al.* Patterns of cerebral and cerebellar white matter degeneration in ALS. *J Neurol Neurosurg Psychiatry* **86** (2014).

17 de Schipper, L. J. *et al.* Age- and disease-related cerebral white matter changes in patients with Parkinson's disease. *Neurobiol Aging* **80**, 203-209 (2019). https://doi.org/10.1016/j.neurobiolaging.2019.05.004

18 Gold, B. T., Johnson, N. F., Powell, D. K. & Smith, C. D. White matter integrity and vulnerability to Alzheimer's disease: preliminary findings and future directions. *Biochim Biophys Acta* **1822**, 416-422 (2012). https://doi.org/10.1016/j.bbadis.2011.07.009

19 Huang, P. *et al.* Disrupted white matter integrity in depressed versus non-depressed Parkinson's disease patients: a tract-based spatial statistics study. *J Neurol Sci* **346**, 145-148 (2014). https://doi.org/10.1016/j.jns.2014.08.011

20 Kantarci, K. *et al.* White-matter integrity on DTI and the pathologic staging of Alzheimer's disease. *Neurobiol Aging* **56**, 172-179 (2017). https://doi.org/10.1016/j.neurobiolaging.2017.04.024

21 Novak, M. J. *et al.* White matter integrity in premanifest and early Huntington's disease is related to caudate loss and disease progression. *Cortex* **52**, 98-112 (2014). https://doi.org/10.1016/j.cortex.2013.11.009

22 Reading, S. A. *et al.* Regional white matter change in pre-symptomatic Huntington's disease: a diffusion tensor imaging study. *Psychiatry Res* **140**, 55-62 (2005). https://doi.org/10.1016/j.pscychresns.2005.05.011

23 Stricker, N. H. *et al.* Decreased white matter integrity in late-myelinating fiber pathways in Alzheimer's disease supports retrogenesis. *Neuroimage* **45**, 10-16 (2009). https://doi.org/10.1016/j.neuroimage.2008.11.027

24 van der Burgh, H. K. *et al.* Multimodal longitudinal study of structural brain involvement in amyotrophic lateral sclerosis. *Neurology* **94**, e2592-e2604 (2020). https://doi.org/10.1212/WNL.0000000000009498

25 Zhang, J. *et al.* Regional alterations in cortical thickness and white matter integrity in amyotrophic lateral sclerosis. *J Neurol* **261**, 412-421 (2014). https://doi.org/10.1007/s00415-013-7215-5

26 Abe, O. *et al.* Amyotrophic lateral sclerosis: diffusion tensor tractography and voxel-based analysis. *NMR Biomed* **17**, 411-416 (2004). https://doi.org/10.1002/nbm.907

27 Agosta, F. *et al.* Assessment of white matter tract damage in patients with amyotrophic lateral sclerosis: a diffusion tensor MR imaging tractography study. *AJNR Am J Neuroradiol* **31**, 1457-1461 (2010). https://doi.org/10.3174/ajnr.A2105

28 Kitamura, S. *et al.* Longitudinal white matter changes in Alzheimer's disease: a tractography-based analysis study. *Brain Res* **1515**, 12-18 (2013). https://doi.org/10.1016/j.brainres.2013.03.052

29 Kok, J. G. *et al.* Structural Network Analysis Using Diffusion MRI Tractography in Parkinson's Disease and Correlations With Motor Impairment. *Front Neurol* **11**, 841 (2020). https://doi.org/10.3389/fneur.2020.00841

30 Lo, C. Y. *et al.* Diffusion tensor tractography reveals abnormal topological organization in structural cortical networks in Alzheimer's disease. *J Neurosci* **30**, 16876-16885 (2010). https://doi.org/10.1523/JNEUROSCI.4136-10.2010

31 Phillips, O. *et al.* Tractography of the corpus callosum in Huntington's disease. *PLoS One* **8**, e73280 (2013). https://doi.org/10.1371/journal.pone.0073280

32 Zhang, Y. *et al.* Diffusion tensor imaging of the nigrostriatal fibers in Parkinson's disease. *Mov Disord* **30**, 1229-1236 (2015). https://doi.org/10.1002/mds.26251

33 Freidlin, R. Z. *et al.* Diffusion Tensor MR Microscopy of Adult Zebrafish. *Proc. Intl. Soc. Mag. Reson. Med.* **11** (2004).

34 Ullmann, J. F., Calamante, F., Collin, S. P., Reutens, D. C. & Kurniawan, N. D. Enhanced characterization of the zebrafish brain as revealed by super-resolution track-density imaging. *Brain Struct Funct* **220**, 457-468 (2015). https://doi.org/10.1007/s00429-013-0667-7

35 Dhollander, T., Raffelt, D. & Connelly, A. *Unsupervised 3-tissue response function estimation from single-shell or multi-shell diffusion MR data without a co-registered T1 image*. (2016).

36 Dhollander, T., Raffelt, D., Mito, R. & Connelly, A. Improved white matter response function estimation for 3-tissue constrained spherical deconvolution. *Conference Paper* (2019).

37 Jeurissen, B., Tournier, J. D., Dhollander, T., Connelly, A. & Sijbers, J. Multi-tissue constrained spherical deconvolution for improved analysis of multi-shell diffusion MRI data. *Neuroimage* **103**, 411-426 (2014). https://doi.org/10.1016/j.neuroimage.2014.07.061

38 Krug, J. R. *et al.* Assessing spatial resolution, acquisition time and signal-to-noise ratio for commercial microimaging systems at 14.1, 17.6 and 22.3 T. *J Magn Reson* **316**, 106770 (2020). https://doi.org/10.1016/j.jmr.2020.106770

39 He, J. *et al.* Leptin deficiency affects glucose homeostasis and results in adiposity in zebrafish. *J Endocrinol* **249**, 125-134 (2021). https://doi.org/10.1530/JOE-20-0437

40 Carr, H. Y. & Purcell, E. M. Effects of Diffusion on Free Precession in Nuclear Magnetic Resonance Experiments. *Physical Review* **94**, 630-638 (1954). https://doi.org/10.1103/PhysRev.94.630

41 Kenney, J. W. *et al. A 3D adult zebrafish brain atlas (AZBA) for the digital age*, <http://azba.wayne.edu/> (2021).

42 Wullimann, M. F., Rupp, B. & Reichert, H. *Neuroanatomy of the zebrafish brain A topological atlas*. (1996).

43 Milford, D., Rosbach, N., Bendszus, M. & Heiland, S. Mono-Exponential Fitting in T2-Relaxometry: Relevance of Offset and First Echo. *PLoS One* **10**, e0145255 (2015). https://doi.org/10.1371/journal.pone.0145255
44 Tournier, J. D. *et al.* MRtrix3: A fast, flexible and open software framework for medical image processing and visualisation. *Neuroimage* **202**, 116137 (2019). https://doi.org/10.1016/j.neuroimage.2019.116137
45 Veraart, J., Fieremans, E. & Novikov, D. S. Diffusion MRI noise mapping using random matrix theory. *Magn Reson Med* **76**, 1582-1593 (2016). https://doi.org/10.1002/mrm.26059
46 Basser, P. J., Mattiello, J. & Lebihan, D. Estimation of the Effective Self-Diffusion Tensor from the NMR Spin Echo. *Journal of Magnetic Resonance* **B**, 8 (1994). https://doi.org/https://doi.org/10.1006/jmrb.1994.1037.
47 Veraart, J., Sijbers, J., Sunaert, S., Leemans, A. & Jeurissen, B. Weighted linear least squares estimation of diffusion MRI parameters: strengths, limitations, and pitfalls. *Neuroimage* **81**, 335-346 (2013). https://doi.org/10.1016/j.neuroimage.2013.05.028
48 Tournier, J. D., Calamante, F. & Connelly, A. Determination of the appropriate b value and number of gradient directions for high-angular-resolution diffusion-weighted imaging. *NMR Biomed* **26**, 1775-1786 (2013). https://doi.org/10.1002/nbm.3017
49 Tournier, J. D., Calamante, F. & Connelly, A. Robust determination of the fibre orientation distribution in diffusion MRI: non-negativity constrained super-resolved spherical deconvolution. *Neuroimage* **35**, 1459-1472 (2007). https://doi.org/10.1016/j.neuroimage.2007.02.016
50 Tournier, J. D., Calamante, F. & Connelly, A. MRtrix: Diffusion tractography in crossing fiber regions. *International Journal of Imaging Systems and Technology* **22**, 53-66 (2012). https://doi.org/10.1002/ima.22005
51 Calamante, F., Tournier, J. D., Jackson, G. D. & Connelly, A. Track-density imaging (TDI): super-resolution white matter imaging using whole-brain track-density mapping. *Neuroimage* **53**, 1233-1243 (2010). https://doi.org/10.1016/j.neuroimage.2010.07.024
52 Bottomley, P. A., Foster, T. H., Argersinger, R. E. & Pfeifer, L. M. A review of normal tissue hydrogen NMR relaxation times and relaxation mechanisms from 1-100 MHz: dependence on tissue type, NMR frequency, temperature, species, excision, and age. *Med Phys* **11**, 425-448 (1984). https://doi.org/10.1118/1.595535
53 de Graaf, R. A. *et al.* High magnetic field water and metabolite proton T1 and T2 relaxation in rat brain in vivo. *Magn Reson Med* **56**, 386-394 (2006). https://doi.org/10.1002/mrm.20946
54 Korb, J. P. & Bryant, R. G. Magnetic field dependence of proton spin-lattice relaxation times. *Magn Reson Med* **48**, 21-26 (2002). https://doi.org/10.1002/mrm.10185
55 van de Ven, R. C. *et al.* T(1) relaxation in in vivo mouse brain at ultra-high field. *Magn Reson Med* **58**, 390-395 (2007). https://doi.org/10.1002/mrm.21313
56 Kara, F. *et al.* In vivo measurement of transverse relaxation time in the mouse brain at 17.6 T. *Magn Reson Med* **70**, 985-993 (2013). https://doi.org/10.1002/mrm.24533
57 Hamilton, N., Allen, C. & Reynolds, S. Longitudinal brain studies in adult zebrafish by MRI. (2022). https://doi.org/10.1101/2022.06.09.495545
58 Baliyan, V., Das, C. J., Sharma, R. & Gupta, A. K. Diffusion weighted imaging: Technique and applications. *World J Radiol* **8**, 785-798 (2016). https://doi.org/10.4329/wjr.v8.i9.785
59 Ogura, A. *et al.* Apparent Diffusion Coefficient Value Is Not Dependent on Magnetic Resonance Systems and Field Strength Under Fixed Imaging Parameters in Brain. *J Comput Assist Tomogr* **39**, 760-765 (2015). https://doi.org/10.1097/RCT.0000000000000266
60 Basser, P. J., Pajevic, S., Pierpaoli, C., Duda, J. & Aldroubi, A. In vivo fiber tractography using DT-MRI data. *Magnetic Resonance in Medicine* **44**, 625-632 (2000). https://doi.org/10.1002/1522-2594(200010)44:4<625::Aid-mrm17>3.0.Co;2-o
61 Jeurissen, B., Leemans, A., Jones, D. K., Tournier, J. D. & Sijbers, J. Probabilistic fiber tracking using the residual bootstrap with constrained spherical deconvolution. *Hum Brain Mapp* **32**, 461-479 (2011). https://doi.org/10.1002/hbm.21032

62 Jeurissen, B., Leemans, A., Tournier, J. D., Jones, D. K. & Sijbers, J. Investigating the prevalence of complex fiber configurations in white matter tissue with diffusion magnetic resonance imaging. *Hum Brain Mapp* **34**, 2747-2766 (2013). https://doi.org/10.1002/hbm.22099

63 Jillings, S. *et al.* Multi-tissue constrained spherical deconvolution in a murine brain. *Proc. Intl. Soc. Mag. Reson. Med.* **28** (2020).

5. APPENDIX

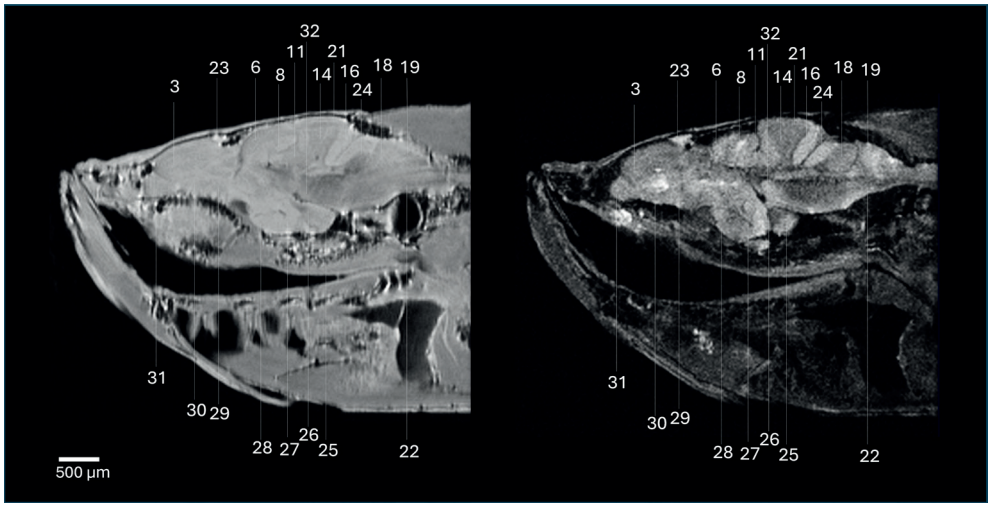

Figure S2.1. Superior identification of brain structures based on diffusion-weighted imaging (DWI) contrast as compared to RARE image contrast. [Left] *A representative sagittal slice of RARE image taken in the head of a zebrafish acquired at 28.2 T. RARE acquisition details: TR = 3000 ms, TE = 5.6 ms, ns = 16, resolution 23 µm × 23 µm × 200 µm, RARE factor 4. SNR maps generated from RARE images (right column);* ***[Right]*** *A representative sagittal slice of DWI measurement taken in the head of a zebrafish at a b-values of 1000 s/mm2. Acquisition details: TR = 1000 ms, TE = 20.2 ms, ns = 4, resolution 23 µm × 23 µm × 200 µm. Structure numbering (kept same as in Figure 3.2): 3 – Medial zone of dorsal telencephalon; 4 – Posterior zone of dorsal telencephalon area; 5 – Dorsal habenular nucleus; 6 – Optic tectum; 7 – Tectal ventricle; 8 – Longitudinal torus; 9 – Periventricular grey zone of optic tectum; 10 – Ventrolateral nucleus of semicircular torus; 11 – Medial division of valvula cerebelli, molecular level; 12 - Medial division of valvula cerebelli, granular layer; 13 – Granular eminence; 14 – Cerebellar corpus, granular layer; 15 – Rhombencephalic ventricle; 16 – Caudal lobe of cerebellum; 17 – Medial octavolateralis nucleus; 18 – Facial lobe; 19 – Vagal lobe; 20 – Medial funicular nucleus; 21 – Cereberal corpus, molecular layer; 22 – Medial longitudinal fascicle; 23 – Dorsal sac, 24 – Cerebellar crest; 25 – Diffuse nucleus of the inferior lobe; 26 – Mammillary body; 27 – Caudal zone of periventricular hypothalamus; 28 – Ventral zone of periventricular hypothalamus; 29 – Parvocellular preoptic nucleus, anterior part; 30 – Ventral nucleus of ventral telencephalon area; 31 – Olfactory bulb; 32 – Interpeduncular nucleus.*

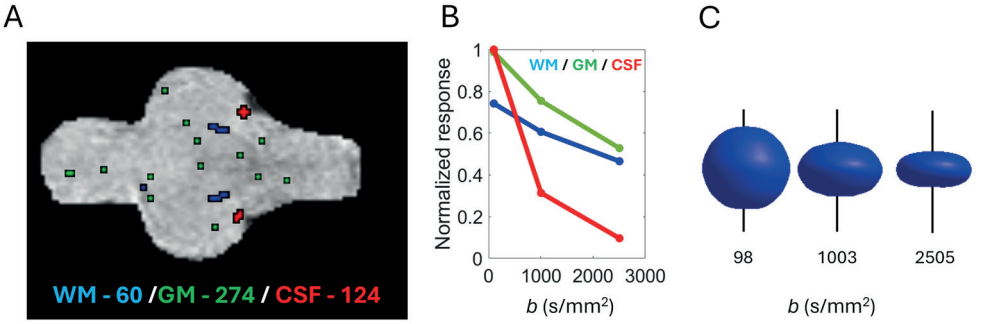

Figure S2.2. Response function estimation from DTI dataset of adult zebrafish brain. [A] *Voxels used for the estimation of response function; WM (blue), GM (green), and CSF (red). The total number of voxels selected for the response function estimation was 60 (WM), 274 (GM), and 124 (CSF).* ***[B]*** *Average normalized tissue response for WM, GM, and CSD as a function of b-values,* ***[C]*** *average angular WM response at applied b-values.*

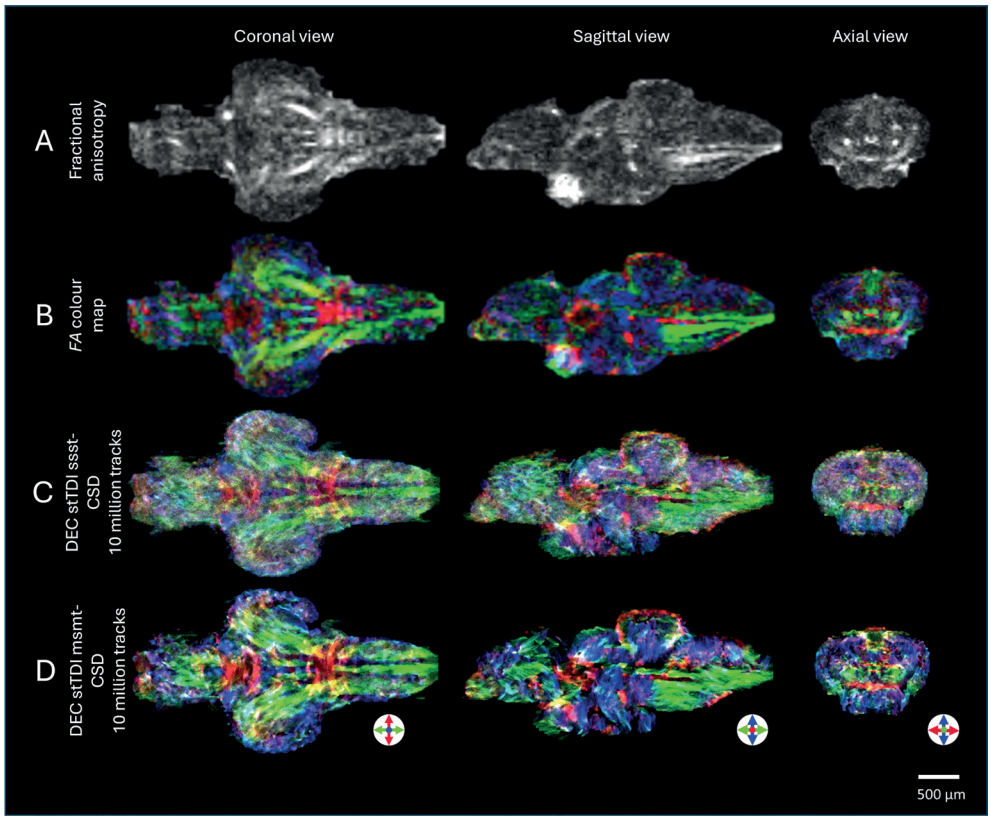

Figure S2.3. 3D DTI results of adult zebrafish brain, showing coronal, sagittal, and axial slices, acquired at 28.2 T. *Diffusion tensors were used to calculate* ***[A]*** *the fractional anisotropy and* ***[B]*** *FA colour map. Short track (st) tractography with Constrained Spherical Deconvolution (CSD) was applied, comparing two different algorithms for the estimation of the response function.* ***[C]*** *Super-resolution DEC stTDI maps calculated from single-shell single-tissue (ssst) CSD using the tournier algorithm (Tournier et al., 2004) [48] to estimate the response function.* ***[D]*** *Super-resolution DEC stTDI map calculated from white-matter response function which was estimated by multi-shell multi-tissue (msmt) CSD using the dHollander algorithm [35]. Tractography performed by generating ten million streamlines, with a minimal length of twice the voxel size (70 µm) and a maximum length of ten times the voxel size (350 µm). DEC is used to indicate orientation; green – rostral/caudal, blue – dorsal/ventral, and red – medial/lateral. Acquisition details: TR = 2000 ms, TE = 9 ms, ns = 4, isotropic resolution 35 µm, effective b-value range 100, 1000, or 2500 s/mm2, with 4, 12 or 24 diffusion-encoding directions respectively.*

3

ULTRA-HIGH FIELD DIFFUSION MRI UNCOVERS INTRIGUING MICROSTRUCTURAL CHANGES IN THE ADULT ZEBRAFISH BRAIN CAUSED BY TLR2 GENOMIC DELETION*

* This chapter was published in NMR BIOMED 2024; doi:10.1002/nbm.5170

ABSTRACT

The toll-like receptor 2 (TLR2) belongs to the TLR protein family that plays an important role in the immune and inflammation response system. While TLR2 is predominantly expressed in immune cells, its expression has also been detected in the brain, specifically in microglia and astrocytes. Recent studies indicate that genomic deletion of TLR2 can result in impaired neurobehavioral function. It is currently not clear if the genomic deletion of TLR2 leads to any alterations in the microstructural features of the brain. In the current study, we non-invasively assess microstructural changes in the brain of TLR2 deficient (*tlr2*$^{-/-}$) zebrafish using state-of-the art MRI methods at ultra-high magnetic field strength (17.6 T). A significant increase in cortical thickness and an overall trend towards increased brain volumes were observed in young *tlr2*$^{-/-}$ zebrafish. An elevated T_2 relaxation time and significantly reduced apparent diffusion coefficient (*ADC*) unveil brain wide microstructural alterations, potentially indicative of cytotoxic edema and astrogliosis in the *tlr2*$^{-/-}$ zebrafish. Multi-component analysis of the *ADC* diffusivity signal by the phasor approach shows an increase in the slow *ADC* component associated with restricted diffusion. Diffusion tensor imaging and diffusion kurtosis imaging analysis revealed diminished diffusivity and enhanced kurtosis in various white matter tracks in *tlr2*$^{-/-}$ as compared to control zebrafish, identifying the microstructural underpinnings associated with compromised white matter integrity and axonal degeneration. Taken together, our findings demonstrate that the genomic deletion of TLR2 results in severe alterations to the microstructural features of the zebrafish brain. This study also highlights the potential of ultra-high field diffusion MRI techniques in discerning exceptionally fine microstructural details within the small zebrafish brain, offering potential for investigating microstructural changes in zebrafish models of various brain diseases.

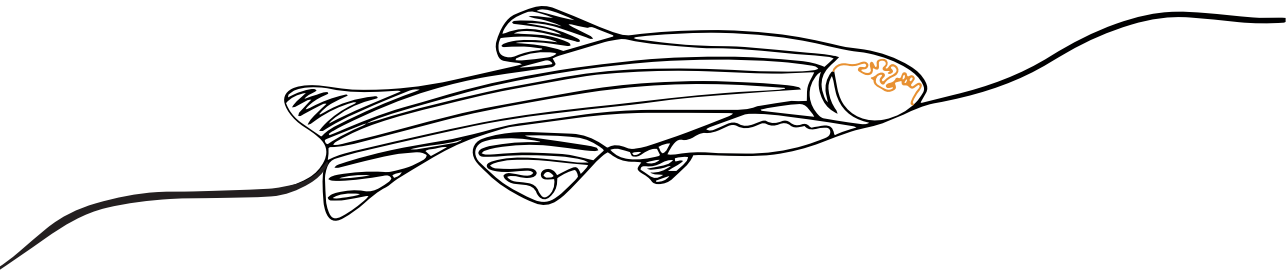

1. INTRODUCTION

Pattern recognition receptors (PRRs), encoded in the germline DNA, play a crucial role in the animal immune defence as part of the innate immune system[1]. Unlike T cells and B cells, expressing antigen recognition receptors with a high specificity, PRRs initiate immune response by recognizing a diverse array of pathogen-associated molecular patterns (PAMPs), found on various microorganisms. PRRs also recognise danger-associated molecular patterns (DAMPs), produced as a consequence of damaged tissue. Among the eight PRR groups[2], Toll-like receptors (TLRs) stand out as vital components of the innate immune system. Structurally, TLRs consist of three distinct parts[3]; (1) an N-terminal ectodomain on the membrane outside, responsible for recognizing and binding to specific PAMPs or DAMPs, (2) a transmembrane domain spanning the lipid bilayer of the cell membrane, to anchor the receptor in its place, and (3) a C-terminal to initiate downstream signalling on the intracellular side of the membrane. Within the TLR family, specific TLRs play crucial roles in distinguishing unique PAMPs and DAMPs. Interestingly, the number of TLRs expressed in various vertebrate species varies. For example, humans possess 10 TLRs encoded in their genome, whereas mice and zebrafish have genomes encoding for at least 12, and 20 functional TLRs, respectively[4,5]. Toll-like receptor 2 (TLR2), one such member of the TLR family, plays a particularly important role in the immune- and inflammation response system and has orthologs in humans, mice, and zebrafish. TLR2 is expressed on the cell surface of endothelial, epithelial, and immune cells, including macrophages, dendritic cells and monocytes[6], and forms heterodimers with TLR1 or TLR6[2]. The broad recognition spectrum of TLR2 encompasses a wide range of PAMPs and DAMPs ligands[2]. In addition to its crucial role in the immune and inflammatory response system, TLR2 has become a focal point of interest due to its dual function in the infection processes. While TLR2-mediated inflammatory responses are important for effective bacterial clearance, excessive or inappropriate TLR2 signalling can lead to unintended tissue damage, inflammatory disorders, or delayed healing[7,8]. In the brain, excessive TLR2 signalling has emerged as potential player in the pathogenesis of neuroinflammatory and neurodegenerative disorders, including in the pathogenesis of Alzheimer's disease, Parkinson's disease, amyotrophic lateral sclerosis, and ischemic strokes[9]. There are rather conflicting reports on the role of TLR2 deficiency in the brain. Some reports suggest that a deficiency of TLR2 may improve neurobehavioral functions and protect against neurodegenerative diseases[10]. On the other hand, other reports have shown that a deficiency of TLR2 itself could induce cognitive disabilities, decreased locomotor activity, and increased anxiety and depression[11,12]. In a TLR2-deficient mouse model, aggravated white matter damage and deteriorated neurobehavioral functions have been observed in the absence of an infection or neurodegenerative inducing mutations[11]. Thus, the exact role of TLR2 in regulating normal neurological functions and inducing neuroinflammatory processes remains to be established.

In a recent study, we utilized zebrafish (*Danio rerio*) larvae as an *in vivo* model to investigate the metabolic control functions of TLR2 through transcriptomic and metabolomic approaches[2]. We showed that the deficiency of TLR2 in zebrafish larvae leads to many metabolic changes compared to controls and proposed that in addition to its function in immunity and inflammatory processes, TLR2 has a function in controlling metabolism in the absence of infection. However, the impact of TLR deficiency on brain structure and function and neuroinflammation in the absence of infection is not clear. A comprehensive, non-invasive system-level study would be necessary to clarify this. Magnetic resonance imaging (MRI) is a well-established, non-invasive technique. MRI provides distinct advantages compared to other microscopic techniques, even those potentially reaching higher resolutions. This includes its capability for whole-organ imaging, including full three-dimensional analysis, while eliminating the necessity for sectioning or chemical staining. Moreover, recent advancements in MRI gradient systems and ultra-high magnetic field strength provide the ability to achieve very high spatial resolutions[13]. In our earlier studies we developed MRI methods for (*in vivo)* imaging of zebrafish[14,15], which we applied to study various models including cystic leukoencephalopathy[16], Lowe syndrome[17], *in vivo* analysis of tumors[18] and microstructural changes in the muscle tissue of leptin-deficient zebrafish[19]. *In vivo* MRI also allowed longitudinal studies of live adult zebrafish brain as reported by Hamilton *et al.* [20]. However, getting access to microstructural details in the tiny zebrafish brain is challenging. MRI at ultra-high field in conjunction with mathematical modelling can probe microstructural changes in tiny zebrafish brain. In addition, diffusion-based MRI (dMRI) offer a remarkable sensitivity to water movement, encompassing techniques including diffusion-weighted imaging (DWI), diffusion tensor imaging (DTI), and diffusion kurtosis imaging (DKI). These techniques provide unique ways for exploring microstructural alterations in the brain and offer non-invasive opportunities to monitor the progression of neurodegenerative disorders[21,22]. Furthermore, dMRI tractography enables the visualization of white matter structures within the zebrafish brain, thereby enabling the precise examination of these anatomical structures[23].

To elucidate the precise involvement of TLR2 in regulating normal neurological functions and neuroinflammatory processes, we employed TLR2 knockout (*tlr2*$^{-/-}$) zebrafish as a model organism. By utilizing state-of-the-art MRI methods at ultra-high magnetic field (17.6 T) we explored the impact of TLR2 deficiency on the microarchitecture of the brain. Ultra-high field micro-MRI with strong field gradients provides the necessary resolution and signal-to-noise required to study the micro-structural changes in the tiny zebrafish brain. Furthermore, diffusion-weighted MRI provided superior anatomical and substructural details of the zebrafish brain as compared to traditional anatomical imaging. DTI tractography by short-track track-density imaging enabled us to see changes in specific white matter structures in *tlr2*$^{-/-}$ zebrafish as compared to controls. Our results show that TLR2 deficiency leads to

microstructural changes associated with compromised white matter integrity and axonal degeneration.

2. METHODS

Zebrafish husbandry

In this study, the wild type AB/TL strain and *tlr2*^{sa19423} zebrafish line, obtained from the Sanger Institute Zebrafish Mutation Resource (Hinxton, Cambridge, UK) were utilized. The homozygote carriers of the TLR2 mutation, along with their wild type control, were subjected to over five rounds of outcrossing, resulting in the *tlr2*$^{-/-}$ (mutant) and *tlr2*$^{+/+}$ (control) siblings used for the experiments described in this work. Screening and raising of *tlr2*$^{-/-}$ and control zebrafish were performed as previously described[24,25], complying with university animal welfare committee guidelines (Licence numbers AVD1060020171767 and AVD10600202216175), following EU Animal Protection Directive international guidelines (2010/63/EU), and according to standard protocols (www.zfin.org). For imaging, five male pairs of three-month-old (84 days) *tlr2*$^{-/-}$ and control zebrafish, were euthanized through immobilization by submersion in ice water (0 – 4 °C) for approximately 10 minutes, followed by cessation of opercular movement. Specimen were then fixed in 4% buffered paraformaldehyde (Zinc Formal-Fixx, ThermoShandon, UK) for 4 days.

Magnetic Resonance Imaging

MR imaging experiments were conducted with a Bruker vertical bore system (Bruker Biospin GmbH, Germany) operating at 17.6 T (750 MHz). The system was equipped with a water-cooled Micro5 gradient system, offering a gradient strength (G_{max}) up to 3 T/m. Additionally, a birdcage transmit and receive radiofrequency (RF) coil with a 5 mm inner diameter and a GREAT60 gradient power supply were employed. Data acquisition and processing was performed with a Linux workstation, running ParaVision 360 v3.3 imaging software (Bruker BioSpin GmbH, Germany). For all experiments, zebrafish were transferred to 5 mm NMR tubes and embedded in perfluoropolyether (Fomblin Y, Solvay Solexis S.P.A.) to remove background signals whilst having a susceptibility close to tissue[26]. Maximum signal intensity and magnetic field homogeneity were achieved by aligning the zebrafish brain to the centre of the RF coil and automatic second-order shimming. Prior to each experiment, the frequency calibration was fine-tuned, and the reference power and receiver gain were optimized.

For the estimation of T_2, we utilized a multi-slice multi-echo (MSME) pulse sequence, based on the Carr-Purcell Meiboom-Gill (CPMG) sequence[27]. MSME measurements were performed with 60 echoes per excitation, with a CPMG refocusing pulse interval τ = 6.0 ms, a repetition time TR = 3000 ms, and ns = 4 for averaging. The field of view (FOV) was 6 × 6 mm, with a

matrix size of 128 × 128, resulting in an in-plane resolution of 47 × 47 μm, at a slice thickness of 500 μm and a total scan time of ~ 25 minutes.

In a diffusion-based MRI (dMRI) experiment, a 90° excitation RF pulse is succeeded by a 180° refocusing RF pulse. Manifestation of diffusion dependency is achieved through application of gradient pulses both before and after the refocusing RF pulse, as originally developed by Stejskal and Tanner[28]. The strength (G), gradient pulse interval (Δ) and gradient pulse length (δ) of these gradient pulses are summarised in the b-value according to $b = \gamma^2 \cdot G^2 \cdot \delta^2 \cdot \left(\Delta - \frac{\delta}{3}\right)$, where γ is the gyromagnetic ratio. DWI experiments were performed with a diffusion-weighted spin echo sequence, applying an echo time TE = 13.0 ms, TR = 1000 ms, ns = 4, δ = 1 ms, Δ = 7 ms, and an effective b-value range of 50, 500, 1000, 1500, 2000, 2500, or 3000 s/mm^2. The FOV was 6 × 6 mm, with a matrix size of 128 × 128, resulting in an in-plane resolution of 47 × 47 μm, at a slice thickness of 200 μm and a total scan time of ~ 48 minutes. DTI utilizing echo-planar imaging (EPI) was employed for anatomical imaging of the zebrafish brain. Additionally, this technique enabled the estimation of various diffusion metrics including axial diffusivity ($D_{\parallel}$), radial diffusivity ($D_{\perp}$), mean diffusivity (MD), fractional anisotropy (FA), as well as axial kurtosis ($K_{\parallel}$), radial kurtosis ($K_{\perp}$) mean kurtosis tensor (MK), and kurtosis fractional anisotropy (KFA). In addition, DTI facilitated tractography was used to explore the connectivity of neural pathways within the zebrafish brain. 2D DTI experiments were performed with TE = 12.4 ms, TR = 2000 ms, ns = 32, and an EPI factor of 8. Multi-shell DTI experiments were performed with δ = 1.5 ms, Δ = 6 ms, and an effective b-value range of 4, 1000, 3500, or 6000 s/mm^2, with 8, 12, 24, or 36 diffusion-encoding directions, respectively. The FOV was 5 × 5 mm, with a matrix size of 200 × 200, resulting in an in-plane resolution of 25 × 25 μm, at a slice thickness of 200 μm and a total scan time of 11 hours, 22 minutes. 3D DTI experiments were performed with TE = 9.1 ms, TR = 2000 ms, ns = 4, and an EPI factor of 8. Multi-shell diffusion experiments were performed with δ = 1.5 ms, Δ = 4 ms, and an effective b-value range of 100, 1000, or 2500 s/mm^2, with 4, 12, or 24 diffusion-encoding directions, respectively. The FOV was 2.52 × 4.97 × 1.82 mm, with a matrix size of 72 × 142 × 52, resulting in an isotropic resolution of 35 μm and a total scan time of 36 hours, 58 minutes.

Data processing

Brain structure identification. Identification of brain regions and white matter structures was based on various available zebrafish brain atlases and similar sources[29-31]. The cortical thickness of the longitudinal torus (TL), the molecular layer of the cerebellar corpus (CCem), and the optic tectum (TeO) were estimated using the distance measuring tools in Paravision software (Bruker BioSpin GmbH, Germany). The estimation was based on the central sagittal or coronal slice at a b-value of 2500 s/mm^2 from 3D DTI measurements obtained at 17.6 T. The volume of the main brain regions, including the total brain volume, was estimated using Matlab

R2021b (mathworks.com). Raw DTI data was imported into Matlab with a modified version of read_2dseq[32]. The mean intensity of the largest acquired *b*-value was calculated, as it provided the optimal contrast for segmenting the brain into its main regions. The segmentation of brain regions was performed in the Volume Segmenter tool of Matlab, after which their volumes were calculated based on the applied resolution.

Estimation of T_2. The estimation of T_2 was performed using MSME data. Uneven echoes were excluded from the data fitting to compensate for imperfect refocusing pulses[33], and the first 12 remaining echoes (12 – 144 ms) were used for fitting. After 144 ms, the signal-to-noise ratio (SNR) fell below the threshold value for a Gaussian distribution of the T_2 signal (see Supplementary Figure S3.1.), required for reliable line-fitting. T_2 was estimated with a non-linear least square algorithm for the exponential fit function according to

$$I_{\mathrm{TE}} = A + I_0 \cdot \exp^{\frac{-TE}{T_2}} \quad , \tag{3.1}$$

where I_{TE} is the signal intensity at echo time *TE*, *A* is the absolute bias, I_0 is the signal intensity at TE_0, and *TE* is the echo time (ms).

Estimation of *ADC*. The estimation of the apparent diffusion coefficient (*ADC*) was performed from DWI data, with a non-linear least square algorithm for the exponential fit function

$$I_{\mathrm{b}} = A + I_0 \cdot \exp^{-b \cdot ADC} \quad . \tag{3.2}$$

Here I_b is the signal intensity at *b* and I_0 is the signal intensity at time b_0.

***ADC* multi-component analysis by the phasor approach.** Mono- and multi-component *ADC* analysis by the phasor approach was performed using Matlab. Raw DWI data was imported into Matlab. DWI data is transformed to phasor plot coordinates by selecting region of interest (ROI) using the volume segmenter tool. Next, for each individual *ADC* decay curve in the ROI a stepwise approach was followed. (1) An absolute bias systematic error correction was performed, based on a Rayleigh probability distribution fit of the background signal (see Supplementary Figure S3.2.). (2) Next, the data was filtered by an arithmetic mean filter with filter size 2, (3) followed by normalization to the [0, 1] range, (4) fast-Fourier transformation, (5) selection of the first harmonics, and finally (6) plotting the real versus the imaginary part. The semi-circle of the phasor plot, representing the phasor coordinates of mono-component *ADC*, is added for *ADC* between 0 and 0.001 mm^2/s based on Eq.3.2. Mono-component analysis of DWI is performed by projecting the phasor plot coordinates of the ROIs onto the semi-circle using the Matlab dsearchn() function. In addition, a bi-component analysis was performed,

based on the bi-exponential fit function

$$I_{\mathrm{b}} = a\cdot \exp^{-b\cdot ADC_{\mathrm{slow}}} + c\cdot \exp^{-b\cdot ADC_{\mathrm{fast}}} \quad . \tag{3.3}$$

Here *a* and *c* are the areas of component ADC_{slow} and ADC_{fast}, respectively. For this, ADC_{slow} was taken between 0 and $4\cdot10^{-4}$ mm²/s, ADC_{fast} between $4.1\cdot10^{-4}$ and $1\cdot10^{-3}$ mm²/s, with a step-size of $1\cdot10^{-5}$ mm²/s, and step-sizes of 1% for *a* and *c*. Obtained values were verified by determining the fit (R^2) using the curve fitting tool in Matlab.

Processing of DTI data. DTI data processing, including diffusion metrics estimation and white matter connectivity analysis by tractography, was conducted using MRtrix3 software[34] and Matlab. Brain masks were generated using the Volume Segmenter tool in Matlab. Raw DTI data was denoised based on the random matrix theory and potential Gibbs ringing artifacts were removed based on the method of local subvoxel-shifts[35], implemented through MRtrix3 functionality[36]. The estimations of the (apparent) diffusions tensors (**D**) and (apparent) diffusion kurtosis tensors (**W**) were also executed through functionalities available within MRtrix3. **D** and **W** were derived from logarithmically transformed and pre-processed DTI data through a two-stage procedure. First, the fitting process employed weighted least-squares methodology, which were based on empirical signal intensities. Second, an iterated weighted least-squares approach was used, utilizing the signal predictions from preceding iteration to inform subsequent iterations. In total, two iterations are performed. Due to their full symmetric, **D** and **W** have 6 and 15 degrees of freedom, respectively. Construction of **W** requires a minimum of 22 diffusion-weighted images taken at 3 distinct *b*-values towards 15 unique diffusion-encoding directions[37]. Full descriptions of the methodology is provided by Basser *et al.* for **D**, and Veraart *et al.* for **W** [38,39]. Diffusion tensor metrics ($D_{\parallel}$, $D_{\perp}$, *MD*, and *FA*) were estimated from **D**, according to

$$D_{\parallel} = \lambda_1 \tag{3.4}$$

$$D_{\perp} = \frac{\lambda_2+\lambda_3}{2} \tag{3.5}$$

$$MD = \frac{\lambda_1+\lambda_2+\lambda_3}{3} \text{ , and} \tag{3.6}$$

$$FA = \frac{\|D-MD\cdot I^{(2)}\|}{\|D\|} = \sqrt{\frac{\frac{3}{2}\left((\lambda_1-MD)^2+(\lambda_2-MD)^2+(\lambda_3-MD)^2\right)}{\lambda_1{}^2+\lambda_2{}^2+\lambda_3{}^2}} \tag{3.7}$$

The λ_1, λ_2, and λ_3 are the eigenvalues of **D**, arranged such that $\lambda_1 \geq \lambda_2 \geq \lambda_3$, $\mathbf{I}^{(2)}$ is the fully symmetric rank 2 isotropic tensor, and $||..||$ denote the application of the Frobenius norm. For the estimation of the diffusion kurtosis tensor metrics, **W** was utilized[40,41]. Estimation of *MK*

was based on the equation for rapid *MK* estimation as defined by Hansen and Jespersen[42],

$$MK = \frac{1}{5}\mathrm{Tr}(\mathbf{W}) \tag{3.8A}$$

$$MK = \frac{1}{5}\left(W_{1111} + W_{2222} + W_{3333} + 2\,W_{1122} + 2\,W_{1133} + 2\,W_{2233}\right) \tag{3.8B}$$

Where W_{ijkl} are the diffusion kurtosis tensor elements. Estimation of $K_{\parallel}$ was based on

$$K_{\parallel} = \frac{\lambda_1+\lambda_2+\lambda_3}{9\cdot{\lambda_1}^2} W_{1111} \quad . \tag{3.9}$$

Estimation of $K_{\perp}$ was based on

$$K_{\perp} = G_1 W_{2222} + G_1 W_{3333} + G_2 W_{2233} \quad . \tag{3.10}$$

with

$$G_1 = \frac{(\lambda_1+\lambda_2+\lambda_3)^2}{18\lambda_2\cdot(\lambda_2+\lambda_3)^2} \cdot \left(2\lambda_2 + \frac{{\lambda_3}^2 - 3\lambda_2\cdot\lambda_3}{\sqrt{\lambda_2\cdot\lambda_3}}\right) \quad \text{and} \tag{3.11A}$$

$$G_2 = \frac{(\lambda_1+\lambda_2+\lambda_3)^2}{3\cdot(\lambda_2+\lambda_3)^2} \cdot \left(\frac{\lambda_2+\lambda_3}{\sqrt{\lambda_2\cdot\lambda_3}} - 2\right) \quad . \tag{3.11B}$$

The estimation of *KFA* was based on

$$KFA = \frac{||W - MK\cdot I^{(4)}||}{||W||} \quad , \tag{3.12}$$

where $\mathbf{I}^{(4)}$ is the fully symmetric rank 4 isotropic tensor and **W** was formed by permutating its 15 unique elements, which were acquired from MRtrix3 software.

White matter structure identification by DTI tractography. To identify white matter structures in the zebrafish brain, tractography was employed using super-resolution (5 µm) short-track track-density imaging by multi-shell multi-tissue constraint spherical deconvolution (stTDI msmt CSD) conducted using the MRtrix3 software[34]. Estimation of the msmt CSD response functions was performed by the Dhollander algorithm[43], selecting the top 10.0%, 2.0% and 10.0% of refined white matter, grey matter, and cerebrospinal fluid (CSF) voxels, respectively. Crude segmentation of white matter from grey matter and CSF was performed at *FA* = 0.15. Fibre orientation distribution functions (fODFs) were estimated using the msmt-CSD algorithm[44]. Whole brain short track tractography was performed with the iFOD1 algorithm[45], generating 10 million tracks, with a length between two and ten voxels. Generated tracks were converted to super-resolution TDI[46], obtaining connectivity images at an approximate 5 µm resolution, in which the orientation of tracks is indicated by directional encoded colour (DEC).

Statistical analysis. All statistical analysis of data was performed using Matlab and GraphPad Prism version 9.0.0 for Windows, (Graphpad Software, San Diego, California, USA, www.graphpad.com). Test of significance was performed using the unpaired *t*-test, assuming Gaussian distribution, with a p of < 0.05 considered as a significant difference between the two groups. Possible outliers were identified and removed based on three scaled median absolute deviations (MAD) from the median value.

3. RESULTS AND DISCUSSION

In this study, we probed the effect of genomic deletion of TLR2 on microstructural changes observed in the brain of *tlr2*$^{-/-}$ adult zebrafish non-invasively, utilizing state-of-the-art MR imaging at an ultra-high magnetic field strength of 17.6 T.

Changes in brain morphology observed in tlr2*$^{-/-}$ *zebrafish brain.

Figure 3.1 presents high-resolution images of control and *tlr2*$^{-/-}$ male zebrafish, acquired using 3D DTI at a *b*-value of 2500 s/mm^2. DTI offered enhanced contrast compared to conventional anatomical imaging techniques, enabling clear separation of tiny zebrafish brain structures. Differences in the cortical thickness of brain structures were observed in the cerebellum and the mesencephalon (Figure 3.1A). In the cerebellum, the thickness of the molecular layer of the cerebellar corpus (CCem) was found significantly enlarged by approximately 38% in *tlr2*$^{-/-}$ zebrafish compared to the control group (Figure 3.1C). Similar observations were made in the mesencephalon, where the volumes of the longitudinal torus (TL) and optic tectum (OT) were significantly increased by approximately 29% and 27%, respectively. To expand upon pathologically derived differences in brain structure observed in *tlr2*$^{-/-}$ zebrafish, brain volumes were estimated utilizing 3D DTI data. The zebrafish brain was divided into its main regions[29,30]; the olfactory bulb (OB), pallium (Pa), diencephalon (DC), mesencephalon (MC), cerebellum (CB), and rhombencephalon (RC) (Figure 3.1B). In *tlr2*$^{-/-}$ zebrafish, a significant increase in the volume of the CB and RC was observed ($p < 0.05$, $n = 3$) compared to the control group. Our results demonstrate an increase in the cortical thickness and trend toward increased brain volume of the *tlr2*$^{-/-}$ zebrafish compared to the control group, while the differences in body length and weight between three-month old *tlr2*$^{-/-}$ and control zebrafish was negligible (data not shown). Previously, a significant reduction in the cortex thickness, in combination with white matter damage and neuronal loss was reported for TLR2 deficient mice[11]. In addition, *tlr2*$^{-/-}$ was associated with significantly reduced levels of insulin-like growth factor 1 (IGF-1), which has neuroprotective properties and plays an important role in neuronal viability and prevention of apoptosis[47]. While neurodegenerative disorders are typically linked to cortical thinning and reduced brain volumes in their advanced stages, it has been observed that cortical thickening and volumetric increase occur in the initial phases as a reaction to underlying pathological

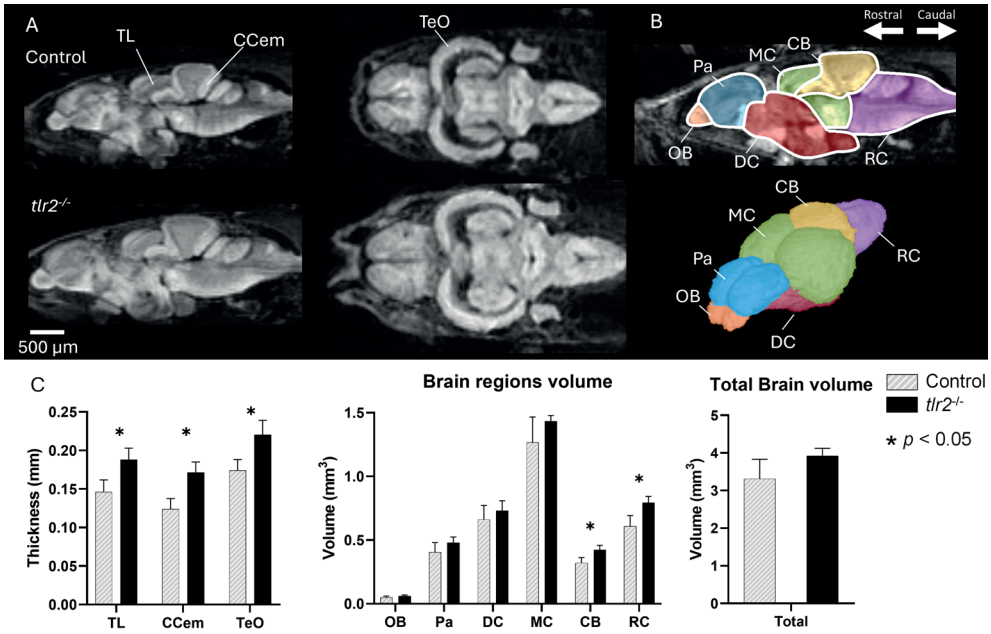

Figure 3.1. Comparison of brain structure and volume in tlr2$^{-/-}$ and control adult zebrafish. [A] *Representative sagittal and coronal slice of DTI of control and tlr2$^{-/-}$adult zebrafish obtained at 17.6 T.* ***[B]*** *2D and 3D representation of the zebrafish brain, divided into its main regions, providing a comprehensive view of its anatomical organisation.* ***[C]*** *Comparison of the cortical thickness of the longitudinal torus (TL), molecular layer of the cerebellar corpus (CCem), and optic tectum (TeO) shows a significant increase in tlr2$^{-/-}$ zebrafish compared to control. Furthermore, a significant increase in the volume of the cerebellum (CB) and rhombencephalon (RC) were observed. In all other brain region, as for the total brain volume, a similar trend is observed, albeit non-significantly ($p > 0.05$). Acquisition details: TR = 2000 ms, TE = 9 ms, ns = 4, isotropic resolution 35 µm, effective b-value range 100, 1000, or 2500 s/mm^2, with 4, 12 or 24 diffusion-encoding directions respectively. TL – Longitudinal torus; CCem – Cerebellar corpus, molecular layer; OB – Olfactory bulb; Pa – Pallium; DC – Diencephalon; MC – Mesencephalon; CB – Cerebellum; RC – Rhombencephalon. Statistical analysis was performed using the unpaired t-test, assuming Gaussian distribution, with $p < 0.05$ considered to imply significant differences between the control and tlr2$^{-/-}$ group.*

processes[48,49]. The observed increase in cortical thickness could be an early indicator of neurodegenerative processes associated with TLR2 deficiency. Furthermore, increase brain volume may be associated with swelling of the brain due to cerebral edema, *i.e.* the abnormal swelling of brain cells by accumulation of fluid. Previous studies in *tlr2$^{-/-}$* mice have shown hypoperfusion in the brain that could indirectly signify cytotoxic edema[50]. A longitudinal study, outside the scope of the current work, would be required to provide more insight in the development of changes in cortical thickness and brain volume of *tlr2$^{-/-}$* zebrafish.

T_2 and ADC changes underpinning cytotoxic edema and astrogliosis in tlr2$^{-/-}$ brain.

To zoom into microstructural changes in the zebrafish brain, we utilized T_2 and *ADC* estimation. Previously, quantitative T_2 and *ADC* measurements were used for evaluation of normal and affected brain tissue, including regular ageing, strokes, tumours, and neurodegenerative diseases[51-58]. In this study, prior to conducting T_2 measurements, we examined the potential influence of magnetic field disturbances on estimated T_2 by investigating the impact of the CPMG refocusing pulse interval, as described previously[51]. The influence of pulse intervals between 6 to 18 ms on brain T_2 was negligible (see Supplementary Figure S3.3.), suggesting insignificant impact of magnetic field disturbances on estimated T_2. In addition, the differences in T_2 times between single-slice MSME and multi-slice MSME were also negligible (see Supplementary Figure S3.3.), highlighting a minimal influence of magnetization transfer-related bias of the water signal[59]. Figure 3.2 shows T_2 and *ADC* changes in six areas in control and *tlr2$^{-/-}$* zebrafish brain. ROIs were selected in various brain regions; the granular layer of the cerebellar corpus (CCeg), the CCem, the TL, the medial longitudinal torus (MLF), the diffusive nucleus of the inferior lobe (DIL), and the medial zone of the dorsal telencephalon (DM). An overall increase in the T_2 relaxation time was observed in all selected brain regions of the *tlr2$^{-/-}$* zebrafish brain (Figure 3.2B) ranging between 17% in the DM and 28% in the CGeg. Complementary, *ADC* analysis showed a significant reduction of the diffusivity in the CCeg, CCem, and DM by 42%, 39%, and 23%, respectively. Other ROIs showed a similar trend towards reduced diffusivity. The elevation in T_2, coupled with the reduction in *ADC* could be an indication of elevated astrogliosis and astroglia scarring[60,61], as documented in earlier studies for *tlr2$^{-/-}$* mice[62]. Moreover, in contrast to vasogenic edema which exhibits significant increases in diffusivity, cytotoxic edema results in restricted diffusion and reduced *ADC*[63,64], most profoundly occurring in astrocytes[65]. An increase in potential biomarkers of edema such as aquaporin 4 (AQP4), that regulate brain water and CSF water movement, have been detected in models of neurodegeneration disease [21]. It is intriguing that an increase in cortical thickness in asymptomatic mutation carriers was reported along with a substantial reduction in the mean diffusivity, almost a decade prior to the predicted clinical onset[48], a finding that parallels the alterations in cerebral volume and reduced diffusivity in the current study. In the present work, zebrafish were subjected to formalin fixation to mitigate degradation processes during analysis. In this context, it is noteworthy to acknowledge that formalin fixation might affect T_2 and diffusion characteristics as compared to *in vivo* situation[20,66]. Nevertheless, to get relevant comparison between fixed control and *tlr2$^{-/-}$* fish, we follow strictly same fixation protocol for both groups. Moreover, formalin fixation shortens T_1 relaxation times, allowing for the use of shorter repetition times compared to those required *in vivo*. This poses a valid challenge when translating our methods for *in vivo* measurements, as longer repetition times would be required, consequently extending total scan times further.

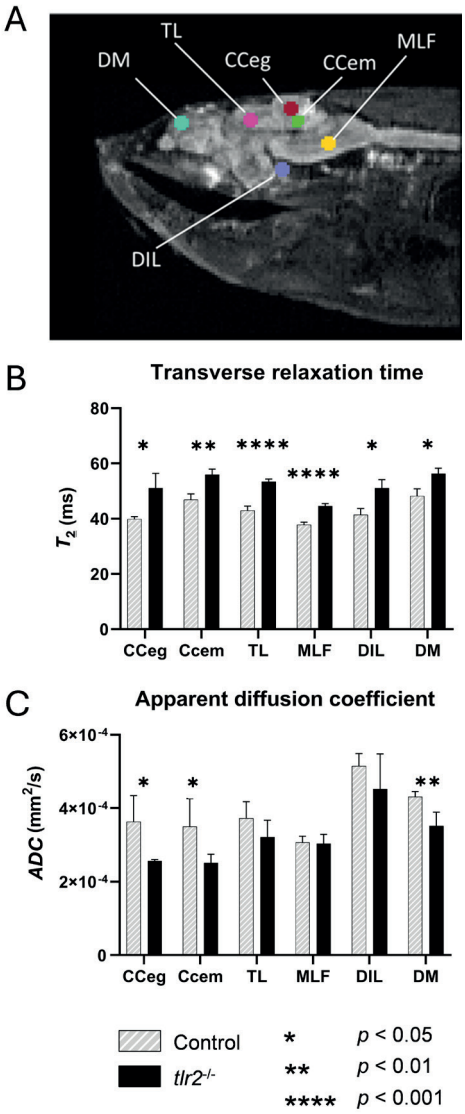

Figure 3.2. T_2 relaxation time and ADC measurement in various brain regions of control and tlr2 mutant (tlr2$^{-/-}$) zebrafish. [A] *Anatomical DWI image (b = 1000 s/mm^2), sagittal slice, showing ROIs used for T_2 and ADC estimation.* ***[B]*** *Estimated T_2 relaxation times in selected ROIs of control and tlr2$^{-/-}$ zebrafish.* ***[C]*** *Estimated ADC in selected ROIs of control and tlr2$^{-/-}$ zebrafish. Acquisition details MSME: TR = 3000, τ = 6.0 ms, ns = 4, resolution 47 × 47 µm, and a slice thickness 500 µm. DWI: TR = 1000 ms, TE = 13 ms, ns = 4, resolution 47 × 47 µm, slice thickness 200 µm, effective b-value range 50, 500, 1000, 1500, 2000, 2500, or 3000 s/mm^2. Statistical analysis was performed using the unpaired t-test, assuming Gaussian distributions, with $p < 0.05$ considered to imply significant differences between the control and tlr2$^{-/-}$ group. * $p < 0.05$, ** $p < 0.01$, **** $p < 0.001$. DM – Medial zone of dorsal telencephalon; TL – Longitudinal torus; Cceg – Granular layer of the cerebellar corpus; Ccem – Molecular layer of the cerebellar corpus; MLF – Medial longitudinal fascicle; DIL – Diffuse nucleus of the inferior lobe.*

Phasor-based multi-component analysis reveals restricted diffusivity in tlr2$^{-/-}$ zebrafish brain.

To obtain further insight in the nature of the observed reduced diffusivity, multi-component analysis of exponential *ADC* decay curves was performed by the phasor approach[67]. *ADC* is influenced by the mobility of water molecules in different tissue compartments, with each compartment exhibiting distinct *ADC* components. Several studies have shown bi-exponential diffusion decay in the brain, characterised by slow and fast diffusion compartments[68-70]. In this context, the slow diffusion component represents compartments within the brain that exhibit hindered diffusion, while the fast diffusion component represents compartments with relatively unrestricted diffusion. Although it has been suggested that these compartments represent intracellular and extracellular populations, there is evidence indicating that both compartments partly originate from the intracellular space[70]. The current work refers to these compartments as slow and fast diffusion components rather than intracellular and extracellular diffusivity. Here, we chose the CCem structure as our prime example for conducting a multi-component *ADC* analysis due to its notable alterations in T_2 and *ADC*. In this context, our emphasis was on exploring the multi-component characteristics of the *ADC* signal within affected brain tissue in *tlr2$^{-/-}$* zebrafish. Multi-component analysis of the *ADC* decay curve was conducted employing the phasor approach (Figure 3.3). Phasor data from the CCem of *tlr2$^{-/-}$* and control zebrafish brain demonstrated nearly complete separation (Figure 3.3A), indicating significant differences in the *ADC* of both groups. Figure 3.3B displays the mono-component analysis of *ADC* value changes in the CCem of *tlr2$^{-/-}$* showing that the *ADC* of *tlr2$^{-/-}$* was significantly reduced compared to the control group, which is well in line with the results of fitting by the non-linear least square algorithm discussed in Figure 3.2. The shape of the phasor data, fully separated from the semi-circle, indicates a bi-component system with a slow ($0 < ADC_{slow} < 4 \cdot 10^{-4}$ mm^2/s) and a fast ($4 \cdot 10^{-4} < ADC_{fast} < 1 \cdot 10^{-3}$ mm^2/s) *ADC* component. The phasor plot coordinates of the CCem were fitted to bi-component *ADC* systems, based on the bi-exponential fit function [Eq.3]. Mean ADC_{slow} and ADC_{fast} found for the CCem of *tlr2$^{-/-}$* and control zebrafish by the phasor approach, as well as their area (%) are summarised in Figure 3.3C-E. The bi-component analysis showed a significant reduction in the absolute value of ADC_{fast}, and a substantial increase in the area of ADC_{slow}. These findings imply diffusivity in the CCem of *tlr2$^{-/-}$* zebrafish is primarily influenced by slow diffusion compartments, to a greater extent than observed in the control group. In addition, they point to microstructural changes occurring within the fast diffusivity compartments. Various biological processes could lead to restricted diffusion. Among these, astrogliosis, cytotoxic edema and inflammatory processes have been previously reported for *tlr2$^{-/-}$* models, although conflicting reports are available for pro-inflammatory processes in TLR2 deficiency[71,72]. In the current work, we applied very short diffusion encoding times which facilitated exploration of water diffusion over very short distances (micrometre regime), reducing the influence of potential interaction occurring during

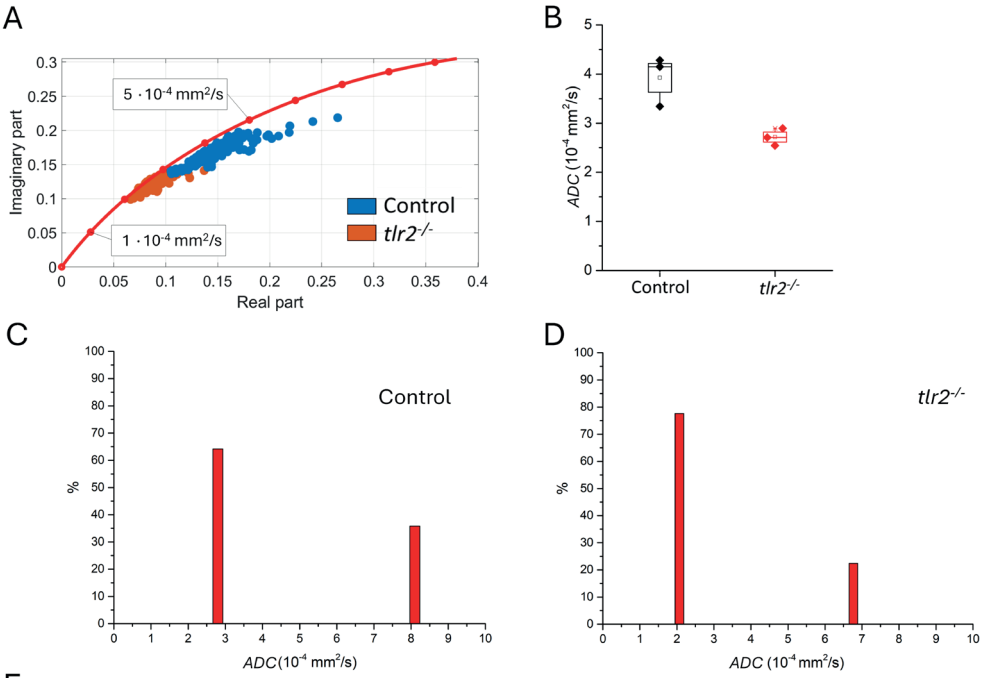

E

	Control		*tlr2*$^{-/-}$	
	ADC · 10^{-4} (mm^2/s)	Area (%)	*ADC* · 10^{-4} (mm^2/s)	Area (%)
Slow component	2.8 ± 0.2	64.2 ± 2.4	2.1 ± 0.0	77.6 ± 2.4*
Fast component	8.1 ± 0.3	35.8 ± 2.4	6.8 ± 0.2*	22.4 ± 2.4*
R^2 of fit	0.9992		0.9993	

Figure 3.3. Phasor analysis of the experimental ADC curves. [A] *Phasor plot of the molecular layer of the cerebellar corpus (Ccem) of tlr2*$^{-/-}$ *and control, relative to the phasor plot semi-circle (red). On the semi-circle, 0 mm*^{2}*/s is located at [0,0], with steps of 1·10*$^{-4}$ *mm*^{2}*/s indicated as red dots on the semi-circle.* ***[B]*** *Mono-component analysis shows the ADC in tlr2*$^{-/-}$ *is significantly reduced, while multi-component analysis of the ADC decay curve in the Ccem* ***[C-E]*** *shows a significant increase in the area of the slow diffusion component in tlr2*$^{-/-}$*, associated with restricted diffusion. Acquisition details DWI used for phasor plot analysis: TR = 1000 ms, TE = 13 ms, ns = 4, resolution 47 × 47 µm, slice thickness 200 µm, effective b-value range 50, 500, 1000, 1500, 2000, 2500, or 3000 s/mm*^{2}*. Statistical analysis was performed using the unpaired t-test, assuming Gaussian distribution, with* $p < 0.05$ *considered to imply significant differences between the control and tlr2*$^{-/-}$ *group. * p < 0.05.*

the application of longer diffusion times[73]. The spatial regime achieved in our work may not be currently feasible with clinical system due to lack of strong field gradients.

DTI and DKI analysis reveal diminished diffusivity and enhanced kurtosis in tlr2$^{-/-}$ brain.
To further evaluate potential alterations in the microstructure in *tlr2$^{-/-}$* zebrafish brain, DTI was utilized. DTI expands upon traditional dMRI. It enhances the understanding of structural characteristics by utilizing the effects of anisotropic diffusion, accessed by measuring the diffusion-weighted MR signal in at least six different diffusion directions. These diffusion-weighted MR signals are translated into a diffusion tensor, represented as an ellipsoid model, of which the eigenvectors ($\boldsymbol{\varepsilon}_1$, $\boldsymbol{\varepsilon}_2$, $\boldsymbol{\varepsilon}_3$) and eigenvalues ($\lambda_1$, λ_2, λ_3) represent the principal axis frame of the diffusion tensor and the diffusivity, respectively. Here, the eigenvectors are arranged such that $\lambda_1 \geq \lambda_2 \geq \lambda_3$. In white matter structures, the diffusivity along the axons is the least restricted and represented by the largest principal eigenvalue, the axial diffusivity ($D_{\parallel}$, λ_1). The diffusivity perpendicular to the axons is represented by the average of the eigenvalues λ_2 and λ_3, the radial diffusivity ($D_{\perp}$). The mean diffusivity is estimated as the average intensity of the three eigenvectors (*MD*). Finally, *FA* is used to estimate the extent of the directional preference of the diffusivity, where an *FA* of 0 indicated full isotropic diffusivity and an *FA* of 1 indicates full anisotropic diffusivity. In the current study, DTI data was used to generate $D_{\parallel}$, $D_{\perp}$, *MD*, and *FA* maps (Figure 3.4A) and estimate mean $D_{\parallel}$, $D_{\perp}$, *MD*, and *FA* of major brain regions (Figure 3.4C).

Differences in $D_{\parallel}$, $D_{\perp}$, and *MD* in the major brain region were found negligible, although a robust and consistent trend towards decreased $D_{\parallel}$, $D_{\perp}$, and *MD* was observed, aligning closely with the reduced *ADC* found by DWI and previous reports[10]. Notably, *FA* exhibited a significant reduction in the pallium and mesencephalon, in line with earlier observations for *tlr2$^{-/-}$* mice[11]. In other brain regions, a similar tendency towards reduced *FA* was consistently observed in *tlr2$^{-/-}$* zebrafish relative to the control group, albeit non-significant.

Further insight was obtained by employing DKI. DWI and DTI rely on the assumption that diffusivity follows a Gaussian distribution, thus simplifying the true complexity of diffusivity in the brain[74]. Considering these limitations, DKI is an extended dMRI technique for the characterisation of non-Gaussian diffusion, describing the kurtosis of the diffusion distribution. To quantify kurtosis, application of higher *b*-values is required as the diffusion signal is mostly influenced by Gaussian diffusion at lower *b*-values[75]. In our findings, we observe the emergence of kurtosis effects at *b*-values exceeding 2000 s/mm^2, and it is increasing at larger *b*-values (see Supplementary Figure S3.4.). DKI data was used to generate $K_{\parallel}$, $K_{\perp}$, *MK*, and *KFA* maps (Figure 3.4B) and estimate mean $K_{\parallel}$, $K_{\perp}$, *MK*, and *KFA* of major brain regions (Figure 3.4C). We observed a significant increase in $K_{\perp}$ in the rhombencephalon and cerebellum,

and a significant increase in the *MK* of the rhombencephalon of *tlr2*$^{-/-}$ zebrafish compared to the control group. Elevated diffusion kurtosis signify a greater departure from the Gaussian distribution of water molecule diffusion, suggesting an elevated degree of diffusion restriction. These findings are in full agreement with our mono- and multi-component analysis of the *ADC* signal, indicating strongly restricted diffusion.

In general, the diffusion metrics $D_{\parallel}$ and $D_{\perp}$ are indicative of myelin integrity and axonal damage, *MD* is associated with edema and proliferation of cells in neoplastic growth, and *FA* serves as a highly sensitive biomarker for assessing the integrity of white matter. In this context, diminished *FA* was related to loss of neurons, myelin swellings, and severe cytotoxic edema, and reduced *MD* were related to glial cell death and loss[76]. Regarding kurtosis metrics, $K_{\parallel}$ is particularly responsive to intracellular structures, whereas $K_{\perp}$ is influenced by alterations in cellular membranes and myelin layers. *MK*, on the other hand, is more broadly linked to the microstructural complexity of the brain. An increase in *MK* is may be associated with denser cell packing or greater cellular complexity, while a decrease in *MK* may be attributed to a loss of cellular structure[74]. Moreover, diffusion kurtosis metrics provides some advantages over diffusion tensor metrics for their increased sensitivity for isotropic grey matter[77].

Based on our findings in three-month old *tlr2*$^{-/-}$ zebrafish, when compared to a control group, we observed several changes in brain metrics. These include an increased in brain volume, strong T_2 signals, reduced *ADC*, restricted diffusivity, and alterations in various diffusion tensor and diffusion kurtosis metrics, such as diminished $D_{\parallel}$, $D_{\perp}$, *MD*, and *FA*, coupled with an increase in $K_{\parallel}$, $K_{\perp}$, *MK*. Demyelination is typically associated with increased $D_{\perp}$, unadjusted $D_{\parallel}$, reduced *FA*, and decreased $K_{\perp}$ and *MK*[78-80]. Reactive astrogliosis was previously found to lead to decreased $D_{\parallel}$, stable $D_{\perp}$, reduced *MD*, increased *FA*, and increased *MK*[81,82]. Our findings suggest axonal degeneration or cytotoxic edema within the analysed brain regions. For axonal degeneration, reduced $D_{\parallel}$, $D_{\perp}$, and *FA* were reported, with apparent increase of kurtosis[79,83-85]. A decrease in diffusivity ($D_{\parallel}$, $D_{\perp}$, *MD*), decrease in *FA*, and increase in kurtosis ($K_{\parallel}$, $K_{\perp}$, *MK*) was previously observed in early hypoxic-ischemic brain edema[86].

We conducted an examination to assess the impact of *b*-value dependency on the reliability of estimated diffusion tensor and diffusion kurtosis metrics. Our study extends previous research conducted in single and double shell DTI and DKI measurements[87], whereas we employed triple shell DTI and DKI at ultra-high magnetic field strengths (see Supplementary Figure S3.5.). Upon analysis, we observed the majority of diffusion tensor and diffusion kurtosis metrics did not exhibit a significant shift in response to significant changes in the *b*-value range. This suggests that the majority of diffusion tensor and diffusion kurtosis metrics, obtained at ultra-high magnetic fields and with four distinct *b*-values (b_0 included), are robust and

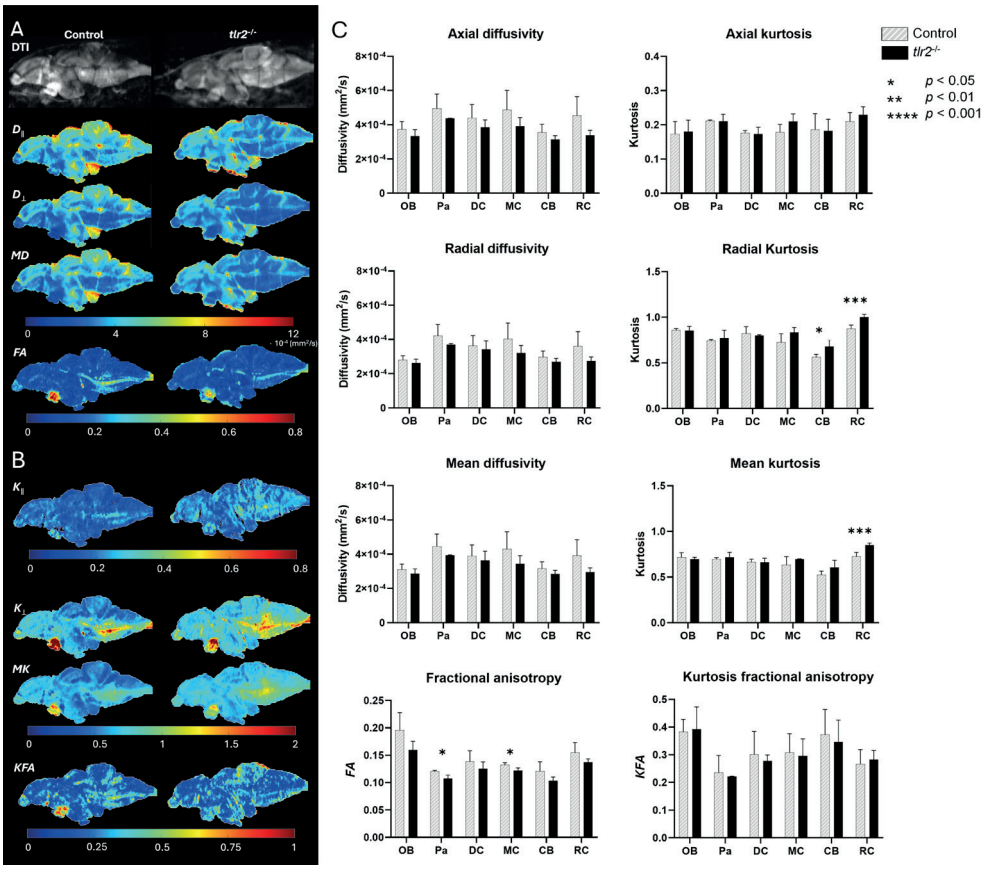

Figure 3.4. Comparison of DTI result in main brain regions of tlr2$^{-/-}$ and control adult zebrafish. *Representative central slice of DTI measurements of control and tlr2$^{-/-}$ adult zebrafish.* ***[A]*** *From these slices, the diffusion tensor metrics were estimated; $D_{\parallel}$, $D_{\perp}$, MD, and FA,* ***[B]*** *as well as the diffusion kurtosis metrics; $K_{\parallel}$, $K_{\perp}$, MK, and KFA.* ***[C]*** *DTI and DKI results of tlr2$^{-/-}$ adult zebrafish compared to controls reveals a noteworthy trend towards decreased $D_{\parallel}$, $D_{\perp}$, and MD, reduced FA, as well as increased $K_{\parallel}$, $K_{\perp}$, and MK. Additionally, a significant decrease in KFA is observed in the tlr2$^{-/-}$ group. Acquisition details: TR = 2000 ms, TE = 12.4 ms, ns = 32, resolution 25 µm × 25 µm × 200 µm, effective b-value range 4, 1000, 3500, or 6000 s/mm2, with 8, 12, 24, or 36 diffusion-encoding directions respectively. Statistical analysis was performed using the unpaired t-test, assuming Gaussian distribution, with $p < 0.05$ considered to imply significant differences between the control and tlr2$^{-/-}$ group. * $p < 0.05$, *** $p < 0.005$. OB – Olfactory bulb; Pa – Pallium; DC – Diencephalon; MC – Mesencephalon; CB – Cerebellum; RC – Rhombencephalon.*

relatively unaffected by variations in the *b*-value range. Based on these findings, we conclude future studies with somewhat similar *b*-value ranges may therefore find our data a valuable reference point.

Genomic deletion of TLR2 signifies compromised integrity in white matter tracks.
Subsequently, we investigated the effect of genomic deletion of TLR2 on white matter integrity in adult zebrafish by DTI. Seven white matter structures were identified and localized in the zebrafish brain using dMRI tractography by stTDI CSD (Figure 3.5A); the posterior commissure (Cpost), the commissure of the secondary gustatory nuclei (Cgus), the ansulate commissure (Cans), the ventral rhombencephalic commissure (Cven), the medial longitudinal fascicle (MLF), the optic tract (OT), and the lateral longitudinal fascicle (LLF). The integrity of these white matter structures was monitored by comparing DTI and DKI metrics. Significantly lower $D_{\parallel}$, *MD* and *FA* were observed in the Cven of *tlr2*$^{-/-}$ zebrafish, along with increased $K_{\parallel}$, $K_{\perp}$, *MK*, and *FKA*. In the Cgus, we observed a significantly lower *FA* and increased $K_{\perp}$. In addition, the Cpost showed reduced $D_{\parallel}$ and *MD*, with increased $K_{\perp}$, the MLF showed increased $K_{\perp}$, and for the LLF reduced $D_{\parallel}$, $D_{\perp}$, and *MD*, in combination with increased $K_{\perp}$, and *MK* are reported. Overall, DTI and DKI data of white matter structures in *tlr2*$^{-/-}$ zebrafish shows a consistent trend of reduced diffusivity ($D_{\parallel}$, $D_{\perp}$, and *MD*) and *FA* across most white matter structures. Moreover, we observed a trend indicating increased kurtosis ($K_{\parallel}$, $K_{\perp}$, and *MK*) and *KFA* when compared to the control group. Previously, increased kurtosis, in combination with decreased diffusivity levels and reduced *FA*, have been attributed to microstructural changes in the brain. APP/PS1 Alzheimer's disease mouse models show a significant increase in kurtosis in the hippocampus, cortex and thalamus, linked to significant increase in amyloid beta (Aβ) plaque loads[88]. A longitudinal report of the same pathological model showed similar observations, including significant drops in *FA* in various brain regions[89]. It has been suggested that TLR2 plays a significant role in clearing toxic Aβ, shown in an APP Alzheimer's disease mouse model[90]. Another observation made in *tlr2*$^{-/-}$ mouse models was increased astrogliosis and demyelination in white matter structures[62]. On the other hand, cuprizone-induced demyelination and inflammation reduced $K_{\parallel}$, $K_{\perp}$, and *MK* in the cortex and corpus callosum[80], contrary to the observations in the current study. Increased mean kurtosis was reported as a potential biomarker of reactive astrogliosis, although the same report did not see any significant alterations in *FA* or *MD*[82].

Our analysis has revealed compelling evidence of a compromise in the integrity of various white matter structures within the brain of *tlr2*$^{-/-}$ zebrafish. The alterations of the neural architecture suggest a potential link to neurobehavioral changes observed in other *tlr2*$^{-/-}$ models. Here, we found evidence for microstructural changes in the Cven, a bundle of nerves carrying signals between the two halves of the hind brain. These signals originate from different parts of the brain, including the sensory area for touch and balance, as well as groups of cells related to sensing and moving[91]. Lampreys (*Lampetra fluviatilis*) with a transected Cven exhibited compromised spontaneous locomotion and altered movements[91], illustrating the role played by the Cven in orchestrating and regulating these motor behaviours. These observations are consistent with the diminished spontaneous activity observed in *tlr2*$^{-/-}$

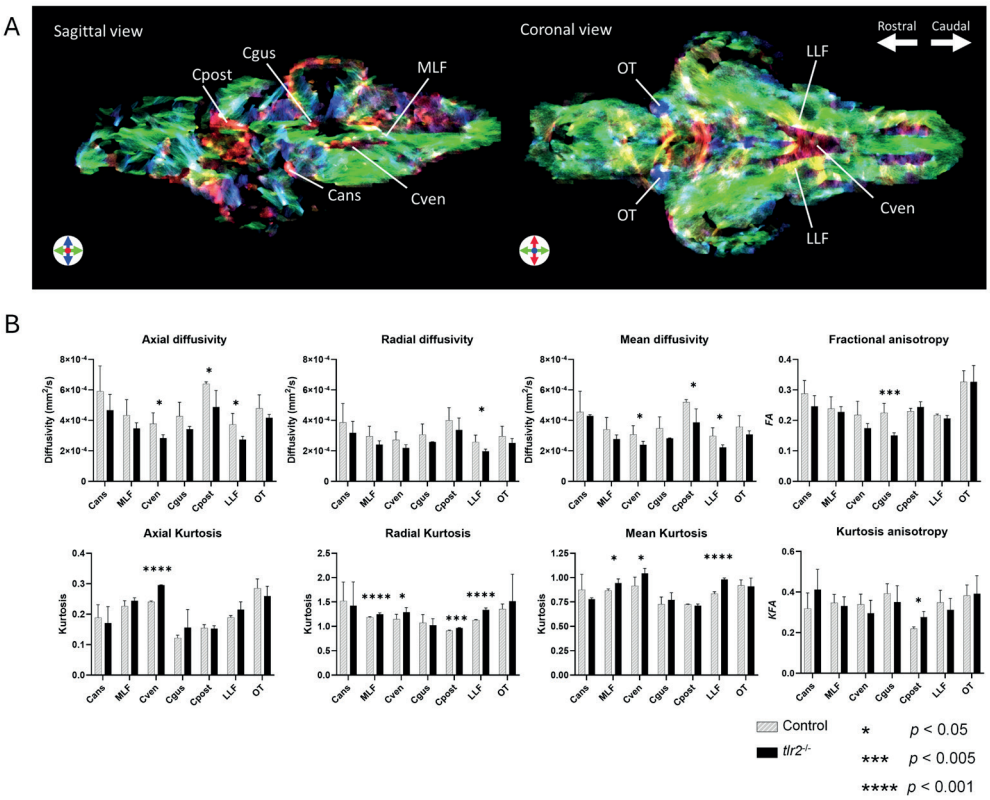

Figure 3.5. Comparison of DTI results of white matter structures of tlr2$^{-/-}$ and control adult zebrafish. [A] *Sagittal and coronal slice of DEC stTDI msmt-CSD map, used for the identification of white matter structures in the zebrafish brain. Acquisition details: TR = 2000 ms, TE = 9 ms, ns = 4, isotropic resolution 35 µm, effective b-value range 100, 1000, or 2500 s/mm^2, with 4, 12, or 24 diffusion-encoding directions respectively.* ***[B]*** *Diffusion metrics estimated by DTI results, show reduced $D_{\parallel}$, $D_{\perp}$, and MD, reduced FA, increased $K_{\parallel}$, $K_{\perp}$, and MK and KFA anisotropy in white matter structures in the tlr2$^{-/-}$ zebrafish brain. Acquisition details: TR= 2000 ms, TE = 12.4 ms, ns = 32, resolution 25 µm × 25 µm × 200 µm, effective b-value range 4, 1000, 3500, or 6000 s/mm2, with 8, 12, 24, or 36 diffusion-encoding directions respectively. Cpost – posterior commissure; Cgus – commissure of the secondary gustatory nuclei; Cans – ansulate commissure; Cven – ventral rhombencephalic commissure; MLF – medial longitudinal fascicle; OT – optic tract; LLF – lateral longitudinal fascicle. Statistical analysis was performed using the unpaired t-test, assuming Gaussian distribution, with p < 0.05 considered to imply significant differences between the control and tlr2$^{-/-}$ group. * p < 0.05, *** p < 0.005, **** p < 0.001.*

mice[11]. Our insight into microstructural alterations in the Cven of *tlr2*$^{-/-}$ zebrafish shed light on this phenomenon. Parallel to the Cven, the Cgus was found affected in *tlr2*$^{-/-}$ zebrafish. The Cgus is the neural pathway connecting the secondary gustatory nuclei present on both sides of the zebrafish brain, which are involved in processing taste-related information as part of the gustatory system[92]. Our observations in microstructural changes in the Cgus could contribute to explaining previous observations in *tlr2*$^{-/-}$ mice, showing diminished food consumption[93], as disrupted communication with the secondary gustatory nuclei might lead to difficulties in processing and perceiving taste sensation. The Cpost is a diencephalic nerve bundle, involved in facilitating communication with the pretectal nuclei[30], involved in visual processing, circadian rhythms and motor control[94]. Previous studies showed disrupted circadian rhythms in *tlr2*$^{-/-}$ mice[93], to which our observations might provide further insight.

4. CONCLUSION AND FUTURE OUTLOOK

In summary, our study unveils the impact of genomic TLR2 deletion in zebrafish, leading to microstructural alterations within diverse brain tissues. Applying dMRI at ultra-high magnetic fields provided the necessary SNR and contrast that has enabled us to discriminate and characterise major brain regions as well as specific white matter structures, thereby unravelling the microstructural changes associated with *tlr2*$^{-/-}$ zebrafish. Distinct dMRI techniques provided a diverse array of diffusion metrics, each offering a unique perspective into the architectural framework and transformations occurring in the pathological model. Notably, our study showed significant changes in the diffusivity and kurtosis profiles of multiple white matter structures, which mirror neurobehavioral shifts observed in *tlr2*$^{-/-}$ models. These findings contribute an additional layer of insight to improve our understanding of the origin of these behavioural changes.

In future, to extrapolate our results to a broader context, research should prioritize replicating these findings with a larger sample size, encompassing both male and female zebrafish across various age groups, including older fish. This approach will facilitate more robust statistical analyses and thorough exploration of potential variables and interactions. Furthermore, techniques such as histological staining and spectroscopic methods including localized spectroscopy and high-resolution magic angle spinning, could offer further insight towards increased understanding of the precise microstructural and metabolic changes in the brain of *tlr2*$^{-/-}$ models. In essence, our research provides insight on the relation between TLR2 and the microstructural architecture of the brain. Especially, our utilization of diffusion MRI at ultra-high magnetic fields signifies a substantial advancement, finally providing the required foundation for investigating these relationships in the tiny zebrafish brain.

ACKNOWLEDGEMENTS

Experiments at the 17.6 T instrument were supported by the uNMR-NL Grid: A distributed, state-of-the-art Magnetic Resonance facility for the Netherlands (NWO grant 184.032.207). The authors thank Karthick Sai Sankar Gupta, Fons Lefeber, and Maria Nardella for technical help provided at the 17.6 T instrument, and Volker Lehmann, Antonios Papaioannou, and Thomas Oerther from Bruker for help troubleshooting and their assistance during the experimental design.

REFERENCES

1 Li, D. & Wu, M. Pattern recognition receptors in health and diseases. *Signal Transduct Target Ther* **6**, 291 (2021). https://doi.org/10.1038/s41392-021-00687-0

2 Hu, W. & Spaink, H. P. The Role of TLR2 in Infectious Diseases Caused by Mycobacteria: From Cell Biology to Therapeutic Target. *Biology (Basel)* **11** (2022). https://doi.org/10.3390/biology11020246

3 Sameer, A. S. & Nissar, S. Toll-Like Receptors (TLRs): Structure, Functions, Signaling, and Role of Their Polymorphisms in Colorectal Cancer Susceptibility. *Biomed Res Int* **2021**, 1157023 (2021). https://doi.org/10.1155/2021/1157023

4 Behzadi, P., Garcia-Perdomo, H. A. & Karpinski, T. M. Toll-Like Receptors: General Molecular and Structural Biology. *J Immunol Res* **2021**, 9914854 (2021). https://doi.org/10.1155/2021/9914854

5 Meijer, A. H. *et al.* Expression analysis of the Toll-like receptor and TIR domain adaptor families of zebrafish. *Mol Immunol* **40**, 773-783 (2004). https://doi.org/10.1016/j.molimm.2003.10.003

6 Oliveira-Nascimento, L., Massari, P. & Wetzler, L. M. The Role of TLR2 in Infection and Immunity. *Front Immunol* **3**, 79 (2012). https://doi.org/10.3389/fimmu.2012.00079

7 Dasu, M. R. *et al.* TLR2 expression and signaling-dependent inflammation impair wound healing in diabetic mice. *Lab Invest* **90**, 1628-1636 (2010). https://doi.org/10.1038/labinvest.2010.158

8 Marks, K. E., Cho, K., Stickling, C. & Reynolds, J. M. Toll-like Receptor 2 in Autoimmune Inflammation. *Immune Netw* **21**, e18 (2021). https://doi.org/10.4110/in.2021.21.e18

9 Pascual, M. *et al.* Toll-like receptors in neuroinflammation, neurodegeneration, and alcohol-induced brain damage. *IUBMB Life* **73**, 900-915 (2021). https://doi.org/10.1002/iub.2510

10 McDonald, C. L. *et al.* Inhibiting TLR2 activation attenuates amyloid accumulation and glial activation in a mouse model of Alzheimer's disease. *Brain Behav Immun* **58**, 191-200 (2016). https://doi.org/10.1016/j.bbi.2016.07.143

11 Zhou, C. *et al.* Genomic deletion of TLR2 induces aggravated white matter damage and deteriorated neurobehavioral functionsin mouse models of Alzheimer's disease. *Aging* **11** (2019). https://doi.org/10.18632/aging.102260

12 Hu, Y. *et al.* Toll-like receptor-2 gene knockout results in neurobehavioral dysfunctions and multiple brain structural and functional abnormalities in mice. *Brain Behav Immun* **91**, 257-266 (2021). https://doi.org/10.1016/j.bbi.2020.10.004

13 van Schadewijk, R. *et al.* Magnetic Resonance Microscopy at Cellular Resolution and Localised Spectroscopy of Medicago truncatula at 22.3 Tesla. *Sci Rep* **10**, 971 (2020). https://doi.org/10.1038/s41598-020-57861-7

14 Kabli, S., Alia, A., Spaink, H. P., Verbeek, F. J. & De Groot, H. J. Magnetic resonance microscopy of the adult zebrafish. *Zebrafish* **3**, 431-439 (2006). https://doi.org/10.1089/zeb.2006.3.431

15 Kabli, S., Spaink, H. P., De Groot, H. J. & Alia, A. In vivo metabolite profile of adult zebrafish brain obtained by high-resolution localized magnetic resonance spectroscopy. *J Magn Reson Imaging* **29**, 275-281 (2009). https://doi.org/10.1002/jmri.21609

16 Haud, N. *et al.* rnaset2 mutant zebrafish model familial cystic leukoencephalopathy and reveal a role for RNase T2 in degrading ribosomal RNA. *Proc Natl Acad Sci U S A* **108**, 1099-1103 (2011). https://doi.org/10.1073/pnas.1009811107

17 Ramirez, I. B. *et al.* Impaired neural development in a zebrafish model for Lowe syndrome. *Hum Mol Genet* **21**, 1744-1759 (2012). https://doi.org/10.1093/hmg/ddr608

18 Kabli, S. *et al.* In vivo magnetic resonance imaging to detect malignant melanoma in adult zebrafish. *Zebrafish* **7**, 143-148 (2010). https://doi.org/10.1089/zeb.2009.0649

19 Eeza, M. N. H. *et al.* Probing microstructural changes in muscles of leptin-deficient zebrafish by non-invasive ex-vivo magnetic resonance microimaging. *PLoS One* **18**, e0284215 (2023). https://doi.org/10.1371/journal.pone.0284215

20 Hamilton, N., Allen, C. & Reynolds, S. Longitudinal MRI brain studies in live adult zebrafish. *NMR Biomed* **36**, e4891 (2023). https://doi.org/10.1002/nbm.4891

21 Gatto, R. G. *et al.* Ultra-High Field Diffusion MRI Reveals Early Axonal Pathology in Spinal Cord of ALS mice. *Transl Neurodegener* **7**, 20 (2018). https://doi.org/10.1186/s40035-018-0122-z

22 Gatto, R. G. & Wu, Y. C. Editorial: Innovative Imaging Techniques in Preclinical Models of Neurodegenerative Diseases. *Front Neurosci* **15**, 801037 (2021). https://doi.org/10.3389/fnins.2021.801037

23 Ullmann, J. F., Calamante, F., Collin, S. P., Reutens, D. C. & Kurniawan, N. D. Enhanced characterization of the zebrafish brain as revealed by super-resolution track-density imaging. *Brain Struct Funct* **220**, 457-468 (2015). https://doi.org/10.1007/s00429-013-0667-7

24 Hu, W. *et al.* Infection and RNA-seq analysis of a zebrafish tlr2 mutant shows a broad function of this toll-like receptor in transcriptional and metabolic control and defense to Mycobacterium marinum infection. *BMC Genomics* **20**, 878 (2019). https://doi.org/10.1186/s12864-019-6265-1

25 Hu, W. *et al.* A Novel Function of TLR2 and MyD88 in the Regulation of Leukocyte Cell Migration Behavior During Wounding in Zebrafish Larvae. *Front Cell Dev Biol* **9**, 624571 (2021). https://doi.org/10.3389/fcell.2021.624571

26 Iglesias, J. E. *et al.* Effect of Fluorinert on the Histological Properties of Formalin-Fixed Human Brain Tissue. *J Neuropathol Exp Neurol* **77**, 1085-1090 (2018). https://doi.org/10.1093/jnen/nly098

27 Carr, H. Y. & Purcell, E. M. Effects of Diffusion on Free Precession in Nuclear Magnetic Resonance Experiments. *Physical Review* **94**, 630-638 (1954). https://doi.org/10.1103/PhysRev.94.630

28 Stejskal, E. O. & Tanner, J. E. Spin Diffusion Measurements: Spin Echoes in the Presence of a Time-Dependent Field Gradient. *The Journal of Chemical Physics* **42**, 288-292 (1965). https://doi.org/10.1063/1.1695690

29 Kenney, J. W. *et al. A 3D adult zebrafish brain atlas (AZBA) for the digital age*, <http://azba.wayne.edu/> (2021).

30 Wullimann, M. F., Rupp, B. & Reichert, H. *Neuroanatomy of the zebrafish brain A topological atlas*. (1996).

31 Haynes, E. M., Ulland, T. K. & Eliceiri, K. W. A Model of Discovery: The Role of Imaging Established and Emerging Non-mammalian Models in Neuroscience. *Front Mol Neurosci* **15**, 867010 (2022). https://doi.org/10.3389/fnmol.2022.867010

32 read_2dseq :Quickly Reads Bruker's 2dseq MRI Images v. 1.0.1 (Mathworks, MATLAB Central File Exchange, 2020).

33 Milford, D., Rosbach, N., Bendszus, M. & Heiland, S. Mono-Exponential Fitting in T2-Relaxometry: Relevance of Offset and First Echo. *PLoS One* **10**, e0145255 (2015). https://doi.org/10.1371/journal.pone.0145255

34 Tournier, J. D. *et al.* MRtrix3: A fast, flexible and open software framework for medical image processing and visualisation. *Neuroimage* **202**, 116137 (2019). https://doi.org/10.1016/j.neuroimage.2019.116137

35 Kellner, E., Dhital, B., Kiselev, V. G. & Reisert, M. Gibbs-ringing artifact removal based on local subvoxel-shifts. *Magn Reson Med* **76**, 1574-1581 (2016). https://doi.org/10.1002/mrm.26054

36 Veraart, J., Fieremans, E. & Novikov, D. S. Diffusion MRI noise mapping using random matrix theory. *Magn Reson Med* **76**, 1582-1593 (2016). https://doi.org/10.1002/mrm.26059

37 Collier, Q. *Robust estimation of diffusion tensor and diffusion kurtosis imagingparameters* PhD thesis, Universiteit Antwerpen, (2018).

38 Basser, P. J., Mattiello, J. & Lebihan, D. Estimation of the Effective Self-Diffusion Tensor from the NMR Spin Echo. *Journal of Magnetic Resonance* **B**, 8 (1994). https://doi.org/https://doi.org/10.1006/jmrb.1994.1037.

39 Veraart, J., Sijbers, J., Sunaert, S., Leemans, A. & Jeurissen, B. Weighted linear least squares estimation of diffusion MRI parameters: strengths, limitations, and pitfalls. *Neuroimage* **81**, 335-346 (2013). https://doi.org/10.1016/j.neuroimage.2013.05.028

40 Hansen, B. & Jespersen, S. N. Kurtosis fractional anisotropy, its contrast and estimation by proxy. *Sci Rep* **6**, 23999 (2016). https://doi.org/10.1038/srep23999

41 Tabesh, A., Jensen, J. H., Ardekani, B. A. & Helpern, J. A. Estimation of tensors and tensor-derived measures in diffusional kurtosis imaging. *Magn Reson Med* **65**, 823-836 (2011). https://doi.org/10.1002/mrm.22655

42 Hansen, B. & Jespersen, S. N. Recent Developments in Fast Kurtosis Imaging. *Frontiers in Physics* **5** (2017). https://doi.org/10.3389/fphy.2017.00040

43 Dhollander, T., Raffelt, D., Mito, R. & Connelly, A. Improved white matter response function estimation for 3-tissue constrained spherical deconvolution. *Conference Paper* (2019).

44 Jeurissen, B., Tournier, J. D., Dhollander, T., Connelly, A. & Sijbers, J. Multi-tissue constrained spherical deconvolution for improved analysis of multi-shell diffusion MRI data. *Neuroimage* **103**, 411-426 (2014). https://doi.org/10.1016/j.neuroimage.2014.07.061

45 Tournier, J. D., Calamante, F. & Connelly, A. MRtrix: Diffusion tractography in crossing fiber regions. *International Journal of Imaging Systems and Technology* **22**, 53-66 (2012). https://doi.org/10.1002/ima.22005

46 Calamante, F., Tournier, J. D., Jackson, G. D. & Connelly, A. Track-density imaging (TDI): super-resolution white matter imaging using whole-brain track-density mapping. *Neuroimage* **53**, 1233-1243 (2010). https://doi.org/10.1016/j.neuroimage.2010.07.024

47 Bohacek, I. *et al.* Toll-like receptor 2 deficiency leads to delayed exacerbation of ischemic injury. *Journal of Neuroinflammation* **9**, 17 (2012). https://doi.org/https://doi.org/10.1186/1742-2094-9-191

48 Fortea, J. *et al.* Increased cortical thickness and caudate volume precede atrophy in PSEN1 mutation carriers. *J Alzheimers Dis* **22**, 909-922 (2010). https://doi.org/10.3233/JAD-2010-100678

49 Espeseth, T. *et al.* Accelerated age-related cortical thinning in healthy carriers of apolipoprotein E epsilon 4. *Neurobiol Aging* **29**, 329-340 (2008). https://doi.org/10.1016/j.neurobiolaging.2006.10.030

50 Kang, K. *et al.* Abnormal cortical thickening and thinning in idiopathic normal-pressure hydrocephalus. *Sci Rep* **10**, 21213 (2020). https://doi.org/10.1038/s41598-020-78067-x

51 Roy, U. *et al.* Degeneration of the suprachiasmatic nucleus in an Alzheimer's disease mouse model monitored by in vivo magnetic resonance relaxation measurements and immunohistochemistry. *J Alzheimers Dis* **69**, 363-375 (2019). https://doi.org/10.3233/JAD-190037

52 Kara, F. *et al.* In vivo measurement of transverse relaxation time in the mouse brain at 17.6 T. *Magn Reson Med* **70**, 985-993 (2013). https://doi.org/10.1002/mrm.24533

53 Ndengera, M. *et al.* Relaxation time of brain tissue in the elderly assessed by synthetic MRI. *Brain Behav* **12**, e2449 (2022). https://doi.org/10.1002/brb3.2449

54 Gideon, P., Thomsen, C. & Henriksen, O. Increased self-diffusion of brain water in normal aging. *J Magn Reson Imaging* **4**, 185-188 (1994). https://doi.org/10.1002/jmri.1880040216

55 Knight, M. J. *et al.* Determining T2 relaxation time and stroke onset relationship in ischaemic stroke within apparent diffusion coefficient-defined lesions. A user-independent method for quantifying the impact of stroke in the human brain. *Biomed Spectrosc Imaging* **8**, 11-28 (2019). https://doi.org/10.3233/bsi-190185

56 McGarry, B. L. *et al.* A Comparison of T(2) Relaxation-Based MRI Stroke Timing Methods in Hyperacute Ischemic Stroke Patients: A Pilot Study. *J Cent Nerv Syst Dis* **12**, 1179573520943314 (2020). https://doi.org/10.1177/1179573520943314

57 Chatel, M., Darcel, F., Certaines de, J., Benoist, L. & Bernard, A. M. T1 and T2 Proton Nuclear Magnetic Resonance (N.M.R.) relaxation times in vitro and human intracranial tumours *Journal of Neuro-Oncology* **3**, 7 (1986).

58 Maier, S. E., Sun, Y. & Mulkern, R. V. Diffusion imaging of brain tumors. *NMR Biomed* **23**, 849-864 (2010). https://doi.org/10.1002/nbm.1544

59 Radunsky, D. *et al.* Analysis of magnetization transfer (MT) influence on quantitative mapping of T(2) relaxation time. *Magn Reson Med* **82**, 145-158 (2019). https://doi.org/10.1002/mrm.27704

60 Lee, D. *et al.* Longer T(2) relaxation time is a marker of hypothalamic gliosis in mice with diet-induced obesity. *Am J Physiol Endocrinol Metab* **304**, E1245-1250 (2013). https://doi.org/10.1152/ajpendo.00020.2013

61 Schroeter, M., Franke, C., Stoll, G. & Hoehn, M. Dynamic changes of magnetic resonance imaging abnormalities in relation to inflammation and glial responses after photothrombotic cerebral infarction in the rat brain. *Acta Neuropathol* **101**, 114-122 (2001). https://doi.org/10.1007/s004010000262

62 Kigerl, K. A. *et al.* Toll-like receptor (TLR)-2 and TLR-4 regulate inflammation, gliosis, and myelin sparing after spinal cord injury. *J Neurochem* **102**, 37-50 (2007). https://doi.org/10.1111/j.1471-4159.2007.04524.x

63 Goyal, M., Sinha, S., Ravishankar, S. & Shivshankar, J. Case report: Reversible restricted diffusion and cytotoxic edema in the perilesional zone following continuous partial seizures. *Indian Journal of Radiology and Imaging* **18** (2008).

64 Koch, S., Rabinstein, A., Falcone, S. & Forteza, A. Diffusion-weighted Imaging Shows Cytotoxic and Vasogenic Edema in Eclampsia. *American Journal of Neuroradiology* **22** (2001).

65 Rosenblum, W. I. Cytotoxic Edema: Monitoring Its Magnitude and Contribution to Brain Swelling. *Journal of Neuropathology & Experimental Neurology* **66** (2007).

66 Shepherd, T. M., Thelwall, P. E., Stanisz, G. J. & Blackband, S. J. Aldehyde fixative solutions alter the water relaxation and diffusion properties of nervous tissue. *Magn Reson Med* **62**, 26-34 (2009). https://doi.org/10.1002/mrm.21977

67 Vergeldt, F. J. *et al.* Multi-component quantitative magnetic resonance imaging by phasor representation. *Sci Rep* **7**, 861 (2017). https://doi.org/10.1038/s41598-017-00864-8

68 Clark, C. A. & Le Bihan, D. Water diffusion compartmentation and anisotropy at high b values in the human brain. *Magnetic Resonance in Medicine* **44**, 852-859 (2000). https://doi.org/10.1002/1522-2594(200012)44:6<852::Aid-mrm5>3.0.Co;2-a

69 Mulkern, R. V. *et al.* Multi-component apparent diffusion coefficients in human brain. *NMR in Biomedicine* **12**, 51-62 (1999). https://doi.org/10.1002/(sici)1099-1492(199902)12:1<51::Aid-nbm546>3.0.Co;2-e

70 Sehy, J. V., Ackerman, J. J. & Neil, J. J. Evidence that both fast and slow water ADC components arise from intracellular space. *Magn Reson Med* **48**, 765-770 (2002). https://doi.org/10.1002/mrm.10301

71 Echchannaoui, H. *et al.* Toll-like receptor 2-deficient mice are highly susceptible to Streptococcus pneumoniae meningitis because of reduced bacterial clearing and enhanced inflammation. *J Infect Dis* **186**, 798-806 (2002). https://doi.org/10.1086/342845

72 Winters, L. *et al.* Expression analysis of genes involved in TLR2-related signaling pathway: Inflammation and apoptosis after ischemic brain injury. *Neuroscience* **238**, 87-96 (2013). https://doi.org/10.1016/j.neuroscience.2013.02.001

73 Pyatigorskaya, N., Le Bihan, D., Reynaud, O. & Ciobanu, L. Relationship between the diffusion time and the diffusion MRI signal observed at 17.2 Tesla in the healthy rat brain cortex. *Magn Reson Med* **72**, 492-500 (2014). https://doi.org/10.1002/mrm.24921

74 Steven, A. J., Zhuo, J. & Melhem, E. R. Diffusion kurtosis imaging: an emerging technique for evaluating the microstructural environment of the brain. *AJR Am J Roentgenol* **202**, W26-33 (2014). https://doi.org/10.2214/AJR.13.11365

75 Jensen, J. H., Helpern, J. A., Ramani, A., Lu, H. & Kaczynski, K. Diffusional kurtosis imaging: the quantification of non-gaussian water diffusion by means of magnetic resonance imaging. *Magn Reson Med* **53**, 1432-1440 (2005). https://doi.org/10.1002/mrm.20508

76 Lee, J. K. *et al.* Fractional anisotropy from diffusion tensor imaging correlates with acute astrocyte and myelin swelling in neonatal swine models of excitotoxic and hypoxic-ischemic brain injury. *J Comp Neurol* **529**, 2750-2770 (2021). https://doi.org/10.1002/cne.25121

77 Jensen, J. H. *et al.* Preliminary observations of increased diffusional kurtosis in human brain following recent cerebral infarction. *NMR Biomed* **24**, 452-457 (2011). https://doi.org/10.1002/nbm.1610

78 Song, S. K. *et al.* Dysmyelination revealed through MRI as increased radial (but unchanged axial) diffusion of water. *Neuroimage* **17**, 1429-1436 (2002). https://doi.org/10.1006/nimg.2002.1267

79 Andersen, K. W. *et al.* Disentangling white-matter damage from physiological fibre orientation dispersion in multiple sclerosis. *Brain Commun* **2**, fcaa077 (2020). https://doi.org/10.1093/braincomms/fcaa077

80 Guglielmetti, C. *et al.* Diffusion kurtosis imaging probes cortical alterations and white matter pathology following cuprizone induced demyelination and spontaneous remyelination. *Neuroimage* **125**, 363-377 (2016). https://doi.org/10.1016/j.neuroimage.2015.10.052

81 Budde, M. D., Janes, L., Gold, E., Turtzo, L. C. & Frank, J. A. The contribution of gliosis to diffusion tensor anisotropy and tractography following traumatic brain injury: validation in the rat using Fourier analysis of stained tissue sections. *Brain* **134**, 2248-2260 (2011). https://doi.org/10.1093/brain/awr161

82 Zhuo, J. *et al.* Diffusion kurtosis as an in vivo imaging marker for reactive astrogliosis in traumatic brain injury. *Neuroimage* **59**, 467-477 (2012). https://doi.org/10.1016/j.neuroimage.2011.07.050

83 Song, S.-K. *et al.* Diffusion tensor imaging detects and differentiates axon and myelin degeneration in mouse optic nerve after retinal ischemia,. *NeuroImage* **20**, 1714-1722 (2003). https://doi.org/10.1016/j.neuroimage.2003.07.005

84 Sun, S. W. *et al.* Differential sensitivity of in vivo and ex vivo diffusion tensor imaging to evolving optic nerve injury in mice with retinal ischemia. *Neuroimage* **32**, 1195-1204 (2006). https://doi.org/10.1016/j.neuroimage.2006.04.212

85 Sahin, S. *et al.* White Matter Evaluation in Multiple Sclerosis Through Magnetic Resonance Kurtosis Imaging. *Cureus* **11**, e6424 (2019). https://doi.org/10.7759/cureus.6424

86 Han, Y., Wu, P., Tian, J., Chen, H. & Yang, C. Diffusion kurtosis imaging and diffusion weighted imaging comparison in diagnosis of early hypoxic-ischemic brain edema. *Eur J Med Res* **28**, 159 (2023). https://doi.org/10.1186/s40001-023-01090-x

87 Veraart, J. *et al.* More accurate estimation of diffusion tensor parameters using diffusion Kurtosis imaging. *Magn Reson Med* **65**, 138-145 (2011). https://doi.org/10.1002/mrm.22603

88 Vanhoutte, G. *et al.* Diffusion kurtosis imaging to detect amyloidosis in an APP/PS1 mouse model for Alzheimer's disease. *Magn Reson Med* **69**, 1115-1121 (2013). https://doi.org/10.1002/mrm.24680

89 Praet, J. *et al.* Diffusion kurtosis imaging allows the early detection and longitudinal follow-up of amyloid-beta-induced pathology. *Alzheimers Res Ther* **10**, 1 (2018). https://doi.org/10.1186/s13195-017-0329-8

90 Richard, K. L., Filali, M., Prefontaine, P. & Rivest, S. Toll-like receptor 2 acts as a natural innate immune receptor to clear amyloid beta 1-42 and delay the cognitive decline in a mouse model of Alzheimer's disease. *J Neurosci* **28**, 5784-5793 (2008). https://doi.org/10.1523/JNEUROSCI.1146-08.2008

91 Ullén, F., Deliagina, T. G., Orlovsky, G. N. & Grillner, S. Visual Pathways for Postural Control and Negative Phototaxis inLamprey. *Journal of Neurophysiology* **78**, 960-976 (1997).

92 Yanez, J., Souto, Y., Pineiro, L., Folgueira, M. & Anadon, R. Gustatory and general visceral centers and their connections in the brain of adult zebrafish: a carbocyanine dye tract-tracing study. *J Comp Neurol* **525**, 333-362 (2017). https://doi.org/10.1002/cne.24068

93 DeKorver, N. W., Chaudoin, T. R. & Bonasera, S. J. Toll-Like Receptor 2 Is a Regulator of Circadian Active and Inactive State Consolidation in C57BL/6 Mice. *Front Aging Neurosci* **9**, 219 (2017). https://doi.org/10.3389/fnagi.2017.00219

94 Moore, H. A. & Whitmore, D. Circadian rhythmicity and light sensitivity of the zebrafish brain. *PLoS One* **9**, e86176 (2014). https://doi.org/10.1371/journal.pone.0086176

5. APPENDIX

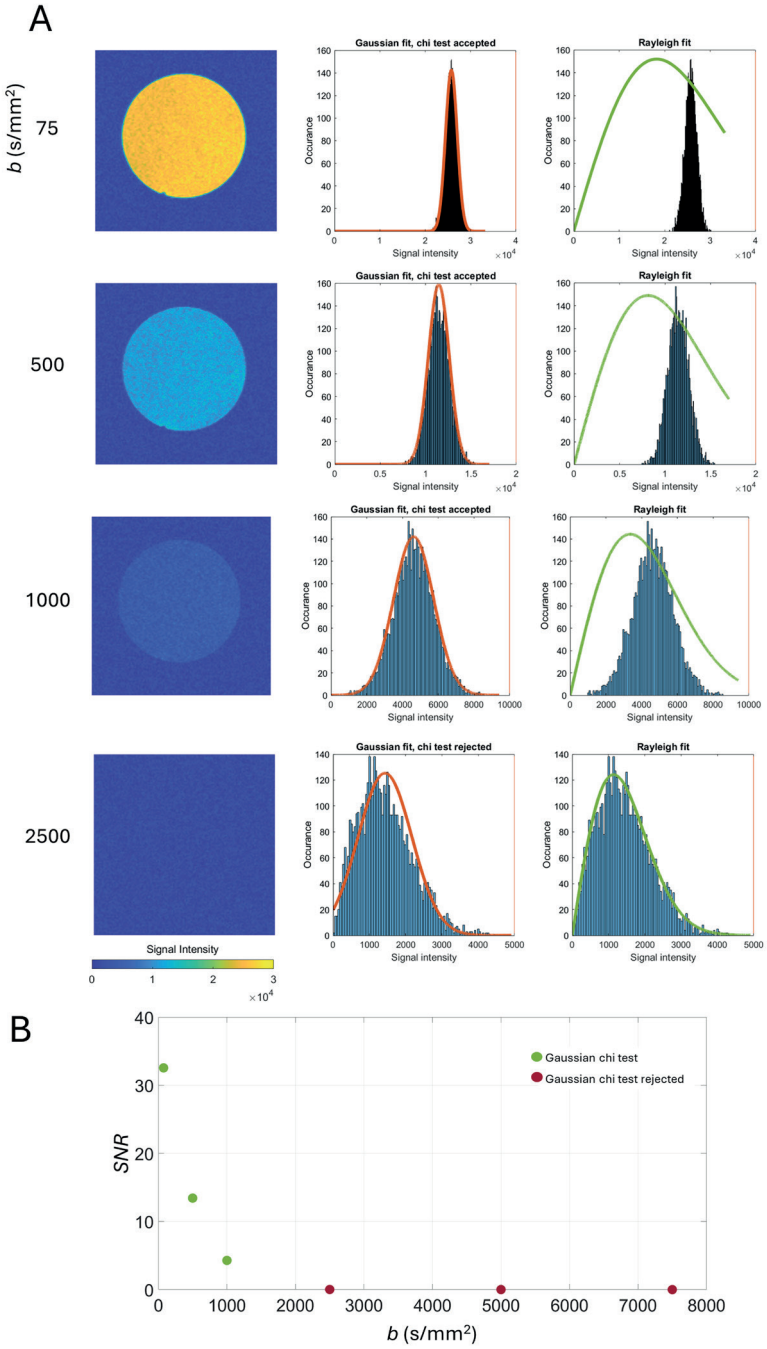
A
b (s/mm²)
75
500
1000
2500
Gaussian fit, chi test accepted
Gaussian fit, chi test rejected
Rayleigh fit
Occurance
Signal intensity
Signal Intensity
B
SNR
b (s/mm²)
Gaussian chi test
Gaussian chi test rejected

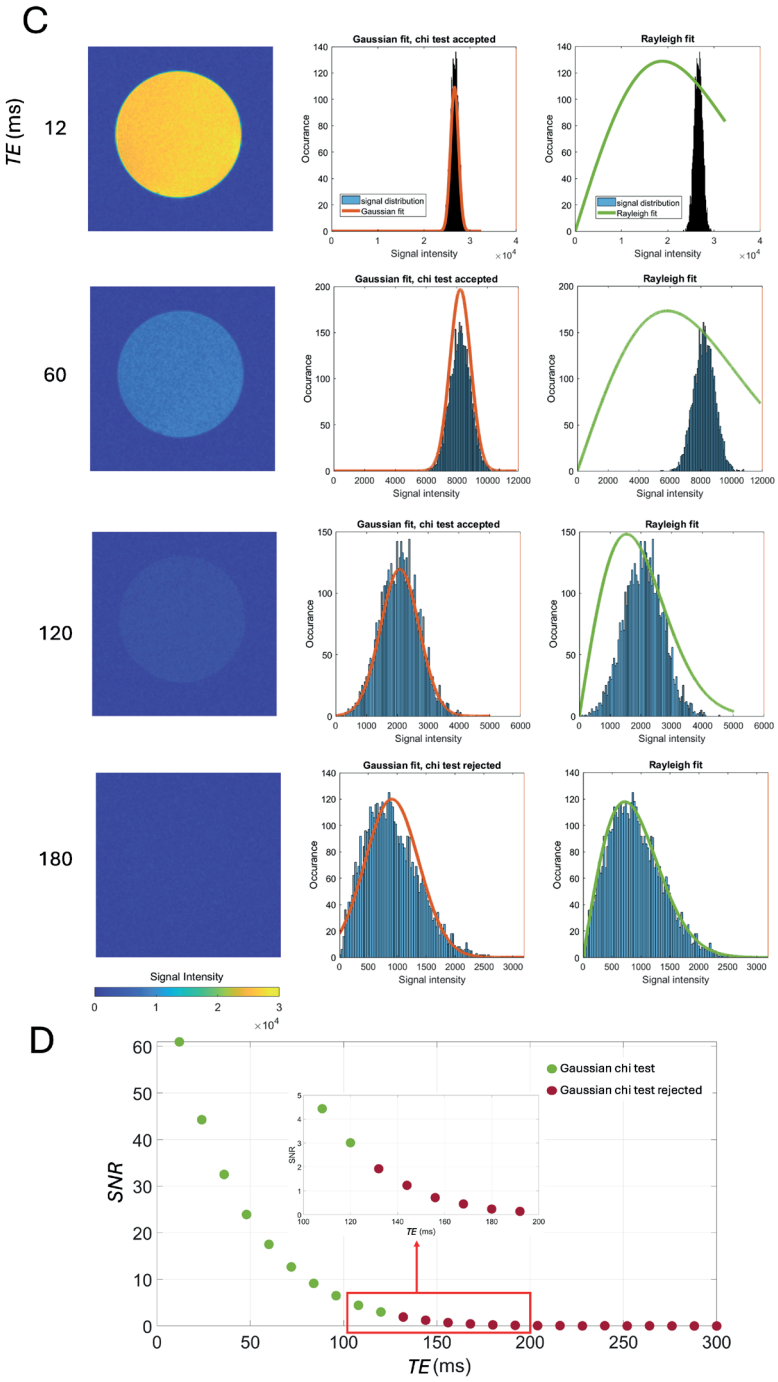
C
TE (ms)
12
60
120
180
Gaussian fit, chi test accepted
Rayleigh fit
Gaussian fit, chi test rejected
signal distribution
Gaussian fit
Rayleigh fit
Occurance
Signal intensity
Signal Intensity
D
SNR
TE (ms)
Gaussian chi test
Gaussian chi test rejected

Figure S3.1. DWI and MSME data profile obtained at 750 MHz, fitted to Gaussian and Rayleigh fit functions. [A] *DWI measurement of $CuSO_4$ in D_2O/H_2O (80%/20%), showcasing the signal intensity profile fitted to a Gaussian and Rayleigh fit.* ***[B]*** *SNR of mean MR signal acquired for $CuSO_4$ in D_2O/H_2O (80%/20%) by DWI at various b-values ranging from 0 to 8000 s/mm^2. According to these the Gaussian chi test performed on the DWI MR signal profile, a Gaussian distribution may be assumed for MR signals with a SNR up to 3.* ***[C]*** *MSME measurement of $CuSO_4$ in D_2O/H_2O (80%/20%), showing the signal intensity profile fitted to a Gaussian and Rayleigh fit at various echo times.* ***[D]*** *SNR of mean MR signal obtained for D_2O/H_2O (80%/20%) by MSME at echo times between 12 and 300 ms. Gaussian chi test of the MR signal profile is accepted the up to an SNR of 3. Acquisition details MSME: TR = 3000 ms, τ = 6.0 ms, ns = 4, resolution 47 × 47 µm, and a slice thickness 500 µm. DWI: TR = 1000 ms, TE = 13 ms, ns = 4, resolution 47 × 47 µm, slice thickness 200 µm, effective b-value range 50, 500, 1000, 1500, 2000, 2500, or 3000 s/mm^2. Figure on the preceding pages.*

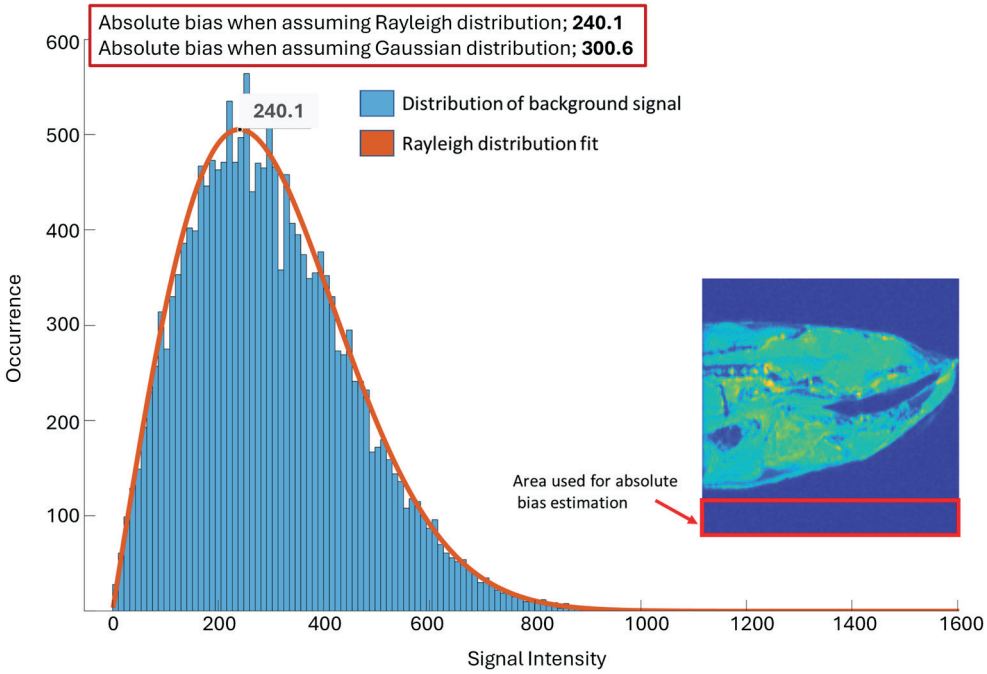

Figure S3.2. Estimation of the absolute bias (systematic error) in DWI at 750 MHz, using Gaussian and Rayleigh fit functions. *[C] Profile of the background signal obtained in a DWI measurement, showing a clear Rayleigh distribution. The plot illustrates how a mean background estimation in the phasor approach by assuming a Gaussian distribution used would overestimates the background signal by 25% compared to the Rayleigh distribution.*

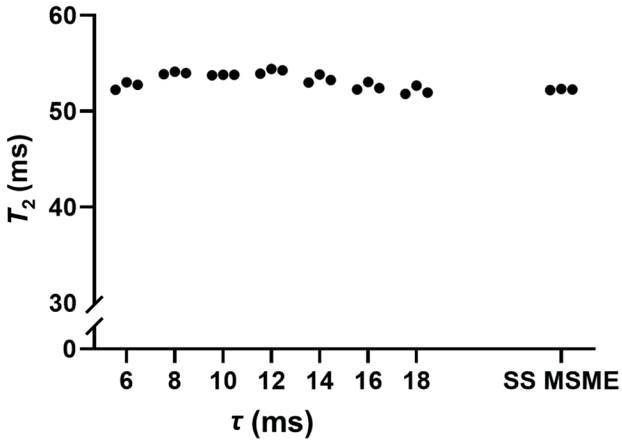

Figure S3.3. Estimated T_2 as a function of CPMG refocusing pulse interval (τ) in multi-slice MSME. *No significant change in the T_2 is observed, indicating reported T_2 are not primarily influenced by magnetic field disturbances. Furthermore, single-slice (SS) MSME was performed for a τ of 6 ms, showing no significant change in T_2 compared to multi-slice MSME, indicating no significant magnetization transfer-related bias of the water signal.*

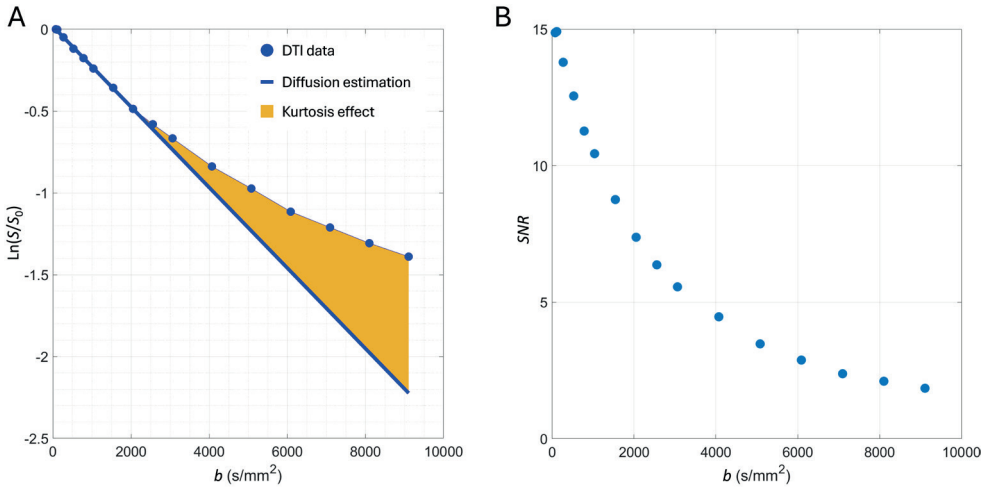

Figure S3.4. Relation between applied b-values in dMRI experiments and the observed kurtosis effect and SNR in the zebrafish brain at 750 MHz. [A] *Relationship between normalized natural logarithmic MR signal obtained by DTI, compared to the expected diffusion-weighted signal and their difference displayed as the kurtosis effect at increasing b-values* ***[B]*** *SNR obtained by DTI at increasing b-values.*

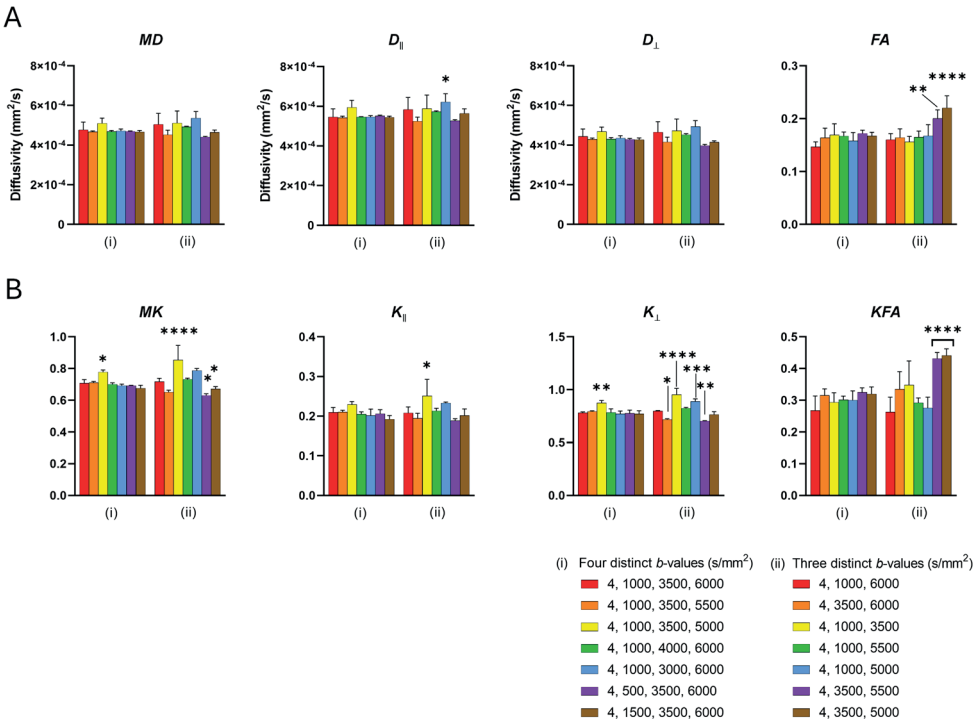

Figure S3.5 Impact of effective b-value range manipulation on diffusion tensor and diffusion kurtosis metrics. *The effect of manipulating the effective b-value range on the estimated* ***[A]*** *diffusion tensor metrics and* ***[B]*** *diffusion kurtosis metrics. (i) The impact of altering the first, second or third b-value shell (b_0 not included) by 500 s/mm² was investigated. The effect on the estimated metrics was found negligible, except if the third b-value shell was lowered to 5000 s/mm², which led to a significant increase in the MK and $K_\perp$ compared to the control. Notably, transitioning from four distinct b-values to three distinct b-values revealed a clear difference, with more statistical variation observed, particularly in the FA and diffusion kurtosis metrics. Data was obtained by conducting repeated DTI measurements (n = 3) on the same zebrafish (control group), extracting data from the cerebellum. Statistical analysis was performed by ordinary one-way ANOVA, comparing the mean of each effective b-value range with the control range applied during measurements, effective b range of 4, 1000, 3500, or 6000 s/mm². A significance level of $p < 0.05$ was employed, denoted by asterisks (*$p < 0.05$, **$p < 0.01$, ***$p < 0.005$, ****$p < 0.001$). Acquisition details: TR = 2000 ms, TE = 12.4 ms, ns = 4, resolution 25 µm × 25 µm × 200 µm, effective b-value range as specified in legend, with 8, 12, 24, or 36 diffusion-encoding directions respectively for the b_0, and the first, second, and third b-value shell.*

4

UNBEATABLE SUPER-RESOLUTION OF VOXEL-BASED MR SPECTROSCOPY OF ZEBRAFISH BRAIN ACHIEVED AT 28.2 T*

* Manuscript in preparation for publication

ABSTRACT

Localized ^{1}H magnetic resonance spectroscopy (MRS) is pivotal in clinical neurology, offering non-invasive insight into neurochemical composition in localized brain regions. Zebrafish (*Danio rerio*) serve as valuable models in neurological research. However, the size of the zebrafish brain and limited MRS sensitivity hinder comprehensive analysis. Here, we investigate the potential of ultra-high field (UHF) MR systems, particularly 28.2 T, for this purpose. This work pioneers application of localized ^{1}H spectroscopy in zebrafish brain at 28.2 T. We explore potentials and challenges associated with UHF localized 1H MRS on the zebrafish brain, emphasizing the acquisition of highly resolved spectra to enable targeted molecular level information of distinct brain regions. Young adult zebrafish (three month old), were sacrificed and directly transferred to 5 mm glass NMR tubes. MR microscopy images were obtained at 28.2 T using a rapid acquisition with relaxation enhancement (RARE) sequence to select a volume of interest. Point resolved spectroscopy (PRESS) sequences was optimized for localized ^{1}H spectroscopy. PRESS sequence preceded by a variable pulse power and optimized relaxation delays (VAPOR) sequence for global water suppression interleaved with outer volume suppression. Chemical shift displacement effects were careful reduced by choosing appropriate bandwidths. Parameters including the gradient strength, excitation frequency, echo time and voxel volume were fine-tuned specifically targeting the 0 – 4.5 ppm chemical shift regions. Highly resolved cerebral metabolite spectra were acquired from localized regions in zebrafish brain, from volumes as small as 125 nL within approximately 30 minutes. This facilitated identification and quantification of several brain metabolites with super high resolution. Localized ^{1}H MRS at 28.2 T significantly enhance signal-to-noise ratio and improved baseline separation of metabolites signals from localized regions in the tiny zebrafish brain.

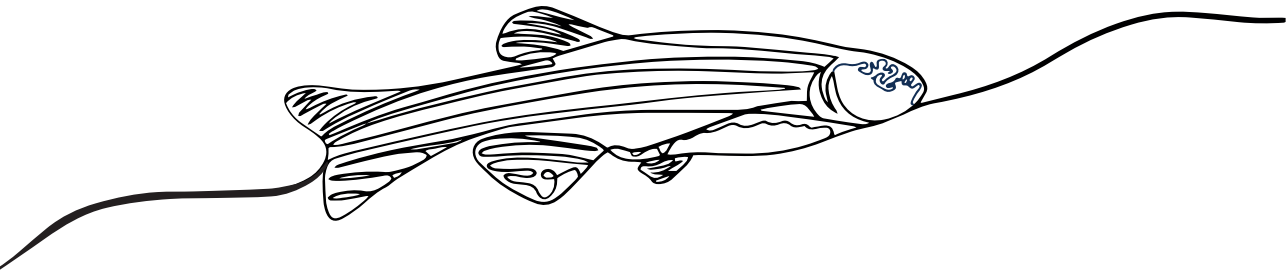

1. INTRODUCTION

Single voxel localized magnetic resonance spectroscopy (MRS) is a well-established, non-invasive, technique for monitoring metabolic changes in human clinical studies and pre-clinical studies using animal models[1]. Unlike various other metabolomic methodologies, localized MRS bypasses the need for laborious extraction procedures. Moreover, it facilitates precise selection of tissue regions, enabling *in vivo* monitoring of metabolites within their native environments. While localized MRS is utilized for various tissue types[2-5], clinical applications predominantly focus on brain tissue across a wide range of neurological disorders[6-12]. In this respect, brain metabolites show a remarkable sensitivity to deviations from physiological homeostasis induced by pathological conditions. Specific metabolites offer insights into distinct cells and their corresponding cellular activities. For instance, localized MRS enables quantification of glutamate (Glu) and γ-aminobutyric acid (GABA), the principal excitatory and inhibitory neurotransmitters in the brain[13,14]. Additionally, N-acetylaspartate (NAA), predominantly localized in neuronal cell bodies and axons, serves as a potential marker for monitoring neuronal integrity[15] and *myo*-inositol (m-Ins), chiefly situated in glial cells, functions as a potential marker for osmotic stress or neuroinflammation[16].

Zebrafish (*Danio rerio*) are exemplary model organisms. For scientific inquiry, zebrafish offer distinct advantages, including cost-effectiveness and easy maintenance, coupled with a rapid developmental pace. Moreover, zebrafish embryos are transparent, particularly beneficial in toxicity studies for precise observation of developmental stages[17]. Furthermore, toxicity studies utilizing zebrafish larvae using high-resolution magic angle spinning (HR-MAS) allows for metabolomic studies to reveal toxicity pathways at a cellular and molecular level[18-23]. Additionally, the entire zebrafish genome is sequenced[24], revealing 84% of genes linked to human diseases possess a corresponding homologous gene in the zebrafish genome. These similarities with humans allow for genetically manipulation to create transgenic zebrafish models to study human diseases. For neurological disorders, extensive zebrafish models are available, including transgenic models of Alzheimer's disease, Parkinson's disease, brain tumours and epilepsy[25-29]. Despite their extensive use in research, studies utilizing localized MRS involving zebrafish are rare. Previously, we presented the first methodology of localized MRS for *in vivo* analysis of cerebral metabolites in zebrafish at 9.4 T (400 MHz)[30]. High-resolution spectra were obtained, allowing for the identification and quantification of the most predominant metabolites, including creatine (Cr), Glu, NAA, m-Ins, glutamine (Gln), taurine (Tau), and GABA. However, the limited sensitivity of localized MRS, in combination with the small size of the zebrafish brain (few mm^3), prevented the application from analysing individual brain structures.

Recent developments in MR systems operating at high fields and ultra-high fields (UHF), offer remarkable potential in elucidating intricate details within the zebrafish brain (Chapter 2). Elevated signal to noise ratios (SNR) in combination with extremely high gradients strengths, unveiled previously unsees details in the zebrafish brain through non-invasive magnetic resonance imaging (MRI), including the identification of tiny white matter structures trough diffusion-based MRI tractography and shown in Chapter 2 and as previously by Ullman *et al.*[31]. However, despite these recent breakthroughs, the application of localized MRS in the zebrafish brain at UHF remains untapped. Integrating localized MRS into UHF MRI studies could provide valuable insights into neurochemical processes, paving the way for comprehensive investigations into zebrafish brain functions and pathology.

Localized MRS at UHFs holds tremendous promise due to anticipated enhancements in SNR and improved baseline separation of metabolites. These advancements enable monitoring of cerebral metabolites in smaller voxels than previously achievable, facilitating the precise examination of specific brain regions. However, utilization of UHFs for single voxel localized MRS also introduces specific challenges, notably increased chemical shift displacement (s_δ). Chemical shift displacement effects, also called chemical shift misregistration or chemical shift artifacts, were first elucidated in 1984 though the registration shift of the fat signal[32]. These effects escalate with elevated magnetic field strengths and recede with stronger magnetic field gradients[33]. Despite UHF MRI systems utilizing gradient strengths (G_{max}) up to 3 T/m[34], considerably higher than the typical strengths of 40 mT/m in medical imaging systems[35], they are insufficient to compensate for the increase in Larmor frequency. Consequently, chemical shift displacements are notably exacerbated in localized MRS utilizing UHF systems. Addressing this challenge requires sophisticated correction methods to accurately quantify metabolite concentrations and interpret spectroscopic data.

In the current study, we utilize localized MRS at 28.2 T. As these data represent the first localized MRS data obtained at 28.2 T, we present both the advantages, challenges, and limitations of this utilization. Besides optimization of sequence parameters involved in chemical shift displacement effects, we explore metabolic profiles at various echo times, voxel volumes, and number of averages. Subsequently, we employ optimized method parameters to generate a localized spectrum with prolonged measurement duration, facilitating the detection of highly resolved cerebral metabolites in the zebrafish brain. Following this, we perform a comparative quantitative assessment of spectra derived from various brain regions, aiming to elucidate cerebral metabolite profiles in specific brain regions.

2. METHODS

Zebrafish husbandry

The husbandry of the zebrafish was performed according to the regulations set forth by the local animal welfare committee of the university of Leiden (Licence numbers AVD1060020171767 and AVD10600202216175), in accordance with the international standards outlined by the EU Animal Protection Directive 2010/63/EU. All procedures followed standard protocols as previously described (www.zfin.org)[36]. In this study, three-month-old male zebrafish were utilized. To minimize any metabolite degradation, zebrafish were euthanized just before the MRI examination, which was induced by immobilization through submersion in ice water at a temperature between 0 – 4 °C for 15 minutes until the halt of opercular movement. Following euthanization, specimens were shortly kept on ice until MRI and MRS measurements were conducted.

Magnetic resonance imaging and spectroscopy

MRI and MRS experiments were conducted using Bruker (Bruker Biospin GmbH, Germany) vertical bore systems operating at 17.6 T (750 MHz) or 28.2 T (1200 MHz), configured with a Micro5 or Micro5 iProbe gradient system, respectively. Both systems were water-cooled, provided G_{max} = 3 T/m, used 5 mm inner diameter birdcage resonators, and GREAT60 gradient power supplies. Measurements were conducted at room-temperature. Data acquisition and processing on both systems was performed with Linux workstations, running Bruker imaging software ParaVision 360 v3.3 (Bruker Biospin GmbH, Germany). During analysis, zebrafish were embedded in perfluoropolyether (Fomblin Y, Solvay Solexis S.P.A.).

T_2-weighted spin echo images were acquired by a rapid acquisition with relaxation enhancement (RARE) pulse sequence to select the position for single voxel localized MRS. RARE measurements were performed with an echo time *TE* = 5.6 ms, a repetition time *TR* = 3000 ms, using 4 refocussing pulses per excitation, and *ns* = 16 averages. The field of view (FOV) was 8 × 8 mm, at a matrix size of 256 × 256 voxels, obtaining a resolution of 31 × 31 µm, with a slice thickness of 200 µm.

For single voxel localized ^{1}H MRS, we utilized a point resolved spectroscopy (PRESS) pulse sequence[37]. The PRESS sequence incorporates three transmitter slice-selective RF pulses (90°-180°-180°), applied simultaneous with *x*, *y*, and *z* gradients to target the specified voxel. Prior to each localized MRS measurement, magnetic field homogeneity within each voxel was achieved by local second-order shimming prior to data acquisition. After parameter optimization, standard PRESS measurements were performed with *TE* = 15 ms, *TR* = 2000 ms, *ns* = 512. The PRESS sequence used 2048 complex points and an acquisition bandwidth of 10 ppm. At 17.6 T and 28.2 T, the transmitter RF pulse bandwidth was *tBW* = 10 kHz or 15

kHz, respectively. The excitation frequency was v_1 = 3 ppm, coinciding with the N(CH_3) total creatine (tCr) signal. For the estimation of regional cerebral metabolite levels, three voxels were selected in the zebrafish brain; (1) in the forebrain, covering part of the pallium, (2) in the midbrain, covering part of the mesencephalon, cerebellum, and diencephalon, and (3) in the hindbrain, covering part of the cerebellum and rhombencephalon. In the midbrain, a PRESS voxel of 0.8 × 0.8 × 0.8 mm^3, with a voxel volume of V_{voxel} = 512 nL was selected. In the forebrain and hindbrain, a PRESS voxel of 0.6 × 0.6 × 0.6 mm^3, with V_{voxel} = 216 nL was selected. For suppression of the water signal, a variable pulse power and optimized relaxation delays (VAPOR) sequence[38] was applied prior to the PRESS pulses. Outer volume suppression (OVS) was integrated in an interleaved manner with the VAPOR sequence. The OVS consists of six suppression slices, each repeated three times and aligned parallel to the PRESS voxel, reducing the PRESS gradient spoilers.

Data processing

Identification and quantification of metabolites. Identification of cerebral metabolites was performed by comparison of obtained ^{1}H spectra to reference spectra of brain metabolites[39-41] and on our previously obtained NMR spectra of zebrafish brain extracts[30]. Quantification of metabolites was executed using Chenomx NMR suite 8.2 (Chenomx Inc., Edmonton, Alberta, Canada). Available reference libraries provided by Chenomx were employed. Metabolite concentrations were estimated relative to tCr [42]. Statistical analysis for NMR quantification involved one-way analysis of variance (ANOVA) by OriginPro v.8 (Originlab, Northhampton, MA, USA). Multiple comparisons were conducted using the *t*-test, and significance was established with $p < 0.05$.

Signal-to-noise ratio estimation. Unless specified otherwise, *SNR* was estimated based on the tCr signal at a chemical shift δ = 3.03 ppm, utilizing build-in TopSpin functionalities with

$$SNR = \frac{I_{tCr}}{2 \cdot N} \quad . \tag{4.1}$$

Here, I_{tCr} is the maximum signal intensity of the tCr signal at δ = 3.03 ppm, and *N* is the noise factor as fully described in the TopSpin manual (Processing commands and parameters user manual, version 007, Bruker Corporation).

Chemical shift displacement estimation. The estimation of s_δ was based on

$$s_\delta\ (\%) = \frac{|v_1 - v_x|}{tBW} \quad , \tag{4.2}$$

where v_x is the Larmor frequency of the metabolite of interest (Hz).

T_2 relaxation time estimation. T_2 relaxation times of individual metabolites were estimated using PRESS signal intensities acquired at various echo times. T_2 was estimated using a non-linear least squares algorithm to fit the mono-exponential function described by

$$I_{\mathrm{TE}} = A + I_0 \cdot \exp^{\frac{-TE}{T_2}} \quad . \tag{4.3}$$

Here, I_{TE} represents the signal intensity at *TE*, *A* is the absolute bias, and I_0 is the signal intensity at TE_0.

3. RESULTS AND DISCUSSION

It is well known that performing localized MRS at high magnetic fields significantly enhances both the SNR and spectral resolution. These improvements enable more precise identification and quantification of metabolites within a given region. However, MRI artifacts, particularly the chemical shift displacement effects, must be carefully considered and managed during method optimization. Here, we explore the challenge of conducting localized MRS at 28.2 T magnetic field strengths on the adult zebrafish brain, particularly addressing the chemical shift displacement effects. Next, we study the impact of *TE* and its consequential influence on acquired spectra. Moreover, we elucidate how the application of UHF localized MRS with ascending echo times can be leveraged to estimate T_2 relaxation times of distinct metabolites within the zebrafish brain. Hereafter, we explore the limits of localized MRS at UHF in terms of voxel volume and number of scans required for metabolite quantification. Finally, we apply optimized method parameters to produce a localized spectrum with extended measurement time, enabling the identification of cerebral metabolites within the zebrafish brain at UHF strengths. We then conduct a comparative quantitative analysis of spectra obtained from different brain regions to gain insights into the cerebral metabolite profiles.

Chemical shift displacement at UHF localized MRS

Single voxel localized MRS at UHF strengths offers the distinct advantage of elevated SNR and enhanced metabolite separation compared to lower magnetic fields. These advancements facilitate advanced identification and quantification of metabolites. However, as the magnetic field strength increases, chemical shift displacement effects become more pronounced[43] (see Supplementary Figure S4.1). For example, in localized MRS spectra acquired with the PRESS sequence at 28.2 T, with *tBW* = 5 kHz and v_1 = 4.7 ppm, the $^3CH_3$ signal of lactate at δ = 1.32 ppm exhibits s_δ = 81% for each transmitter RF pulse. Consequently, only 0.67% of the lactate signal originating from within the selected PRESS voxel is effectively captured. In contrast, employing identical parameters with a clinical system operating at 1.5 T would result in s_δ = 4% per PRESS transmitter RF pulse for the $^3CH_3$ signal of lactate at δ = 1.32 ppm and a

significantly higher proportion, 88%, of the lactate signal from within the voxel is detected. This underscores the importance of understanding the effects of chemical shift displacement when transitioning to ultra-high magnetic field systems for single voxel localized MRS studies. To mitigate the impact of chemical shift displacement on targeted metabolites, v_1 can be adjusted, to put it in closer proximity to the chemical shift of the metabolites of interest (see Equation 4.2). In Figure 4.1, we explored the impact of v_1 on the metabolic profile obtained at 28.2 T. Apparently, a minor adjustment of v_1 by ±1 ppm, equivalent to ±1200 Hz at 28.2 T, leads to notable changes in the obtained metabolic profile. The spectra obtained at v_1 = 1 ppm or v_1 = 4.7 ppm demonstrate metabolites with s_δ > 30% results in an almost complete loss of the metabolite signal. Moreover, it becomes apparent that the chemical shift displacement at 28.2 T significantly alters the signal intensities of metabolites depending on v_1. For specific metabolites, *e.g.* lactate, which show significant differences in chemical shifts between their groups, the displacement of these chemical shifts plays a crucial role during quantification. This effect is clearly demonstrated in Table 4.1. Here the estimation of the lactate level relative to tCr for various v_1 reveals significant discrepancies. At v_1 = 2 ppm, the ^{2}CH lactate signal at δ = 4.12 ppm indicates a concentration of 0.41 relative to tCr, whereas the $^3CH_3$ signal at δ = 1.32 ppm indicates a concentration of 2.89 relative to tCr. This underscores the importance of using consistent signals for metabolite quantification at specific excitation frequencies during metabolite comparison studies. For our specific objectives, the majority of brain metabolites exhibit signals within the range of δ = 4.1 ppm to δ = 2 ppm. These include Lac, Glu, Gln, m-Ins, Tau, tCr, GABA, and NAA.

Besides the impact of v_1, *tBW* of the excitation and refocussing pulses impact the magnitude of s_δ. In Figure 4.2A, we probed the impact of *tBW* on the localized MRS spectra, acquired with v_1 = 3 ppm. At *tBW* = 5 kHz, a significant impact of lipid signals is visible especially around δ = 1.3 ppm. The zebrafish brain is encapsulated by lipids, elucidated in Supplementary Figure S4.2, suppressing metabolite signals such as lactate and alanine. Although the PRESS voxel was fully placed inside the brain, chemical shift displacement effects caused the detection of the lipid signals at *tBW* = 5 kHz. At *tBW* = 10 kHz, the lipid signal is still observed, although significantly reduced. At *tBW* = 15 kHz or *tBW* = 20 kHz, the lipid signals are no longer observed, allowing for the identification and quantification of the lactate and alanine signals at δ = 1.32 ppm and δ = 1.47 ppm, respectively. However, as illustrated in Figure 4.2B, increasing *tBW* leads to diminished SNR, exhibiting a notable decrease of approximately 25% between *tBW* = 15 kHz to 20 kHz. In contrast, the decrease in SNR is less between 10 kHz and 15 kHz, at around 10%. Accordingly, further localized MRS acquisitions are performed utilizing *tBW* = 15 kHz, unless otherwise specified.

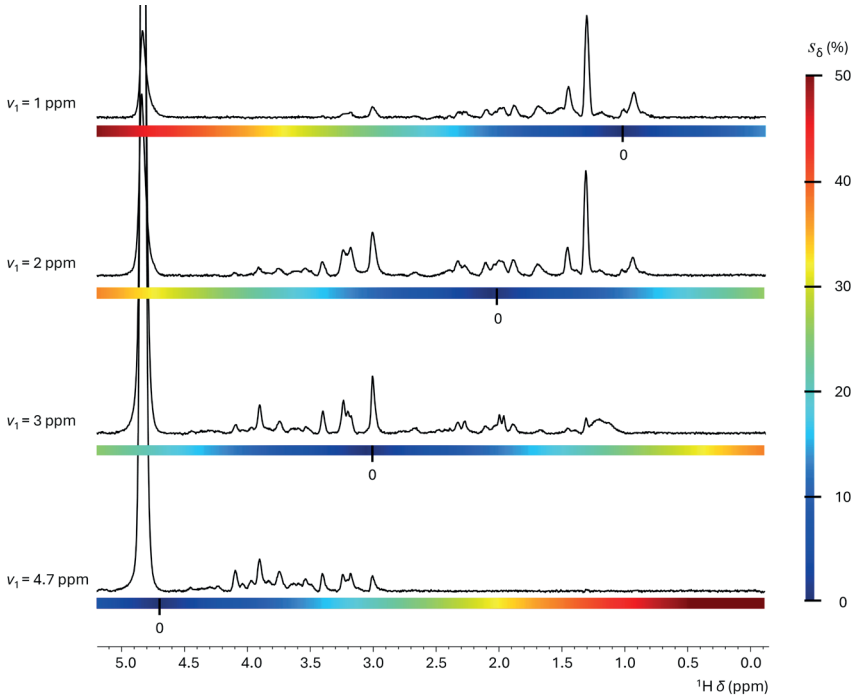

Figure 4.1. Impact of the excitation frequency v_1 on the acquired single voxel localized ^{1}H MRS spectra from adult zebrafish mid-brain at 28.2 T. *All PRESS spectra were acquired from the same precise location within the zebrafish brain, employing uniform parameters as specified, while adjusting v_1 as specified for each spectrum, delineated by s_δ = 0. To facilitate direct comparison, spectral intensities were normalized based on the noise level of the base line. The s_δ colour bars show the magnitude of chemical shift displacement per transmitter pulse, further elucidated in Supplementary Figure S4.1B. Acquisition details: TR = 2000 ms, TE = 15 ms, ns = 1024, a voxel size of 0.8 × 0.8 × 0.8 mm^3 with V_{voxel} = 512 nL, 2048 acquisition points, acquisition bandwidth 11904 Hz / 9.91 ppm, 4 dummy scans, tBW = 10 kHz. Water suppression and outer volume suppression were applied as specified in the method section.*

Table 4.1. *Impact of v_1 on the lactate level estimation for both the ^{2}CH group at δ = 4.12 ppm and the $^3CH_3$ group at δ = 1.32 ppm. (-) indicates the concentration could not be estimated. All concentrations are given relative to the tCr signal at δ = 3.03 ppm.*

Excitation frequency	^{2}CH Lac δ = 4.12 ppm	$^3CH_3$ Lac δ = 1.32 ppm
4.7	6.04	-
3	0.64	0.35
2	0.41	2.89
1	-	7.17

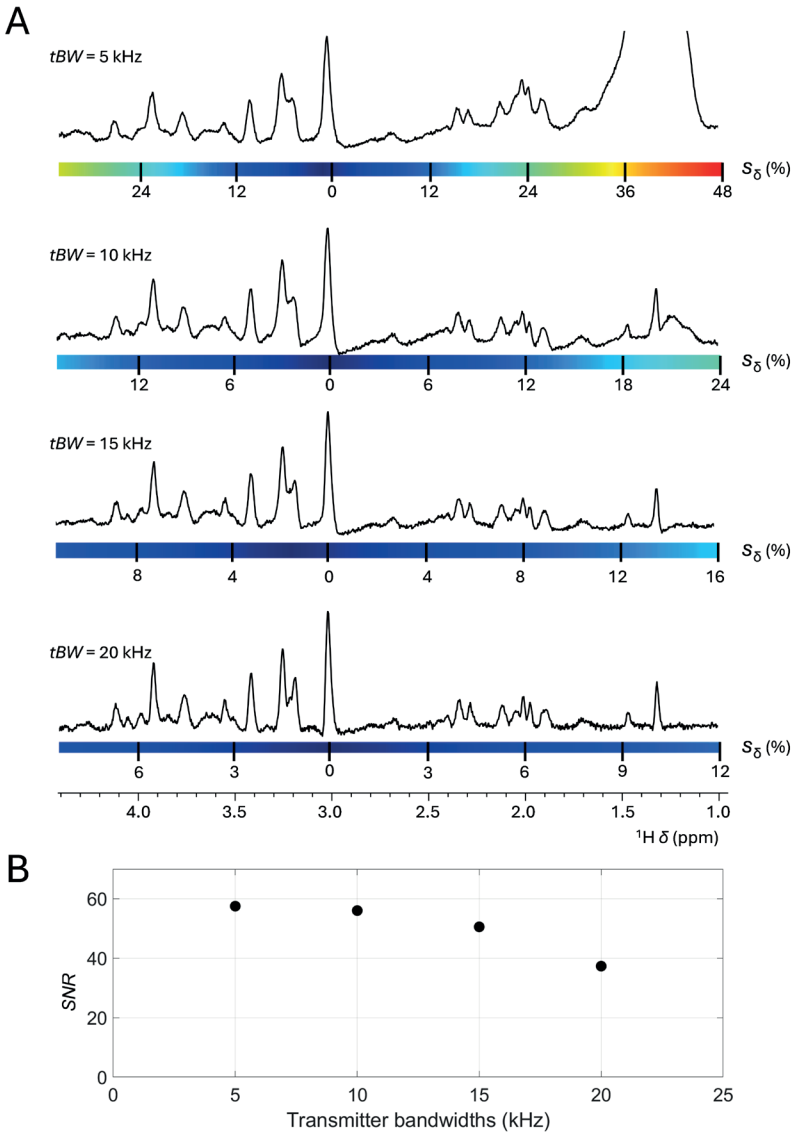

Figure 4.2. Impact of the transmitter RF pulse bandwidth tBW on the acquired single voxel localized ^{1}H MRS spectra from adult zebrafish mid-brain at 28.2 T. [A] *Single voxel localized MRS spectra acquired for various tBW.* ***[B]*** *SNR of the tCr signal at δ = 3.03 ppm as a function of tBW. All PRESS spectra were acquired from the same precise location within the zebrafish brain, employing uniform parameters, while adjusting tBW as specified for each spectrum. To facilitate direct comparison, spectral intensities were normalized relative to the tCr signal at δ = 3.03 ppm. The s_δ colour bars show the magnitude of chemical shift displacement per transmitter pulse, further elucidated in Supplementary Figure S4.1B. Acquisition details: TR = 2000 ms, TE = 15 ms, ns = 1024, voxel size 0.8 × 0.8 × 0.8 mm^3 with V_{voxel} = 512 nL, 2048 acquisition points, acquisition bandwidth 11904 Hz / 9.91 ppm, 4 dummy scans, v_1 = 3 ppm. Water suppression and outer volume suppression were applied as specified in the method section. Signal-to-noise ratios estimated based on the tCr signal at δ = 3.03 ppm.*

Single voxel localized MRS at variable echo times

The applied echo time plays a pivotal role in the acquired metabolic profile and warrants careful consideration during experimental design. A well-established effect is the diminishing of signal intensities at elevated echo times as a consequence of the T_2 relaxation times of metabolites. Thus, shorter echo times are frequently favoured to enhance obtained SNR. Nonetheless, deliberate selection of longer echo times can yield substantial enhancements in metabolite identification and quantification within acquired profiles. Furthermore, applying a range of echo times allows for the estimation of T_2 relaxation times of individual metabolites. Figure 4.3A shows the cerebral metabolite profile at increasing echo times obtained at 17.6 T. A full comparison of the cerebral metabolite profile at both 17.6 T and 28.2 T is shown in Supplementary Figure S4.3. Beyond echo times of 60 ms, the lipid signals around δ = 0.9 ppm and δ = 2.0 ppm become indiscernible amidst the background noise due to the short T_2 relaxation time of macromolecules. This facilitates improved identification and quantification of cerebral metabolites with chemical shifts overlapping with lipid signals, *e.g.* Lac, Ala, GABA, NAA, and NAAG. Additionally, water exhibits a significantly shorter T_2 relaxation time compared to most presented cerebral metabolites (data not shown). Consequently, the suppression of the broad and predominant water signal is notably improved at higher echo times. In addition to alterations in their relative abundance, the T_2 relaxation times of cerebral metabolites offers insight in changes within their respective environments. For instance, in Alzheimer's disease, a significant increase in the T_2 of NAA was reported, while no significant change was observed in the T_2 of water in the same tissue[44]. Unlike the T_2 of water, which reflects properties of both intracellular and extracellular spaces, NAA is confined solely intracellular, thus furnishing more nuanced and compartment-specific details[44]. The signal intensity of various metabolite

Table 4.2. *T_2 relaxation times estimated for brain metabolites at 28.2 T, compared to 17.6 T. Measurements presented were performed once (n = 1) as a proof-of-principle, and therefore lack the statistical robustness required for comparison with other values. While this single instance serves to demonstrate the feasibility of the method, reported values should not be extrapolated or compared with other datasets due to the absence of a statistical basis.*

Metabolite	Group	δ (ppm)	Multiplicity	T_2 at 28.2 T	T_2 at 17.6 T
tCr	$^2CH_2$	3.91	s	75.5 ms	112.4 ms
	$N(CH_3)$	3.03	s	40.6 ms	111.2 ms
Glx	Glu ^2CH / Gln ^2CH	3.74 / 3.75	dd / t	24.8 ms	33.4 ms
NAAG	$^2CH_3$	2.04	s	99.8 ms	149.4 ms
NAA	$^2CH_3$	2.01	s	47.7 ms	51.8 ms
GABA	$^3CH_2$	1.89	t	25.3 ms	25.2 ms

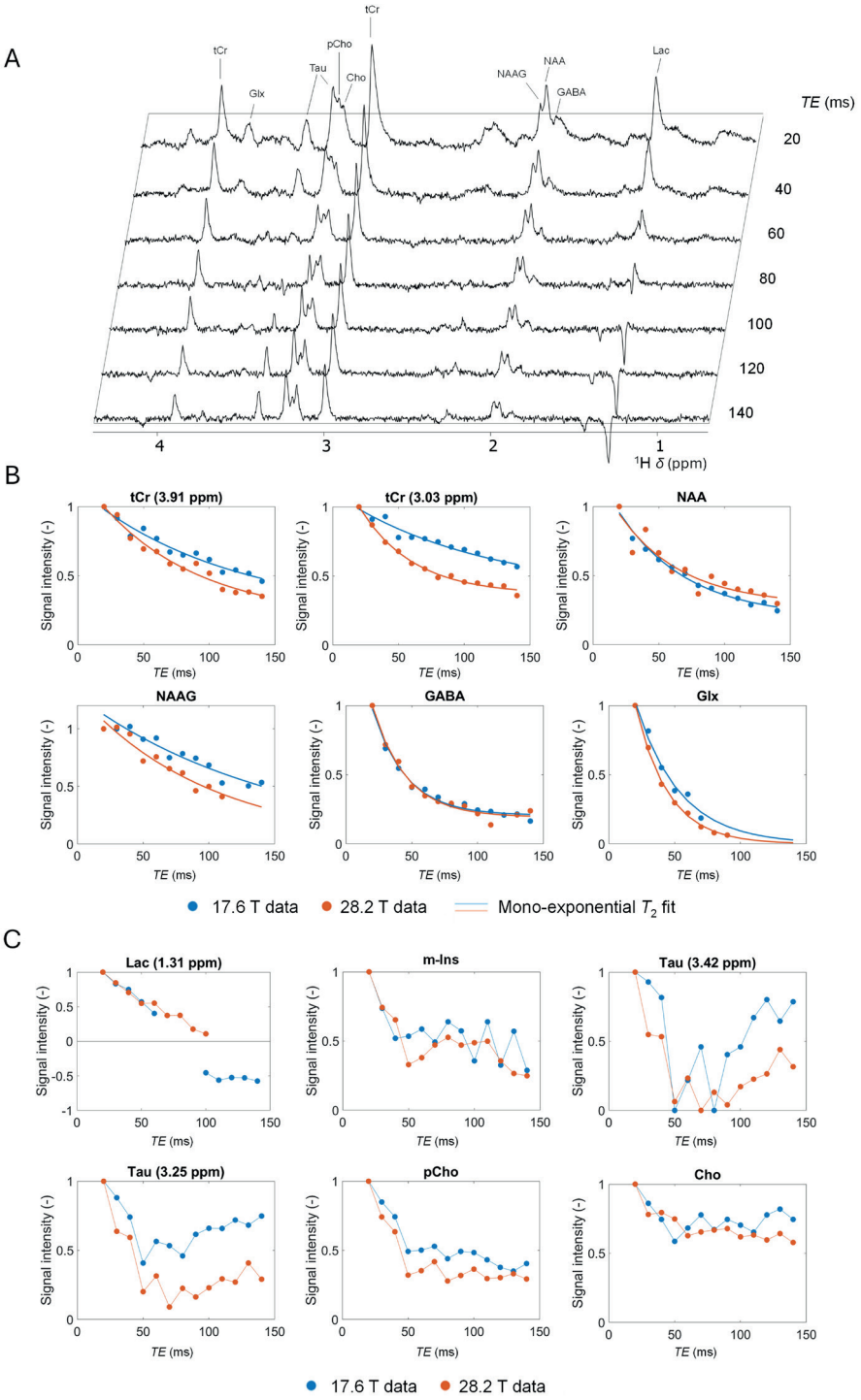
A
tCr
Glx
Tau
pCho
Cho
tCr
NAAG
NAA
GABA
Lac
TE (ms)
20
40
60
80
100
120
140
4
3
2
1
¹H δ (ppm)
B
tCr (3.91 ppm)
tCr (3.03 ppm)
NAA
NAAG
GABA
Glx
Signal intensity (-)
TE (ms)
17.6 T data
28.2 T data
Mono-exponential T2 fit
C
Lac (1.31 ppm)
m-Ins
Tau (3.42 ppm)
Tau (3.25 ppm)
pCho
Cho
Signal intensity (-)
TE (ms)
17.6 T data
28.2 T data

Figure 4.3. Impact of the echo time on the acquired single voxel localized ^{1}H MRS spectra from adult zebrafish mid-brain at 17.6 T and 28.2 T. [A] *Single voxel localized MRS spectra acquired for echo times ranging from 20 to 140 ms at 17.6 T.* ***[B]*** *Signal decay observed for various cerebral metabolites with an apparent consistent mono-exponential decrease with echo time. Mono-exponential decay curve from T_2 relaxation time estimation fitted through data.* ***[C]*** *Signal decay of cerebral metabolites with a more complex signal intensity evolution, contributed to J-coupling induced signal dephasing. Acquisition details: TR = 2000 ms, TE = 20, 40, 60, 80, 100, 120, or 140 ms, ns = 1024, a voxel size of 0.8 × 0.8 × 0.8 mm^3 with V_{voxel} = 512 nL, 2048 acquisition points, acquisition bandwidth 11904 Hz / 9.91 ppm, tBW = 10 kHz for all RF pulses, 4 dummy scans, v_1 = 3 ppm. Water suppression and outer volume suppression were applied as specified in the method section. An extended comparison of spectra with ranging echo times acquired at 17.6 T and 28.2 T is presented in Supplementary Figure S4.3. Figure on the preceding page.*

signals, including the tCr signal at δ = 3.91 ppm ($^2CH_2$) and δ = 3.03 ppm ($N(CH_3)$), the NAA signal at δ = 2.01 ppm ($^2CH_3$), the NAAG signal at δ = 2.04 ppm ($^2CH_3$), the GABA signal at δ = 1.89 ppm ($^3CH_2$), and the Glx (Glu + Gln) signal at δ = 3.75 ppm (Glu ^{2}CH and Gln ^{2}CH) appeared to consistently decrease exponentially with increasing echo time (see Figure 4.3B) allowing for direct T_2 estimation (see Table 4.2).

Other cerebral metabolite signals show a complex signal intensity evolution with increasing echo times (see Fig 4.3C). Most noticeable, the Lac signal at δ = 1.31 ppm ($^3CH_3$) shows an anti-phase pattern between 60 ms – 100 ms and a 180° phase shift at echo times above 100 ms. This shift evolution is contributed to the J-coupling of the Lac signals, estimated in the range of 6.9 – 7.3 Hz [45]. Consequently, the Lac signals are negative in-phase at $TE = J^{-1}$ ~ 140 ms and anti-phase at $TE = ½ J^{-1}$ ~ 70 ms. This characteristic facilitates distinct lactate identification by applying echo times around 140 ms, but also imposes limitations on echo times due to the complex anti-phase behaviour observed within the 60 – 100 ms echo time range. Other metabolites showing a complex echo time evolution include Tau at δ = 3.42 ppm ($^1CH_2$) and δ = 3.25 ppm ($^2CH_2$), pCho at δ = 3.21 ppm ($N(CH_3)_3$), and Cho at δ = 3.19 ppm ($N(CH_3)_3$), contributed to J-coupling induced signal dephasing. For Tau and m-Ins, the presented signal evolution is consistent with previous observation[46], showing an initial steep signal decline with a local minimum around 50 ms – 80 ms due to anti-phasing (TE ~ ½ J^{-1}), after which the signal recovers between 100 ms – 140 ms due to rephasing (TE ~ J^{-1}). T_2 relaxation time estimation of singlet resonance signals, *e.g.* both tCr signals, NAA, and NAAG, is straightforward due to the lack of J-coupling modulation. Estimation of T_2 relaxation times for metabolites with a more complex signal intensity evolution, requires quantum mechanics simulations, as previously reported [46,47].

Voxel volume and averaging strategies

One of the main advantages of performed localized MRS is the ability to non-invasively study the cerebral metabolic profile in specific brain regions. However, the tiny size of the

zebrafish brain, in combination with the uneven shape, limits the utilization of voxel sizes. Here, we explore the limits of acquisition of highly resolved single voxel localized MRS spectra in the zebrafish brain in terms of the voxel size and number of averages required for cerebral metabolite identification and quantification. Figure 4.4A shows spectra acquired with *ns* = 1024 in approximately 34 minutes with V_{voxel} ranging between 1000 µL to 125 nL, obtained from

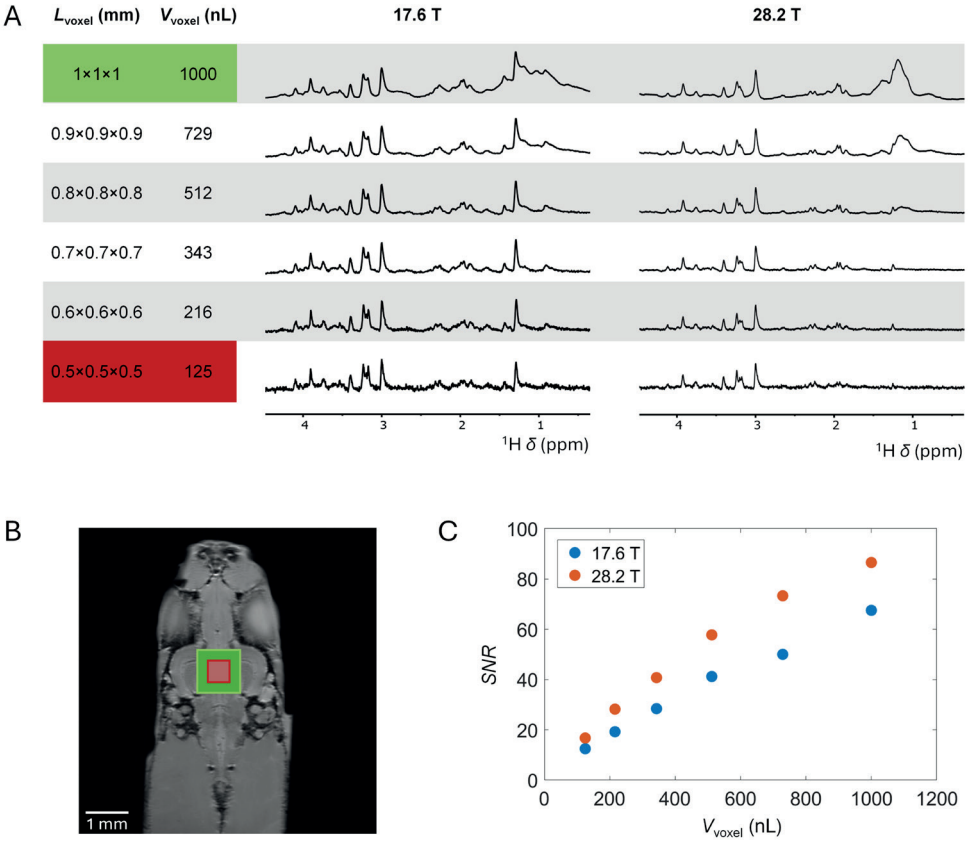

Figure 4.4. Effect of the voxel volume V_{voxel} on localized ^{1}H MRS spectra from adult zebrafish mid-brain at 17.6 T and 28.2 T. [A] *Cerebral metabolic spectra obtained with localized ^{1}H MRS at 28.2 T compared to 17.6 T at various V_{voxel}, ranging from 1000 nL to 125 nL.* ***[B]*** *Anatomical RARE image, coronal slice, of zebrafish brain regions to indicate position of selected PRESS voxels. V_{voxel} = 1000 nL (green) and V_{voxel} = 125 nL (red) are highlighted. The remaining voxels are situated between these indicated voxels.* ***[C]*** *SNR of the N(CH_3) tCr signal at δ = 3.03 ppm as a function of V_{voxel} at 17.6 T and 28.2 T. On average, an SNR increase of 40% was observed at 28.2 T compared to 17.6 T. Acquisition details: TR = 2000 ms, TE = 15 ms, ns = 1024, 2048 acquisition points, acquisition bandwidth 7462 Hz / 9.95 ppm at 17.6 T and 11904 Hz / 9.91 ppm at 28.2 T, 4 dummy scans, v_1 = 3 ppm, tBW = 10 kHz for all RF pulses. Water suppression and outer volume suppression were applied as specified in the method section.*

the zebrafish midbrain (Figure 4.4B) at 17.6 T and 28.2 T. Overall, a noteworthy 40% increase in SNR was observed at 28.2 T compared to 17.6 T (Figure 4.4C). However, it is important to note that during this analysis, the impact of increased magnetic field strength on elevated T_1 relaxation times was not accounted for[48-50]. Hence, it is plausible that a more significant enhancement of the SNR could be achieved by adjusting the repetition time to accommodate the increase in T_1. Given the small size of the zebrafish brain and its predominantly lipid-rich surrounding, elucidated in Supplementary Figure S4.2, voxels with isotropic dimensions surpassing beyond the brain tissue show broad and predominant lipid signals. These lipid signals are clearly visible around δ = 1.3 ppm and δ = 2.0 ppm and overlap with various cerebral metabolites, posing challenges for precise spectral analysis. In our examination of the midbrain, we observed that beyond a voxel volume of 512 nL, corresponding to a voxel size of 0.8 × 0.8 × 0.8 mm^3, interference from lipid signals became noticeable. Conversely, in the forebrain and hindbrain, which are both smaller and more elongated compared to the midbrain, we found for a voxel volume of 216 nL, corresponding to a voxel size of 0.6 × 0.6 × 0.6 mm^3, before interference from lipid signals became noticeable. We did not explore the potential benefits of non-isotropic voxel dimensions, which could potentially expand the brain coverage and thus enhance the signal obtained.

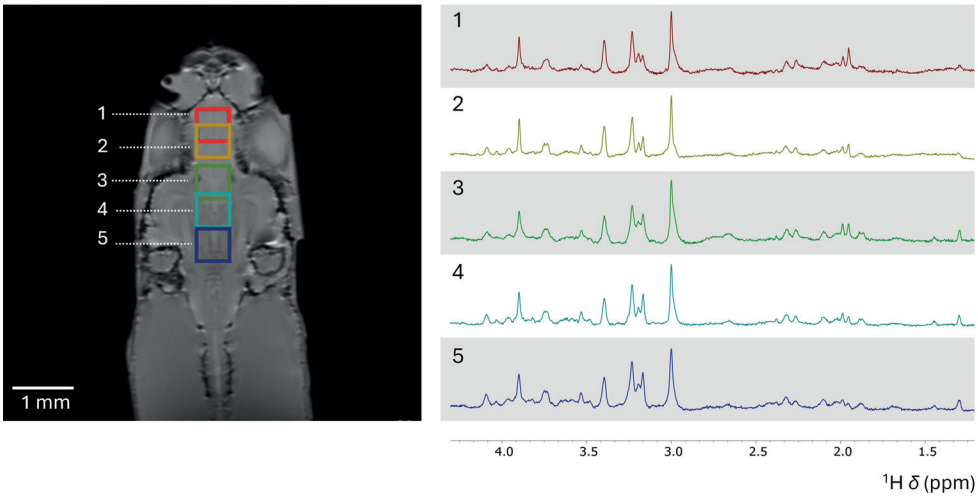

Figure 4.5. Optimized single voxel localized ^{1}H MRS spectra obtained from various locations in the adult zebrafish brain at 28.2 T. *Anatomical RARE image, coronal slice, of zebrafish brain regions to indicate position of selected PRESS voxels. Highly resolved spectra were obtained from 5 distinct brain locations. Here, location 1 and 2 are situated in the forebrain, while 3 – 5 are situated in the zebrafish mid-brain. Acquisition details: TR = 2000 ms, TE = 15 ms, ns = 4096, a voxel size of 0.6 × 0.6 × 0.6 mm^3 with V_{voxel} = 216 nL, 2048 acquisition points, acquisition bandwidth 11904 Hz / 9.91 ppm, tBW = 15 kHz, 4 dummy scans, v_1 = 3 ppm. Water suppression and outer volume suppression were applied as specified in the method section.*

Both at the UHF strength of 17.6 T and 28.2 T, spectra were acquired conducive to the identification and quantification of several cerebral metabolites, even at V_{voxel} = 125 nL, corresponding to a voxel size of 0.5 × 0.5 × 0.5 mm^3. The ability to obtain high-resolution spectra from such small PRESS voxels allows for the identification and quantification of cerebral metabolites in various small regions in the zebrafish brain. This is elucidated in Figure 4.5, where at 28.2 T the cerebral metabolic profiles were obtained from five distinct voxels with V_{voxel} = 216 nL, corresponding to a voxel size of 0.6 × 0.6 × 0.6 mm^3, utilizing *ns* = 4096, *tBW* = 15 kHz, and v_1 = 3 ppm. Highly resolved spectra were obtained. By focussing on specific regions of the zebrafish brain, insight can be gained on metabolic processes occurring in that particular area, providing valuable information about its function. Furthermore, it allows for monitoring metabolic changes in specific brain regions during neurodegenerative processes by utilizing pathological models.

Figure 4.6 shows that at 28.2 T, PRESS with V_{voxel} = 512 nL, corresponding to a voxel size of 0.8 × 0.8 × 0.8 mm^3, acquired in approximately 2 minutes allow the identification and quantification of predominant cerebral metabolites, including tCr (δ = 3.02 ppm and δ = 3.91 ppm), Tau (δ = 3.42 ppm and δ = 3.25 ppm), Glx (δ = 3.75 ppm), and Lac (δ = 1.3 ppm). Increasing the number of scans significantly improves the spectral quality. This augmentation enables the identification and quantification of additional metabolites, while increasing the SNR in alignment with $SNR \sim \sqrt{n}$, as illustrated in Figure 4.6B. At 17.6 T we achieved adequate SNR for identifying our target metabolites with V_{voxel} 512 nL, and *ns* = 1024, resulting in approximately 34 minutes scan time. For V_{voxel} = 216 nL, *ns* = 2048 was utilized, resulting in approximately 1 hour and 8 minutes total scan time. With the enhanced SNR at 28.2 T of approximately 40%, see Figure 4.4C, approximately half of the measurement time was required to obtain adequate SNR for each voxel volume (data not shown).

Metabolite identification and quantification at UHF

Based on presented results, single voxel localized MRS acquisition parameters were optimized to acquire a spectrum with extended measurement time of approximately 4.5 hours. Figure 4.7 shows the highly resolved spectrum obtained at 28.2 T from a PRESS voxel with V_{voxel} = 512 nL, *tBW* = 15 kHz and v_1 = 3 ppm. Compared to previous results obtained from *in vivo* analysis at 400 MHz[30], significantly improved spectra were obtained. This is most evident in the region between δ = 1.5 – 3.0 ppm, where important cerebral metabolite signals are present, *e.g.* GABA, NAA, NAAG, Glu, and Gln. Previously, the use of lower field strength required a larger PRESS voxel, *i.e.* V_{voxel} = 3375 nL, to acquire ample signal from cerebral metabolites for quantification. Consequently, the PRESS voxel surpassed beyond the brain tissue. This led to significant overlap of lipid- and cerebral metabolite signals. However, in our current analysis, improvements in the SNR acquired by utilization of UHF systems allow for smaller

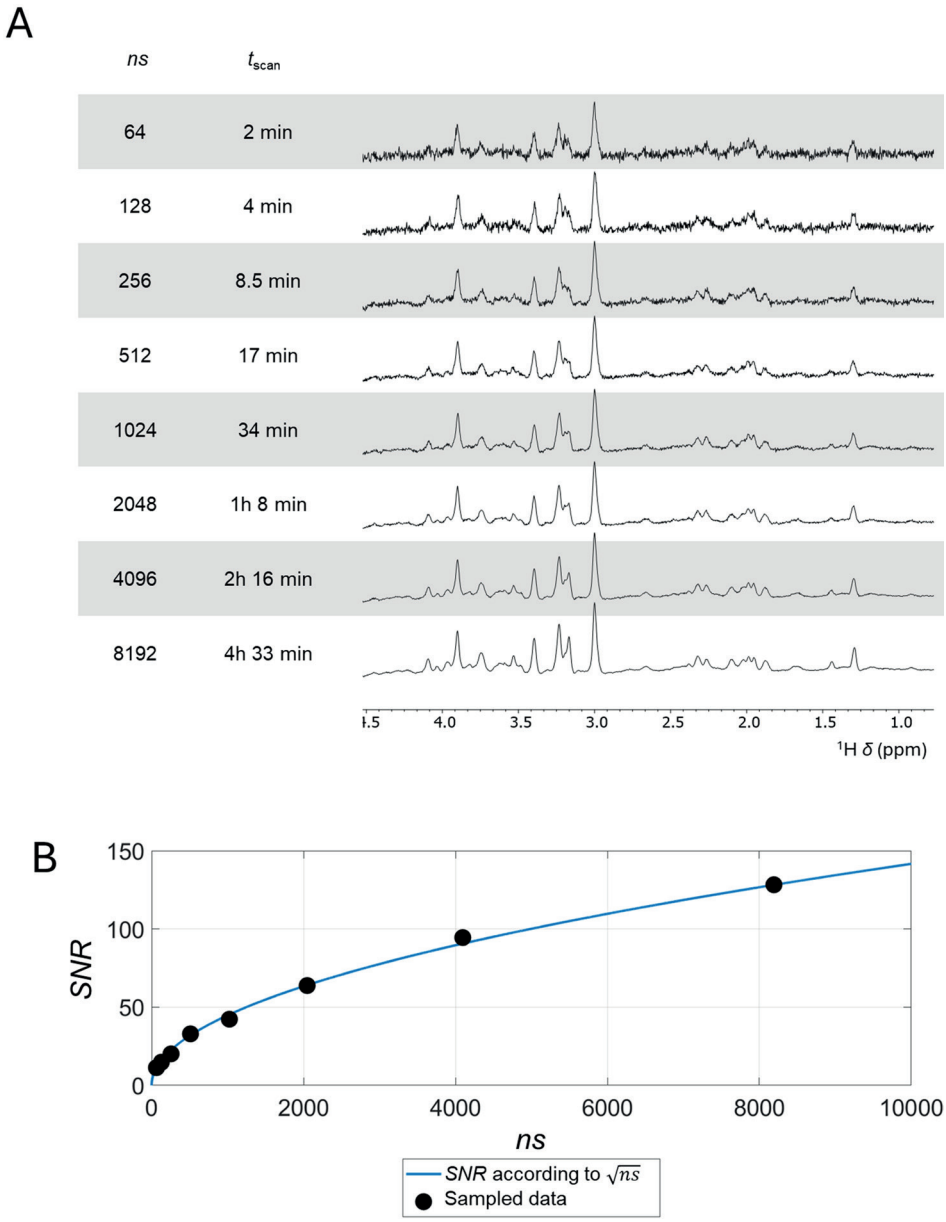

Figure 4.6. Impact of ns in localized ^{1}H MRS from adult zebrafish mid-brain at 28.2 T. [A] *Single voxel localized MRS spectra acquired from the mid-brain of an adult zebrafish, acquired with increasing ns* ***[B]*** *SNR of the tCr signal at δ = 3.03 ppm as a function of ns. Acquisition details: TR = 2000 ms, TE = 15 ms, a voxel size of 0.8 × 0.8 × 0.8 mm^3 with V_{voxel} = 512 nL, 2048 acquisition points, acquisition bandwidth 11904 Hz / 9.91 ppm, tBW = 15 kHz, 4 dummy scans, v_1 = 3 ppm. Water suppression and outer volume suppression were applied as specified in the method section.*

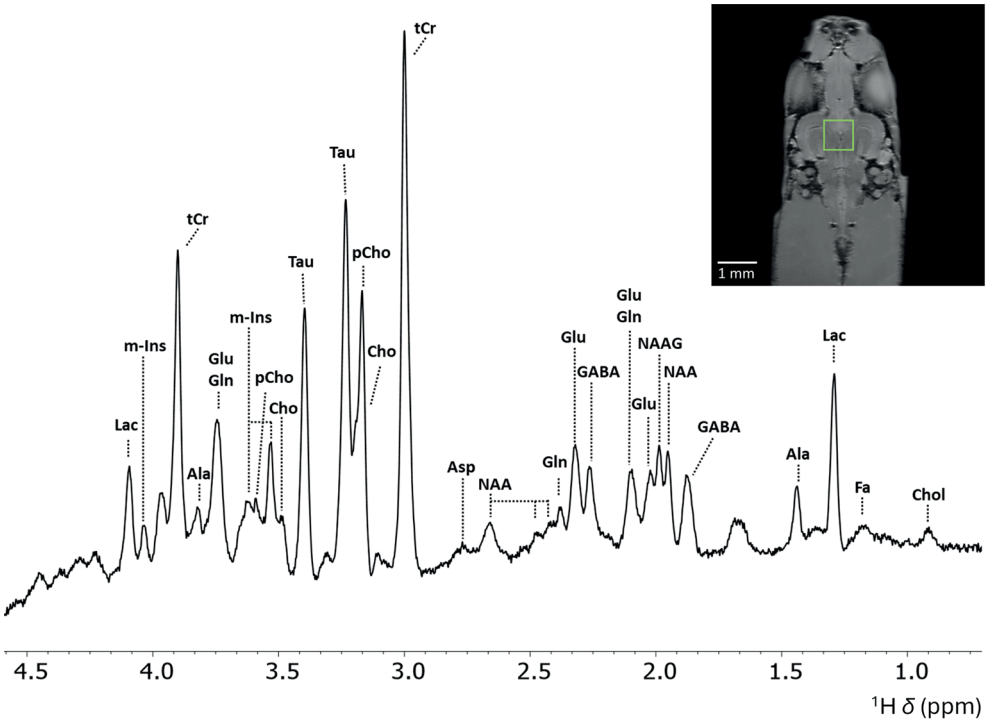

Figure 4.7. Optimized single voxel localized ^{1}H MRS spectrum from adult zebrafish mid-brain at 28.2 T. *Anatomical RARE image, coronal slice, of zebrafish brain regions to indicate position of selected PRESS voxel. Acquisition details: TR = 2000 ms, TE = 15 ms, a voxel size of 0.8 × 0.8 × 0.8 mm^3 with V_{voxel} = 512 nL, ns = 8192, scan time 4 hours 33 minutes, 2048 acquisition points, acquisition bandwidth 11904 Hz / 9.91 ppm at 28.2 T, 4 dummy scans, v_1 = 3 ppm, tBW = 15 kHz. Water suppression and outer volume suppression were applied as specified in the method section. Abbreviations; Lac – Lactate, m-Ins – myo-inositol, tCr – total creatine, Ala – alanine, Glu – glutamate, Gln – glutamine, pCho – phosphocholine, Cho – choline, Tau – taurine, Asp – aspartate, NAAG - N-acetylaspartyl-glutamate, NAA - N-acetylaspartate, GABA - γ-aminobutyric acid, FA – fatty acids, Chol – cholesterol.*

PRESS voxels and the lipid signals are no longer detected. Moreover, the $^2CH_3$ signals of NAA and NAAG are resolved, and are separated by $\Delta\delta$ = 0.04 ppm[39]. Frequently, due to spectral overlap, the $^2CH_3$ signals of NAA and NAAG are reported as the tNAA[51] signal or simply as NAA[6,7,9,10], given the predominant contribution of NAA in the human brain. Post-processing techniques enable to resolve these signals[52], or alternatively, quantification can be achieved through carefully designed sequences specifically for NAA and NAAG detection, such as the MEGA-PRESS sequence by Edden *et al.* [53]. Previously the separation of NAA and NAAG signals was achieved using high-resolution localized two-dimensional COSY MRS in mouse brain[54]. As demonstrated here, direct separation of NAA and NAAG signals can be achieved through

single voxel localized one-dimensional MRS at UHF strengths. Furthermore, we observe a very clear separation of the GABA, Glu and Gln signals, providing a solid basis for comparing levels of compounds involved in the glutamate/GABA – glutamine brain cycle.

In Figure 4.8, we present statistical analysis of the cerebral metabolic profile obtained from different regions in the zebrafish brain, acquired at 28.2 T (n = 3). In the midbrain, PRESS was performed with V_{voxel} = 512 nL and a voxel size of 0.8 × 0.8 × 0.8 mm^3. In the forebrain

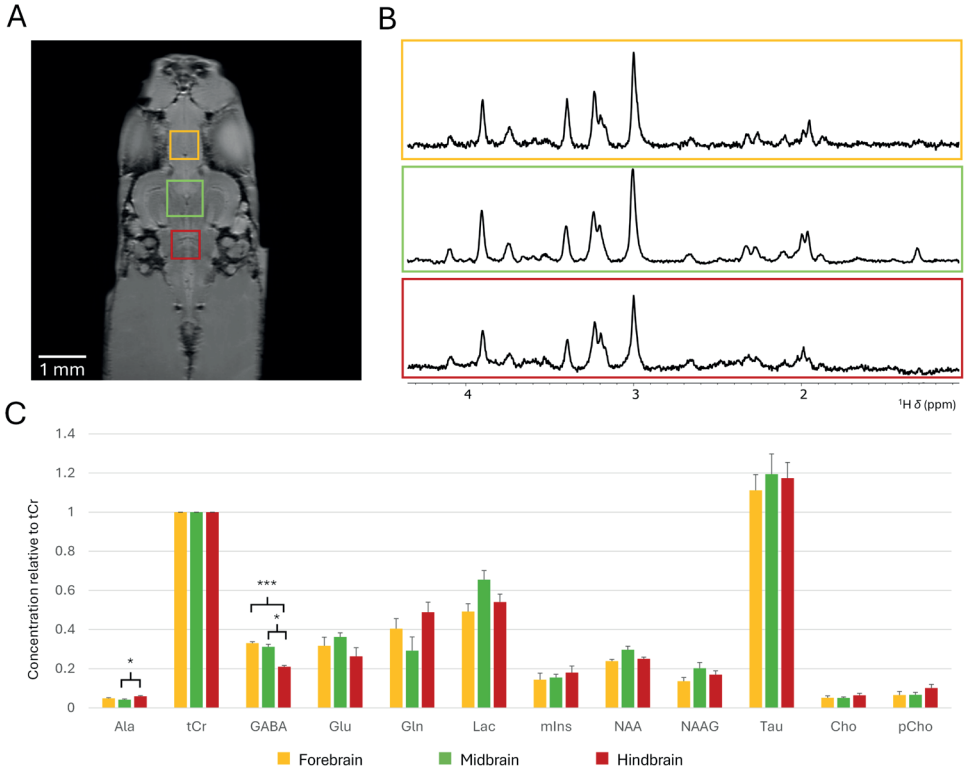

Figure 4.8. Comparison of cerebral metabolites levels in the forebrain, midbrain, and hindbrain of adult zebrafish at 28.2 T [A] *Anatomical RARE image, coronal slice, of zebrafish brain regions to indicate position of selected PRESS voxels in the forebrain, midbrain, and hindbrain* ***[B]*** *Single voxel localized ¹H MRS spectra obtained from the forebrain, midbrain, and hindbrain.* ***[C]*** *Comparison of cerebral metabolite levels relative to tCr signal at δ = 3.03 ppm. Statistically significant differences in metabolite levels between different brain regions obtained by unpaired t-test, assuming Gaussian distribution, n = 3, with p < 0.05 considered to indicate a significant difference. * p < 0.05, *** p < 0.05. 28.2 T. In all images, yellow label indicates the forebrain, green the midbrain, and red the hindbrain. Abbreviations; Ala – alanine, tCr – total creatine, GABA - γ-aminobutyric acid, Glu – glutamate, Gln – glutamine, Lac – Lactate, m-Ins – myo-inositol, NAA - N-acetylaspartate, NAAG - N-acetylaspartyl-glutamate, Tau – taurine, Cho – choline, pCho – phosphocholine*

and hindbrain, PRESS was performed with V_{voxel} = 216 nL and a voxel size of 0.6 × 0.6 × 0.6 mm^3 (see Figure 4.8A). Highly resolved spectra were obtained from each region (see Figure 4.8B). Quantification of metabolites was performed with Chenomx. As indicated, chemical shift displacement effects necessitate quantification utilizing consistent chemical groups of a specific metabolite for all analysis, as utilizing different signals can lead to different quantitative outcomes (see Table 4.1). A full overview of the signals used for quantification is given in Table 4.3. We observed minimal variation in metabolite levels across the studied brain regions. However, significantly lower levels of GABA were found in the hindbrain compared to the forebrain ($p < 0.005$) and midbrain ($p < 0.05$). This discrepancy can be attributed to voxel placement. Throughout the zebrafish brain, GABAergic neurons are not uniformly distributed. Regions including the optic tectum, the subpallium, and the corpus cerebelli exhibit higher densities of GABAergic neurons[55,56]. In our analysis, PRESS voxels in the forebrain and midbrain predominantly overlapped with these GABAergic neuron rich regions. However, the hindbrain voxel, situated just posterior to the cerebellar corpus, appears to have been positioned within a region characterised by lower levels of GABAergic neurons, thereby elucidating the observe difference in GABA levels.

Table 4.3. *Estimated concentrations of brain metabolites at 28.2 T, relative to the tCr signal at 3.03 ppm, in the forebrain, midbrain, and hindbrain in young adult zebrafish (n = 3). Annotation of the molecular groups is consistent with those used by Govindaraju et al.* [39].

Metabolite	Group used for quantification (ppm)	Forebrain Conc. rel. tCr (± *SE*)	Midbrain Conc. rel. tCr (± *SE*)	Hindbrain Conc. rel. tCr (± *SE*)
Ala	$^3CH_3$ (δ = 1.47 ppm)	0.049 ± 0.008	0.042 ± 0.004	0.059 ± 0.003
GABA	$^3CH_2$ (δ = 1.89 ppm)	0.331 ± 0.029	0.312 ± 0.013	0.21 ± 0.007
Glu	$^4CH_2$ (δ = 2.45 ppm)	0.317 ± 0.025	0.362 ± 0.021	0.263 ± 0.044
Gln	^2CH (δ = 3.75 ppm)	0.405 ± 0.006	0.293 ± 0.07	0.489 ± 0.051
Lac	^2CH (δ = 4.09 ppm)	0.492 ± 0.044	0.655 ± 0.047	0.541 ± 0.04
m-Ins	^4CH (δ = 3.61 ppm)	0.144 ± 0.016	0.155 ± 0.017	0.18 ± 0.034
NAA	$^2CH_3$ (δ = 2.01 ppm)	0.239 ± 0.034	0.297 ± 0.018	0.25 ± 0.009
NAAG	$^2CH_3$ (δ = 2.04 ppm)	0.136 ± 0.02	0.203 ± 0.03	0.17 ± 0.019
Tau	$^2CH_2$ (δ = 3.25 ppm)	1.111 ± 0.017	1.145 ± 0.138	1.174 ± 0.081
Cho	$N(CH_3)_3$ (δ = 3.19 ppm)	0.052 ± 0.004	0.05 ± 0.006	0.064 ± 0.01
pCho	$N(CH_3)_3$ (δ = 3.21 ppm)	0.065 ± 0.004	0.067 ± 0.012	0.059 ± 0.003

4. CONCLUSION

In conclusion, single voxel localized magnetic resonance spectroscopy at ultra-high magnetic fields provides distinct advantages and challenges for the identification and quantification of cerebral metabolites in the tiny zebrafish brain. Chemical shift displacements are significant and need to be taken into account not only during the experimental design, but also during data processing. However, ultra-high fields provide the necessary signal-to-noise and spectral separation required to identify and quantify a wide range of cerebral metabolites in a volume as small as 125 nL.

In future, our optimized methods, with relatively short measurement times of up to 30 minutes, are well-suited for implementation in *in vivo* studies. *In vivo* measurements enable the utilization of various zebrafish models of human pathological diseases for longitudinal studies by allowing continuous and non-invasive monitoring of metabolic changes over time. This approach facilitates the study of disease progression and the long-term effects of therapeutic interventions within the same subjects, providing a more comprehensive understanding of the underlying mechanisms. Furthermore, various other non-invasive MRS measurements could be tested and optimized for UHFs, not discussed in the current work. This includes the optimization and comparison of other available single voxel localized ^{1}H MRS methods including stimulated echo acquisition mode (STEAM) or semi-localization by adiabatic-selective refocusing (sLASER) sequences. Furthermore, multi-voxel MRS methods including chemical shift imaging (CSI) for whole brain analysis could be optimized. Besides different methods, a metabolic region that was not taken into consideration during the experiments presented here, was the chemical shift region between δ = 6.00 ppm and δ = 8.00 ppm. This chemical shift region contains the signals of various energy metabolites, including ATP, ADP, NADH, NAD+, NADPH, and NADP+. Monitoring these metabolites non-invasively would potentially provide valuable information during metabolic analysis of, for instance, neurodegenerative diseases. However, these metabolites are separated by $\Delta\delta$ = 3 - 5 ppm from tCr for quantification, which could potentially make quantification difficult as a consequence of chemical shift displacement effects. Finally, localized MRS utilizing different nuclei might provide valuable information. In particular, localized ^{31}P MRS can provide valuable information on phosphorus-containing (cerebral) metabolites including phosphocholine, glycerosphocholine, ATP, and NADH.

ACKNOWLEDGEMENTS

Experiments at the 28.2 T and 17.6 T instruments were supported by the uNMR-NL Grid: A distributed, state-of-the-art Magnetic Resonance facility for the Netherlands (NWO grant 184.032.207). The authors thank Andrei Gurinov for the technical help provided at the 28.2 T instrument, Karthick Sai Sankar Gupta and Maria Nardella for technical help provided at the 17.6 T instrument, and Holger Scheidt for the technical help provided at the 14.1 T instrument.

REFERENCES

1 Alger, J. R. in *Encyclopedia of Neuroscience* (ed Larry R. Squire) 601-607 (Academic Press, 2009).

2 Sharma, U. & Jagannathan, N. R. Metabolism of prostate cancer by magnetic resonance spectroscopy (MRS). *Biophys Rev* **12**, 1163-1173 (2020). https://doi.org/10.1007/s12551-020-00758-6

3 Cowin, G. J. *et al.* Magnetic resonance imaging and spectroscopy for monitoring liver steatosis. *J Magn Reson Imaging* **28**, 937-945 (2008). https://doi.org/10.1002/jmri.21542

4 Ali, H. A. *et al.* Predictive Value of *In vivo* MR Spectroscopy With Semilocalization by Adiabatic Selective Refocusing in Differentiating Clear Cell Renal Cell Carcinoma From Other Subtypes. *AJR Am J Roentgenol* **214**, 817-824 (2020). https://doi.org/10.2214/AJR.19.22023

5 Brown, J. J., Mirowitz, S. A., Sandstrom, J. C. & Perman, W. H. MR Spectroscopy of the heart. *American Journal of Roentgenology* **155** (1990).

6 Graff-Radford, J. & Kantarci, K. Magnetic resonance spectroscopy in Alzheimer's disease. *Neuropsychiatr Dis Treat* **9**, 687-696 (2013). https://doi.org/10.2147/NDT.S35440

7 Weinberg, B. D., Kuruva, M., Shim, H. & Mullins, M. E. Clinical Applications of Magnetic Resonance Spectroscopy in Brain Tumors: From Diagnosis to Treatment. *Radiol Clin North Am* **59**, 349-362 (2021). https://doi.org/10.1016/j.rcl.2021.01.004

8 Nakahara, T. *et al.* Glutamatergic and GABAergic metabolite levels in schizophrenia-spectrum disorders: a meta-analysis of (1)H-magnetic resonance spectroscopy studies. *Mol Psychiatry* **27**, 744-757 (2022). https://doi.org/10.1038/s41380-021-01297-6

9 Kalra, S. Magnetic Resonance Spectroscopy in ALS. *Front Neurol* **10**, 482 (2019). https://doi.org/10.3389/fneur.2019.00482

10 Pan, J. W. & Kuzniecky, R. I. Utility of magnetic resonance spectroscopic imaging for human epilepsy. *Quant Imaging Med Surg* **5**, 313-322 (2015). https://doi.org/10.3978/j.issn.2223-4292.2015.01.03

11 Sajja, B. R., Wolinsky, J. S. & Narayana, P. A. Proton magnetic resonance spectroscopy in multiple sclerosis. *Neuroimaging Clin N Am* **19**, 45-58 (2009). https://doi.org/10.1016/j.nic.2008.08.002

12 Shoeibi, A. *et al.* Brain proton magnetic resonance spectroscopy in patients with Parkinson's disease. *Curr J Neurol* **21**, 156-161 (2022). https://doi.org/10.18502/cjn.v21i3.11108

13 Pal, M. M. Glutamate: The Master Neurotransmitter and Its Implications in Chronic Stress and Mood Disorders. *Front Hum Neurosci* **15**, 722323 (2021). https://doi.org/10.3389/fnhum.2021.722323

14 Ochoa-de la Paz, L. D., Gulias-Cañizo, R., D´Abril Ruíz-Leyja, E., Sánchez-Castillo, H. & Parodí, J. The role of GABA neurotransmitter in the human central nervous system, physiology, and pathophysiology. *Revista Mexicana de Neurociencia* **22** (2021). https://doi.org/10.24875/rmn.20000050

15 Kalra, S. & Arnold, D. L. Magnetic Resonance Spectroscopy for Monitoring Neuronal Integrity in Amyotrophic Lateral Sclerosis. *Advances in experimental medicine and biology* **576** (2006). https://doi.org/https://doi.org/10.1007/0-387-30172-0

16 Bertran-Cobo, C. *et al.* A Neurometabolic Pattern of Elevated Myo-Inositol in Children Who Are HIV-Exposed and Uninfected: A South African Birth Cohort Study. *Front Immunol* **13**, 800273 (2022). https://doi.org/10.3389/fimmu.2022.800273

17 Bashirova, N. *et al.* A mechanistic understanding of the effects of polyethylene terephthalate nanoplastics in the zebrafish (Danio rerio) embryo. *Sci Rep* **13**, 1891 (2023). https://doi.org/10.1038/s41598-023-28712-y

18 Annunziato, M. *et al.* An integrated systems-level model of the toxicity of brevetoxin based on high-resolution magic-angle spinning nuclear magnetic resonance (HRMAS NMR) metabolic profiling of zebrafish embryos. *Sci Total Environ* **803**, 149858 (2022). https://doi.org/10.1016/j.scitotenv.2021.149858

19 Annunziato, M. *et al.* An Integrated Metabolomics-Based Model, and Identification of Potential Biomarkers, of Perfluorooctane Sulfonic Acid Toxicity in Zebrafish Embryos. *Environ Toxicol Chem* (2024). https://doi.org/10.1002/etc.5824

20 Annunziato, M. *et al.* High-Resolution Magic Angle Spinning (HRMAS) NMR Identifies Oxidative Stress and Impairment of Energy Metabolism by Zearalenone in Embryonic Stages of Zebrafish (Danio rerio), Olive Flounder (Paralichthys olivaceus) and Yellowtail Snapper (Ocyurus chrysurus). *Toxins (Basel)* **15** (2023). https://doi.org/10.3390/toxins15060397

21 Hu, W. *et al.* Transcriptomic and Metabolomic Studies Reveal That Toll-like Receptor 2 Has a Role in Glucose-Related Metabolism in Unchallenged Zebrafish Larvae (Danio rerio). *Biology (Basel)* **12** (2023). https://doi.org/10.3390/biology12020323

22 Eeza, M. N. H. *et al.* An integrated systems-level model of ochratoxin A toxicity in the zebrafish (Danio rerio) embryo based on NMR metabolic profiling. *Sci Rep* **12**, 6341 (2022). https://doi.org/10.1038/s41598-022-09726-4

23 Berry, J. P. *et al.* High-Resolution Magic Angle Spinning Nuclear Magnetic Resonance of Intact Zebrafish Embryos Detects Metabolic Changes Following Exposure to Teratogenic Polymethoxyalkenes from Algae. *Zebrafish* **13**, 456-465 (2016). https://doi.org/10.1089/zeb.2016.1280

24 Howe, K. *et al.* The zebrafish reference genome sequence and its relationship to the human genome. *Nature* **496**, 498-503 (2013). https://doi.org/10.1038/nature12111

25 Saleem, S. & Kannan, R. R. Zebrafish: an emerging real-time model system to study Alzheimer's disease and neurospecific drug discovery. *Cell Death Discov* **4**, 45 (2018). https://doi.org/10.1038/s41420-018-0109-7

26 Basheer, F., Dhar, P. & Samarasinghe, R. M. Zebrafish Models of Paediatric Brain Tumours. *Int J Mol Sci* **23** (2022). https://doi.org/10.3390/ijms23179920

27 Doyle, J. M. & Croll, R. P. A Critical Review of Zebrafish Models of Parkinson's Disease. *Front Pharmacol* **13**, 835827 (2022). https://doi.org/10.3389/fphar.2022.835827

28 D'Amora, M. *et al.* Zebrafish as an Innovative Tool for Epilepsy Modeling: State of the Art and Potential Future Directions. *Int J Mol Sci* **24** (2023). https://doi.org/10.3390/ijms24097702

29 Fontana, B. D., Mezzomo, N. J., Kalueff, A. V. & Rosemberg, D. B. The developing utility of zebrafish models of neurological and neuropsychiatric disorders: A critical review. *Exp Neurol* **299**, 157-171 (2018). https://doi.org/10.1016/j.expneurol.2017.10.004

30 Kabli, S., Spaink, H. P., De Groot, H. J. & Alia, A. In vivo metabolite profile of adult zebrafish brain obtained by high-resolution localized magnetic resonance spectroscopy. *J Magn Reson Imaging* **29**, 275-281 (2009). https://doi.org/10.1002/jmri.21609

31 Ullmann, J. F., Calamante, F., Collin, S. P., Reutens, D. C. & Kurniawan, N. D. Enhanced characterization of the zebrafish brain as revealed by super-resolution track-density imaging. *Brain Struct Funct* **220**, 457-468 (2015). https://doi.org/10.1007/s00429-013-0667-7

32 Soila, K. P., Viamonte, M. & Starewicz, P. M. Chemical shift misregistraton effect in magnetic resonance imaging. *Radiology* **153** (1984).

33 Lufkin, R., Anselmo, M., Crues, J. & Smoker, W. Magnetic field strength dependence of chemical shift artifacts. *Computerized Medical Imaging and Graphics* **12**, 8 (1988). https://doi.org/https://doi.org/10.1016/0895-6111(88)90002-X

34 Krug, J. R. *et al.* Assessing spatial resolution, acquisition time and signal-to-noise ratio for commercial microimaging systems at 14.1, 17.6 and 22.3 T. *J Magn Reson* **316**, 106770 (2020). https://doi.org/10.1016/j.jmr.2020.106770

35 Hidalgo-Tobon, S. S. Theory of gradient coil design methods for magnetic resonance imaging. *Concepts in Magnetic Resonance Part A* **36A**, 223-242 (2010). https://doi.org/10.1002/cmr.a.20163

36 He, J. *et al.* Leptin deficiency affects glucose homeostasis and results in adiposity in zebrafish. *J Endocrinol* **249**, 125-134 (2021). https://doi.org/10.1530/JOE-20-0437

37 Bottomley, P. A. Selective volume method for performing localized NMR spectroscopy. United States of America patent (1984).

38 Tkac, I., Starcuk, Z., Choi, I. Y. & Gruetter, R. In vivo1H NMR spectroscopy of rat brain at 1 ms echo time. *Magnetic Resonance in Medicine* **41**, 649-656 (1999). https://doi.org/10.1002/(sici)1522-2594(199904)41:4<649::Aid-mrm2>3.0.Co;2-g

39 Govindaraju, V., Young, K. & Maudsley, A. A. Proton NMR chemical shifts and coupling constants for brain metabolites. *NMR in Biomedicine* **13** (2000).
40 Akhtar, M. T., Mushtaq, M. Y., Verpoorte, R., Richardson, M. K. & Choi, Y. H. Zebrafish as a Model for Systems Medicine R&D: Rethinking the Metabolic Effects of Carrier Solvents and Culture Buffers Determined by (1)H NMR Metabolomics. *OMICS* **20**, 42-52 (2016). https://doi.org/10.1089/omi.2015.0119
41 Markley, J. L. *et al.* New bioinformatics resources for metabolomics. *Pacific symposium on biocomputing* **157** (2007).
42 Graaf de, R. A. *In-vivo NMR Spectroscopy: Principles and Techniques*. (John Wiley & Sons, 2007).
43 Kreis, R. Issues of spectral quality in clinical 1H-magnetic resonance spectroscopy and a gallery of artifacts. *NMR Biomed* **17**, 361-381 (2004). https://doi.org/10.1002/nbm.891
44 Dumoulin, M., Zimmerman, E., Hurd, R. & Hancu, I. Increased brain metabolite T2 relaxation times in patients with Alzheimer's disease *Proc. Intl. Soc. Mag. Reson. Med.* **13** (2005).
45 Isobe, T. *et al.* Effect of J coupling at T2 relaxation in assessing of methyl lactate signal using PRESS sequence MR spectroscopy. *jpn. j. med. phys* **25** (2005).
46 Xin, L., Gambarota, G., Mlynarik, V. & Gruetter, R. Proton T2 relaxation time of J-coupled cerebral metabolites in rat brain at 9.4 T. *NMR Biomed* **21**, 396-401 (2008). https://doi.org/10.1002/nbm.1205
47 Mulkern, R. & Bowers, J. Density Matrix Calculations of AB Spectra from Multipulse Sequences: Quantum Mechanics Meets In Vivo Spectroscopy. *Concepts in magnetic resonance* **6** (1994).
48 Bottomley, P. A., Foster, T. H., Argersinger, R. E. & Pfeifer, L. M. A review of normal tissue hydrogen NMR relaxation times and relaxation mechanisms from 1-100 MHz: dependence on tissue type, NMR frequency, temperature, species, excision, and age. *Med Phys* **11**, 425-448 (1984). https://doi.org/10.1118/1.595535
49 de Graaf, R. A. *et al.* High magnetic field water and metabolite proton T1 and T2 relaxation in rat brain in vivo. *Magn Reson Med* **56**, 386-394 (2006). https://doi.org/10.1002/mrm.20946
50 Korb, J. P. & Bryant, R. G. Magnetic field dependence of proton spin-lattice relaxation times. *Magn Reson Med* **48**, 21-26 (2002). https://doi.org/10.1002/mrm.10185
51 Reischauer, C. *et al.* In-vivo evaluation of neuronal and glial changes in amyotrophic lateral sclerosis with diffusion tensor spectroscopy. *Neuroimage Clin* **20**, 993-1000 (2018). https://doi.org/10.1016/j.nicl.2018.10.001
52 Provencher, S. W. Estimation of metabolite concentrations from localized in vivo proton NMR spectra. *Magnetic Resonance in Medicine* **30** (1993).
53 Edden, R. A., Pomper, M. G. & Barker, P. B. In vivo differentiation of N-acetyl aspartyl glutamate from N-acetyl aspartate at 3 Tesla. *Magn Reson Med* **57**, 977-982 (2007). https://doi.org/10.1002/mrm.21234
54 Braakman, N., Oerther, T., de Groot, H. J. & Alia, A. High resolution localized two-dimensional MR spectroscopy in mouse brain in vivo. *Magn Reson Med* **60**, 449-456 (2008). https://doi.org/10.1002/mrm.21662
55 Satou, C. *et al.* Transgenic tools to characterize neuronal properties of discrete populations of zebrafish neurons. *Development* **140**, 3927-3931 (2013). https://doi.org/10.1242/dev.099531
56 Tabor, K. M. *et al.* Brain-wide cellular resolution imaging of Cre transgenic zebrafish lines for functional circuit-mapping. *Elife* **8** (2019). https://doi.org/10.7554/eLife.42687

5. APPENDIX

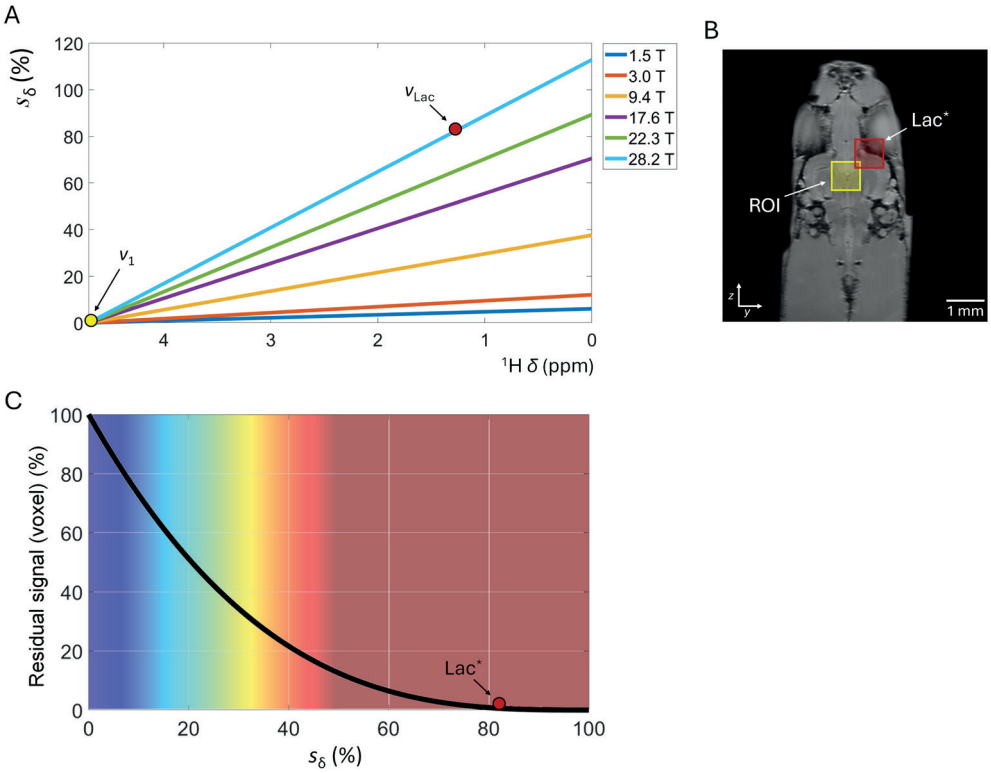

Figure S4.1. Chemical shift displacement effect in single voxel localized MRS [A] *s_δ (%) at chemical shift of ^{1}H (ppm) for increasing magnetic field strengths for PRESS. ν_1, excitation frequency (ppm); ν_{Lac}, chemical shift of the $^3CH_3$ group lactate at δ = 1.32 ppm.* ***[B]*** *Impact of the chemical shift displacement on the selected ROI and the actual location from which the lactate signal is obtained at 28.2 T. In this illustration, only the chemical shift displacement in the z and y direction are shown.* ***[C]*** *s_δ (%) versus the remaining fraction of the signal from the selected voxel (%). Colour code is used to visualize severity of s_δ. Exceeding a chemical shift displacement effect of 50% per transmitter RF pulse, almost 90% of the signal falls beyond the selected PRESS voxel. The theoretical signal loss is determined as the percentage of the signal that extends beyond the selected PRESS voxel due to chemical shift displacement. * Chemical shift displacement of lactate assuming $\mathbf{B}_0$ = 28.2 T, tBW = 5 kHz, a voxel size of 0.8 × 0.8 × 0.8 mm^3 with V_{voxel} = 512 nL, and ν_1 = 4.7 ppm.*

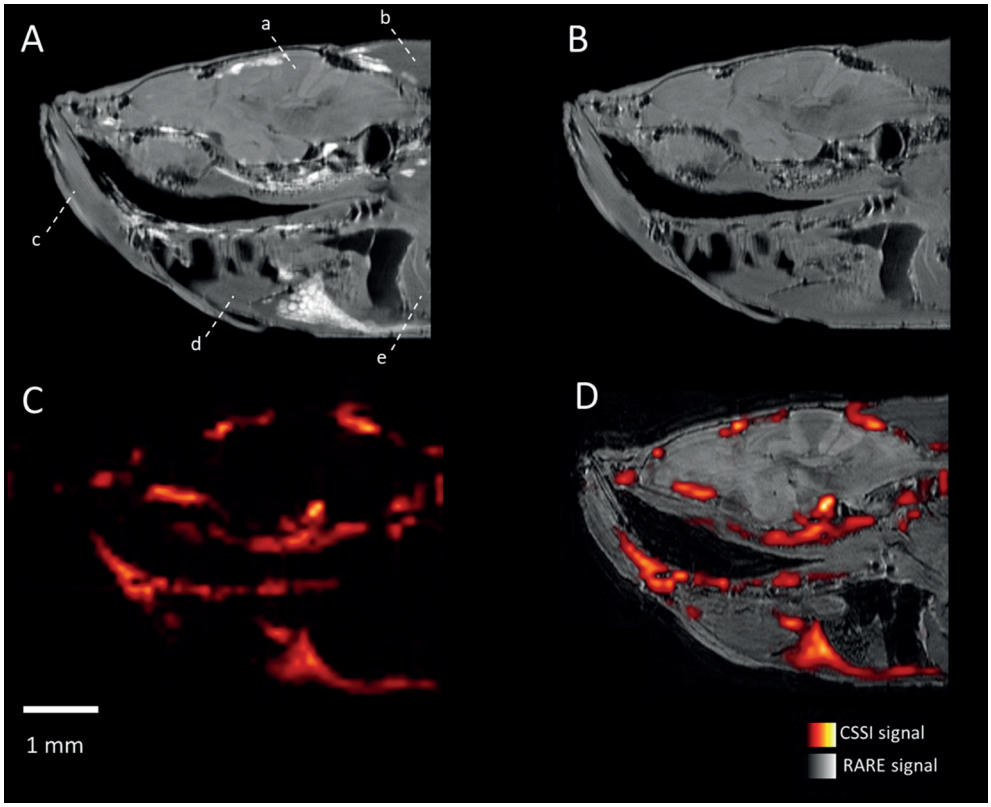

Figure S4.2. Chemical shift selective imaging (cssi) for the visualization of lipid distribution in the zebrafish head at 28.2 T. *For these measurements, wild-type three-month-old adult-zebrafish, fixed in 4% buffered paraformaldehyde were utilized as described previously.* ***[A]*** *Sagittal 2D RARE image without fat suppression. Chemical shift artifact causes displacement of lipids in the frequency-encode direction, which increases with* B_0. ***[B]*** *Sagittal 2D RARE image with fat suppression.* ***[C]*** *Lipid signal obtained by 3D cssi.* ***[D]*** *3D cssi signal (red colour scale) overlayed on 3D RARE image (grey colour scale), showing the distribution of lipids in the zebrafish head. Data acquisition and processing were performed using Paravision 360 v3.3. Acquisition details: 2D RARE images: TR = 3000 ms, TE = 5.6 ms, ns = 64, resolution 23 µm × 23 µm × 100 µm, RARE factor 4. 3D RARE image: TR = 1800 ms, TE = 6.1 ms, ns = 4, resolution 23 µm × 23 µm × 47 µm, RARE factor 16. 3D cssi image: TR = 2000 ms, TE = 4.5 ms, ns = 1, resolution 94 µm × 94 µm × 188 µm, shift selective excitation frequency 1200.7 MHz (1.24 ppm), excitation pulse bandwidth 2000 Hz (1.6 ppm). (a) brain; (b) muscle; (c) dentary; (d) sternohyoid; (e) liver*

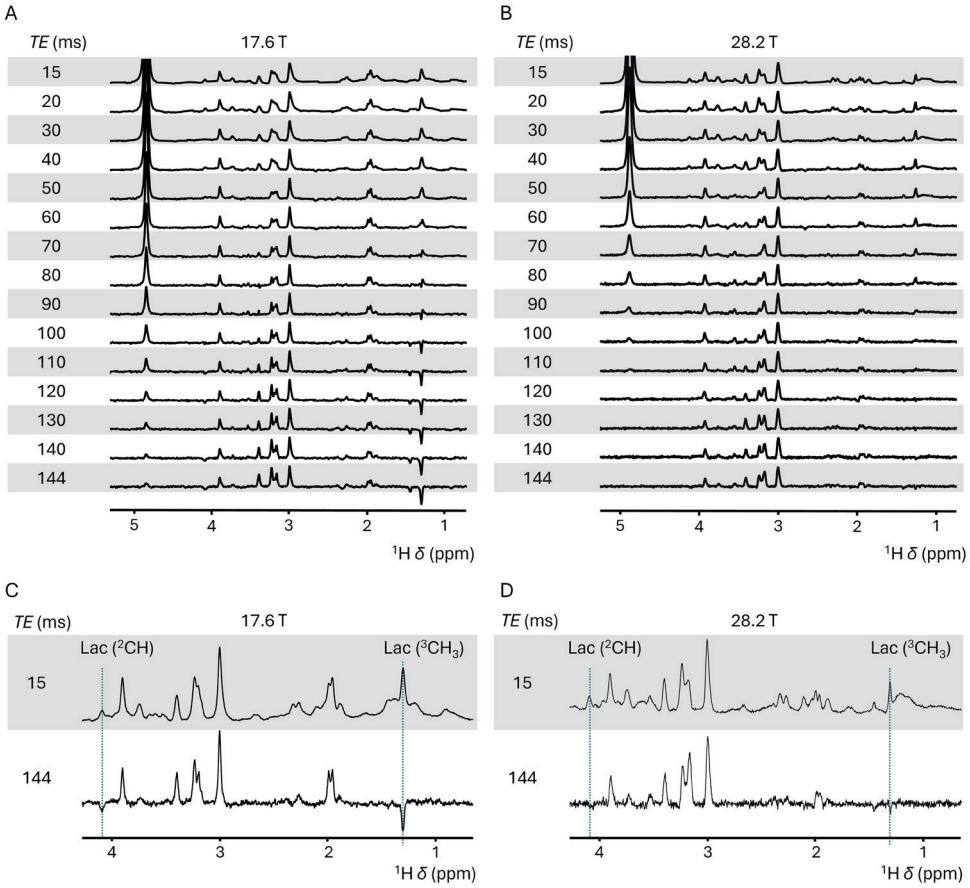

Figure S4.3. Full comparison of echo times in single voxel localized ^{1}H MRS spectrum from adult zebrafish midbrain at 17.6 T and 28.2 T, in the range between 15 ms and 144 ms. [A – B] *Single voxel localized MRS spectra acquired for echo times at 17.6 T and 28.2 T, respectively.* ***[C - D]*** *Comparison of spectra obtained at a short echo time of 15 ms and a long echo time of 144 ms at 17.6 T and 28.2 T. Particular attention is directed towards the lactate 180° phase shift at 144 ms, contributed to J-coupling induced signal dephasing. This effect is prominently evident at 17.6 T. However, at 28.2 T, due to escalated chemical shift displacement effects, the lactate signal acquired at 144 ms is submerged within spectral noise, highlighting the necessity for compensation strategies to address these effects.*

5

LOCALIZED MRS AT 28.2 T REVEALS ALTERATION OF CEREBRAL METABOLITES IN TOLL-LIKE RECEPTOR 2 DEFICIENT ZEBRAFISH*

* Manuscript in preparation for publication

ABSTRACT

Toll-like receptor 2 (TLR2), a member of the TLR protein family, is crucial for immune and inflammatory responses. Although TLR2 is mainly found in immune cells, it is also present in the brain, particularly in microglia and astrocytes. In our recent work using diffusion MRI, we showed that a deficiency in the TLR2 gene causes specific changes in the brain microstructure, potentially indicative of compromised white matter integrity and axonal degeneration. However, it remains largely unclear if genomic deletion of TLR2 also has a direct effect on the cerebral metabolism. In the current work, we utilize non-invasive nuclear magnetic resonance spectroscopy techniques, namely high-resolution magic angle spinning nuclear magnetic resonance (HR-MAS NMR) and localised ^{1}H magnetic resonance spectroscopy (MRS) to study metabolic changes in the brain of adult TLR2 deficient (*tlr2*$^{-/-}$) zebrafish. HR-MAS NMR at 14.1 T (600 MHz) provided highly resolved metabolic spectra of whole intact brain samples, showing significant changes in the levels of several neurotransmitters, energy-, and cell-specific metabolites in the *tlr2*$^{-/-}$ group compared to a control group. To compare metabolic profile from very specific brain regions, we applied localized ^{1}H MRS at the state-of-the-art magnetic field strength of 28.2 T. Our results show a brain-wide increase in lactate and reduced levels of N-acetyl aspartate (NAA) in areas with specific white matter structures in the *tlr2*$^{-/-}$ group compared to a control group, indicating reduced white matter integrity. Furthermore, we observed an alteration in the balance of excitatory and inhibitory neurotransmitters, as well as a shifts in cell-specific metabolites indicative of neuroinflammation. These results suggest that TLR2 deficiency directly affects the cerebral metabolic profile, supporting previous findings of microstructural changes in the brains of *tlr2*$^{-/-}$ zebrafish.

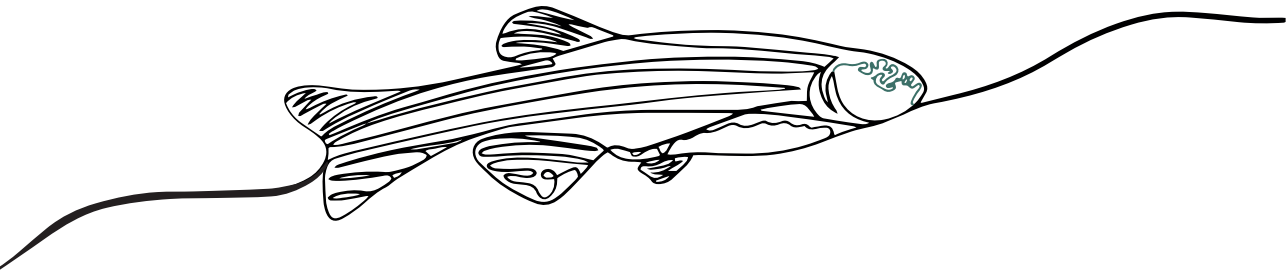

1. INTRODUCTION

Toll-like receptors (TLRs) have a vital role in the innate immune system as part of the pattern recognition receptors (PPR) [1]. The N-terminal ectodomain located on the outside of the TLR membrane recognises and binds to specific pathogen-associated molecular patterns (PAMPs) or danger-associated molecular patterns (DAMPs), originating from potentially harmful microorganisms and damaged host tissue, respectively[2]. Activation of TLRs by PAMPs or DAMPs initiates events leading to the syntheses of antimicrobial peptides and pro-inflammatory cytokines[3]. Specific TLRs can distinguish specific DAMPs and PAMPs [4,5]. Among the TLRs, TLR2 stands out as a focal point of research. First identified in 1998[6,7], TLR2 exhibits a remarkable captivity to recognise a diverse array of PAMPs and DAMPs[1], with particular interest for its pivotal role in the immune response to *Mycobacterium tuberculosis*[8] – an infection responsible for developing tuberculosis. TLR2 is expressed on the cell surface of various cell types, including macrophages, dendritic cells and monocytes[9], where it is expressed as heterodimers with TLR1 or TLR6[1]. Additionally, expression of TLR2 is conserved across species including humans, mice, and zebrafish. Although inflammatory responses mediated by TLR2 play a pivotal role in effective bacterial clearance, excessive or misguided TLR2 signalling can unintentionally lead to tissue damage[10,11]. Particularly in the brain, TLR2 activation is targeted as a contributor to neuroinflammatory and neurodegenerative conditions[12]. More recently, the role of TLR2 in maintaining normal brain function has gained attention. Genomic deletion of TLR2 causes significant neurobehavioral changes in TLR2-deficient models [13,14]. Furthermore, utilizing state-of-the-art magnetic resonance imaging (MRI) methods at ultra-high magnetic fields revealed TLR2 deficiency causes significant cerebral microstructural changes in the zebrafish (*Danio rerio*) (Chapter 3) and mouse models [13], including changes in the cortical thickness, restricted diffusion, and compromised white matter integrity. Moreover, transcriptomics and metabolomics on TLR2 deficient zebrafish larvae revealed the involvement of TLR2 in the transcription level of glycolysis genes and the role of TLR2 in controlling metabolism homeostasis[15]. Deficiency of TLR2 leads to downregulation of the glycolysis and gluconeogenesis pathways and significant metabolic changes in zebrafish larvae[15]. In addition, Bajorat *et al.*, showed TLR2 deficiency significantly elevates glucose uptake in all brain regions by 34.6%[16]. Their results suggest TLR2 has a role in controlling the cerebral amino acid, neurotransmitter, and energy metabolism, even in the absence of infection. However, the precise role of TLR2 in cerebral metabolism and its correlation to observed microstructural changes in the brain remains largely unclear.

In the current study, we utilize TLR2 knockout (*tlr2*$^{-/-}$) zebrafish as a model to study the effect of TLR2 deficiency on the cerebral metabolism. Nuclear magnetic resonance spectroscopy techniques, including high-resolution magic angle spinning (HR-MAS) and localized magnetic resonance spectroscopy (MRS), are well-established techniques for monitoring (cerebral)

metabolic changes. Monitoring metabolic changes through HR-MAS or MRS provides sensitive indicators of various (pathological) processes. In recent years, robust HR-MAS methods have been developed for monitoring metabolic changes in intact zebrafish embryos, successfully applied in toxicology studies of larvae exposed to polymethoxy-1-alkenes[17], nano plastics[18], zearalenone[19], and brevetoxins[20] to reveal the toxicological mechanism. Furthermore, we utilized HR-MAS to analyse metabolic changes in the suprachiasmatic nucleus (SCN) in an Alzheimer's disease mouse model[21], showing the potential of the technique to specifically monitor metabolic changes in brain tissue. Beyond HR-MAS Localized MRS is a spectroscopic technique utilizing magnetic gradient systems to facilitate precisely select specific tissue areas, allowing for *in vivo* monitoring of metabolites directly within their natural environment. Furthermore, in contrast to many other approaches in metabolomics, localized MRS eliminates the necessity for time-consuming extraction or surgical techniques. Previously, we utilized localized MRS to acquire the cerebral metabolic profile of zebrafish *in vivo*, allowing for the quantification of several metabolites[22]. However, despite its potential, the confined sensitivity of localized MRS and the tiny size of the zebrafish brain remained challenging. Very recently, we were able to utilize the full potential of recent developments in ultra-high field systems equipped with powerful gradient systems to obtain highly resolved ^{1}H localized MRS spectra from the zebrafish brain from a PRESS voxel with a volume as small as 125 nL (Chapter 4). Here, we apply optimized ^{1}H point-resolved spectroscopy (PRESS) sequences to compare local metabolic profiles from various brain regions of *tlr2*$^{-/-}$ zebrafish to a control group.

We utilize HR-MAS at 14.1 T and ultra-high field localized ^{1}H MRS at 28.2 T to obtain cerebral metabolic spectra of zebrafish. Our results reveal genomic deletion of TLR2 significantly changes the cerebral metabolic profile. We observe an increase in *myo*-inositol (m-Ins) and decrease of levels of N-acetyl aspartate (NAA), markers for glial and neuronal cells, respectively. In addition we observe increased levels of the neurotransmitters glutamate (Glu) and γ-aminobutyric acid (GABA) and the amino acid alanine (Ala). Furthermore, we observe increased levels of lactate (Lac), indicating elevated energy requirement in the brain of TLR2 -deficient zebrafish. Based on our findings and previous observations, we propose a model of the mechanism of TLR2 deficiency and its influence on cerebral metabolic and microstructural changes.

2. METHODS

Zebrafish husbandry

This study utilized the wild type AB/TL strain and the *tlr2*^{sa19423} zebrafish line from the Sanger Institute Zebrafish Mutation Resource (Hinxton, Cambridge, UK). *Tlr2*$^{-/-}$ (mutant) and *tlr2*$^{+/+}$ (control) zebrafish were obtained by subjecting zebrafish with homozygous TLR2 mutations

and their wild type counterparts to five rounds of outcrossing, respectively. Screening and breeding of zebrafish was carried out following previously described protocols[23,24], in compliance with university animal welfare committee guidelines (Licence numbers AVD1060020171767 and AVD10600202216175), EU animal protection directive international guidelines (2010/63/EU), and standard protocols (www.zfin.org). For HR-MAS, 28-months-old female *tlr2*$^{-/-}$ and control zebrafish were euthanized by immersion in ice water (0 – 4 °C) for approximately 15 minutes, causing cessation of opercular movement. All specimens were euthanized during the same daytime period to minimize potential metabolic variation arising from circadian rhythms. After euthanizing, the brain was dissected, rapidly frozen in liquid nitrogen, and stored at -80 °C until usage. For MRI and MRS analysis, three-month-old male *tlr2*$^{-/-}$ and control zebrafish were euthanized as described for HR-MAS analysis and kept on ice until usage. MRI and MRS analysis were performed on the same day as sacrifice.

^{1}H High-resolution magic angle spectroscopy

Metabolic profiling of the brain of *tlr2*$^{-/-}$ and control zebrafish by ^{1}H HR-MAS was performed with a Bruker 14.1 T (600 MHz) NMR spectrometer (Bruker Biospin GmbH, Germany), equipped with a 4 mm HR-MAS ^{1}H/^{13}C inverse probe, a magic angle gradient system, and a Bruker BVT30 temperature control unit. Dissected zebrafish brains (n = 3 for the control group, n = 4 for the *tlr2*$^{-/-}$ group) were transferred to 4-mm zirconium oxide rotors (Bruker BioSpin AG, Switzerland) and 10 µL of deuterated phosphate buffer (100 mM, pH 7.0) containing 0.1 % (w/v) 3-trimetylsilyl-2, 2, 3, 3-tetradeuteropropionic acid (TSP) was added as a reference with its ^{1}H chemical shift δ = 0 ppm. All spectra were acquired at a spinning frequency of 6 kHz.

5

One-dimensional ^{1}H HR-MAS NMR spectra were recorded using a CPMG pulse sequence from Bruker's standard pulse program library with water suppression. Spectra were recorded using a spectral width of 8000 Hz and 16k data points. The data was averaged with *ns* = 512 and without dummy scans. A constant receiver gain of 2050, and an acquisition time of 0.17 s were used. The relaxation delay was set to a small value of 2 s to exclude high molecular weight molecules with short T_2 times, such as lipids. All spectra were processed by an exponential window function corresponding to a line broadening of 1 Hz and zero-filled before Fourier transformation. All spectra underwent processing involving an exponential window function corresponding to a line broadening of 1 Hz and zero-filling before Fourier transformation. Manual and automatic phasing, as well as baseline correction were performed using Topspin version 4.0.6.

Two-dimensional ^{1}H-^{1}H homonuclear correlation spectroscopy (COSY) HR-MAS spectra were recorded using a magnitude-mode 2D COSY with presaturation (cosyprqf) sequence from Bruker's standard pulse program library with water suppression. COSY spectra were acquired

with a spectral width of 9 kHz, corresponding to 15 ppm at 14.1 T, employing 1024 data points in the t_2 domain and 512 data points in the t_1 domain. This configuration resulted in a FID resolution of 8.80 Hz for t_2 and 17.58 Hz for t_1. COSY data were recorded with *ns* = 4, 16 dummy scans, a relaxation delay of 2 s, and an acquisition time of 114 and 56 ms for t_2 and t_1, respectively. The data were zero-filled to 2048 data points, providing a square matrix. Spectra were symmetrised to reduce noise and obtain well defined cross-signals.

Magnetic resonance imaging and spectroscopy

MRI and MRS experiments were conducted using a Bruker (Bruker Biospin GmbH, Germany) vertical bore system operating at 28.2 T (1200 MHz), configured with a Micro5 iProbe gradient system. The system was water-cooled, provided maximum gradient strengths (G_{max}) of 3 T/m, and was equipped with a 5 mm inner diameter birdcage resonator, and a GREAT60 gradient power supply. Data acquisition and processing was performed with a Linux workstation, running Bruker imaging software ParaVision 360 v3.3 (Bruker Biospin GmbH, Germany). During analysis, zebrafish (*n* = 3 for the control group, *n* = 5 for the *tlr2*$^{-/-}$ group) were embedded in perfluoropolyether (Fomblin Y, Solvay Solexis S.P.A.).

Three T_1-weighted gradient echo images, oriented perpendicularly relative to each other to obtain axial, coronal, and sagittal slices, were simultaneously acquired using a fast low angle shot (FLASH) pulse sequence. This facilitated the precise selection of the volume of interest for localized 1H MRS. FLASH measurements were performed with an echo time *TE* = 4 ms, a repetition time *TR* = 100 ms, at a flip angle of 30°, and *ns* = 1. The field of view (FOV) was 8 × 8 mm, at a matrix size of 128 × 128 voxels, obtaining a resolution of 63 × 63 µm, at a slice thickness of 300 µm, making the total scan time 13 seconds.

T_2 -weighted spin echo images were acquired by the multi-slice rapid acquisition with relaxation enhancement (RARE) pulse sequence to show the position of selected MRS voxels at a high resolution. RARE measurements were performed with *TE* = 5.6 ms, *TR* = 3000 ms, using 4 refocussing pulses per excitation, and *ns* = 16. The FOV was 8 × 8 mm, at a matrix size of 256 × 256 voxels, obtaining a resolution of 31 × 31 µm, at a slice thickness of 200 µm, making the total scan time 51 minutes.

For one-dimensional ^{1}H localized MRS, we utilized a PRESS pulse sequence[25]. The PRESS sequence incorporates three slice-selective RF pulses (90°-180°-180°), applied simultaneous with *z*, *y*, and *x* gradients to target the specified voxel. PRESS measurements were performed with *TE* = 15 ms, *TR* = 2000 ms. The PRESS sequence used 2048 complex points and an acquisition bandwidth of 12 kHz / 10 ppm. Three voxels were selected in the zebrafish brain; (1) in the forebrain, covering part of the pallium, (2) in the midbrain, covering part of the

mesencephalon, cerebellum, and diencephalon, and (3) in the hindbrain, covering part of the cerebellum and rhombencephalon. In the midbrain, voxels with a size of 0.8 × 0.8 × 0.8 mm^3 and V_{voxel} = 512 nL were selected. Data were acquired with *ns* = 512, with a total scan time of 17 minutes. In the forebrain and hindbrain, voxels of 0.6 × 0.6 × 0.6 mm^3 and V_{voxel} = 216 nL were selected, and data were acquired with *ns* = 1024, with a total scan time of 34 minutes. To limit the effects of chemical shift displacement, the excitation and refocusing RF pulses had a transmitter bandwidth *tBW* = 15 kHz as previously reported (Chapter 4), resulting in a spatial fat-water shift of 224 μm along the *z*, *x*, and *y* axes. The excitation frequency was applied at v_1 = 3.0 ppm, minimizing the chemical shift displacement for signals emerging from our target metabolites within the range of δ = 4.5 – 2.0 ppm. For suppression of the water signal, a variable pulse power and optimized relaxation delays (VAPOR) sequence[26] was applied prior to the PRESS pulses. Outer volume suppression (OVS) was integrated in an interleaved manner with the VAPOR sequence. The OVS consists of six suppression slices, each repeated three times and aligned parallel to the PRESS voxel, reducing the PRESS gradient spoilers. Magnetic field homogeneity within each voxel was achieved by automatic local second-order shimming prior to data acquisition.

Data processing

Metabolites identification was performed by comparison of obtained ^{1}H spectra to references as described in Chapter 4. Metabolite quantification was performed through Chenomx NMR suite 8.2 (Chenomx Inc., Edmonton, Alberta, Canada). The tCr at δ = 3.03 ppm was used to estimate the relative metabolic concentartions. A one-way analysis of variance (ANOVA) was utilized for statistical analysis by OriginPro v.8 (Originlab, Northhampton, MA, USA), with $p < 0.05$ considered to indicate significant differences.

5

3. RESULTS

HR-MAS based metabolic profile of TLR2 deficient zebrafish brain

.Figure 5.1 shows a representative one-dimensional ^{1}H HR-MAS spectrum acquired from an adult zebrafish brain. The spectrum exhibits high resolution, enabling the identification and quantification of multiple brain metabolites. Metabolic signal assignment was based on reference ^{1}H spectra[22,27-29]. The tCr signal showed strong signals at δ = 3.03 ppm and δ = 3.94 ppm, allowing the relative quantification of metabolites. Creatine normalization is commonly used for the quantification of cerebral metabolites for its strong ^{1}H NMR signal and low variability[30].

Figure 5.2 shows a two-dimensional ^{1}H-^{1}H COSY HR-MAS spectrum acquired from the adult zebrafish brain. The 2D COSY spectrum clearly reveals metabolites which are severely

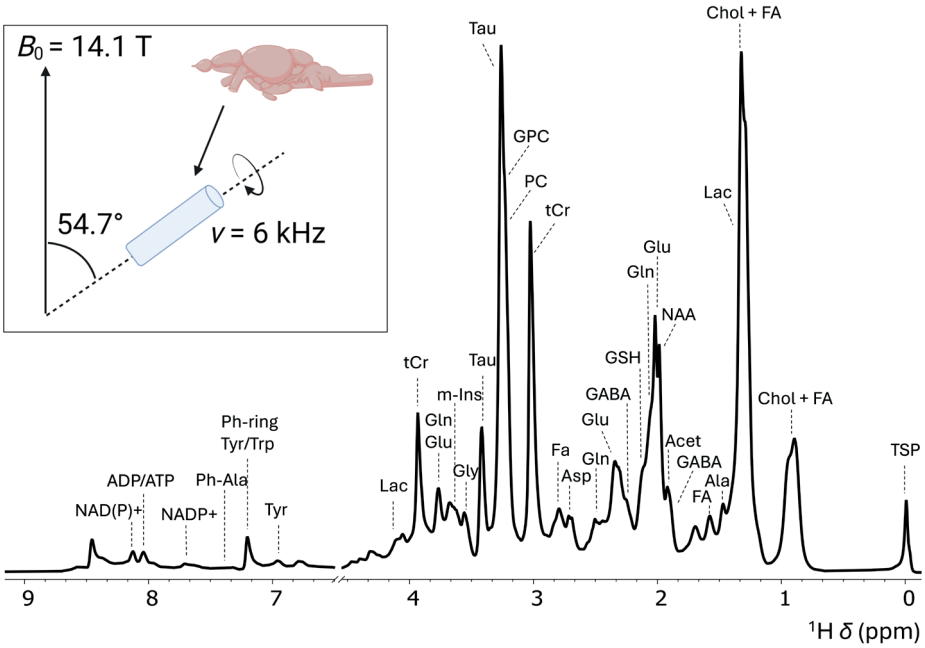

Figure 5.1. Representative ^{1}H HR-MAS spectrum acquired from the dissected brain of an adult female zebrafish. *HR-MAS measurements were performed with a Bruker 14.1 T (600 MHz) NMR spectrometer at a temperature of 277 K (4 °C), at a rotation frequency v = 6 kHz. For the acquisition of ^{1}H HR-MAS spectra, a CPMG pulse sequence was utilized with water suppression, ns = 512, and a relaxation delay of 2 s. TSP was used to calibrate the ^{1}H chemical shift (at 0 δ = ppm). Acet, acetate; ADP, adenosine diphosphate; Ala, alanine; Asp, aspartate; ATP, adenosine triphosphate; Chol, cholesterol; Fa, fatty acids; GABA, γ-aminobutyric acid; Gln, glutamine; Glu, glutamate; Gly, glycine; GPC, glycerophosphocholine; GSH, glutathione; Lac, Lactate; m-Ins, myo-inositol; NAA, N-acetyl aspartate; NAD(P)+, nicotinamide adenine dinucleotide phosphate; PC, phosphocholine; Ph-Ala, Phenylalanine; Ph-ring, Phenyl ring; Tau, taurine; tCr, total creatine; TSP, 3-trimetylsilyl-2, 2, 3, 3-tetradeuteropropionic acid; Trp, tryptophan; Tyr, tyrosine;*

overlapping in 1D ^{1}H NMR spectra, based on their cross-peaks. Prominent correlations include the cross-peak for Lac at δ(4.11, 1.32) ppm, GABA at δ(1.88, 2.28) ppm, NAA at δ(2.49, 2.68) ppm, m-Ins at δ(3.51, 4.06) ppm, and Ala at δ(1.56, 3.76) ppm. Furthermore, the cross-peaks of Glu and glutamine (Gln) were found well resolved at δ(2.08, 2.33) ppm and δ(2.12, 2.43) ppm, respectively. In addition, we observed the cross-peak signals of macromolecules previously assigned by Behar and Ogino [31], labelled M1→5 and M4→7 at δ(0.95, 2.05) ppm and δ(1.67, 2.98) ppm, respectively. A detailed overview of correlations assigned from metabolites found in the zebrafish brain is shown in Table 5.1.

Figure 5.3A shows 1D ^{1}H HR-MAS spectra from *tlr2*$^{-/-}$ and control adult zebrafish brain. Cerebral metabolic profiles indicated increased levels of various metabolites, including the neurotransmitter Glu and GABA. In addition, elevated signals of Ala, acetate, NAA, aspartate, taurine, m-Ins, adenosine diphosphate/adenosine triphosphate (ADP/ATP), and nicotinamide adenine dinucleotide phosphate (NADP^{+}) were observed in the *tlr2*$^{-/-}$ group compared to the control group. Quantitative analysis of metabolites in *tlr2*$^{-/-}$ and control zebrafish brain

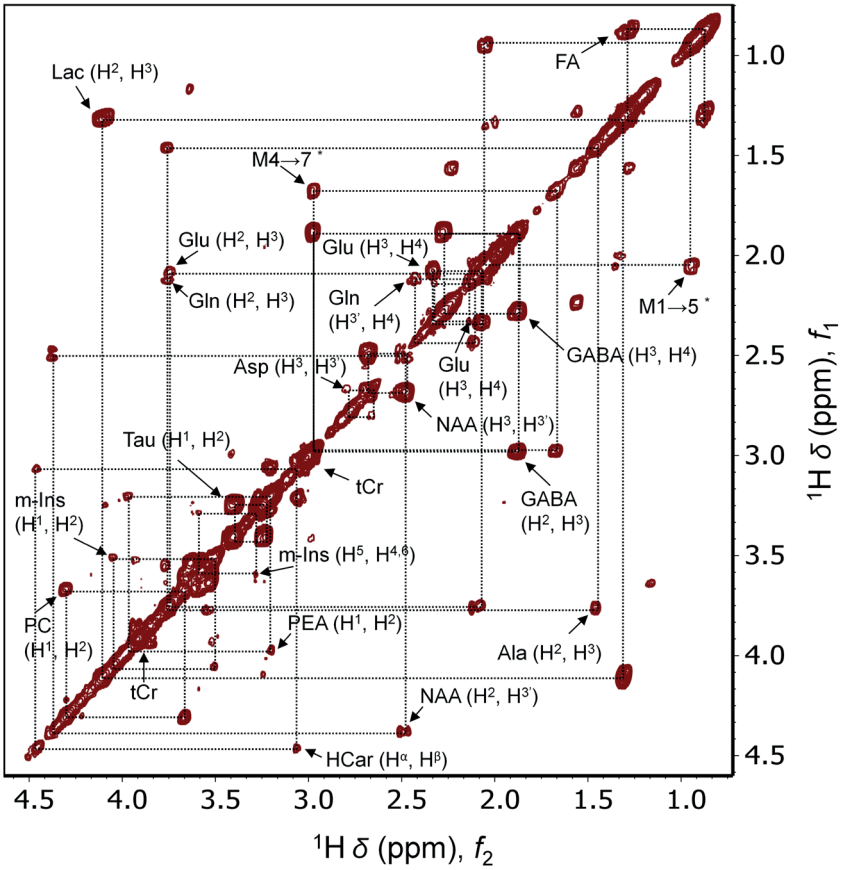

Figure 5.2. Representative ^{1}H-^{1}H homonuclear correlated spectroscopy (COSY) HR-MAS spectrum acquired from the dissected brain of an adult female zebrafish. *HR-MAS measurements were performed with a Bruker 14.1 T (600 MHz) NMR spectrometer at a temperature of 277 K (4 °C), at a rotation frequency of 6 kHz. TSP was used to calibrate the ^{1}H chemical shift (at 0 ppm). Ala, alanine; Asp, aspartate; Fa, fatty acids; GABA, γ-aminobutyric acid; Gln, glutamine; Glu, glutamate; HCar, homocarnosine; Lac, Lactate; m-Ins, myo-inositol; NAA, N-acetyl aspartate; PC, phosphocholine; PEA, phosphoryl ethanolamine; Tau, taurine; tCr, total creatine. * M1→5 and M4→7 arise from macromolecules as assigned by Behar and Ogino[31].*

revealed statistically significantly changes in the cerebral metabolite level of *tlr2*$^{-/-}$ zebrafish compared to the control group (Figure 5.3B). Significantly elevated levels of Glu (0.987 *tlr2*$^{-/-}$ *versus* 0.8767 control; p = 0.040), Gln (0.3454 *tlr2*$^{-/-}$ *versus* 0.2743 control; p = 0.049), and GABA (1.033 *tlr2*$^{-/-}$ *versus* 0.7997 control; p = 0.031) were observed, metabolites involved in the glutamate/GABA-glutamine cycle.

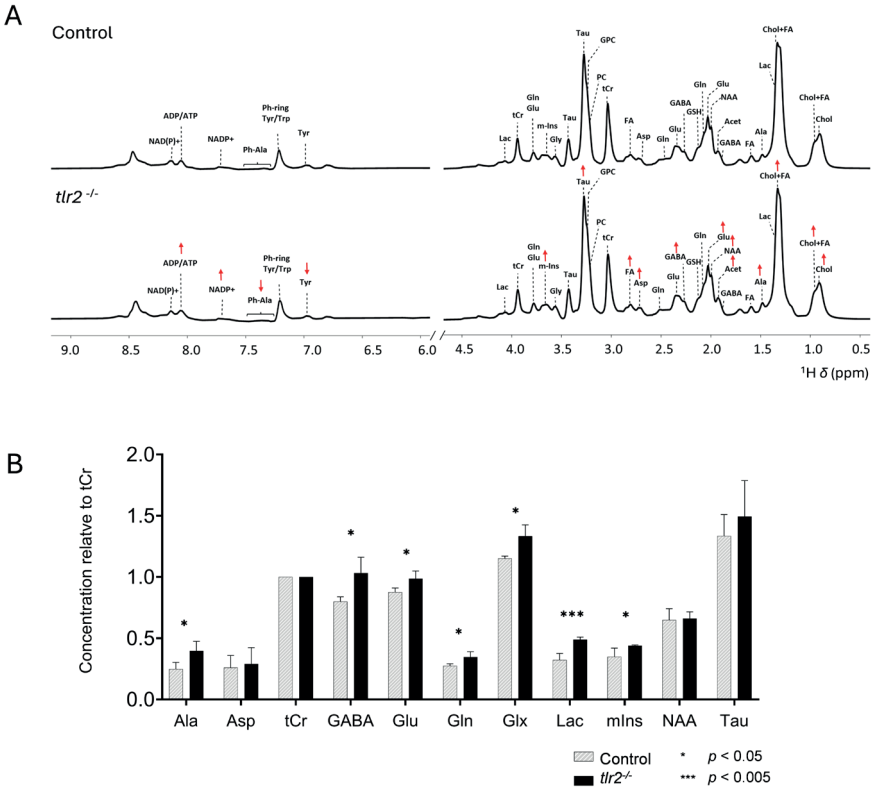

Figure 5.3. [A] *One-dimensional ¹H HR-MAS NMR spectra acquired from the dissected brain of adult control and tlr2*$^{-/-}$ *zebrafish (n = 3 for the control group, n = 4 for the tlr2*$^{-/-}$ *group). Spectra were normalized to the intensity of the total creatine (tCr) signal at δ = 3.03 ppm for comparison. Upregulated metabolites are indicated by upward facing red arrows (↑), downregulated metabolites by downward facing red arrows (↓). Calibration of the ¹H chemical shift was performed utilizing TSP (at δ = 0 ppm).* ***[B]*** *Metabolic profile of whole brain HR-MAS analysis of control and tlr2*$^{-/-}$ *adult zebrafish. Concentrations are reported relative to the total creatine (tCr) signal. Statistical analysis was performed by the t-test, and significance was established with a p < 0.05. Acet, acetate; ADP, adenosine diphosphate; Ala, alanine; Asp, aspartate; ATP, adenosine triphosphate; Chol, cholesterol; Fa, fatty acids; GABA, γ-aminobutyric acid; Gln, glutamine; Glu, glutamate; Glx, ; Glu + Gln; Gly,glycine; GPC, glycerophosphocholine; GSH, glutathione; Lac, Lactate; m-Ins, myo-inositol; NAA, N-acetyl aspartate; NAD(P)+, nicotinamide adenine dinucleotide phosphate; PC, phosphocholine; Ph-Ala, Phenylalanine; Ph-ring, Phenyl ring; Tau, taurine; tCr, total creatine; TSP, 3-trimetylsilyl-2, 2, 3, 3-tetradeuteropropionic acid; Trp, tryptophan; Tyr, tyrosine;*

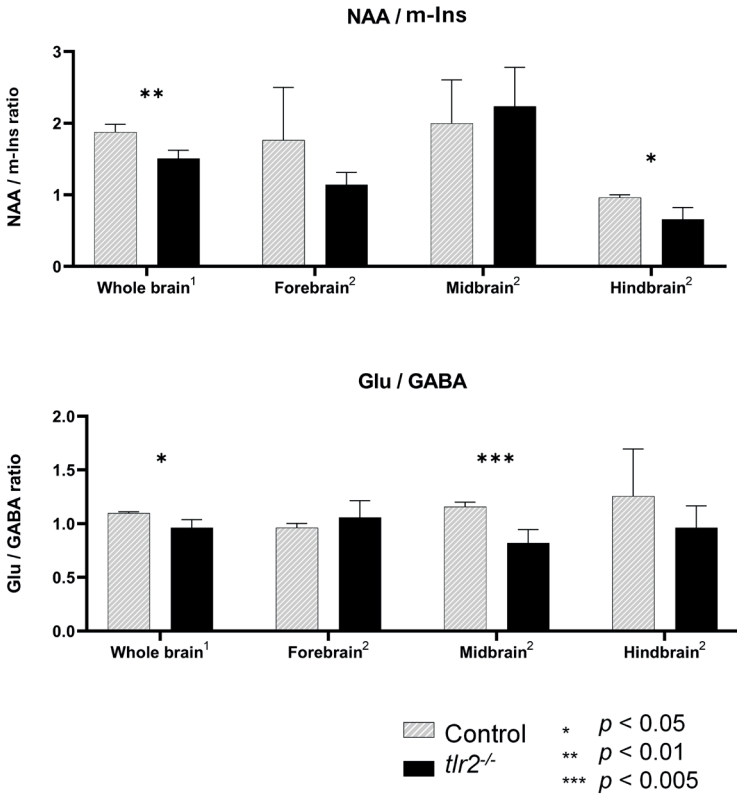

Figure 5.4. [Top] *NAA / m-Ins ratio and* ***[bottom]*** *Glu/GABA ratio found in whole brain analysis and in localized regions. For localized spectroscopy, voxels were selected in the pallium (forebrain), the mesencephalon, cerebellum, and diencephalon (midbrain), and in the cerebellum and rhombencephalon (hindbrain). Statistical analysis was performed by the t-test, and significance was established for p < 0.05. [1] Whole brain analysis was performed utilizing HR-MAS at 14.1 T. [2] Regional brain analysis was performed utilizing localized MRS at 28.2 T.*

Additionally, a significantly lower Glu/GABA ratio was observed for *tlr2*$^{-/-}$ zebrafish compared to the control group (0.9622 *tlr2*$^{-/-}$ *versus* 1.097 control; p = 0.030). This indicated a relative shift towards increased GABA levels (see Figure 5.4). Furthermore, increased levels of Ala (0.3970 *tlr2*$^{-/-}$ *versus* 0.2486 control; p = 0.038) and Lac (0.4893 *tlr2*$^{-/-}$ *versus* 0.3229 control; p = 0.002) were identified, both integral constituents of the "astrocyte-neuron lactate shuttle" mechanism. Moreover, elevations of m-Ins were found for *tlr2*$^{-/-}$ zebrafish compared to the control group, as well as a significantly reduced NAA/m-Ins ratio (1.508 *tlr2*$^{-/-}$ *versus* 1.877 control; p = 0.008), indicative of a relative increase of m-Ins (see Figure 5.4).

Table 5.1. *^{1}H-chemical shift and connectivity assignment of metabolites observed in ^{1}H-^{1}H COSY HR-MAS spectra of the adult zebrafish brain. Assignment and annotation based on reference ^{1}H spectra[22,27-29]. Ala, alanine; Asp, aspartate; Fa, fatty acids; GABA, γ-aminobutyric acid; Gln, glutamine; Glu, glutamate; HCar, homocarnosine; Lac, Lactate; m-Ins, myo-inositol; NAA, N-acetyl aspartate; PC, phosphocholine; PEA, phosphoryl ethanolamine; Tau, taurine*

Metabolite	Group	*δ* (ppm)	Cross-peak
Ala	^{2}CH	2.77	2 – 3
	$^{3}CH_3$	1.47	3 – 2
Asp	$^{3}CH_2$	2.81	3 – 3’
		2.67	3’ – 3
GABA	$^{2}CH_2$	3.00	2 – 3
	$^{3}CH_2$	1.89	3 – 2, 3 – 4
	$^{4}CH_2$	2.29	4 - 3
Gln	^{2}CH	3.77	2 – 3
	$^{3}CH_2$	2.13	3 – 2, 3 – 4
	$^{4}CH_2$	2.44	4 – 3
Glu	^{2}CH	3.75	2 – 3
	$^{3}CH_2$	2.08	3 – 2, 3 – 4
		2.15	3’ – 4
	$^{4}CH_2$	2.35	4 – 3, 4 – 3’
HCar	$^{\alpha}CH$	4.48	α – β
	$^{\beta}CH_2$	3.07	β – α
Lac	^{2}CH	4.12	2 – 3
	$^{3}CH_3$	1.32	3 – 2
m-Ins	^{1}CH	3.52	1 – 2
	^{2}CH	4.07	2 – 1
	^{4}CH	3.60	4 – 5
	^{5}CH	3.29	5 – 4, 5 – 6
	^{6}CH	3.60	6 – 5
NAA	^{2}CH	4.39	2 – 3’
	$^{3}CH_2$	2.69	3 – 3’
		2.52	3’ – 2, 3’ – 3
PC	$^{1}CH_2$	4.32	1 – 2
	$^{2}CH_2$	3.68	2 - 1
PEA	$^{1}CH_2{}^{2}$	3.99	1 – 2
	^{2}CH	3.21	2 – 1
Tau	$^{1}CH_2$	3.41	1 – 2
	$^{2}CH_2$	3.24	2 – 1

Localized 1H MRS spectra of zebrafish brain regions at 28.2 T

Single voxel localized ^{1}H MRS at 28.2 T was conducted across three distinct regions in the zebrafish brain. Given the irregular morphology of the zebrafish brain, voxel volumes were tailored to accommodate the shape and volume of selected brain regions, aiming to mitigate extracerebral lipid or metabolite signal interference. PRESS voxels were selected in the forebrain, midbrain, and hindbrain of the zebrafish as illustrated in Figure 5.5A. The midbrain permitted a PRESS voxel of 0.8 × 0.8 × 0.8 mm^3, corresponding to V_{voxel} = 512 nL. The selected voxel covered parts of the mesencephalon, cerebellum, and diencephalon. For the forebrain and hindbrain regions, a voxel size of 0.6 × 0.6 × 0.6 mm^3 was used, corresponding to V_{voxel} = 216 nL. In the forebrain, the selected voxel was precisely positioned in the pallium. In the hindbrain, the selected region overlapped with the cerebellum and rhombencephalon. To address the smaller voxel sizes utilized in the forebrain and hindbrain, the total number of scans was doubled compared to those conducted in midbrain analysis. For all brain regions, highly resolved spectra were obtained from control and *tlr2*$^{-/-}$ adult zebrafish (Figure 5.5 B – D), allowing for the identification and quantification of brain metabolites. To ensure accurate quantification of cerebral metabolites in localized MRS data, consistent use of metabolite signals, *i.e.* chemical shift, is required due to chemical shift displacement effects. Table 5.2 shows the metabolite signals utilized for quantification, in alignment with our previous report (see Chapter 4). In the forebrain (Figure 5.5B) we observed a significant increase in Lac level (0.6938 *tlr2*$^{-/-}$ *versus* 0.4922 control; p = 0.034). In the midbrain (Figure 5.5C), a significant increase in Ala relative to tCr (0.0804 *tlr2*$^{-/-}$ *versus* 0.0417 control; p = 0.001), GABA relative to tCr (0.3689 *tlr2*$^{-/-}$ *versus* 0.3122 control; p = 0.005), and Lac relative to tCr (0.9036 *tlr2*$^{-/-}$ *versus* 0.6551 control; p = 0.030) was observed. Additionally, a significant decrease in the Glu / GABA ratio was observed in the midbrain of the *tlr2*$^{-/-}$ group compared to the control group (0.8201 *tlr2*$^{-/-}$ *versus* 1.158 control; p = 0.0047), indicating a relative shift to GABA (see Figure 5.4). In the hindbrain (Figure 5.5D), a significant increase in Lac relative to tCr (1.123 *tlr2*$^{-/-}$ *versus* 0.5412 control; p = 0.0004) and significant decrease in NAA relative to tCr (0.1467 *tlr2*$^{-/-}$ *versus* 0.2502 control; p = 0.0006) were observed. Additionally, the hindbrain showed a significant decrease in the NAA / m-Ins ratio (0.6594 *tlr2*$^{-/-}$ *versus* 0.9626 control; p = 0.022), indicating a relative shift towards m-Ins (see Figure 5.4).

4. DISCUSSION

In this study, we utilized HR-MAS and localized MRS to conduct a comprehensive metabolic analysis of intact adult zebrafish brain. One-dimensional ^{1}H HR-MAS provided high-resolution metabolic spectra of intact adult zebrafish brain, allowing for quantitative analysis based on peak area. Additionally, highly resolved two-dimensional homonuclear ^{1}H-^{1}H COSY HR-MAS was utilized to identify relevant metabolites based on their cross-peaks. To acquire regional

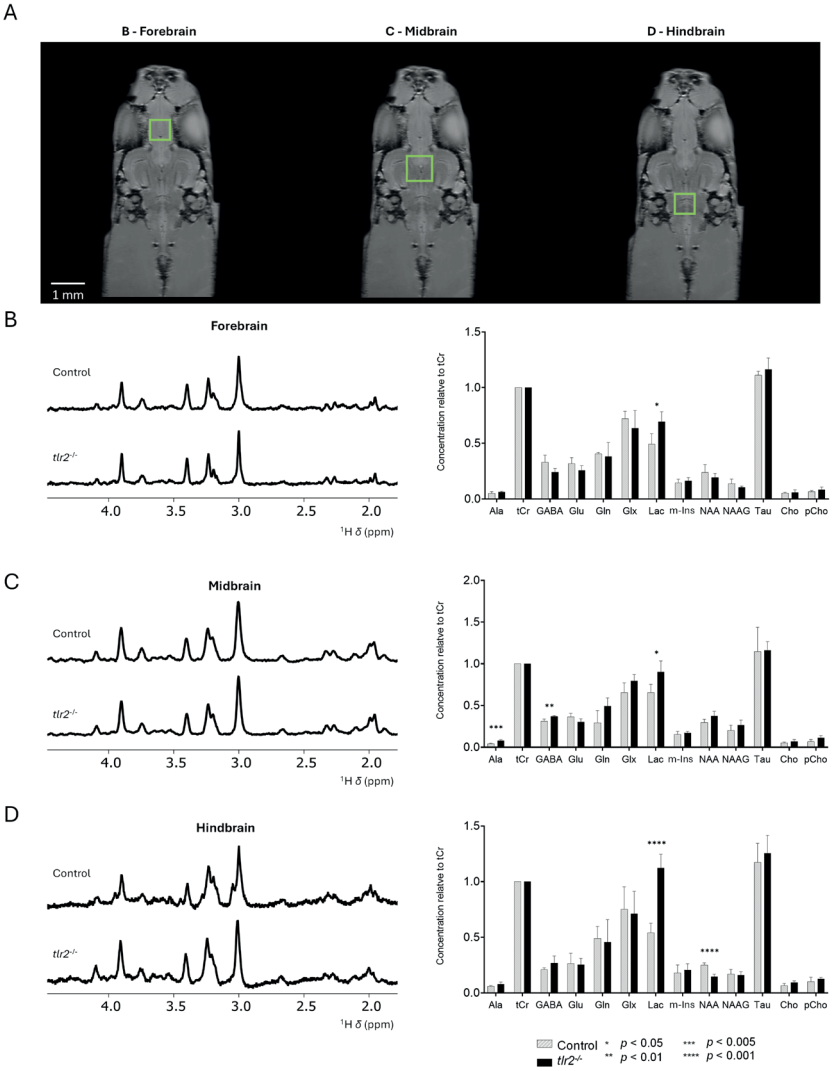

Figure 5.5. Localized ^{1}H MRS analysis of brain metabolites from tlr2$^{-/-}$ adult male zebrafish compared to a control group. [A] *Anatomical RARE image, coronal slice, of a zebrafish brain highlighting selected PRESS voxels in the forebrain, midbrain, and hindbrain. In the forebrain and hindbrain, PRESS voxels of 0.6 × 0.6 × 0.6 mm^3 with V_{voxel} = 216 nL were selected. In the midbrain a PRESS voxel of 0.8 × 0.8 × 0.8 mm^3 with V_{voxel} = 512 nL was selected. Highly resolved one-dimensional localized ^{1}H MRS of the control and tlr2$^{-/-}$ group were obtained from the **[B]** forebrain, **[C]** midbrain, and **[D]** hindbrain used for the quantification of cerebral metabolites. The localized ^{1}H MRS spectra are all normalized to the intensity of the tCr signal at δ = 3.03 ppm. Quantification of cerebral metabolites is performed relative to the tCr signal at δ = 3.03 ppm, utilizing specific ^{1}H signals for each metabolite as indicated in Table 5.2. Statistical analysis was performed by the t-test, and significance was established for p < 0.05. Ala – alanine, tCr – total creatine, GABA - γ-aminobutyric acid, Glu – glutamate, Gnl – glutamine, Lac – Lactate, m-Ins – myo-inositol, NAA - N-acetylaspartate, NAAG - N-acetylaspartyl-glutamate, Tau – taurine, Cho – choline, pCho – phosphocholine*

Table 5.2 *Concentrations of cerebral metabolites detected in the forebrain, midbrain, and hindbrain of TLR2 deficient (tlr2$^{-/-}$) and control zebrafish, utilizing localized ^{1}H magnetic resonance spectroscopy at 28.2 T. Functional groups and their chemical shift (in ppm) used for quantification per metabolite is indicated. Quantification performed relative to the total creatine (tCr) signal at 3.03 ppm. . Statistical analysis was performed by the Tukey test, and significance was established with a p-value of < 0.05. * p < 0.05; ** p < 0.01; *** p < 0.005; **** p < 0.001. Ala – alanine, tCr – total creatine, GABA - γ-aminobutyric acid, Glu – glutamate, Gnl – glutamine, Lac – Lactate, m-Ins – myo-inositol, NAA - N-acetylaspartate, NAAG - N-acetylaspartyl-glutamate, Tau – taurine, Cho – choline, pCho – phosphocholine*

Metabolite	Group used for quantification	Forebrain Concentration rel. tCr		Midbrain Concentration rel. tCr		Hindbrain Concentration rel. tCr	
		Control	tlr2$^{-/-}$	Control	tlr2$^{-/-}$	Control	tlr2$^{-/-}$
Ala	$^{3}CH_3$ (δ = 1.47 ppm)	0.049 ± 0.008	0.063 ± 0.003	0.042 ± 0.004	0.076 ± 0.002 ***	0.059 ± 0.003	0.078 ± 0.01
GABA	$^{3}CH_2$ (δ = 1.89 ppm)	0.331 ± 0.029	0.242 ± 0.017	0.312 ± 0.013	0.369 ± 0.007 **	0.21 ± 0.007	0.27 ± 0.033
Glu	$^{4}CH_2$ (δ = 2.45 ppm)	0.317 ± 0.025	0.255 ± 0.022	0.362 ± 0.021	0.311 ± 0.019	0.263 ± 0.044	0.255 ± 0.029
Gln	^{2}CH (δ = 3.75 ppm)	0.405 ± 0.006	0.38 ± 0.063	0.293 ± 0.07	0.49 ± 0.057	0.489 ± 0.051	0.456 ± 0.105
Lac	^{2}CH (δ = 4.09 ppm)	0.492 ± 0.044	0.694 ± 0.045 *	0.655 ± 0.047	0.89 ± 0.073 *	0.541 ± 0.04	1.123 ± 0.063 ****
m-Ins	^{4}CH (δ = 3.61 ppm)	0.144 ± 0.016	0.169 ± 0.009	0.155 ± 0.017	0.169 ± 0.011	0.18 ± 0.034	0.227 ± 0.013 *
NAA	$^{2}CH_3$ (δ = 2.01 ppm)	0.239 ± 0.034	0.193 ± 0.018	0.297 ± 0.018	0.391 ± 0.025	0.25 ± 0.009	0.147 ± 0.011 ****
NAAG	$^{2}CH_3$ (δ = 2.04 ppm)	0.136 ± 0.02	0.102 ± 0.006	0.203 ± 0.03	0.29 ± 0.014	0.17 ± 0.019	0.159 ± 0.016
Tau	$^{2}CH_2$ (δ = 3.25 ppm)	1.111 ± 0.017	1.162 ± 0.052	1.195 ± 0.103	1.171 ± 0.059	1.174 ± 0.081	1.254 ± 0.084
Cho	$N(CH_3)_3$ (δ = 3.19 ppm)	0.052 ± 0.004	0.058 ± 0.012	0.05 ± 0.006	0.076 ± 0.01	0.064 ± 0.01	0.093 ± 0.007
pCho	$N(CH_3)_3$ (δ = 3.21 ppm)	0.065 ± 0.004	0.082 ± 0.012	0.067 ± 0.012	0.123 ± 0.009	0.101 ± 0.019	0.127 ± 0.007

insights, one-dimensional ^{1}H localized MRS was performed to study potential variation in the metabolic changes in different region of the zebrafish brain. Building upon our previous discovery of TLR2's involvement in metabolic regulation in zebrafish larvae[15], our current findings shed light on significant alterations in cerebral metabolites attributed to TLR2 deficiency.

Elevated astrogliosis and diminished neuronal integrity in TLR2 deficient zebrafish

A significant increase in m-Ins concentration was found in the brain of *tlr2*$^{-/-}$ zebrafish compared to the control group. Of the nine inositol stereoisomers, m-Ins is the primary form found in all tissue types of vertibrates[32]. M-Ins is found in membrane phosphatidylinositol (phospholipids) and mediates volume and osmosisregulation[33]. In the brain, m-Ins is primarily found in glial cells, *e.g.* astrocytes[33]. Elevated levels of m-Ins are consistently observed in neurodegenerative and neurological conditions characterised by reactive glial cells, *i.e.* astrogliosis. For example, heightened levels of cerebral m-Ins were found in Alzheimer's disease[21,34], multiple sclerosis[35], and gliomatosis cerebri[36]. Furthermore, we observed significantly lower levels of NAA in the hindbrain of *tlr2*$^{-/-}$ male zebrafish. NAA is found predominantly in the cell body and axons of neurons. Reduced levels of NAA correlated to neuronal integrity loss in neurodegenerative disorders, including Alzheimer's disease[13]. Elevated cerebral m-Ins levels in TLR2 deficient zebrafish may signify an upsurge in reactive glial cells, while diminished NAA potentially reflects a loss of neuronal integrity, thus reflecting the environment of cell populations. Previously, upregulated astrogliosis was reported for a TLR2-knockout mouse model with Alzheimers's disease, indicating TLR2 deficiency increases sensitivity for astrocytic reactivity[13]. Additionally, TLR2 deficiency exhibits compromised blood-brain barrier (BBB) integrity, attributed to diminished levels of tight junction proteins[14]. Reduced BBB integrity may partially account for increased sensitivity to astrogliosis and loss of neuronal integrity, as the infiltration of blood-borne factors and/or pathogens into the central nervous system, facilitated by BBB breaches, is recognised a contributing factor to initiate reactive astrogliosis[37]. Furthermore, diminished BBB integrity can lead to neuronal degeneration[38] and is targeted as a contributing factor in the pathology of neurodegenerative diseases including Alzheimer's disease, Parkinson's disease, amyotrophic lateral sclerosis (ALS), MS, and Huntington's disease[39]. In addition, our findings of reduced NAA in the brain of the *tlr2*$^{-/-}$ zebrafish compared to control is in line with expectations based on previous reports of neuronal integrity loss caused by TLR2 deficiency. Previously (Chapter 3), we reported significant changes in diffusion MRI tensor and kurtosis metrics indicative of compromised white matter integrity and degeneration of axons in the brain of *tlr2*$^{-/-}$ adult zebrafish. Furthermore, Zhou *et al.* found genomic deletion causes reduced cortical thickness, diminished neuronal density, and white matter damage[13]. Beyond the individual levels of m-Ins and NAA, we found a significant shift in the NAA / m-Ins ratio towards m-Ins in the *tlr2*$^{-/-}$ zebrafish brain. Previously, a similar shift in the NAA / m-Ins ratio

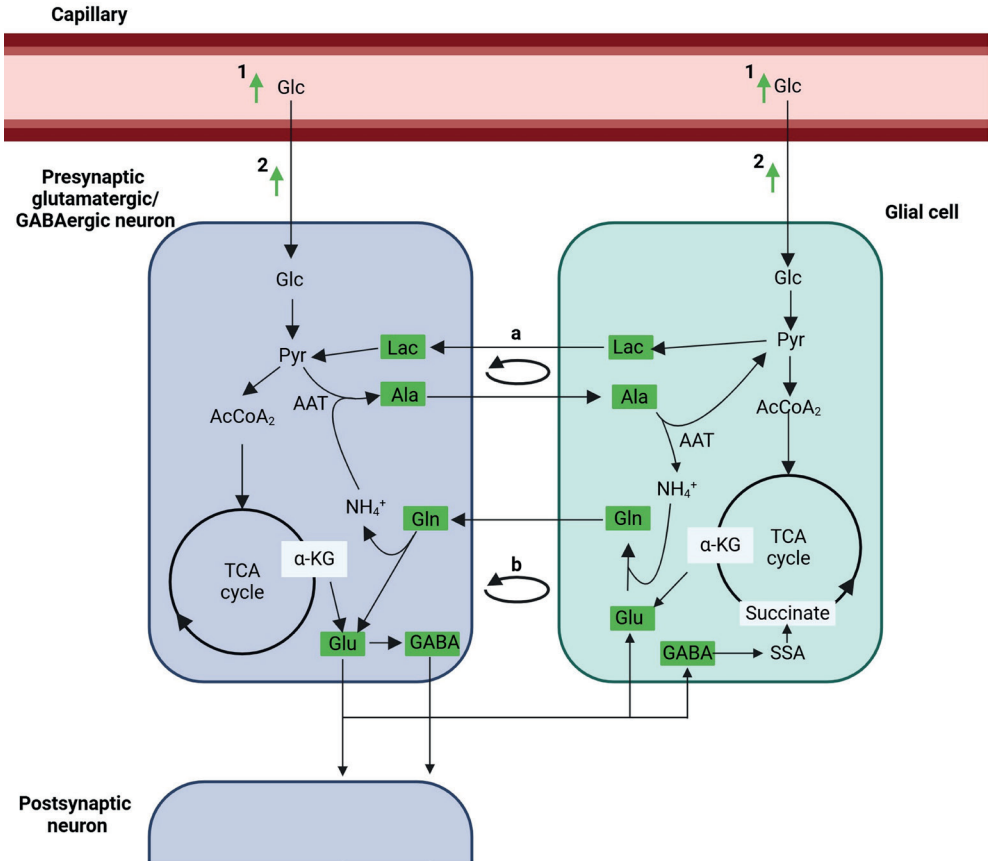

Figure 5.6. Overview of observed metabolic changes in the brain of TLR2 deficient zebrafish, highlighting disrupted neurotransmitter homeostasis. *This simplified illustration depicts two crucial metabolic cycles occurring between neuronal and glial cells; (a) the lactate-alanine cycle [57] and (b) the glutamate/GABA-glutamine cycle [57]. These cycles are interconnected through alanine transaminase (AAT) and ammonia (NH_4). Metabolites highlighted in green (Lactate, alanine, glutamine, glutamate, and GABA) were significantly upregulated in the brain of tlr2$^{-/-}$ zebrafish compared to a control group. Furthermore, green arrows indicate (1) elevated glucose levels[15] and (2) increased cerebral glucose uptake[16] previously observed in TLR2-deficient models. Created with biorender.com.*

correlated to the neurodegenerative progression of Alzheimer's disease[40]. With localized MRS, we found a similar shift in the NAA / m-Ins ratio, specifically in the *tlr2*$^{-/-}$ zebrafish hindbrain. In the zebrafish hindbrain, several major white-matter structures are situated, including the ventral rhombencephalic commissure (Cven), medial longitudinal fascicle (MLF), and lateral longitudinal fascicle (LLF). In a quantitative diffusion MRI analysis, we found significant changes in diffusivity and kurtosis metrics of these white-matter structures, indicative of compromised

white matter integrity and axonal degeneration, processes for which diminished levels of NAA are expected. Alternatively, elevated levels of m-Ins and diminished levels of NAA may stem from an augmented baseline of astrocyte cell numbers. TLR2 deficiency has an impact on neural progenitor cells (NPCs) development, altering cellular composition arising from NPCs[41]. Specifically, deficiency in TLR2 compromised neurogenesis, leads to a diminished population of neurons and an increased abundance of astrocytes derived from NPCs[41]. As m-Ins is primarily found in glial cells and NAA in neurons, this shift in cellular population caused by genomic deletion of TLR2 could lead to elevated levels of m-Ins and lower NAA concentration.

Beyond m-Ins and NAA, we found significantly elevated Lac levels in the *tlr2*$^{-/-}$ brain compared to the control group. In the brain, Lac is involved in several processes. Beyond used to meet the energetic needs of neurons, Lac acts as a signalling molecule, exerting influence over excitability, plasticity, and the consolidation of memory. Furthermore, Lac participates in regulating essential homeostatic functions[42]. Cerebral Lac is primarily generated in glial cells, with 85% of the glucose consumed by glial cells released in the form of Lac under normal resting conditions[43]. In glial cells, Lac is produced through aerobic glycolysis. This metabolic pathway generates energy from glucose (or alternatively glycogen) via pyruvate, rather than undergoing conversion through the tricarboxylic acid (TCA) cycle. From glial cells, Lac is transported to neurons via the astrocyte-neuron lactate shuttle mechanism, where it is converted to pyruvate to produce energy via the TCA-cycle (see Figure 5.6). In the context of cerebral energetics, neurons are the predominant energy consumers, accounting for approximately 80% of the energy expenditure in the brain[44]. Intriguingly, despite the substantial variation in energy demand between neurons and glial cells, the total cerebral glucose uptake by these cell types is similar[45]. Additionally, elevated cerebral glucose uptake during intensified neuronal activity is primarily accounted for by glial cells, with neurons maintaining stability[46]. Furthermore, significantly elevated glucose uptake is indicative of increased metabolic activity within the astrocytic network[46]. Previously, Hu *et al.* found a TLR2 deficiency significantly elevates glucose levels in *tlr2*$^{-/-}$ zebrafish larvae, possibly caused by downregulated glycolysis and gluconeogenesis. Furthermore, Bajorat *et al.* reported brain wide increased glucose consumption as a consequence of TLR2 deficiency[16]. Here, we observe that TLR2 deficiency causes a significant increase of Lac in three distinct locations of the zebrafish brain; in the forebrain, midbrain, and hindbrain. Previously, significantly elevated Lac levels were also observed in *tlr2*$^{-/-}$ zebrafish larvae[15]. Several neurological processes could account for changes in cerebral Lac levels. Elevated Lac was correlated to cerebral inflammation across various conditions[47-53], a process of which astrocyte activation is a fundamental process[54]. Thus, elevated Lac levels in combination with an increased m-Ins level is a strong indication of elevated numbers of reactive astrocytes in TLR2 deficient zebrafish. However, cerebral cortical hypoperfusion, observed in TLR2 deficient mice[14], could also

account for increased Lac levels. Under normal oxygen tension conditions, neurons produce energy through glycolysis, forming 32 – 36 ATP molecules from each glucose molecule via the TCA cycle. Under hypoxic or anoxic conditions, the number of ATP molecules formed from each glucose molecule is reduced to 2 and the reduced availability of oxygen shifts glucose metabolism to anaerobic glycolysis, increasing Lac levels[55]. Reactive glial cells as a direct consequence of hypoperfusion might also explain observed metabolic changes, as hypoperfusion potentially causes mild astrogliosis[56].

TLR2 deficiency causes disrupted neurotransmitter balance

The majority of the cerebral energy consumption is linked to glutamatergic and GABAergic neurotransmission[58]. Therefore, changes in cerebral glucose uptake and the adjustments in glycolysis and gluconeogenesis observed in TLR2 deficient models likely impact, or are connected to, neurotransmission homeostasis. Maintaining the equilibrium between neuronal excitation and inhibition is important as disruptions in this balance can result in various brain related pathological conditions[59]. In previous work, a notable increase in Glu was found utilizing whole-body *tlr2*$^{-/-}$ zebrafish larvae analysis[15]. These changes in Glu levels, the primary excitatory neurotransmitter, might indicate TLR2 has a role in the metabolism of the central nerve system[15]. Building upon this, our current investigation delves deeper, affirming and expanding upon these earlier results. Specifically, we demonstrate that the elevated Glu level extends beyond the larval stage, persisting specifically within the adult *tlr2*$^{-/-}$ zebrafish brain. Glu plays a pivot role in various neuroplasticity mechanisms and is important for areas relying on neuroplasticity to adapt to changes in environmental conditions, including cognition, learning, and mood[60]. In zebrafish, Glu is found omnipresent in the brain and spinal cord[61], although higher concentrations of glutamatergic neurons are reported in specific brain regions, including the olfactory bulb, the stratum periventricular of the optic tectum, and the habenula[62]. Following exocytosis release, there is a substantial increase in Glu levels within the extracellular fluid. Maintaining balance of the extracellular Glu level is crucial for neurological health. Glu disbalance disrupts brain homeostasis, potentially leading to adverse effects. Insufficient extracellular Glu can lead to a depletion in the available energy, affecting cellular functioning. Conversely, an excess of extracellular Glu can result in overexcitement of nerve cells, potentially leading to cell death in a process known as excitotoxicity[63]. Elevated Glu levels have been observed in various neurodegenerative and neurological disorders, including ALS and Parkinson's disease[64,65]. Astrocytes play a pivot role in the removal of excess Glu. In the glutamate-glutamine cycle, extracellular Glu is up taken by astrocytes and converted to Gln in an enzymatic reaction of involving glutamine synthetase (GS) and ammonia. Subsequently, Gln is released by astrocytes and taken up by neurons and synthesized to Glu, releasing ammonia.

Besides a significant increase in Glu, we observed a significant increase in Gln and Ala. Ala accounts for approximately 25% of the conversion of Gln to Glu in glutamatergic neurons[66]. The ammonia released in neurons in the conversion of Glu to Gln is (partially) used in the production of Ala utilizing alanine transaminase (AAT). The Ala is transported to astrocytes as part of the lactate-alanine cycle, where it converts to ammonia for the synthesis of Gln in the glutamate-glutamine cycle[57]. In this way, the glutamate-glutamine cycle and lactate-alanine cycle are connected and changes in molecular levels involving one metabolic pathway may influence the other pathway. For example, disrupted energy metabolism and decreased glucose levels cause decreased levels of both Glu and Ala in Huntington's disease [67]. Contrary, TLR2 deficiency causes increased cerebral glucose uptake[16] and increased glucose levels[15], which may explain increased Glu, Gln, and Ala levels presented in the current work. Another possible explanation for elevated cerebral Glu and Ala levels could arise from cerebral ammonia intoxication as a consequence of diminished BBB integrity observed in *tlr2*$^{-/-}$ model[14]. Under normal conditions, ionic ammonia (NH_4^+) is unable to freely pass through the BBB[68]. Although gaseous ammonia (NH_3) may diffuse through the BBB, this only forms a minor fraction of the total ammonia in the blood[68]. Cerebral hyperammonemia can result in excessive extracellular Glu and increased levels of Ala and Gln[69-72]. Furthermore, hyperammonemia can induce neuroinflammation[73]. However, to the best of our knowledge, no studies have been conducted to monitor whether the diminished BBB integrity in TLR2 deficient models results in cerebral hyperammonemia. Thus, at present, no evidence is available to substantiate this hypothesis.

Alongside increased levels of Glu, we found elevated GABA in the brain of TLR2 deficient zebrafish. GABA is the major inhibitory neurotransmitter and synthesised from Glu. In the zebrafish brain, GABA is mainly expressed in the olfactory bulb, preoptic nuclei, retina, telencephalon, ventral thalamus, subpallium, pretectum, hypothalamus, and posterior tubercular nuclei of the zebrafish brain[62,74]. In these regions, GABA mediates processes including memory and learning, motor functions, and neural development[61]. A disruption GABA regulation can profoundly affect the brain, with altered GABA reported in neurological disorders, including attention deficit hyperactivity disorder (ADHD), autism spectrum disorder (ASD), epilepsy, depression, anxiety, and neurodegenerative diseases including Parkinson's disease and Alzheimer's disease (reviewed by Yoo Sung Kim and Bo-Eun Yoon[75]). Specifically, elevated levels of GABA, as well as a decreased glutamate/GABA ratio, are observed in ASD[59,76] and during stress[77]. Alternatively, hypoperfusion, previously observed as a consequence of TLR2 deficiency[14], may also lead to long lasting increase in GABA levels[78].

Metabolic changes in TLR2 deficient zebrafish mimic schizophrenia

Previously, TLR2-deficient models revealed genomic deletion of TLR2 causes significant changes in their behaviour[13,79]. Noteworthy, TLR2 deficient mice showed parallels with

schizophrenia[80], with behavioural changes including symptoms reminiscent of psychosis, including increased movement, withdrawal from social interactions, cognitive impairments and anxiety (negative schizophrenia symptoms). Additionally, TLR2 deficiency caused ventricle enlargement, another hallmark of schizophrenia[80]. Remarkably, we report metabolic changes similar to those observed in schizophrenia patients, including elevated Glu[81,82], Gln [81], m-Ins [83], and Lac [81]. GABA levels in schizophrenia report conflicting results, although most studies reported GABA levels are affected in schizophrenia[84-86]. In addition, significantly elevated cerebral glucose uptake is reported in both TLR2 deficiency[16,87], 70% of schizophrenia patients exhibited reactive astrogliosis[87,88], and both hypoperfusion and hyperperfusion was observed in the brain of schizophrenia patients, although hypoperfusion is more commonly associated with negative schizophrenia symptoms, *e.g.* blunted affect, alogia, and anhedonia, while hyperperfusion is associated with positive symptoms, *e.g.* hallucination, thought disorder, and delusions [89]. While our study may not specifically investigate the origin of the striking parallels observed between schizophrenia and TLR2 deficiency, our findings shed light on intriguing metabolic alterations within the brain that seem to mirror each other.

5. CONCLUSION AND FUTURE OUTLOOK

In conclusion, we report TLR2 plays a role in maintaining the cerebral metabolic homeostasis even in the absence of infections. Genomic deletion of TLR2 causes significant changes in the level of several metabolites in the zebrafish brain. This includes changes in the excitatory and inhibitory neurotransmitter balance, potentially explaining neurobehavioral and cerebral microstructural changes observed in TLR2 deficient models. Furthermore, we observed changes in cell-specific metabolites, indicative of neuroinflammation and neurodegeneration, also in line with previous observations. In future work, advanced MRI and MRS techniques could provide further insight in the effect of TLR2 deficiency on metabolic changes in the zebrafish brain. Amongst these techniques, chemical exchange saturation transfer (CEST) for glucose (glucoCEST), glutamate (gluCEST), and *myo*-inositol (MICEST) could provide detailed spatial information regarding the distribution of these metabolites over the brain of *tlr2*$^{-/-}$ zebrafish.

ACKNOWLEDGEMENTS

Experiments at the 28.2 T instrument were supported by the uNMR-NL Grid: A distributed, state-of-the-art Magnetic Resonance facility for the Netherlands (NWO grant 184.032.207). The authors thank Andrei Gurinov for technical help provided at the 28.2 T instrument and Holger Scheidt for help provided during HR-MAS measurements at the 14.1 T system.

REFERENCES

1 Hu, W. & Spaink, H. P. The Role of TLR2 in Infectious Diseases Caused by Mycobacteria: From Cell Biology to Therapeutic Target. *Biology (Basel)* **11** (2022). https://doi.org/10.3390/biology11020246

2 Sameer, A. S. & Nissar, S. Toll-Like Receptors (TLRs): Structure, Functions, Signaling, and Role of Their Polymorphisms in Colorectal Cancer Susceptibility. *Biomed Res Int* **2021**, 1157023 (2021). https://doi.org/10.1155/2021/1157023

3 O'Neill, L. A. J. The Interleukin-1 Receptor/Toll-like Receptor Superfamily: Signal Transduction During Inflammation and Host Defense. *Sci. STKE* **2000** (2000). https://doi.org/https://doi.org/10.1126/stke.442000re1

4 Behzadi, P., Garcia-Perdomo, H. A. & Karpinski, T. M. Toll-Like Receptors: General Molecular and Structural Biology. *J Immunol Res* **2021**, 9914854 (2021). https://doi.org/10.1155/2021/9914854

5 Meijer, A. H. *et al.* Expression analysis of the Toll-like receptor and TIR domain adaptor families of zebrafish. *Mol Immunol* **40**, 773-783 (2004). https://doi.org/10.1016/j.molimm.2003.10.003

6 Yang, R. B. *et al.* Toll-like receptor-2 mediates lipopolysaccharide-induced cellular signalling. *Nature* **395**, 5 (1998).

7 Kirschning, C. J., Wesche, H., Merrill Ayres, T. & Rothe, M. Human toll-like receptor 2 confers responsiveness to bacterial lipopolysaccharide. *J Exp Med* **188**, 7 (1998).

8 Harding, C. V. & Boom, W. H. Regulation of antigen presentation by Mycobacterium tuberculosis: a role for Toll-like receptors. *Nat Rev Microbiol* **8**, 296-307 (2010). https://doi.org/10.1038/nrmicro2321

9 Oliveira-Nascimento, L., Massari, P. & Wetzler, L. M. The Role of TLR2 in Infection and Immunity. *Front Immunol* **3**, 79 (2012). https://doi.org/10.3389/fimmu.2012.00079

10 Dasu, M. R. *et al.* TLR2 expression and signaling-dependent inflammation impair wound healing in diabetic mice. *Lab Invest* **90**, 1628-1636 (2010). https://doi.org/10.1038/labinvest.2010.158

11 Marks, K. E., Cho, K., Stickling, C. & Reynolds, J. M. Toll-like Receptor 2 in Autoimmune Inflammation. *Immune Netw* **21**, e18 (2021). https://doi.org/10.4110/in.2021.21.e18

12 Pascual, M. *et al.* Toll-like receptors in neuroinflammation, neurodegeneration, and alcohol-induced brain damage. *IUBMB Life* **73**, 900-915 (2021). https://doi.org/10.1002/iub.2510

13 Zhou, C. *et al.* Genomic deletion of TLR2 induces aggravated white matter damage and deteriorated neurobehavioral functionsin mouse models of Alzheimer's disease. *Aging* **11** (2019). https://doi.org/10.18632/aging.102260

14 Hu, Y. *et al.* Toll-like receptor-2 gene knockout results in neurobehavioral dysfunctions and multiple brain structural and functional abnormalities in mice. *Brain Behav Immun* **91**, 257-266 (2021). https://doi.org/10.1016/j.bbi.2020.10.004

15 Hu, W. *et al.* Transcriptomic and Metabolomic Studies Reveal That Toll-like Receptor 2 Has a Role in Glucose-Related Metabolism in Unchallenged Zebrafish Larvae (Danio rerio). *Biology (Basel)* **12** (2023). https://doi.org/10.3390/biology12020323

16 Bajorat, R. *et al.* Early Post-ischemic Brain Glucose Metabolism Is Dependent on Function of TLR2: a Study Using [(18)F]F-FDG PET-CT in a Mouse Model of Cardiac Arrest and Cardiopulmonary Resuscitation. *Mol Imaging Biol* **24**, 466-478 (2022). https://doi.org/10.1007/s11307-021-01677-y

17 Berry, J. P. *et al.* High-Resolution Magic Angle Spinning Nuclear Magnetic Resonance of Intact Zebrafish Embryos Detects Metabolic Changes Following Exposure to Teratogenic Polymethoxyalkenes from Algae. *Zebrafish* **13**, 456-465 (2016). https://doi.org/10.1089/zeb.2016.1280

18 Bashirova, N. *et al.* A mechanistic understanding of the effects of polyethylene terephthalate nanoplastics in the zebrafish (Danio rerio) embryo. *Sci Rep* **13**, 1891 (2023). https://doi.org/10.1038/s41598-023-28712-y

19 Annunziato, M. *et al.* High-Resolution Magic Angle Spinning (HRMAS) NMR Identifies Oxidative Stress and Impairment of Energy Metabolism by Zearalenone in Embryonic Stages of Zebrafish (Danio rerio), Olive Flounder (Paralichthys olivaceus) and Yellowtail Snapper (Ocyurus chrysurus). *Toxins (Basel)* **15** (2023). https://doi.org/10.3390/toxins15060397

20 Annunziato, M. *et al.* An integrated systems-level model of the toxicity of brevetoxin based on high-resolution magic-angle spinning nuclear magnetic resonance (HRMAS NMR) metabolic profiling of zebrafish embryos. *Sci Total Environ* **803**, 149858 (2022). https://doi.org/10.1016/j.scitotenv.2021.149858

21 Eeza, M. N. H. *et al.* Metabolic Profiling of Suprachiasmatic Nucleus Reveals Multifaceted Effects in an Alzheimer's Disease Mouse Model. *J Alzheimers Dis* (2021). https://doi.org/10.3233/JAD-201575

22 Kabli, S., Spaink, H. P., De Groot, H. J. & Alia, A. In vivo metabolite profile of adult zebrafish brain obtained by high-resolution localized magnetic resonance spectroscopy. *J Magn Reson Imaging* **29**, 275-281 (2009). https://doi.org/10.1002/jmri.21609

23 Hu, W. *et al.* Infection and RNA-seq analysis of a zebrafish tlr2 mutant shows a broad function of this toll-like receptor in transcriptional and metabolic control and defense to Mycobacterium marinum infection. *BMC Genomics* **20**, 878 (2019). https://doi.org/10.1186/s12864-019-6265-1

24 Hu, W. *et al.* A Novel Function of TLR2 and MyD88 in the Regulation of Leukocyte Cell Migration Behavior During Wounding in Zebrafish Larvae. *Front Cell Dev Biol* **9**, 624571 (2021). https://doi.org/10.3389/fcell.2021.624571

25 Bottomley, P. A. Selective volume method for performing localized NMR spectroscopy. United States of America patent (1984).

26 Tkac, I., Starcuk, Z., Choi, I. Y. & Gruetter, R. In vivo1H NMR spectroscopy of rat brain at 1 ms echo time. *Magnetic Resonance in Medicine* **41**, 649-656 (1999). https://doi.org/10.1002/(sici)1522-2594(199904)41:4<649::Aid-mrm2>3.0.Co;2-g

27 Govindaraju, V., Young, K. & Maudsley, A. A. Proton NMR chemical shifts and coupling constants for brain metabolites. *NMR in Biomedicine* **13** (2000).

28 Akhtar, M. T., Mushtaq, M. Y., Verpoorte, R., Richardson, M. K. & Choi, Y. H. Zebrafish as a Model for Systems Medicine R&D: Rethinking the Metabolic Effects of Carrier Solvents and Culture Buffers Determined by (1) H NMR Metabolomics. *OMICS* **20**, 42-52 (2016). https://doi.org/10.1089/omi.2015.0119

29 Markley, J. L. *et al.* New bioinformatics resources for metabolomics. *Pacific symposium on biocomputing* **157** (2007).

30 Graaf de, R. A. *In-vivo NMR Spectroscopy: Principles and Techniques*. (John Wiley & Sons, 2007).

31 Behar, K. L. & Ogino, T. Characterization of macromolecules resonances in the 1H NMR spectrum of rat brain. *Magnetic Resonance in Medicine* **30**, 7 (1993). https://doi.org/10.1002/mrm.1910300107

32 Majumder, A. L., Johnson, M. J. & Henry, S. A. 1l-myo-Inositol-1-phosphate synthase. *Biochimica et Biophysica Acta (BBA)* **1348**, 11 (1997). https://doi.org/https://doi.org/10.1016/S0005-2760(97)00122-7.

33 Brand, A., Richter-Landsberg, C. & Leibfritz, D. Multinuclear NMR studies on the energy metabolism of glial and neuronal cells. *Dev Neurosci* **15**, 289-298 (1993).

34 Miller, B. L. *et al.* Alzheimer disease: depiction of increased cerebral myo-inositol with proton MR spectroscopy. *Radiology* **187**, 4 (1993). https://doi.org/10.1148/radiology.187.2.8475286.

35 Fernando, K. T. *et al.* Elevated white matter myo-inositol in clinically isolated syndromes suggestive of multiple sclerosis. *Brain* **127**, 1361-1369 (2004). https://doi.org/10.1093/brain/awh153

36 Saraf-Lavi, E. *et al.* Proton MR spectroscopy of gliomatosis cerebri: case report of elevated myoinositol with normal choline levels. *American Journal of Neuroradiology* **24** (2003).

37 Andersen, J. V., Schousboe, A. & Verkhratsky, A. Astrocyte energy and neurotransmitter metabolism in Alzheimer's disease: Integration of the glutamate/GABA-glutamine cycle. *Prog Neurobiol* **217**, 102331 (2022). https://doi.org/10.1016/j.pneurobio.2022.102331

38 Daneman, R. & Prat, A. The blood-brain barrier. *Cold Spring Harb Perspect Biol* **7**, a020412 (2015). https://doi.org/10.1101/cshperspect.a020412

39 Knox, E. G., Aburto, M. R., Clarke, G., Cryan, J. F. & O'Driscoll, C. M. The blood-brain barrier in aging and neurodegeneration. *Mol Psychiatry* **27**, 2659-2673 (2022). https://doi.org/10.1038/s41380-022-01511-z

40 Waragai, M., Moriya, M. & Nojo, T. Decreased N-Acetyl Aspartate/Myo-Inositol Ratio in the Posterior Cingulate Cortex Shown by Magnetic Resonance Spectroscopy May Be One of the Risk Markers of Preclinical Alzheimer's Disease: A 7-Year Follow-Up Study. *J Alzheimers Dis* **60**, 1411-1427 (2017). https://doi.org/10.3233/JAD-170450

41 Rolls, A. *et al.* Toll-like receptors modulate adult hippocampal neurogenesis. *Nat Cell Biol* **9**, 1081-1088 (2007). https://doi.org/10.1038/ncb1629

42 Magistretti, P. J. & Allaman, I. Lactate in the brain: from metabolic end-product to signalling molecule. *Nat Rev Neurosci* **19**, 235-249 (2018). https://doi.org/10.1038/nrn.2018.19

43 Bolanos, J. P., Peuchen, S., Heales, S. J., Land, J. M. & Clark, J. B. Nitric oxide-mediated inhibition of the mitochondrial respiratory chain in cultured astrocytes. *J. Neurochem* **63**, 7 (1994). https://doi.org/10.1046/j.1471-4159.1994.63030910.x

44 Hyder, F., Rothman, D. L. & Bennett, M. R. Cortical energy demands of signaling and nonsignaling components in brain are conserved across mammalian species and activity levels. *Proc Natl Acad Sci U S A* **110**, 3549-3554 (2013). https://doi.org/10.1073/pnas.1214912110

45 Nehlig, A., Wittendorp-Rechenmann, E. & Lam, C. D. Selective uptake of [14C]2-deoxyglucose by neurons and astrocytes: high-resolution microautoradiographic imaging by cellular 14C-trajectography combined with immunohistochemistry. *J Cereb Blood Flow Metab* **24**, 1004-1014 (2004). https://doi.org/10.1097/01.WCB.0000128533.84196.D8

46 Chuquet, J., Quilichini, P., Nimchinsky, E. A. & Buzsaki, G. Predominant enhancement of glucose uptake in astrocytes versus neurons during activation of the somatosensory cortex. *J Neurosci* **30**, 15298-15303 (2010). https://doi.org/10.1523/JNEUROSCI.0762-10.2010

47 Bitsch, A. *et al.* Inflammatory CNS demyelination: histopathologic correlation with in vivo quantitative proton MR spectroscopy. *Am J Neuroradiol* **9**, 1619-1627 (1999).

48 Mader, I., Rauer, S., Gall, P. & Klose, U. (1)H MR spectroscopy of inflammation, infection and ischemia of the brain. *Eur J Radiol* **67**, 250-257 (2008). https://doi.org/10.1016/j.ejrad.2008.02.033

49 Young, S. P. *et al.* The impact of inflammation on metabolomic profiles in patients with arthritis. *Arthritis Rheum* **65**, 2015-2023 (2013). https://doi.org/10.1002/art.38021

50 Cocco, E. *et al.* (1)H-NMR analysis provides a metabolomic profile of patients with multiple sclerosis. *Neurol Neuroimmunol Neuroinflamm* **3**, 1-9 (2016). https://doi.org/10.1212/NXI.0000000000000185

51 Kim, H. H. *et al.* Metabolomic profiling of CSF in multiple sclerosis and neuromyelitis optica spectrum disorder by nuclear magnetic resonance. *PLoS One* **12**, 21 (2017). https://doi.org/10.1371/journal.pone.0181758

52 Battini, S. *et al.* Metabolomics approaches in experimental allergic encephalomyelitis. *J Neuroimmunol* **314**, 94-100 (2018). https://doi.org/10.1016/j.jneuroim.2017.11.018

53 French, C. D. *et al.* NMR metabolomics of cerebrospinal fluid differentiates inflammatory diseases of the central nervous system. *PLOS Negl Trop Dis* **12**, 1-17 (2018). https://doi.org/10.1371/journal.pntd.0007045

54 Li, K., Li, J., Zheng, J. & Qin, S. Reactive astrocytes in neurodegenerative diseases. *Aging Dis* **10**, 664-675 (2019). https://doi.org/10.14336/AD.2018.0720

55 Meregalli, A., Oliveira, R. P. & Friedman, G. Occult hypoperfusion is associated with increased mortality in hemodynamically stable, high-risk, surgical patients. *Crit Care* **8**, R60-65 (2004). https://doi.org/10.1186/cc2423

56 Farkas, E. *et al.* Experimental cerebral hypoperfusion induces white matter injury and microglial activation in the rat brain. *Acta Neuropathol* **108**, 57-64 (2004). https://doi.org/10.1007/s00401-004-0864-9

57 Gladden, L. B. Lactate metabolism: a new paradigm for the third millennium. *J Physiol* **558**, 5-30 (2004). https://doi.org/10.1113/jphysiol.2003.058701

58 Howarth, C., Gleeson, P. & Attwell, D. Updated energy budgets for neural computation in the neocortex and cerebellum. *J Cereb Blood Flow Metab* **32**, 1222-1232 (2012). https://doi.org/10.1038/jcbfm.2012.35

59 Yizhar, O. *et al.* Neocortical excitation/inhibition balance in information processing and social dysfunction. *Nature* **477**, 171-178 (2011). https://doi.org/10.1038/nature10360

60 Pal, M. M. Glutamate: The Master Neurotransmitter and Its Implications in Chronic Stress and Mood Disorders. *Front Hum Neurosci* **15**, 722323 (2021). https://doi.org/10.3389/fnhum.2021.722323
61 Verma, R., Raj Choudhary, P., Kumar Nirmal, N., Syed, F. & Verma, R. Neurotransmitter systems in zebrafish model as a target for neurobehavioural studies. *Materials Today: Proceedings* **69**, 1565-1580 (2022). https://doi.org/10.1016/j.matpr.2022.07.147
62 Tabor, K. M. *et al.* Brain-wide cellular resolution imaging of Cre transgenic zebrafish lines for functional circuit-mapping. *Elife* **8** (2019). https://doi.org/10.7554/eLife.42687
63 Zhou, Y. & Danbolt, N. C. Glutamate as a neurotransmitter in the healthy brain. *J Neural Transm (Vienna)* **121**, 799-817 (2014). https://doi.org/10.1007/s00702-014-1180-8
64 Kazama, M. *et al.* Astrocytes release glutamate via cystine/glutamate antiporter upregulated in response to increased oxidative stress related to sporadic amyotrophic lateral sclerosis. *Neuropathology* **40**, 587-598 (2020). https://doi.org/10.1111/neup.12716
65 Iovino, L., Tremblay, M. E. & Civiero, L. Glutamate-induced excitotoxicity in Parkinson's disease: The role of glial cells. *J Pharmacol Sci* **144**, 151-164 (2020). https://doi.org/10.1016/j.jphs.2020.07.011
66 Schousboe, A., Sonnewald, U. & Waagepetersen, H. S. Differential roles of alanine in GABAergic and glutamatergic neurons. *Neurochem Int* **43**, 311-315 (2003). https://doi.org/10.1016/s0197-0186(03)00017-2
67 Maszka, P. *et al.* Metabolomic Footprint of Disrupted Energetics and Amino Acid Metabolism in Neurodegenerative Diseases: Perspectives for Early Diagnosis and Monitoring of Therapy. *Metabolites* **13** (2023). https://doi.org/10.3390/metabo13030369
68 Lockwood, A. H., Finn, R. D., Campbell, J. A. & Richman, T. B. Factors that affect the uptake of ammonia by the brain: the blood-brain pH gradient. *Brain research* **181** (1980).
69 Wilkinson, D. J., Smeeton, N. J. & Watt, P. W. Ammonia metabolism, the brain and fatigue; revisiting the link. *Prog Neurobiol* **91**, 200-219 (2010). https://doi.org/10.1016/j.pneurobio.2010.01.012
70 Tsacopoulos, M., Poitry-Yamate, C. I. & Poitry, S. Ammonium and Glutamate Released by Neurons Are Signals Regulating the Nutritive Function of a Glial Cell. *The journal of neuroscience* **17** (1997).
71 Tofteng, F. *et al.* Persistent arterial hyperammonemia increases the concentration of glutamine and alanine in the brain and correlates with intracranial pressure in patients with fulminant hepatic failure. *J Cereb Blood Flow Metab* **26**, 21-27 (2006). https://doi.org/10.1038/sj.jcbfm.9600168
72 Lemberg, A. & Alejandra Fernández, M. Hepatic encephalopathy, ammonia, glutamate, glutamine and oxidative stress. *Annals of Hepatology* **8**, 95-102 (2009). https://doi.org/10.1016/s1665-2681(19)31785-5
73 Hernandez-Rabaza, V. *et al.* Neuroinflammation increases GABAergic tone and impairs cognitive and motor function in hyperammonemia by increasing GAT-3 membrane expression. Reversal by sulforaphane by promoting M2 polarization of microglia. *Journal of Neuroinflammation* **13** (2016). https://doi.org/10.1186/s12974-016-0549-z
74 Satou, C. *et al.* Transgenic tools to characterize neuronal properties of discrete populations of zebrafish neurons. *Development* **140**, 3927-3931 (2013). https://doi.org/10.1242/dev.099531
75 Kim, Y. S. & Yoon, B. E. Altered GABAergic Signaling in Brain Disease at Various Stages of Life. *Exp Neurobiol* **26**, 122-131 (2017). https://doi.org/10.5607/en.2017.26.3.122
76 Park, G. *et al.* Decreased in vivo glutamate/GABA ratio correlates with the social behavior deficit in a mouse model of autism spectrum disorder. *Mol Brain* **15**, 19 (2022). https://doi.org/10.1186/s13041-022-00904-z
77 Drouet, J. B. *et al.* Differences in prefrontal cortex GABA/glutamate ratio after acute restraint stress in rats are associated with specific behavioral and neurobiological patterns. *Neuroscience* **285**, 155-165 (2015). https://doi.org/10.1016/j.neuroscience.2014.10.058
78 Sieklucka, M., Heim, C., Block, F. & Sontag, K. H. Transient reduction of cerebral blood flow leads to longlasting increase in GABA content in vulnerable structures and decreased susceptibility to bicuculline induced seizures. *Journal of Neural Transmission* **88**, 8 (1992). https://doi.org/10.1007/BF01244814
79 DeKorver, N. W., Chaudoin, T. R. & Bonasera, S. J. Toll-Like Receptor 2 Is a Regulator of Circadian Active and Inactive State Consolidation in C57BL/6 Mice. *Front Aging Neurosci* **9**, 219 (2017). https://doi.org/10.3389/fnagi.2017.00219

80 Park, S. J. *et al.* Toll-like receptor-2 deficiency induces schizophrenia-like behaviors in mice. *Sci Rep* **5**, 8502 (2015). https://doi.org/10.1038/srep08502

81 McCutcheon, R. A., Krystal, J. H. & Howes, O. D. Dopamine and glutamate in schizophrenia: biology, symptoms and treatment. *World Psychiatry* **19**, 19 (2020).

82 Plitman, E. *et al.* Elevated Myo-Inositol, Choline, and Glutamate Levels in the Associative Striatum of Antipsychotic-Naive Patients With First-Episode Psychosis: A Proton Magnetic Resonance Spectroscopy Study With Implications for Glial Dysfunction. *Schizophr Bull* **42**, 415-424 (2016). https://doi.org/10.1093/schbul/sbv118

83 Liu, S. *et al.* Lactate levels in the brain and blood of schizophrenia patients: A systematic review and meta-analysis. *Schizophr Res* **264**, 29-38 (2024). https://doi.org/10.1016/j.schres.2023.11.013

84 Reyes-Madrigal, F. *et al.* Prefrontal γ-Aminobutyric Acid Levels in Never-Medicated Individuals With Chronic Schizophrenia. *JAMA Psychiatry* **80** (2023). https://doi.org/10.1001/jamapsychiatry.2023.3157

85 Yoon, J. H. *et al.* GABA concentration is reduced in visual cortex in schizophrenia and correlates with orientation-specific surround suppression. *J Neurosci* **30**, 3777-3781 (2010). https://doi.org/10.1523/JNEUROSCI.6158-09.2010

86 Fujihara, K. Beyond the gamma-aminobutyric acid hypothesis of schizophrenia. *Front Cell Neurosci* **17**, 1161608 (2023). https://doi.org/10.3389/fncel.2023.1161608

87 Soyka, M., Koch, W., Moller, H. J., Ruther, T. & Tatsch, K. Hypermetabolic pattern in frontal cortex and other brain regions in unmedicated schizophrenia patients. Results from a FDG-PET study. *Eur Arch Psychiatry Clin Neurosci* **255**, 308-312 (2005). https://doi.org/10.1007/s00406-005-0563-0

88 Tarasov, V. V. *et al.* Alterations of Astrocytes in the Context of Schizophrenic Dementia. *Front Pharmacol* **10**, 1612 (2019). https://doi.org/10.3389/fphar.2019.01612

89 Percie du Sert, O. *et al.* Cerebral blood flow in schizophrenia: A systematic review and meta-analysis of MRI-based studies. *Progress in Neuro-Psychopharmacology and Biological Psychiatry* **121** (2023). https://doi.org/10.1016/j.pnpbp.2022.110669

6

CONCLUSIONS AND FUTURE OUTLOOK

Toll-like receptors (TLRs), and specifically TLR2, play a pivotal role in the immune system by recognizing pathogens and initiating inflammatory responses. However, there is growing evidence that TLR2 is also involved in the pathology of neurological disorders, acting as a double-edged sword. While TLR2's activation can help combat infections, its dysregulation may contribute to neuroinflammation and neurodegeneration. Despite its critical functions, the complete involvement of TLR2 in normal brain functioning remains poorly understood, necessitating further research to elucidate its complex roles in both health and disease.

Magnetic resonance (MR) techniques, including magnetic resonance imaging (MRI) and magnetic resonance spectroscopy (MRS), are non-invasive methods offering a broad range of information on the microstructural and biochemical environment of tissues. Utilizing the same basic principles of nuclear magnetic resonance (NMR), MRI provides detailed anatomical images and microstructural information through local relaxation times, while MRS delivers insights into the local chemical composition of tissue. Furthermore, diffusion-based MRI (dMRI), including diffusion-weighted imaging (DWI), diffusion tensor imaging (DTI), and dMRI tractography extends the capabilities of conventional MRI by measuring the random motion of water molecules within tissues. This allows for the visualization and characterisation of microstructural changes that are not apparent in standard MRI scans. The versatility of MRI data is largely dictated by the specific MR sequences employed, which can be utilized to provide specific tissue contrast, molecular interactions, and physiological processes, making MR techniques invaluable in both clinical and research settings.

The main scope of this thesis was the optimization and application of MRI and MRS techniques at ultra-high magnetic field (UHF) strengths to obtain non-invasive insights into microstructural and neurochemical changes in the zebrafish (*Danio rerio*) brain caused by TLR2 deficiency. Zebrafish have become a prevalent model for studying neurological diseases due to their rapid development, fast reproduction, low maintenance costs, straightforward husbandry, and the comprehensive availability of pathological models stemming from their fully sequenced genome. Despite their growing use in neuroscience research, the application of MRI and MRS to zebrafish has been scarcely explored. These advanced imaging techniques hold great potential for non-invasively investigating the structural and metabolic aspects of neurological conditions in zebrafish, providing new insights that complement traditional methods. However, the relative low sensitivity of MR based techniques in combination with the size of the zebrafish brain, has limited their application.

In this work, we have shown that utilization of UHFs in MRI and MRS, in combination with strong gradient systems up to 3 T/m (G_{max}) provides the necessary signal-to-noise ratio (SNR), spatial resolution, and contrasts required for detailed examination of zebrafish brain structures.

Fast spin echo MRI sequences at 28.2 T provide anatomical images with high tissue-contrast for the identification of a wide range of zebrafish brain structures, with additional contrast obtained through diffusion-weighted MRI (Chapter 2). Additionally, dMRI tractography through short-track track-density imaging using multi-shell multi-tissue constrained spherical deconvolution method (stTDI msmt CSD) provided super-resolution (5 µm) tractography maps of the zebrafish brain for the visualization of tiny white matter structures. In addition to MRI and dMRI, UHF systems significantly enhance the SNR and provide highly resolved spectra of localized brain regions through MRS in the zebrafish brain (Chapter 4). Localized MRS at UHF enables the acquisition of detailed spectra from very small regions, as small as 125 nL, in relatively short measurement times (~30 minutes). This capability is crucial for studying the zebrafish brain, allowing for precise metabolic profiling and improved understanding of neurochemical processes within these minute, localized areas. However, MR artifacts, and specifically chemical shift displacement effects escalate at UHF and need to be corrected. We have shown how these effects can be minimized through optimization of the excitation frequency and excitation- and refocussing RF pulse bandwidths.

We successfully applied these techniques to show TLR2 deficiency causes both microstructural (Chapter 3) and metabolic (Chapter 5) changes in the zebrafish brain. Brain tissue of *tlr2*$^{-/-}$ zebrafish showed significantly elevated transverse relaxation times (T_2) and decreased apparent diffusion coefficient (*ADC*), indicative of microstructural changes in the brain tissue and restricted diffusion, possibly indicative of neuroinflammation, cytotoxic edema, and astrogliosis. Furthermore, we observed significant changes in diffusion tensor and diffusion kurtosis metrics in several white matter structures in the *tlr2*$^{-/-}$ brain compared to a control group, indicative of neuronal damage. Additionally, high-resolution magic angle spinning (HR-MAS) spectroscopy of *tlr2*$^{-/-}$ and control zebrafish brain showed significant alterations in brain metabolites as a consequence of TLR2 deficiency. We report significant changes in the neurotransmitters glutamate and γ-aminobutyric acid (GABA), as well as changes in glutamine, involved in the glutamate/GABA-glutamine cycle. Furthermore, we observed significant changes in metabolites involved in the alanine-lactate cycle, indicative of increased cerebral energy utilization as a consequence of TLR2 deficiency. Utilizing localized MRS, cerebral metabolic profiles were obtained from the zebrafish forebrain, midbrain, and hindbrain, showing TLR2 deficiency causes an increase in lactate in all three major brain regions. Furthermore, significantly lower levels of N-acetyl aspartate (NAA) were found in the *tlr2*$^{-/-}$ hindbrain, indicative of diminished neuron integrity.

Our research on MRI and MRS at UHF demonstrates that these systems open innovative avenues for utilizing zebrafish in neurological research. By combining MRI, dMRI, and MRS data, we can comprehensively study both the microstructural and metabolic aspects of the

zebrafish brain. This integrated approach provides a broad and detailed field of research, enabling the investigation of neurological disorders with unprecedented precision. The high spatial resolution and enhanced SNR offered by UHF systems allow us to observe intricate brain structures and metabolic changes, thus facilitating a deeper understanding of the underlying mechanisms of neurological diseases in zebrafish models.

1. FUTURE OUTLOOK

The techniques presented in this study have the potential to be applied to other pathological zebrafish models, extending their utility beyond the current scope. Additionally, with the appropriate hardware for zebrafish imaging, these methods could be implemented *in vivo*, allowing for real-time observation and analysis. In this section preliminary results will be shared of a leptin-deficient zebrafish model, along with insights into how these techniques could be adapted for *in vivo* applications in future studies.

1.1 PROBING CORRELATION OF WM INTEGRITY AND FAT ACCUMULATION WITH UHF MRI

A biomedical field that could benefit significantly from UHF MRI and dMRI is the impact of body fat accumulation on brain health. Excessive body weight is a growing global health problem, with 39% of the global adult population being overweight and 13% of the global adult population developing obesity[1]. Excessive body weight, and especially obesity, significantly increases the risk of diminished health, including heart diseases[2], increases blood pressure[2], type 2 diabetes[3], liver diseases[4], fertility problems[5], and certain types of cancer[6,7]. Furthermore, recent studies showed a link between obesity and certain types of neurodegenerative diseases, including Alzheimer's disease and Parkinson's disease[8]. However, the precise mechanisms of increased body weight and the development of neurodegenerative diseases remains largely unclear.

Here, we present a pilot study demonstrating the utilization of a leptin-deficient (*lepb*$^{-/-}$) zebrafish model to monitor the effects of fat accumulation on brain microstructure and white matter integrity. Leptin is a hormone involved in the energy and appetite regulation[9]. A deficiency in leptin can cause insufficient leptin levels, leading to increased appetite and a decrease in the body energy expenditure[10]. Previously, we showed that leptin-deficiency in zebrafish causes significant fat infiltration in muscle tissue and muscle wasting [11]. However, the effects of the fat accumulation observed in *lepb*$^{-/-}$ zebrafish and the brain microstructure and neuronal health was not investigated. For the specific imaging of fat, MRI utilizes chemical shift selective imaging (cssi or CHESS)[12]. Cssi differs from regular anatomical imaging in MRI

by its ability to selectively image specific substances within the body based on their distinct resonance frequencies. While regular anatomical MRI produces images based on the overall signal from all tissues, cssi targets particular molecules, such as fat or water, by exploiting differences in their Larmor frequencies. In a pilot study, we utilized cssi to quantify the fat accumulation surrounding the brain and observed a significant increase in *lepb*$^{-/-}$ zebrafish compared to a control group (see Figure 6.1).

Utilizing DTI and dMRI tractography, our preliminary results show significant changes in the diffusivity and diffusion kurtosis of several white matter structures, indicating changes in the white matter microstructure (Figure 6.2). A direct correlation was found between the fat accumulation in the zebrafish head and several dMRI DTI and DKI metrics in white matter structures (see Table 6.1). Interestingly, we found significant changes in DTI and DKI metrics in the commissure of the secondary gustatory nuclei (Cgus) of *lepb*$^{-/-}$ zebrafish compared to a control group, as well as a negative correlation between the axial, radial, and mean diffusivity in the Cgus and the total fat accumulation in the zebrafish head. The Cgus is a neural pathway that connects the secondary gustatory nuclei on both sides of the zebrafish brain, playing a crucial role in processing taste-related information within the gustatory system[13]. Alterations

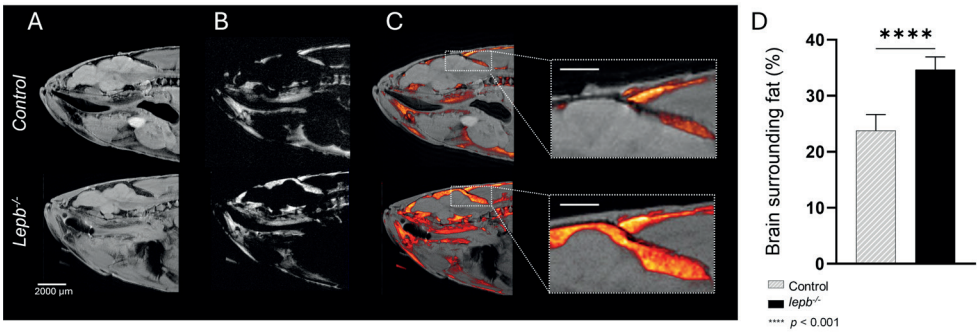

Figure 6.1. *Chemical shift selective imaging of the fat signal in control and lepb-deficient (lepb*$^{-/-}$*) adult zebrafish.* ***[A]*** *Representative sagittal slice of control and lepb*$^{-/-}$ *zebrafish measured by chemical shift selective imaging, selecting the water signal and* ***[B]*** *the fat signal.* ***[C]*** *Overlay of water signal (grey scale) and fat signal (hot colour scale) suggests increased distribution of fat in the head of lepb*$^{-/-}$ *adult zebrafish compared to control. This is elucidated in the zoomed view, shown in the right column. Scale bar in zoomed views indicate 500 µm.* ***[D]*** *Quantification of total area of fat (in %) surrounding brain tissue measured by chemical shift selective imaging. Data represents the mean value of the indicated MRI metric ± standard deviation (error bars). Statistical comparison between both groups performed by t-test, with a significant difference between the population means of control and lepb*$^{-/-}$ *assumed below the 0.05 level, **** $p < 0.001$. $n = 3$ and $n = 6$ for the control and lepb*$^{-/-}$ *groups, respectively. Cssi measurements were performed with a 17.6 T (750 MHz) vertical bore system (Bruker Biospin GmbH, Germany), configured with a Micro2.5 gradient system. Cssi sequence parameters TR = 1500 ms; TE = 12 ms; RARE factor = 4; ns = 4; resolution = 39 × 39 µm; slice thickness = 400 µm; Excitation pulse bandwidth = 2000 Hz.*

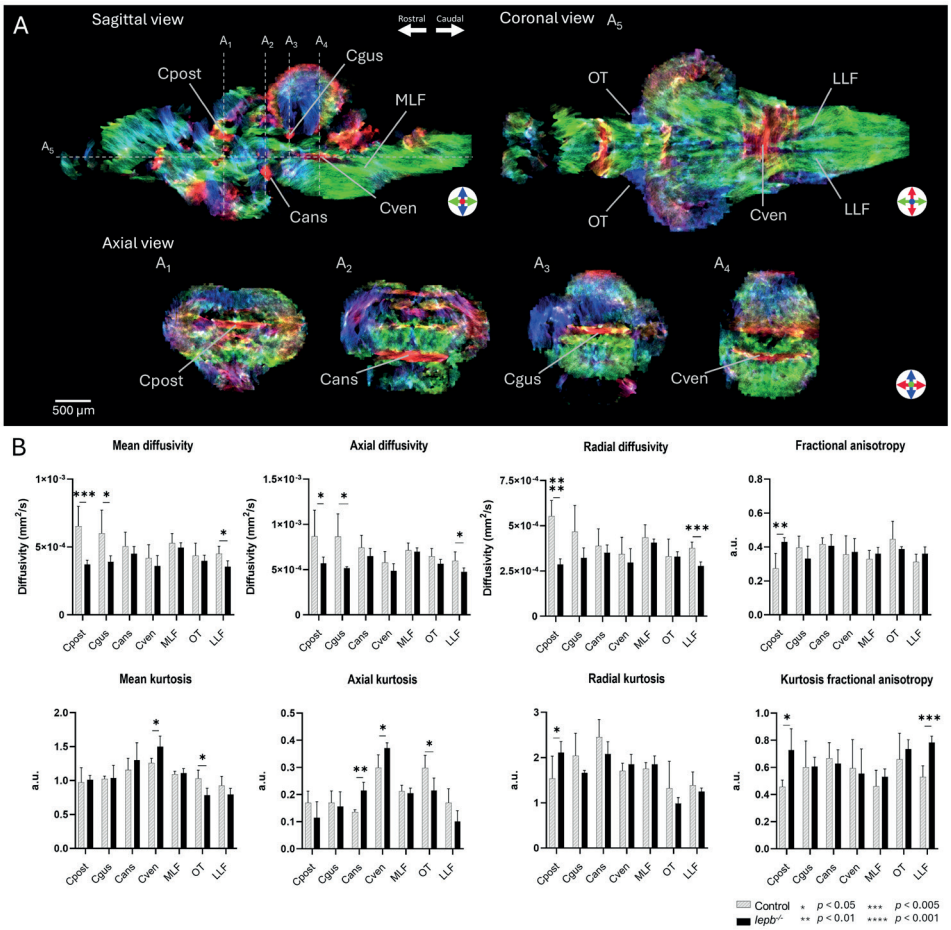

Figure 6.2. *Diffusion tensor imaging metrics and diffusion kurtosis imaging metrics of white matter structures in control and lepb-deficient (lepb$^{-/-}$) adult female zebrafish.* ***[A]*** *Sagittal (right top), coronal (left top) and axial (bottom row) slices of DEC stTDI msmt-CSD map, visualizing the exact location of various white matter structures in the zebrafish brain. Location of axial slices (A1 – A4) and coronal slice (A5) indicated in sagittal slice (dotted lines). Indicated white mater structures, Cpost – posterior commissure; Cgus – commissure of the secondary gustatory nuclei; Cans – ansulate commissure; Cven – ventral rhombencephalic commissure; MLF – medial longitudinal fascicle; OT – optic tract; LLF – lateral longitudinal fascicle.* ***[B]*** *Comparison of diffusion tensor metrics of white matter structures in control and lepb$^{-/-}$ zebrafish. Data represents the mean value of the indicated MRI metric ± standard deviation (error bars). Statistical comparison between both groups performed by t-test, with a significant difference between the population means of control and lepb$^{-/-}$ assumed below the 0.05 level, * $p < 0.05$, ** $p < 0.01$, *** $p < 0.005$, **** $p < 0.001$. n = 3 and n = 6 for the control and lepb$^{-/-}$ group, respectively. DTI measurements were performed with a 17.6 T (750 MHz) vertical bore system (Bruker Biospin GmbH, Germany), configured with a Micro2.5 gradient system. 3D DTI sequence parameters for white matter tractography TR = 1500 ms; TE = 17.3 ms; ns = 4, EPI factor = 7, δ = 1.5 ms, Δ = 10 ms, effective b-value range 160, 1000, or 2500 s/mm2 with 4, 12, or 24 diffusion encoding directions respectively, at an isotropic resolution of 45 µm. 2D DTI sequence parameters for DTI metric estimation TR = 1500 ms; TE = 22.8 ms; ns = 8, EPI factor = 20, δ = 1.5 ms, Δ = 15 ms, effective b-value range 2, 1000, 2500, or 4000 s/mm2 with 4, 12, 24, or 36 diffusion encoding directions respectively, at an isotropic resolution of 50 × 50 µm; slice thickness 300 µm.*

in this neural pathway could affect taste perception and preference, potentially influencing feeding behaviour and dietary choices. Understanding how obesity or increased body fat impacts the Cgus could provide insights into the neural mechanisms underlying altered eating behaviours and contribute to the development of interventions for overweight or obesity. Our research on the effects of fat accumulation and its correlation to changes in white matter integrity in the zebrafish brain demonstrates how UHF MRI and zebrafish models can be effectively utilized to study the impact of body fat on brain structure. This approach highlights the potential of these advanced imaging techniques and animal models to investigate the neural mechanisms underlying obesity and neurodegenerative diseases, providing valuable insights for developing targeted interventions.

1.2 IN VIVO APPLICATION OF MRI, DMRI, AND MRS METHODS AT UHFS

Shifting towards the *in vivo* application of MRI, dMRI, and MRS on zebrafish in pathological studies is crucial for advancing our understanding of neurological disorders in a living organism. *In vivo* imaging allows for the observation of dynamic biological processes and real-time monitoring of disease progression and response to treatments. This approach provides more

Table 6.1 *Statistical correlation analysis between fat infiltration (FI), as observed by cssi, and MR metrics estimated in the observed abnormality in the upper part of the rhombencephalon (see Fig.1A). Upward facing green arrows (↑) indicate significant (P_{corr} < 0.05) positive correlation (R > 0), while a downward facing red arrows (↓) indicate a significant(P_{corr} < 0.05) negative correlation (R < 0). A full overview of the statistical correlation analysis is found in the supplementary information S1. Cpost – posterior commissure; Cgus – commissure of the secondary gustatory nuclei; Cans – ansulate commissure; Cven – ventral rhombencephalic commissure; MLF – medial longitudinal fascicle; OT – optic tract; LLF – lateral longitudinal fascicle. To assess potential correlation between fat infiltration levels and MR metrics, we calculated correlation coefficients, based on the Pearson correlation method. Correlation coefficient values were subsequently cross-validated with their corresponding p values, excluding any correlation without statistical significance (p > 0.05). Potential outliers were detected and removed using a criterion based on three times the scaled median absolute deviation (MAD) from the median value.*

Metric *versus FI*	Cpost	Cgus	Cans	Cven	MLF	OT	LLF
MD	↓	↓	-	-	-	-	↓
$D_{\parallel}$	↓	↓	↓	-	-	-	↓
$D_{\perp}$	↓	↓	-	-	-	-	↓
FA	-	-	-	-	-	-	-
MK	-	-	-	-	-	-	↓
$K_{\parallel}$	-	-	↑	↑	-	-	↓
$K_{\perp}$	-	-	-	-	-	-	-
KFA	↑	-	-	-	-	-	↑

accurate and comprehensive insights into the physiological and metabolic changes occurring within the zebrafish brain, leading to more relevant and translatable findings for human health. Additionally, non-invasive *in vivo* imaging reduces the need for invasive procedures, thereby improving animal welfare and enabling longitudinal studies on the same subjects. This shift towards *in vivo* imaging necessitates specialised hardware to keep the zebrafish alive and under anaesthesia during the procedures[14]. Maintaining stable physiological conditions is essential to ensure accurate and reliable imaging results. Furthermore, to protect animal health, the applied imaging methods need to be as short as possible. This is particularly important if multiple imaging techniques are to be performed during the same session, allowing for precise comparison of different MRI methods within the same specimen.

Many of the high-resolution MR methods presented in this work meet the requirements for measurement time and could be adapted for *in vivo* applications with minimal modifications. However, translating our methods to *in vivo* applications necessitates consideration of the effects of formalin fixation on tissue relaxation times. It is well documented that formalin fixation shortens T_1 relaxation times, allowing for the use of shorter repetition times compared to *in vivo* conditions [15]. Therefore, applying our methods *in vivo* would require longer repetition times, resulting in extended total measurement times. This can be mitigated by reducing the number of scans, as our data indicate that the SNR is sufficient to maintain quality with fewer scans.

Nevertheless, not all presented MRI methods are suitable for *in vivo* application in their current state and require additional optimization. In particular, diffusion tensor imaging (DTI) and dMRI tractography inherently require long measurement times due to the numerous diffusion encoding orientations that must be recorded per voxel at multiple *b*-values. In clinical settings, single-shot EPI significantly reduces the total measurement time. However, the use of single-shot EPI for dMRI measurements on the zebrafish brain at UHFs is hindered by increased susceptibility artifacts. Although correction methods for susceptibility artifacts are available, they can cause significant changes in diffusion data, even in areas far from high distortion[16]. Potential solutions to shorten dMRI and dMRI tractography methods for *in vivo* applications include: (1) reducing the number of averages presented in the current work, albeit with additional noise; (2) reducing the applied resolution, which directly leads to shorter scan times due to fewer phase encoding gradient steps, while simultaneously increasing SNR per voxel, allowing for fewer scans per measurement and further decreasing the total measurement time; (3) further optimizing the number of diffusion encoding orientations and *b*-values beyond those presented in this work. However, for construction of accurate diffusion tensors, and especially diffusion kurtosis, it is recommended to use a high number of diffusion encoding orientations and *b*-values, which helps reduce noise and improve the accuracy of

the obtained diffusion metrics[17]; (4) significantly improving the obtained SNR per scan through the use of cryoprobe technology. As previously demonstrated for anatomical images of the zebrafish brain at 9.4 T (400 MHz), cryoprobe technology improved the SNR by a factor of 3 to 4, potentially shortening the total measurement time by a factor of 16[18].

REFERENCES

1 Organization, W. H. Obesity and overweight. (2017).

2 Klein, B. E. K., Cornoni, J. C., Jones, F. & Boyle, E. Overweight Indices as Correlates of Coronary Heart Diseases and Blood Pressure. *Human Biology* **45**, 329-340 (1973).

3 Long-term effects of lifestyle intervention or metformin on diabetes development and microvascular complications over 15-year follow-up: the Diabetes Prevention Program Outcomes Study. *Lancet Diabetes Endocrinol* **3**, 866-875 (2015). https://doi.org/10.1016/s2213-8587(15)00291-0

4 Hart, C. L., Batty, G. D., Morrison, D. S., Mitchell, R. J. & Smith, G. D. Obesity, overweight and liver disease in the Midspan prospective cohort studies. *International Journal of Obesity* **34**, 1051-1059 (2010). https://doi.org/10.1038/ijo.2010.20

5 Best, D. & Bhattacharya, S. Obesity and fertility. *Hormone Molecular Biology and Clinical Investigation* **24**, 5-10 (2015). https://doi.org/doi:10.1515/hmbci-2015-0023

6 Brawer, R., Brisbon, N. & Plumb, J. Obesity and cancer. *Primary Care: Clinics in Office Practice* **36**, 509-531 (2009).

7 Calle, E. E., Rodriguez, C., Walker-Thurmond, K. & Thun, M. J. Overweight, obesity, and mortality from cancer in a prospectively studied cohort of US adults. *New England Journal of Medicine* **348**, 1625-1638 (2003).

8 Kueck, P. J., Morris, J. K. & Stanford, J. A. Current Perspectives: Obesity and Neurodegeneration - Links and Risks. *Degener Neurol Neuromuscul Dis* **13**, 111-129 (2023). https://doi.org/10.2147/dnnd.S388579

9 Gorissen, M., Flik, G. & Huising, M. Peptides and proteins regulating food intake: a comparative view. *Animal Biology* **56**, 447-473 (2006). https://doi.org/https://doi.org/10.1163/157075606778967829

10 Cui, H., López, M. & Rahmouni, K. The cellular and molecular bases of leptin and ghrelin resistance in obesity. *Nat Rev Endocrinol* **13**, 338-351 (2017). https://doi.org/10.1038/nrendo.2016.222

11 Eeza, M. N. H. *et al.* Probing microstructural changes in muscles of leptin-deficient zebrafish by non-invasive ex-vivo magnetic resonance microimaging. *PLoS One* **18**, e0284215 (2023). https://doi.org/10.1371/journal.pone.0284215

12 Haase, A., Frahm, J., Hänicke, W. & Matthaei, D. 1H NMR chemical shift selective (CHESS) imaging. *Phys Med Biol* **30**, 341-344 (1985). https://doi.org/10.1088/0031-9155/30/4/008

13 Yanez, J., Souto, Y., Pineiro, L., Folgueira, M. & Anadon, R. Gustatory and general visceral centers and their connections in the brain of adult zebrafish: a carbocyanine dye tract-tracing study. *J Comp Neurol* **525**, 333-362 (2017). https://doi.org/10.1002/cne.24068

14 Kabli, S., Alia, A., Spaink, H. P., Verbeek, F. J. & De Groot, H. J. Magnetic resonance microscopy of the adult zebrafish. *Zebrafish* **3**, 431-439 (2006). https://doi.org/10.1089/zeb.2006.3.431

15 Birkl, C. *et al.* Effects of formalin fixation and temperature on MR relaxation times in the human brain. *NMR Biomed* **29**, 458-465 (2016). https://doi.org/10.1002/nbm.3477

16 Begnoche, J. P. *et al.* EPI susceptibility correction introduces significant differences far from local areas of high distortion. *Magnetic Resonance Imaging* **92**, 1-9 (2022). https://doi.org/https://doi.org/10.1016/j.mri.2022.05.016

17 Jones, D. K. The effect of gradient sampling schemes on measures derived from diffusion tensor MRI: a Monte Carlo study. *Magnetic Resonance in Medicine: An Official Journal of the International Society for Magnetic Resonance in Medicine* **51**, 807-815 (2004).

18 Kabli, S. *In vivo high field magnetic resonance imaging and spectroscopy of adult zebrafish*. (Leiden University, 2009).

SUMMARY
SAMENVATTING

SUMMARY

Microstructural and Metabolic Alterations in the Zebrafish Brain Induced by Toll-Like Receptor 2 Deficiency

Insights from Ultra-High Field Magnetic Resonance Imaging and Spectroscopy

Advanced UHF MRI techniques provide powerful tools for studying the zebrafish brain, an emerging model in neurological research. In this work, various MRI and localized MRS methods are optimized and employed for UHF strength for studying the zebrafish brain. Specifically, these techniques are utilized to study the effect of TLR2-deficiency. Toll-like receptors, especially TLR2, are vital for recognizing pathogens and initiating immune responses. There is strong evidence that TLR2 is involved in the pathology of several neurological disorders. While essential for fighting infections, its dysregulation can lead to neuroinflammation and neurodegeneration. The full extent of TLR2's role in normal brain function remains poorly understood, requiring further research. The current work shows advanced imaging techniques allow to monitor microstructural and metabolic changes in the brain of a TLR2 deficient zebrafish model. This approach provides unprecedented detail and accuracy in studying the effects of TLR2 deficiency on zebrafish brain structure and function.

In **Chapter 1**, of this thesis, I provide the context and theoretical background of the various MRI, diffusion-based MRI, and MRS techniques utilized in the research. This chapter lays the foundation by explaining the principles and applications of these imaging methods, detailing how they contribute to our study. Additionally, the scope of the thesis is outlined, highlighting the specific objectives and research questions addressed in the subsequent chapters.

Chapter 2, focuses on the application of UHF MRI at 28.2 T for the visualization of brain structures and white matter tracts in zebrafish. Longitudinal relaxation times T_1, and transverse relaxation times T_2, are estimated for their significance in method optimization and their dependency on the applied magnetic field strength $\mathbf{B}_0$, showing an increase in T_1 and a decrease in T_2 compared to lower field strengths. For the visualization of major brain structures, the RARE sequence is optimized, providing high resolution anatomical images at a resolution of 23 µm × 23 µm. Furthermore, additional contrast is obtained by the utilization of diffusion properties in brain tissue through the utilization of DWI. Additionally, DTI is optimized for the estimation of diffusivity metrics. For the visualization of white matter structures, dMRI tractography employing stTDI msmt CSD is utilized on zebrafish brain data. The first results of these methods for intact zebrafish, show the ability to visualize tiny white matter structures in the zebrafish brain.

In **Chapter 3**, MRI, dMRI, and dMRI tractography methods are utilized for monitoring microstructural changes in the brain of *tlr2*$^{-/-}$ adult zebrafish. Anatomical imaging by RARE sequence reveal significant changes in the *tlr2*$^{-/-}$ brain morphology, while MSME indicate increased T_2 at various brain regions. Mono- and multi component analysis of the DWI data reveals a decrease in the apparent diffusion coefficient, which contributed specifically to an increase in slow component. These results potentially indicate astrogliosis, cytotoxic edema or inflammatory processes in the brain of *tlr2*$^{-/-}$ zebrafish. Zooming in on white matter structures, DTI and DKI reveal significant decrease in diffusivity and increases in diffusivity kurtosis in multiple white matter structures, indicative of reduced white matter integrity or inflammatory processes. Intriguingly, a potential link to neurobehavioral changes observed in *tlr2*$^{-/-}$ models can be made, including diminished spontaneous activity, diminished food consumption and disrupted circadian rhythms. Our results show that UHF MRI, dMRI, and dMRI tractography provides the necessary resolution and SNR to study microstructural changes in tiny structures in the brain of pathological zebrafish models.

Chapter 4 focuses on the optimization of single voxel localized ^{1}H MRS to monitor the neurochemical composition of the zebrafish brain at 28.2 T. UHF MRS provides MR spectra from selected regions as small as 125 nL. Highly resolved spectra were obtained and allow for the direct (relative) quantification of several metabolites, which was not yet achieved at lower magnetic field strengths. Although superior SNR and spectral resolution can be obtained, MR artifacts, specifically chemical shift displacement effects, are pronounced at 28.2 T. This required the utilization of strong gradient pulses with broad transmitter RF pulse bandwidth and a finely tuned excitation frequency for the metabolites of interest. After optimization, stable metabolic profiles are obtained from various locations in the zebrafish brain. This allows for the monitoring of the neurochemical environment across different brain regions. By adjusting acquisition parameters and leveraging the high spectral resolution available at 28.2 T, it is possible to minimize artifacts and maximize the reliability of the metabolite quantification. Consequently, this enables precise and reproducible mapping of metabolic changes, which is crucial for studying the brain's biochemistry under various physiological and pathological conditions.

In **Chapter 5** HR-MAS spectroscopy is utilized to monitor neurochemical changes in the brain of TLR2-deficient zebrafish. These data showed significant changes in the levels of the neurotransmitters glutamate and GABA, glutamine, alanine, lactate and myo-inositol, indicating alterations in neurotransmission and metabolic processes potentially indicative of excitotoxicity, increased cerebral energy demand, and astrogliosis. Furthermore, localized MRS was utilized to provide the metabolic profile of specific brain regions in the zebrafish. By targeting distinct areas within the brain, this technique allowed to measure regional variations

in metabolites, offering a detailed view of metabolic changes associated with TLR2-deficiency. This region-specific metabolic profiling enhances understanding of how TLR2 impacts various brain functions and structures, shedding light on its role in neurodevelopmental and neurodegenerative processes. The forebrain, midbrain, and hindbrain show high levels of lactate, indicating a brain wide increase in energy demand as a consequence of TLR2 deficiency. Furthermore, decreased levels of NAA are observed in the hindbrain, in a region overlapping with important white matter tracts, indicating TLR2-deficiency potentially has an effect on white matter integrity.

Finally, in **Chapter 6**, the general conclusion and future outlook of this work is provided.

SAMENVATTING

Microstructurele en Metabole Veranderingen in het Zebravis Brein veroorzaakt door Toll-Like Receptor 2 Deficiëntie

Inzichten verkregen met Ultra-Hoogveld beeldvorming met magnetische resonantie en Spectroscopie

Geavanceerde UHF MRI technieken bieden krachtige methoden voor onderzoek naar het brein van zebravissen, een opkomend model in neurologisch onderzoek. In dit werk worden verschillende MRI en gelokaliseerde-MRS methoden geoptimaliseerd en toegepast voor gebruik bij UHF-sterkte, specifiek voor onderzoek naar zebravis hersenen. Deze technieken worden gebruikt om het effect van TLR2-deficiëntie te bestuderen. Toll-like receptoren, en met name TLR2, zijn van vitaal belang voor het herkennen van pathogenen en het initiëren van immuunreacties in het lichaam. Er is echter sterk bewijs dat TLR2 ook betrokken is bij de ontwikkeling van verschillende neurologische aandoeningen. Hoewel essentieel voor het bestrijden van infecties, kan TLR2 dysregulatie leiden tot neuro-inflammatie - ontstekingen in het brein, en neurodegeneratie - de geleidelijke afbraak van zenuwcelstructuren. De volledige rol van TLR2 in de normale hersenfunctie is nog steeds slecht begrepen en vereist verder onderzoek. Dit onderzoek toont aan dat geavanceerde MRI technieken het mogelijk maken om microstructurele en metabolische veranderingen in de hersenen van een TLR2-deficientie zebravismodel te monitoren. Deze aanpak biedt ongekende details en nauwkeurigheid bij het bestuderen van de effecten van TLR2-deficientie op de structuur en functie van de zebravishersenen.

Hoofdstuk 1 van dit proefschrift biedt de context en theoretische achtergrond van de verschillende MRI-, diffusie MRI - en MRS-technieken die in dit onderzoek worden gebruikt. Dit hoofdstuk legt de basis door de principes en toepassingen van deze technieken uit te leggen en te beschrijven hoe ze bijdragen aan het onderzoek. Bovendien wordt de reikwijdte van het proefschrift geschetst, waarbij de specifieke doelstellingen en onderzoeksvragen in de volgende hoofdstukken de revue passeren.

Hoofdstuk 2 richt zich op de toepassing van UHF MRI bij 28.2 T voor de visualisatie van hersenstructuren en witte stofbanen in zebravissen. De longitudinale relaxatietijden T_1 en transversale relaxatietijden T_2 worden bepaald, waarbij een toename van T_1 en een afname van T_2 is geobserveerd in vergelijking met lagere veldsterktes. Voor de visualisatie van hersenstructuren wordt de RARE sequentie geoptimaliseerd, wat resulteert in hoog-resolutie anatomische beelden met een resolutie van 23 µm × 23 µm. Bovendien wordt aangetoond dat extra contrast wordt verkregen door gebruik te maken van diffusie-eigenschappen

in hersenweefsel via DWI. Daarnaast wordt DTI geoptimaliseerd voor de schatting van diffusiviteitsmetingen. Voor de visualisatie van witte stofstructuren wordt dMRI-tractografie toegepast met behulp van stTDI msmt CSD. De eerste resultaten van deze methoden voor intacte zebravissen, laten het vermogen zien om kleine witte stofstructuren in de zebravishersenen te visualiseren.

In **hoofdstuk 3** worden MRI-, dMRI- en dMRI-tractografie-methoden gebruikt om microstructurele veranderingen in de hersenen van *tlr2*$^{-/-}$ zebravissen te monitoren. Anatomische MRI onthult significante veranderingen in de *tlr2*$^{-/-}$ hersenmorfologie, terwijl MSME verhoogde T_2 aantoont in verschillende hersengebieden. Mono- en multi-componentanalyse van de DWI-gegevens toont een afname van de ADC, specifiek toe te schrijven aan een toename van de langzame ADC component. Deze resultaten wijzen mogelijk op astrogliosis, cytotoxisch oedeem of ontstekingsprocessen in de hersenen *tlr2*$^{-/-}$ zebravissen. Analyse van witte stofstructuren, onthult een significante afname van de diffusiviteit en een toename van de diffusie-kurtose in meerdere witte stofstructuren, wat wijst op verminderde witte stofintegriteit of ontstekingsprocessen. Opvallend is dat er een mogelijke link kan worden gelegd naar gedragsveranderingen die zijn waargenomen in *tlr2*$^{-/-}$ modellen, zoals verminderde spontane activiteit, verminderde voedselinname en verstoorde circadiane ritmes. De resultaten tonen aan dat UHF MRI, dMRI en dMRI-tractografie de benodigde resolutie en SNR bieden om microstructurele veranderingen in kleine structuren in de hersenen van pathologische zebravismodellen te bestuderen.

Hoofdstuk 4 richt zich op de optimalisatie van enkelvoudige voxel gelokaliseerde ^{1}H MRS om de neurochemische samenstelling van de zebravishersenen bij 28.2 T te monitoren. Er wordt aangetoond dat UHF MRS MR-spectra levert van geselecteerde regio's tot 125 nL. "Chemical shift displacement effects" verstoren de waarnemingen bij 28.2 T, waardoor het gebruik van sterke gradientpulsen en een goed afgestemde excitatiefrequentie specifiek voor de gewenste metabolieten vereist is. Na optimalisatie worden stabiele metabole profielen verkregen op verschillende locaties in de zebravishersenen. Dit maakt monitoring van het neurochemische milieu in verschillende hersengebieden mogelijk. Door acquisitieparameters aan te passen en gebruik te maken van de hoge spectrale resolutie die beschikbaar is bij 28.2 T, is het mogelijk om MRI artefacten te minimaliseren en de betrouwbaarheid van de metabolietkwantificatie te maximaliseren. Dit stelt ons in staat om precieze en reproduceerbare veranderingen van de concentraties van metabolieten te observeren, wat cruciaal is voor het bestuderen van de biochemie van de hersenen onder verschillende fysiologische en pathologische omstandigheden.

In **hoofdstuk 5** wordt HR-MAS spectroscopie gebruikt om neurochemische veranderingen in de hersenen van TLR2-deficiente zebravis te monitoren. Significante veranderingen in de concentraties van glutamaat, GABA, glutamine, alanine, lactaat en myo-inositol werden gevonden. Deze gegevens wijzen op veranderingen in neurotransmissie en metabole processen, mogelijk indicatief voor excitotoxiciteit, verhoogde cerebrale energievraag en astrogliosis. Verder werd gelokaliseerde MRS gebruikt om informatie te verkrijgen over het metabole profiel van specifieke hersenregio's bij de zebravis. Met een focus op verschillende gebieden binnen de hersenen, maakt deze techniek het mogelijk om ruimtelijke variaties in concentraties van metabolieten te meten, waardoor een gedetailleerd beeld ontstond van metabolische veranderingen die geassocieerd zijn met TLR2-deficientie. In de voor-, midden en achterhersenen werden hoge niveaus van lactaat waargenomen, wat wijst op een sterke energievraag in de hersenen als gevolg van TLR2-deficientie. Een laag niveau van NAA in de achterhersenen, in een gebied dat overlapt met belangrijke witte stofbanen, geeft aan dat TLR2-deficientie mogelijk een effect heeft op de integriteit van de witte stof.

Tot slot wordt in **hoofdstuk 6** de algemene conclusie en toekomstige vooruitzichten van dit werk gegeven.

LIST OF PUBLICATIONS
CURRICULUM VITAE
ACKNOWLEDGEMENTS

FULL PUBLICATIONS

1. **Metabolic Profiling of Suprachiasmatic Nucleus Reveals Multifaceted Effects in an Alzheimer's Disease Mouse Model.** Eeza MNH, **Singer R**, Höfling C, Matysik J, de Groot HJM, Roβner S, Alia A. J Alzheimers Dis. **2021**;81(2):797-808. doi: 10.3233/JAD-201575. PMID: 33843677; PMCID: PMC8203226.

2. **Evaluation of suprachiasmatic nucleus in Alzheimer's disease with non-invasive magnetic resonance methods. Singer R**, Alia A. Neural Regen Res. **2022**;17(8):1753-1754. doi: 10.4103/1673-5374.332136. PMID: 35017432; PMCID: PMC8820719.

3. **Probing microstructural changes in muscles of leptin-deficient zebrafish by non-invasive ex-vivo magnetic resonance microimaging.** Eeza MNH, **Singer R**, Ding Y, He J, Zuberi Z, Baelde HJ, de Groot HJM, Matysik J, Spaink HP, Alia A. **2023** PLOS ONE 18(4): e0284215. Doi: 10.1371/journal.pone.0284215

4. **Ultrahigh field diffusion magnetic resonance imaging uncovers intriguing microstructural changes in the adult zebrafish brain caused by Toll-like receptor 2 genomic deletion. Singer R**, Oganezova I, Hu W, Liu L, Ding Y, de Groot HJM, Spaink HP, Alia A. NMR Biomed. **2024** May 14:e5170. doi: 10.1002/nbm.5170. PMID: 38742727.

5. **Unveiling the Exquisite Microstructural Details in Zebrafish Brain Non-Invasively Using Magnetic Resonance Imaging at 28.2 T. Singer R,** Oganezova I, Hu W, Ding Y, Papaioannou A, de Groot HJM, Spaink HP, Alia A. Molecules **2024**, 29, 4637. https://doi.org/10.3390/molecules29194637

CONFERENCE PROCEEDINGS

1. **Magnetic Resonance Imaging of zebrafish (Danio rerio) at ultra-high magnetic field (1.2 GHz). Singer R**, Krug JR, Hu W, Spaink HP, de Groot HJM, Alia A. Proceedings Euromar (2022)

2. **Micro-imaging of zebrafish (*Danio rerio*) at 1.2 GHz (28.2 Tesla). Singer R**, Prompers JJ. Proceedings Euromar (2022). Presented during the satellite meeting of Euromar (2022)

3. **Diffusion-based MRI at 28.2 T to resolve microstructural details and white matter tracts in young adult zebrafish brain. Singer R**, Hu W, Spaink HP, de Groot HJM, Alia A. Proceedings Euromar (2023)

4. **Exploring the potential of ultrahigh magnetic field (1.2GHz) in Diffusion MRI to resolve white matter tracts in zebrafish brain. Singer R**, Alia A. Presented during the annual Dutch NMR Discussion group (NMR DG) meeting (2024).

5. **Unbeatable super-resolution of voxel-based MR spectroscopy of zebrafish brain achieved at 28.2 T. Singer R**, Hu W, Liu L Spaink HP, de Groot HJM, Alia A. Presented during the MRI parallel session during Euromar (2024)

6. **Diffusion MRI and localised spectroscopy of organoids on 1.2 GHz.** Tax C.M.W., Nikolaeva T, **Singer R**, Jakobs C, Alia A, Velders A, Pasterkamp J, Krug J.R. Proceedings Euromar (2024)

7. **The Precision of Ultrahigh Field MRI: Detecting intriguing Microstructural Changes in the Brain of Leptin-Deficient Zebrafish. Singer R**, Velthuyzen A, Ding Y, de Groot HJM, Spaink HP, Alia A. Proceedings Euromar (2024)

CURRICULUM VITAE

Rico Singer was born on the first of July 1993 in 's-Gravenhave (The Hague / Den Haag) in the Netherlands. He obtained his high school diploma in 2011 at the Baken Park Lyceum. For his bachelor's degree, Rico moved to Delft and studied Chemistry at the Hogeschool Rotterdam (Rotterdam University of Applied Sciences). During his studies, Rico participated in the Analytical Science Talent Program (ASTP), an honors program offered by the Top Institute for Comprehensive Analytical Science and Technology (TI COAST). Additionally, Rico completed internships focusing on analytical chemistry. At Royal Dutch Shell in Rijswijk, concentrating on size exclusion chromatography; at BiosparQ B.V. in Leiden, focusing on matrix-assisted laser desorption/ionization (MALDI) mass spectrometry, and for his bachelor's thesis project at the DSM Biotechnology Center in Delft, focusing on method development for semi-preparative liquid chromatography. In 2017, Rico attended the pre-master's program in Chemistry at the University of Amsterdam (UvA) and the Vrije Universiteit (VU), after which he commenced his Master Analytical sciences at the same institutes. During his master, Rico performed another internship at the DSM Biotechnology Center in Delft, focussing on integrating various analytical techniques to isolate and identify bioactive compounds from microorganisms. This involved semi-preparative liquid chromatography, mass-spectrometry, and various nuclear magnetic resonance methods. Alongside his Bachelor and Master degree, Rico was a member of the "Delftse Studenten Roeivereniging Proteus-Eretes", where he was actively involved in the organisation of various events, including rowing competitions, business days, and field trips. Furthermore, he was significantly involved in the organisation of the lustrum year, which spanned an entire year and encompassed numerous activities. Additionally, he managed self-operating sub-committees responsible for organizing specific events during this year.

After his Master degree, Rico started his PhD project in 2020 at the university of Leiden in the Biophysical Organic Chemistry and solid-state NMR (BPOC SSNMR). During his PhD, Rico was supervised by Dr. A. Alia and Prof. Dr. H.J.M. de Groot. Rico's PhD project focused on optimizing and applying a wide range of magnetic resonance imaging (MRI) and magnetic resonance spectroscopy (MRS) techniques for examining the tiny zebrafish (*Danio rerio*) brain at ultra-high fields. This included utilizing the state-of-the-art 28.2 T MR system. During his PhD, Rico presented his work at several scientific conferences, including Euromar 2022 in Utrecht, the Netherlands; Euromar 2023 in Glasgow, United Kingdom; and Euromar 2024 in Bilbao, Spain. Furthermore, he presented his work at the 2023 Dutch NMR Discussion group meeting in Oss and during the 2024 national ultra-high field NMR (uNMR-NL) annual meeting in Utrecht. Rico participated in scientific courses and summer schools, including the course "Scientific Conduct for PhDs" provided by the graduate school of Leiden University and the International Society of Magnetic Resonance (ISMAR) summer school "Theory of NMR" at Schloss Windischleuba in the field of General NMR (2022) and Relaxation (2023).

ACKNOWLEDGEMENTS

Groundbreaking solitary research efforts are rare. Every scientist, whether they're a graduate student or a tenured professor, needs to acknowledge that their accomplishments would not have been able without the help of others. I am no exception to this rule. Although it is often difficult to find the right words to express my gratitude, I will make every effort to do so.

First and foremost, I would like to express my sincere gratitude to **A. Alia** and **Huub de Groot**, for their guidance and support throughout my PhD project. You consistently challenged me to think critically about my work, while also recognizing and celebrating my progress. Thanks to your mentorship, I have developed numerous skills that will undoubtedly be invaluable as I continue my scientific career.

Of course, I would like to thank my paranymphs, **Titus de Haas** and **Bas Kreupeling**, for their invaluable support in helping me bring my PhD journey to a successful conclusion. Your encouragement, assistance, and presence throughout this journey meant a lot to me.

I would also like to acknowledge the help from the master and bachelor students that were involved in various parts of this work, **Ina Oganezova**, **Alexandra Velthuijzen**, and **Camiel Hildenberg**. It was a pleasure to work with you.

In many ways, the Biophysical Organic Chemistry and Solid-State NMR (BPOC/SSNMR) group and its staff deserve my gratitude. Although I was the sole person involved in MRI, there was no lack in scientific discussions which elevated the quality of my research. These past few years would not have been the same without our lunches, drinks, pizzas, coffees, cakes, buitendagen, baby showers, Christmas parties, and unplanned corridor talks. For this, I would like to thank the remaining part of the BPOC/SSNMR group during my time there: **Francesco**, **Anjali**, **Agur, Dario, Suzanne**, **Dario**, **Lolita**, **Serkan**, **Tirong**, **Matthijs**, **Art**, **Padmaja**, **Xinmeng**, **Willem**, **Jan Paul**, **Laura, Rianne, Anouska**, **Chuang**, **Margareth**, **Willemijn**, **Tjeerd**, **Emiel**, **Rick**, **Jonas**, **Jos**, **Sam**, **Roxane**, **Simon**, **Pien**, and **Aegir**. Of course, there is a single person that deserves special thanks. Thank you, **Liesbeth,** for everything these years. You are truly a key member of the group.

For their endless technical support, I would like to thank **Karthick Sai Sankar Gupta**, **Fons Lefeber**, and **Maria Nardella**. You made my long days spend behind the MRI a whole lot better.

For their many hours spend on helping me handle the zebrafish, I would like to thank **Yi Ding**, **Li Liu**, **Herman Spaink**, and most of all **Wanbin Hu**. Without your help, there would have been very little for me to measure in the MRI.

From the Universität Leipzig, **Narmin Bashirova** and **Muhamed Nour Hashem Eeza** deserve my gratitude for the many personal, scientific and philosophical discussions we shared, as well as for their assistance in the field of MRI and HR-MAS.

The micro MRI at UHF community within the Netherlands is rather small. As a result, the support from members of this community proved invaluable throughout my PhD project. I am especially grateful to **Julia Krug** and **Tatiana Nikolaeva** from Wageningen university & Research for always being available. Additionally, I would like to extend my sincere thanks to **Chantal Tax** from UMC Utrecht for generously sharing her expertise in diffusion MRI, involving me in her projects, and providing me the opportunity to present my work to her group.

My thanks to the ultra-high field Nuclear Magnetic Resonance facility in for the Netherlands (uNMR-NL), supported by the Nederlandse Organisatie voor Wetenschappelijk Onderzoek (NWO), for enabling me to perform countless hours of MRI experiments at various ultra-high field MRI systems all over the Netherlands.

I thank **Volker Lehmann**, **Thomas Oerther**, **Antonios Papaioannou**, **Oliver Gruschke**, and **Sarah Mailhiot** from Bruker BioSpin, who were always available to answer my many questions. My sincere gratitude to the **Swaantje Mondt Fonds** and the **Stichting Praesidium Libertatis I** for their generous financial support during my PhD, which enabled me to undertake a research visit to the Institute for Medical Physics and Biophysics at Universität Leipzig, Germany.

For their many hours spend on making this PhD thesis look as good as it does, I would like to thank **Susanne Ottenheym** and **Ward van Zeijl**. You turned my ideas into reality, and for that I am grateful.

It is easy for one to start feeling isolated during a PhD, especially if it coincides with a global pandemic. There are many people, to many to start listing here, which helped me through these years. Not by providing me with any scientific input, but simply by being there for me when I needed some distraction. Without these dear friends, I would not have made it this far. Thank you for everything.

None of what I accomplished would have been possible without the support of my family; **Richard**, **Anoesjka**, **Axl** , **Sanne** and **Diëgo**. Thank you for keeping me sane and continuously reminding me of the things that are truly important in life.

Above all, **Mart**, you helped me through all these years. You told me that you already know how grateful I am for your tireless support and that there is no need to put those words on paper. Nonetheless, I thank you for everything and I truly believe I wouldn't have come this far without you by my side.

Finally, I dedicate my closing words to **Maria Spaans**, **Oma Riet**, whose absence I continue to feel every day. On the fifth of May 2023, in the middle of my PhD, I had to say goodbye to you. The fact that you are no longer here breaks my heart, but I know you would have been extremely proud of me.